ABSTRACT

Title of Document:	DYNAMICS AND HAZARDS OF CASCADING FAILURE IN LITHIUM ION CELL ARRAYS: ANALYSIS, PASSIVE MITIGATION, AND ACTIVE SUPPRESSION
	Ahmed O. Said, Doctor of Philosophy, 2020
Directed By:	Associate Professor Stanislav I. Stoliarov, Department of Fire Protection Engineering, Department of Mechanical Engineering

Exposure of lithium ion battery (LIB) to abnormal operating conditions may result in rapid self-heating accompanied by ejection of flammable materials, this phenomenon is referred to as thermal runaway (TR). In a multi cell array, TR of an individual cell may propagate to neighboring cells, this phenomenon is referred to as cascading failure. Cascading failure is hazardous and may cause large scale fires or explosions. In this work, a new experimental setup was developed to investigate cascading failure in arrays constructed from lithium cobalt oxide (LCO), lithium nickel manganese cobalt oxide (NMC), and lithium iron phosphate (LFP) cells of 18650 form factor. Fully charged cells were arranged in rectangular arrays: 3×4 or 3×6 with no gaps between adjacent cells and were mounted in a specially designed wind tunnel to achieve well-controlled environmental conditions. TR was initiated in one cell using an electric heater and observed to propagate through the array using temperature sensors attached to individual cells. Tests were conducted in N_2 and air to elucidate the flaming combustion impact.

In nitrogen, TR propagation speed showed no significant dependence on the

size of the array. The speed of the propagaion was found to be greater in air than in nitrogen. The LFP cells were the only cells that did not always fully propagate TR. In nitrogen, all cells produced large amounts of hydrocarbons, CO and CO_2, and minor amounts of O_2 and H_2. Total heats generated due to chemical reactions between cell components and flaming combustion of ejected materials normalized by the electrical energy stored were determined to be 3.5, 2.9, and 2.5 for LCO, NMC, and LFP cells, respectively.

Different passive mitigation strategies, including implementing 5 mm gaps between cell groups and inserting physical barrier into these gaps, were investigated. Among the barriers, ceramic fiber board was found to be the most effective, slowing down the propagation by more than a factor of 30. Lastly, the effectiveness of two fire extinguishing agents, Novec1230 and water mist, was investigated. Applying Novec1230 agent at 15.2 vol.% significantly inhibited combustion of ejected materials and prevented complete TR propagation through fully charged LCO cell arrays.

DYNAMICS AND HAZARDS OF CASCADING FAILURE IN LITHIUM ION CELL ARRAYS: ANALYSIS, PASSIVE MITIGATION, AND ACTIVE SUPPRESSION

by

Ahmed O. Said

Dissertation submitted to the Faculty of the Graduate School of the
University of Maryland, College Park, in partial fulfillment
of the requirements for the degree of
Doctor of Philosophy
2020

Advisory Committee:
Professor Stanislav I. Stoliarov, Chair
Professor Dongxia Liu, Dean's Representative
Professor Arnaud Trouve
Professor Marino diMarzo
Professor Peter Sunderland

Acknowledgments

First and foremost, I express my utmost gratitude to Allah, The All-Knowing and The Most Generous, for providing me with the strength and patience needed to finish my dissertation and for reaching this outstanding stage in my career.

I would like to sincerely thank my advisor Prof. Stanislav Stoliarov for offering me the opportunity to join his material flammability research group at the University of Maryland. Without his endless support and constructive feedback, the present work would not have been achieved. His dedication to his research group and passion for research is really impressive. On an academic level, he pushed my mind to its limits, enhanced my technical writing and presentation skills, and taught me how to develop new interesting research ideas. I have learned a lot from his intuitive approach to solving problems. When it comes to discipline and hard work, he is truly a role model. Dr. Stas, I am very grateful and thankful for you and ready to apply the skills and principles I have learned from you. I wish you and your family all the best.

Special thanks go to Chris Lee, whose significant contributions to the project and the current work can never be repaid. Chris and I have spent long times in the lab to build the current experimental facility and run lots of tests. Chris also helped me a lot to review my articles and helped me a lot to enhance my technical writing. Thank you Chris, it has been a pleasure working with you. I also would like to thank Dr. Andre Marshall for helping with designing and building the experimental setup.

I am also very grateful to my dissertation committee members, Prof. Dongxia Liu, Prof Arnaud Trouve, Prof. Marino diMarzo, and Prof. Peter Sunderland, for

accepting to serve in my committee and providing valulable comments on the present work.

I would like to extend my gratitude to my former and current colleagues at the University of Maryland: Xuan, Zhibo, Conor, A. Khalil, A. El Melih, Kiran, Fernando, Isaac, Dushyant, Yan, Josh, Greg, Jacques, Jess, Cara, Gerg, Adam, Lucas, Will, Emily, Alex and Yang. Thank you all for helping me to finish this work.

I would like to thank my family in Egypt for their unwavering support. My parents were always there for me when I needed their guidance and prayers. I am also very thankful and grateful for my wife Aya, who gave me nothing but support and love. Througout this journney, we have faced lots of hardships and have been able to pass all of them together thanks to her patiance and encourgement. I am thankful to my lovely daughters, Farida and Taleya, who made the life easier for me and brought all the joy to our small family.

I would like to acknowledge the support provided by United Technologies Corporation (UTC) [Grant # 4318161]. Also, I am very grateful for the UTC technical team, Fred, Jonathan, Joe, Jeffery, and Bob, for their constructive feedback.

Table of contents

List of Tables

List of Figures

Nomenclature

Acronyms	Descriptions
LIB	Lithium Ion Battery
PVDF	Polyvinylidene Difluoride
PC	Propylene Carbonate
EC	Ethylene Carbonate
DMC	Dimethyl Carbonate
DEC	Diethyl Carbonate
EMC	Ethyl-methyl Carbonate
SEI	Solid Electrolyte Interface
Li+	Lithium Ions
SOC	State of Charge
SV	Safety Venting
TR	Thermal Runaway
DSC	Differential Scanning Calorimeter
ARC	Accelerating Rate Calorimetry
VSP2	Vent Sizing Package 2
TGA	Thermogravimetric Analysis
MCMF	Meso Carbon Microfiber
CSBC	Copper Slug Battery Calorimeter
LCO	Lithium Cobalt Oxide
NMC	Nickel Manganese Cobalt Oxide

LFP	Lithium Iron Phosphate
HRR	Heat Release Rate
THC	Total Unburned Hydrocarbons
FTIR	Fourier-Transform Infrared Spectroscopy
sp	Solid Particulates

Symbols	Descriptions
V_{min}	Minimum Cutoff Voltage
Li_xC_6	Lithiated Carbon Anodes
vol.%	Volumetric percentage
W	Pressure Difference Factor Across the Perforated Screen
ρ	Air Density
V_1	Injector Air Flow Velocity
P_t	Total Pressure
P_2	Static Pressure at the Exit of the Perforated Screen
Q	Air Flow Rate
A_{inj}	Injector Area
N_{inj}	Number of Injectors
K_{plate}	Perforated Plate Factor
A_{open}	Perforated Plate Open Area

Re_D	Reynolds Number
u	Pre-test Section Air Speed
D_h	Tunnel Hydraulic Diameter
ν	Kinematic Viscosity
A_c	Tunnel Cross Section Area
P_w	Tunnel Wetted Perimeter
$\dot{m}_{WM}$	Water Mist Mass Flow Rate
$\dot{m}_{air}$	Air Mass Flow Rate
Y_{WM}	Mass Fraction of Water Mist
P_{std}	Standard Atmospheric Pressure
T_{std}	Standard Atmospheric Temperature
T_0	Initial Temperature of the System
wt.%	Mass Percentage
Y_{WV}	Water Vapor Mass Fraction
T_{LIB}	LIB's Bottom Temperature
dT_{LIB}/dt	Time Derivative of LIB's Bottom Temperature
S_P	Thermal Runaway Propagation Speed
$\dot{m}_{LIBs}$	Mass Flow Rate of Ejected Battery Materials
$m_{initial}\|_i$	Initial Mass of Individual LIB cell
$m_{final}\|_i$	Final Mass of Individual LIB cell
N	Number of Cells

X_j	Volume or Mole Fraction of Gas
$\dot{m}_j$	Mass Flow Rate of Gas
μw_j	Molecular Weight of Gas
$\dot{m}_{N_2}$	Nitrogen Mas Flow Rate
μw_{N_2}	Molecular Weight of Nitrogen
m_j	Mass Yield of Each Gas
t_{exp}	Duration of Cascading Failure Experiment
$LFL_{mixture}$	Lower Flammability Limit of Gas Mixture
m_{THC}	Mass Yield of Methane
m_{CO}	Mass Yield of Carbon Monoxide
m_{H_2}	Mass Yield of Hydrogen
μw_{THC}	Molecular Weight of Methane
μw_{CO}	Molecular Weight of Carbon Monoxide
μw_{H_2}	Molecular Weight of Hydrogen
LFL_{THC}	Lower Flammability Limit of Methane
LFL_{CO}	Lower Flammability Limit of Carbon Monoxide
LFL_{H_2}	Lower Flammability Limit of Hydrogen
V_{flam}	Maximum Enclosure Volume
$\overline{R}$	Universal Gas Constant

P_{CHG}	Rate of Chemical Heat Generation
E_{CHG}	Total Chemical Heat Generation
P_{loss}	Rate of Heat Loss
P_{heater}	Heater Input Power
$\dot{m}_{sp}$	Mass Flow Rate of Solid Particulates
$\bar{C}_{p_j}$	Mean Constant Pressure Heat Capacities
C_{p_j}	Polynomial Pressure Heat Capacities

1. Introduction

1.1 Motivation and Background

For decades, the world has been depending on fossil fuels as a main source of energy and power generation. However, growing concerns associated with the environmental impact of greenhouse gas emissions [1] (caused by combustion of fossil fuels) stimulate exploration of renewable energy sources, which are eco-friendly but tend to be intermittent in nature. Effective utilization of renewable energy sources is only achievable when integrated with reliable energy storage systems [2, 3]. State-of-the-art lithium ion batteries (LIBs) have shown a great promise as building blocks for energy storage systems due to their optimal combination of high energy density, high efficiency, longevity, light weight, portability, form factor variability, and lack of a memory effect [2-4]. Examples of some commercial LIB cells are shown in Figure 1. 1. However, several accidents [5, 6] and mounting empirical evidence [7-11] suggest that LIBs and LIB-based systems may fail catastrophically, causing fire and/or explosion in the enclosures housing those systems. As LIBs are constantly being deployed in a multitude of residential and commercial applications, the safety of LIBs becomes an important area of investigation.

Figure 1. 1. Examples of commercial lithium ion batteries (LIBs) with various form factors (cylindrical, prismatic, and pouch cells) [12].

1.2 Components of LIB Cells

It is essential to identify the major components of LIB cells before studying the failure mechanisms of LIB-based systems. Figure 1. 2 depicts the major components of two representative LIB form factors: cylindrical and prismatic. Typically, an individual LIB cell consists of four primary components: negative electrode (anode), positive electrode (cathode), separator, and electrolyte. Two separator layers sandwich the anode and cathode plate. These layers are then all jelly-rolled or folded and secured in a steel casing. The cathode plate is connected to the positive terminal on the LIB casing while the anode plate is connected to the negative terminal. Each primary component of the LIB cell is discussed in the following subsections.

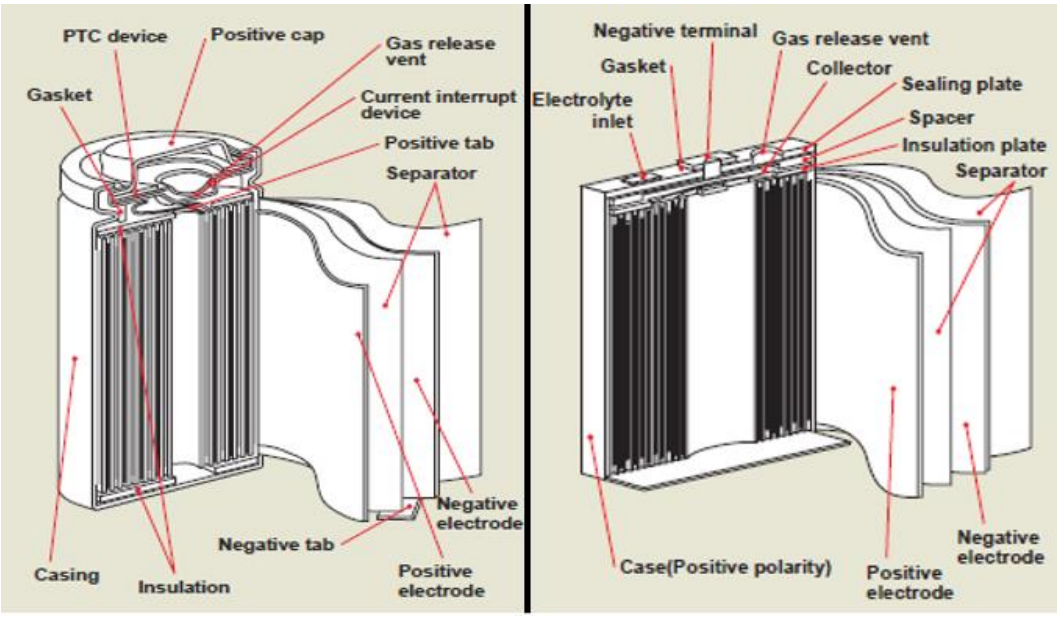

Figure 1. 2. Detailed structures of cylindrical and prismatic LIB cells [13].

1.2.1 Negative Electrode (Anode)

The anode electrode is considered the reducing or fuel element in the battery and composed of > 90% of active material powders and < 10% of binder material. In most commercial LIB cells, the anode active material is carbon (mostly graphite). The nature of carbon can vary considerably in sources (natural or synthetic), purity, size/distribution/porosity/shapes of particles, crystalline phase, and degree of compactness. The powders are combined with a binder material (such as Teflon, or Polyvinylidene difluoride (PVDF) < 10%) and coated as a thin layer onto a metal current collector (typically copper foil or grid) [2, 4, 14, 15].

1.2.2 Positive Electrode (Cathode)

The cathode electrode (oxidizing electrode) is composed of powders (active material, > 90%) that are combined with conductivity enhancers (carbon powders) and a polymeric binder. The mixture is subsequently coated as a thin layer onto a current collector (typically aluminium foil or grid). The most common cathode active materials

in LIB cells are layered oxides (such as lithium cobalt oxide, $LiCoO_2$), polyanions (such as lithium iron phosphate, $LiFePO_4$), spinels (such as lithium manganese oxide, $LiMn_2O_4$), or mixed metal oxides (such as lithium nickel manganese cobalt oxide, $LiNi_XMn_YCo_ZO_2$) [2, 4, 14, 15].

1.2.3 Electrolyte

The electrolyte (ionic conductor) represents the medium for transfer of lithium ions between the anode and cathode electrodes. The electrolyte must have good ionic conductivity, wide electrochemical voltage range (0 to 5 V), high thermal stability (up to 70 °C), and compatibility with other cell components [4]. The electrolyte is typically a mixture of organic carbonates (solvent) containing complexes of lithium ions. Table 1. 1 provides information on critical temperatures and heats of combustion for some common organic carbonates. These non-aqueous electrolytes include non-coordinating anion salts such as lithium hexafluorophosphate ($LiPF_6$), lithium hexafluoroarsenate monohydrate ($LiAsF_6$), lithium perchlorate ($LiClO_4$), and lithium tetrafluoroborate ($LiBF_4$) [2]. Cell manufacturers include low concentrations of additives to improve performance characteristics such as overcharge resistance, cycle life, calendar life, and thermal stability [2, 15]. The additives are also used to reduce electrolyte flammability under cell venting circumstances [14].

Table 1. 1. Critical temperatures and heats of combustion of some typical carbonates utilized in the LIBs electrolyte.

Electrolyte component	Chemical formula	Melting point [°C] [4]	Boiling point [°C] [4]	Flash point [°C] [16]	Auto-ignition temperature [°C] [17, 18]	Heat of combustion [kcal $mole^{-1}$] [19]
Propylene carbonate (PC)	$C_4H_6O_3$	-49	240	132	430	-4.8
Ethylene carbonate (EC)	$C_3H_4O_3$	39	248	151	465	-4.1
Dimethyl carbonate (DMC)	$C_3H_6O_3$	4.6	91	15	458	-3.8
Diethyl carbonate (DEC)	$C_5H_{10}O_3$	-43	126	33	445	-5.0
Ethyl-methyl carbonate (EMC)	$C_4H_8O_3$	-43	109	22	440	N/A

At normal temperature conditions, mixtures of carbon (anode) and organic electrolyte are not thermodynamically stable and reactions between the two materials are likely to occur. These reactions lead to the formation of a passivating layer on the carbon surface of the anode, commonly referred to as the solid electrolyte interphase (SEI) [4, 15]. After the cell is manufactured and assembled, it is slowly charged (and possibly cycled and aged) in a process referred to as formation process [15, 20]. This formation process is intentionally performed to produce a uniform, stable SEI layer on the cell anode to prevent irreversible consumption of the electrolyte and lithium ions.

1.2.4 Separator

The separator is a thin (10 to 30 μm) micro-porous polymer film located between the anode and cathode to prevent internal short circuit. The pores allow transfer of lithium ions by diffusion between the electrodes during charging and discharging. Most commercial separators are made from microporous polyolefin materials (such as polyethylene, polypropylene, or laminates of polyethylene and polypropylene) because of their excellent mechanical properties, high chemical stability, and low cost. Commercial materials have a pore size of 0.03 to 0.1 μm and 30% to 50% porosity. Thermal shutdown separators are widely used in modern LIBs because of their significant role in enhancing safety. If the temperature of an LIB cell abnormally increases, a portion of the separator material will melt and plug the micro size pores. Currently, the shutdown function will also permanently disable the entire cell in the case of an abnormal internal temperature rise to approximately 130 °C. However, if internal temperatures rise significantly above approximately 150 °C, the separator will melt entirely and allow contact (short circuit) between the anode and cathode [2, 4, 14].

1.3 Charging and Discharging Mechanisms of LIB Cells

When an LIB cell is charged, lithium ions (Li+) are de-intercalated from the layered metal oxide (cathode). Figure 1. 3 shows that the lithium ions are subsequently transferred across the electrolyte and intercalated between the layers of graphite of the anode. The electrons flow through an external electrical circuit. This process is reversed during discharge; the red and green dashed lines utilized in Figure 1. 3 demonstrate the difference between the directions of electrons during charging and discharging processes [2, 4, 16].

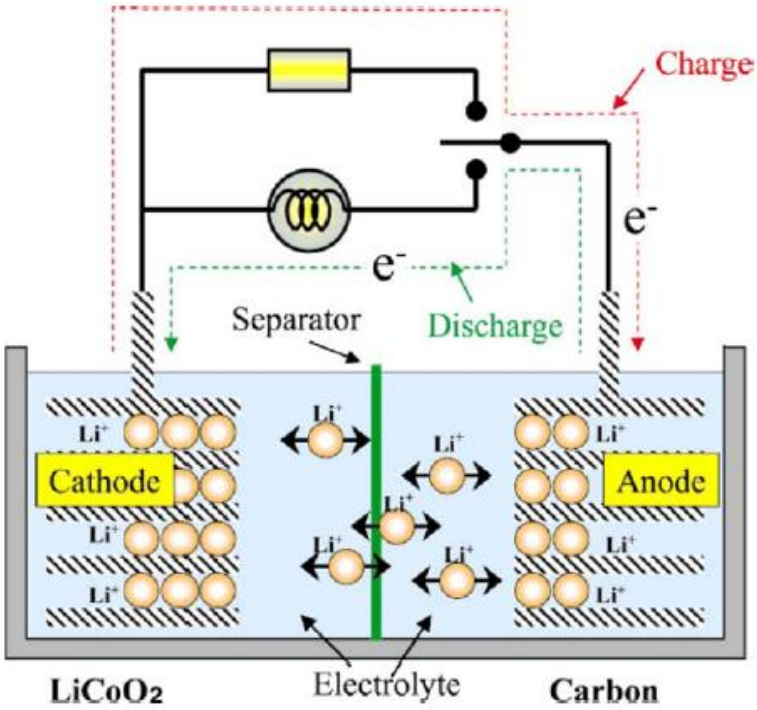

Figure 1. 3. Schematic of the charging and discharging processes of an LIB cell [2].

Individual lithium ion batteries (LIBs) are designed to safely operate (charge and discharge) between limits of minimum and maximum cutoff voltages [4, 21]. For most of the commercial LIBs, the voltage limits are 3.0 V (fully discharged or 0% state of charge, SOC) and 4.2 V (fully charged, 100% SOC). Additionally, the LIBs are classified by a nominal voltage that is defined as the relatively constant voltage maintained by LIB cell during most of its discharge time. The nominal voltage of a typical LIB cell is approximately 3.6 to 3.7 V.

Constant current/constant voltage method [4] is used for charging LIBs. Figure 1. 4 shows that the charging process starts with a relatively high constant current to a given voltage (maximum cutoff voltage provided by the manufacturer) and then tapers charging at a constant voltage to a given current (minimum cutoff current provided by the manufacturer). This method helps to avoid exceeding the maximum allowable voltage, which prevents any damage to the LIB cell.

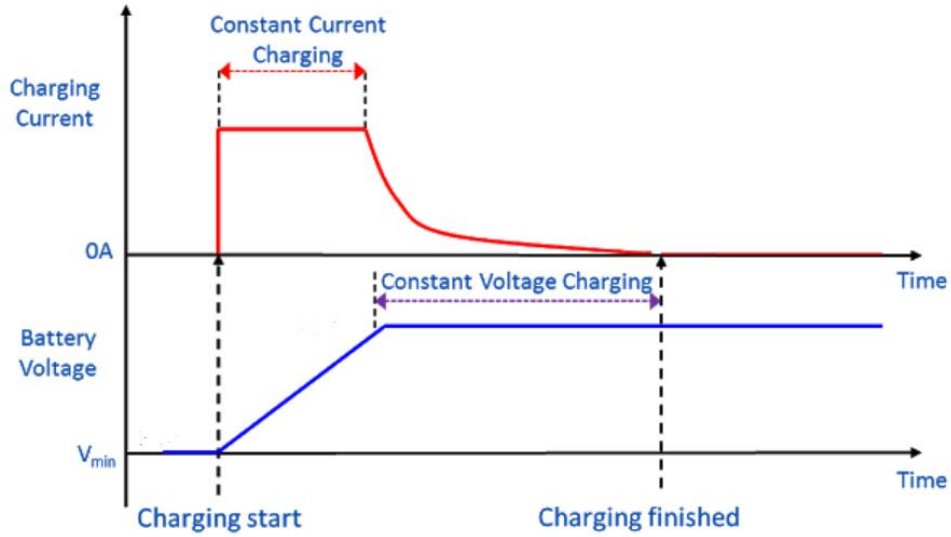

Figure 1. 4. Constant current/constant voltage charging method (V_{min} is the minimum cutoff voltage) [22].

Individual LIB cells are unable to provide the voltage or energy required to power most of the practical electric applications. Instead, LIB arrays or packs made up of multiple LIB cells electrically connected either in series or parallel are typically utilized. Figure 1. 5 shows a set of LIBs electrically connected in parallel or series. Connecting the LIB cells in parallel increases the electrical capacity of the pack, while the series connection increases the voltage of the pack. The commercial LIB packs are labeled with a nominal voltage (which is an indication of the number of series-connected LIBs) and a pack capacity in A h or W h (which is an indication of the number of parallel-connected LIBs).

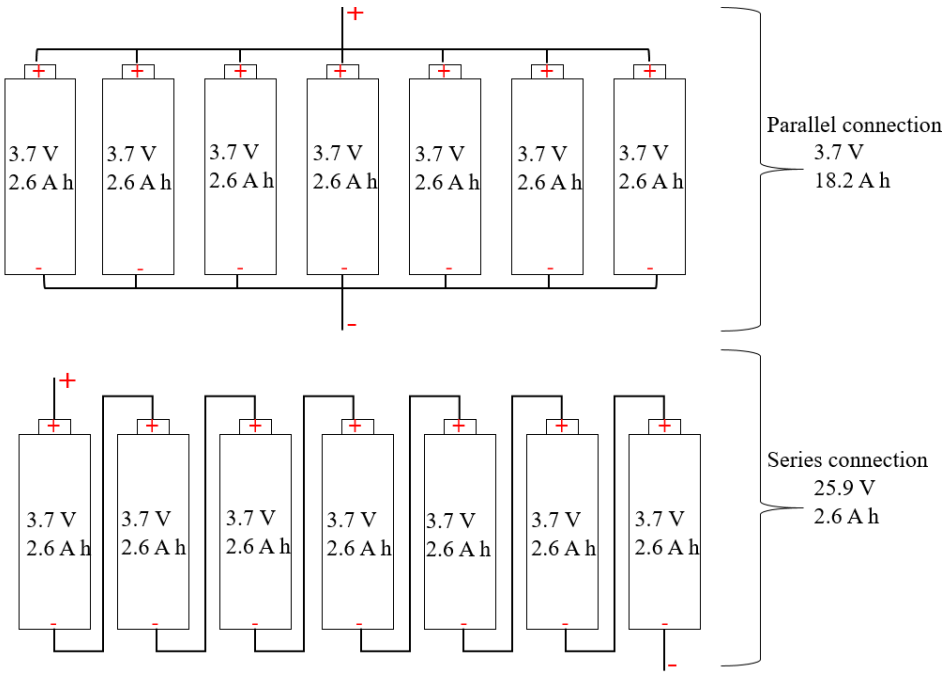

Figure 1. 5. Schematic of cells connected in parallel or series.

1.4 Failure Mechanism of LIB Cells

Exposure of individual LIB cells to abnormal operating circumstances may trigger thermal failure in the cells [2, 14]. Generally, the LIB abuse can be classified into four main categories:

- ❖ Thermal abuse: such as external heating or exposure to nearby fire.
- ❖ Mechanical abuse: such as nail penetration, crush/compression, or drop.
- ❖ Electrical abuse: such as external short-circuit, overcharging, or excessive current.
- ❖ Manufacturing defects: such as defected separator or contaminanted electrolyte.

Figure 1. 6 provides a qualitative understanding of the failure mechanism of an individual LIB cell in an anaerobic environment. In the figure, the cell failure begins with an increase in the cell internal temperature, which can be intiated by any of the aforementioned failure causes. The increase in temperature results in the vaporization

of a portion of the electrolyte and the formation of gases, which raises the pressure inside the enclosure of the LIB cell. When the internal pressure reaches a certain threshold, safety vent ports located on the cell casing open to eject the formed gases at relatively slow rates, consequently reducing the internal pressure and preventing the rupture of cells; this phenomenon is referred to as safety venting (SV) [2, 14]. As the temperature of the cell continues to increase, exothermic reactions between the cell's components are initiated. The cell's increasing temperature accelerates the chemical reaction rates inside the cell, resulting in a rapid self-heating [2, 14]. This heating process eventually causes the cell to reach its thermal runaway (TR) stage during which the temperature and gas ejection rate of the cell increase dramatically [2, 14]. Some solid components of the cell are ejected during TR as well [2]. Occasionally during TR, the LIB cells experience a rupture of their casing because of the rapid increase of internal pressure [23].

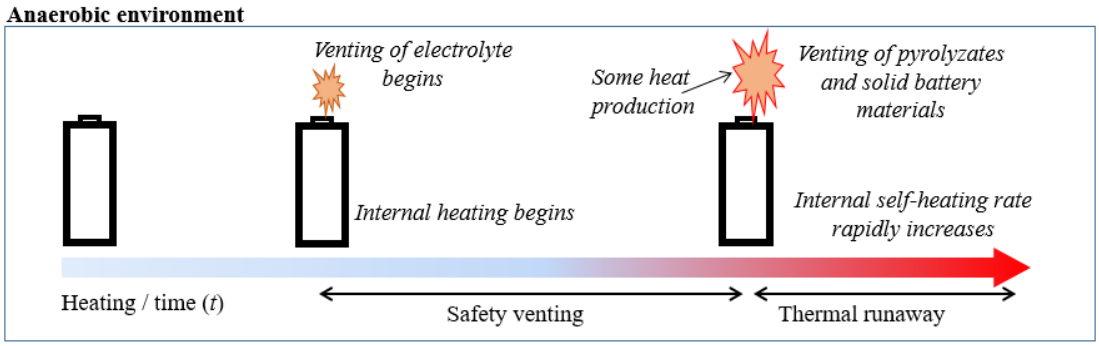

Figure 1. 6. A diagram of thermally induced failure in an anaerobic environment.

When an LIB cell is subject to TR in an anaerobic environment, large amounts of energy are generated due to chemical reactions between the battery components inside the enclosure of the cell. Some ejected materials may continue to react with each other outside of the cell's enclosure, causing additional heat production. In this study,

the total energy released due to these reactions (inside and outside the cell's enclosure) is referred to as chemical heat generation.

Similarly, the failure events of an LIB cell in an air environment begin with an increase in the cell's temperature and pressure and then followed by SV and TR events. However, the air environment aggravates the failure scenarios to be more catastrophic. More specifically, the ejected cell's materials may ignite or burn in air. Figure 1. 7 shows that the ejected electrolyte is ignited as soon as it leaves the safety venting ports in the form of small flames [24, 25]. The flames continue to grow as the LIB cell approaches TR and turn into intermittent jet flames during TR [24, 25]. Upon failure in an air environment, an LIB cell generates two forms of energy: chemical energy (due to chemical reactions between the cell's components inside and outside its enclosure) and flaming combustion energy (due combustion of ejected materials from the cell outside its enclosure).

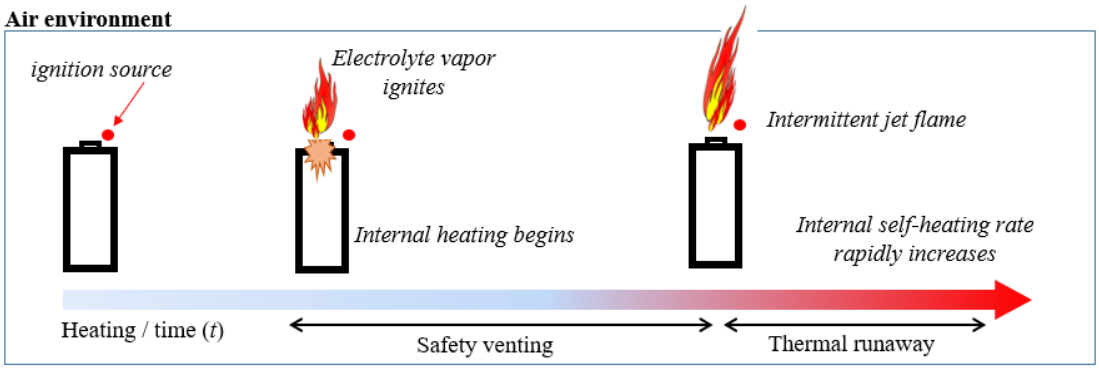

Figure 1. 7. A diagram of thermally induced failure in an air environment.

The hazards of TR are intensified significantly as individual LIB cells are assembled into large cell arrays or battery packs to satisfy high power demands. As shown in Figure 1. 8, the failure of a single cell may initiate TR into the adjacent cells, and subsequrently TR propagates through the entire pack. In this study, TR propagation is also referred to as cascading failure. This propagating failure is primarily driven by

the transport of thermal energy (represented by black arrows in Figure 1. 8) [2, 26]. The thermal transport consists of heat added to the cells by flames and conduction, convection, and radiation heat transfer between neighboring cells.

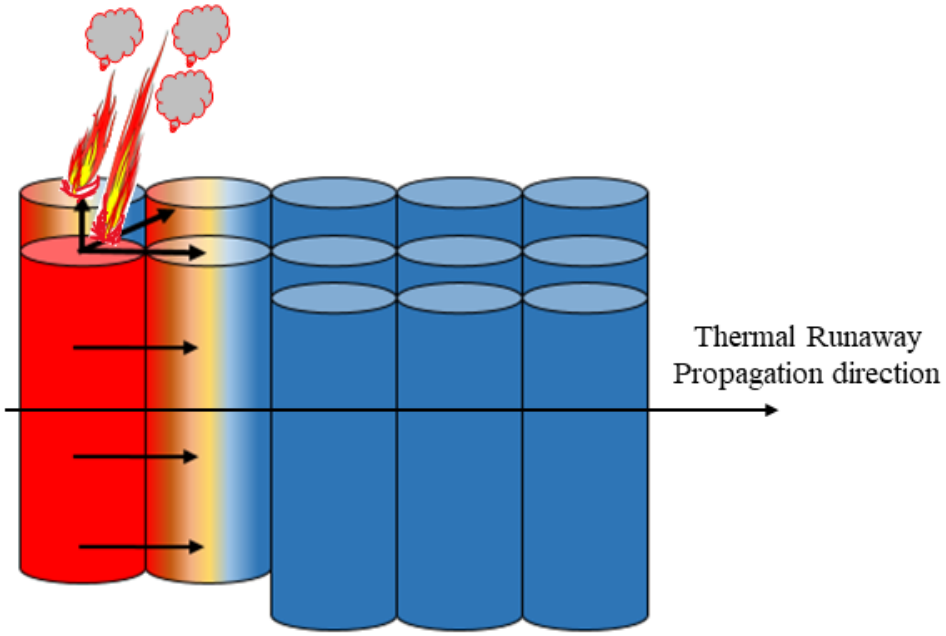

Figure 1. 8. Graphical representation of cascading failure in LIB arrays/packs.

1.5 Chemical Reactions Associated with Thermal Runaway of LIB Cells

As mentioned earlier in this chapter, the exposure of an LIB cell to abnormal conditions may cause an increase in the temperature of this cell, which subsequently initiates decomposition of the main battery components and chemical reactions between these components inside the enclosure of the cell. The majority of those reactions are of exothermic nature and are accompanied by generations of large amounts of heat. The main reactions that possibly take place inside the cell's enclosure are summarized as follows [2]:

- ❖ Decomposition of solid electrolyte interface (SEI) layer.
- ❖ Reactions of intercalated carbon with electrolyte.
- ❖ Decomposition of cathode active material.

- ❖ Reactions of intercalated lithium with electrolyte.
- ❖ Decomposition of electrolyte.
- ❖ Reactions of electrodes with fluorinated binder.

The mentioned reactions should not necessarily occur in the given order. Some reactions may initiate simultaneously and interact thermally. It is also important to mention that the chemical reactions discussed in this section primarily occur inside the enclosure of the battery. However, there is a chance that the ejected materials continue to react outside that enclsoure.

1.5.1 Solid Electrolyte Interface (SEI) Layer Decomposition

As mentioned in section 1.2.3, a solid electrolyte interface (SEI) is an electronically insulating but ionically conducting film that prevents any physical contact between the negative electrode material and the electrolyte. The SEI layer consists of stable components (such as LiF or Li_2CO_3) or metastable components (such as polymers $ROCO_2Li$, $(CH_2OCO_2Li)_2$ or ROLi). The metastable components decompose exothermically at 100-120 ˚C as follows [27]:

$$(CH_2OCO_2Li)_2 \rightarrow Li_2CO_3+C_2H_4+CO_2+0.5O_2 \quad 1.1$$

or reacts with lithium metal as follows [27]:

$$(CH_2OCO_2Li)_2 + 2Li \rightarrow 2Li_2CO_3+C_2H_4 \quad 1.2$$

Additionally, the SEI layer decomposes at a relatively low temperature of 69 °C [28], and once this layer is breached the electrolyte reacts with the lithium intercalated in the anode in a manner similar to the formation process but at a higher uncontrolled temperature, releasing heat and raising the temperature.

1.5.2 Reactions of Intercalated Lithium with Electrolyte

The heat released as a result of the decomposition of SEI layers initiates further exothermic reactions between lithium existing in the intercalated carbon and electrolyte solvent, releasing flammable total hydrocarbon gases [29] as shown in the following examples:

$$2Li + C_3H_4O_3\ (EC) \rightarrow Li_2CO_3 + C_2H_4 \quad (1.3)$$

$$2Li + C_4H_6O_3\ (PC) \rightarrow Li_2CO_3 + C_3H_6 \quad (1.4)$$

$$2Li + C_3H_6O_3\ (DMC) \rightarrow Li_2CO_3 + C_2H_6 \quad (1.5)$$

Typically, these reactions start at 100 °C [28, 29] but can also occur at a temperature as low as 69 °C [28] for some other electrolytes. The gases formed due to the breakdown of the electrolyte do not burn, even though the temperature exceeds the flashpoint because there is no sufficient free oxygen in the cell to sustain a fire. Instead, the gases accumulate and cause the pressure to build up inside the cell.

1.5.3 Decomposition of Cathode Active Material

At around 130 °C, the polymer separator melts, allowing short circuits between the electrodes [30]. Also, the heat generated from the breakdown of electrolyte causes decomposition of the metal oxide cathode material, releasing oxygen. The cathode active materials can dissociate at elevated temperatures as follows [29, 31] ($LiCoO_2$, $Ni_{0.8}Co_{0.2}O_2$, and Mn_2O_4 are shown as examples):

$$2Li_{0.5}CoO_2 \rightarrow LiCoO_2 + Co + O_2 \quad (1.6)$$

$$Ni_{0.8}Co_{0.2}O_2 \rightarrow \frac{1}{3}Ni_{2.4}Co_{0.6}O_4 + \frac{1}{3}O_2 \quad (1.7)$$

$$Mn_2O_4 \rightarrow Mn_2O_3 + \frac{1}{2}O_2 \quad (1.8)$$

The oxygen released from the breakdown of the cathode active material may react with electrolyte solvent as follows [29, 31]:

$$\frac{5}{2}O_2 + C_3H_4O_3\ (EC) \rightarrow 3CO_2 + 2H_2O \quad (1.9)$$

$$4O_2 + C_4H_6O_3\ (PC) \rightarrow 4CO_2 + 3H_2O \quad (1.10)$$

$$3O_2 + C_3H_6O_3\ (DMC) \rightarrow 3CO_2 + 3H_2O \quad (1.11)$$

$$6O_2 + C_5H_{10}O_3\ (DEC) \rightarrow 5CO_2 + 5H_2O \quad (1.12)$$

The breakdown of the cathode is highly exothermic and increases the temperature and pressure even further.

1.5.4 Reactions of Intercalated Lithium with Electrolyte

After the breakdown of the SEI layer, lithium atoms in the intercalated carbon can react with electrolyte producing CO_2 (at 228 °C) and dilithio butylene dialkoxide as follows [32]:

$$2Li + 2C_3H_4O_3\ (EC) \rightarrow Li - O - (CH_2)_4 - O - Li + 2CO_2 \quad (1.13)$$

$$LiPF_6 \rightarrow LiF + PF_5 \quad (1.14)$$

The phosphorus pentafluoride (PF_5) decomposed from lithium hexafluoride salt ($LiPF_6$) reacts with dilithio butylene dialkoxide to produce phosphoryal fluoride (POF_3) (in a temperature range of 200-240 °C) [32] as follows:

$$Li - O - (CH_2)_4 - O - Li + PF_5 \rightarrow Li - O - (CH_2)_4 - F + LiF + POF_3 \quad (1.15)$$

Or $LiPF_6$ reacts with dilithio butylene dialkoxide directly to produce POF_3 as follows:

$$Li - O - (CH_2)_4 - O - Li + LiPF_6 \rightarrow Li - O - (CH_2)_4 - F + 2LiF + POF_3 \quad (1.16)$$

1.5.5 Decomposition of Electrolyte

The electrolyte not only reacts with the electrodes but also decomposes at elevated temperatures (200-300 °C) as follows [33, 34]:

$$C_5H_{10}O_3\ (DEC) + PF_5 \rightarrow C_3H_5O_3PF_4 + HF + C_2H_4 \quad 1.17$$

$$C_2H_4 + HF \rightarrow\ C_2H_5F \quad 1.18$$

$$C_5H_{10}O_3\ (DEC) + PF_5 \rightarrow C_3H_5O_3PF_4 + C_2H_5F \quad 1.19$$

$$C_3H_5O_3PF_4 \rightarrow PF_3O + CO_2 + HF + C_2H_4 \quad 1.20$$

$$C_3H_5O_3PF_4 \rightarrow PF_3O + CO_2 + C_2H_5F \quad 1.21$$

$$C_3H_5O_3PF_4 + HF \rightarrow PF_4OH + CO_2 + C_2H_5F \quad 1.22$$

$$C_2H_5F + C_2H_4 \rightarrow\ C_4H_{10}O \quad 1.23$$

At this point, the pressure inside the cell is extremely high. The formed gases are ejected outside the cell's body to relieve the internal pressure in the cell to reduce the possibility of rupture. As soon as the gases are released to the atmosphere at a temperature close to their auto-ignition temperature, intermittent jet flames may be initiated.

1.5.6 Reactions of Electrodes with Fluorinated Binder

Although the binder provides mechanical strength and maintains the integrity of the electrodes, it affects the thermal stability of the electrode under elevated temperatures. For instance, the binder forms H radicals, which enhances the $LiCoO_2$ decomposition. Furthermore, for the $LiCoO_2$ electrodes containing PVDF, the main surface reaction is related to CoIII→CoII reduction; the major decomposition product is Co_3O_4. This reaction is also accompanied by the oxidation of some electrolyte solution species:

$$4LiCo^{III}O_2 \rightarrow Co^{IV}O_2 + Co^{II}Co_2{}^{III}O_4 + 2Li_2O \xrightarrow{4HF} 4LiF + 2H_2O \quad 1.\ 24$$

The PVDF-Li_xC_6 reactions are strongly affected by the degree of lithiation of the graphite in the anode and the surface area of the anode. In the presence of electrolyte as the acidic medium, PVDF (binder material) is dehydrofluorinated according to the following equation [35]:

$$-CH_2 - CF_2- \xrightarrow{base} -CH = CF- + HF \quad 1.\ 25$$

A possible reaction between the binder and the Li_xC_6 electrode at a temperature greater than 260 °C is as follows [35]:

$$-CH_2 - CF_2- + Li \rightarrow LiF + -CH = CF- + 0.5H_2 \quad 1.\ 26$$

To conclude, all aforementioned reactions produce heat and participates in raising the pressure inside the cell, which results in the expedition of TR phenomenon. These sets of reactions can be utilized along with kinetic and structural parameters for modeling the thermal behavior of LIBs undergoing abuse conditions as discussed in chapter 2.

2. Literature Review and Current Study Objectives

This chapter presents the previous works that focused on studying the thermal behavior of individual LIB cells and LIB cell arrays under failure conditions. In this chapter, the investigations are classified into two main categories: experimental and numerical. First, the experimental studies investigating the thermal, flaming combustion, and chemical hazards associated with TR of single LIB cells are reviewed. Additionally, experimental studies on TR propagation (referred to as cascading failure) in LIB cell arrays are discussed. The last section of this chapter presents the results of modeling of TR and cascading failure phenomena.

2.1 Review of Experimental Studies

2.1.1 Review of Thermal Hazard Associated with Failure of Individual LIBs

The failure of an individual LIB cell presents a thermal hazard because of substantial heat generation and the associated increase in the temperature of the cell's body. Most of the energy associated with the reactions between cell components is released inside the cell. However, some ejected materials may continue to react with each other outside of the cell's body, releasing additional amounts of energy. Several techniques including differential scanning calorimetry (DSC) [35-40], accelerating rate calorimetry (ARC) [37, 41-45], vent sizing package 2 (VSP2) adiabatic calorimetry [46-48], C80 calorimetry [28, 30, 34, 49-51], and modified bomb calorimetry [52] have been employed to measure the energy generation due to the chemical reactions.

DSC is a thermo-analytical technique that measures the heat flow associated with physical and chemical transitions in milligram-sized individual components of LIB cells. The sample is heated linearly at sufficiently slow rates, typically in a range

of 3-30 K min^{-1}, to maintain a spatially uniform temperature within the sample. Pasquier et al. [35] utilized DSC to examine the chemical reactions occurring in lithiated carbon anodes (Li_xC_6) containing PVDF as a binder. The reactions were examined below and above the $LiPF_6$ melting temperature (260 °C). For temperatures below 260 °C, degradation of the SEI passivating layer was found to occur at a temperature range of 120 - 140 °C and was followed by Li_xC_6-electrolyte reactions at around 210 - 230 °C. For temperature greater than 260 °C, chemical reactions between the binder and Li_xC_6 were observed. The latter reactions were found to be strongly affected by the degree of lithiation of the anode.

Maleki et al. [37] employed DSC to examine the thermal stability of the anode and cathode for specific LIB chemistry, graphite/$LiCoO_2$. The total exothermic heats of decomposition of the anode (graphite) and cathode ($LiCoO_2$) were estimated to be 697 and 407 J g^{-1}, respectively. MacNeil et al. [38] utilized DSC to compare the thermal stability of various cathodes in $LiPF_6$/EC/DEC electrolyte. The lithium iron phosphate ($LiFePO_4$) cathode was found to be the best candidate for large LIB cells based on stability and cost. Roth et al. [39] examined thermally induced interactions between several binder materials and representative anode materials with various states of charge (SOCs) and electrolytes. The amount of electrolyte, the surface area of the anode, and SOC significantly impacted the exothermicity of the observed reactions. Yang et al. [40] studied the DSC behaviors of natural graphite, mostly common anode material, with different amounts of intercalated lithium ions. Sharp exothermic peaks were detected at around 327 °C when testing samples containing more than 0.7 lithium

ions per 6 carbons, which was attributed to the structural collapse of the graphitic matrix.

ARC is designed to determine the time, temperature, and pressure relationships for exothermic chemical reactions occurring inside an adiabatic, sealed stainless-steel or titanium chamber of a relatively large volume (10 cm diameter and 10 cm depth). Samples are brought to the desired starting temperature, then checked for self-heating during an equilibrium time period. If the self-heating rate (dT/dt, °C min^{-1}) exceeds a specific threshold, the instrument remains in the adiabatic mode and follows the exotherm [42]. When dT/dt drops below the threshold level, the temperature is increased by constant steps (for example, 10 °C) until another exotherm is detected, or until the designated upper temperature limit is reached. Von Sacken et al. [42] employed ARC to study the effect of anode's specific surface area, SOC, and solvent composition on the thermal stability of the anode soaked in electrolyte. The results showed that an intercalated carbon anode (Li_xC_6) was more thermally stable, and its behavior was more reproducible than a lithium metal anode due to its ability to better maintain its structure. It was also found that the self-heating rate of the intercalated carbon anode increased with the increase in its specific surface area. The carbon anode charged at lower voltages was found to be more reactive because the anode contained more lithium. Additionally, the anode was tested in different electrolyte co-solvents: $LiPF_6$/PC-R where R: EC, DME, DEC, or DMC. The self-heating rate increased in the following order: EC < DME < DEC < DMC.

The usage of ARC was also extended to include investigating TR in complete LIB cells rather than individual components. Hallaj et al. [44] tested commercial Sony

LIB cells (US18650, 1350 mA h, $LiCoO_2$/carbon/PC:DEC+$LiPF_6$) using ARC to determine the TR onset temperatures. For cells with open circuit voltages of 4.06, 3.0, and 2.8 V, onset temperatures were found to be 104, 109, and 144 °C, respectively. Maleki et al. [37] tested prismatic LIB cells with Sn-$LiCoO_2$ cathode in ARC to determine the onset temperatures of exothermic reactions occurring during TR. The obtained results showed that a small self-heating reaction initiated near 112 °C. When the cell reached 123 °C, it started to slowly self-heat until highly exothermic reactions (corresponding to TR) were observed at 167 °C. The self-heating peaks observed at 112 and 123 °C corresponded to the SEI layer breakdown and the electrolyte/electrode reactions captured during experiments conducted in DSC and thermogravimetric analyzer (TGA). The TR onset temperature (167 °C, ARC data) was related to the onset of chemical decomposition of cathode (167 °C, DSC/TGA data), confirming that the cathode processes lead to TR.

In another work by Maleki and Howard [43], thermal stability of two different prismatic LIB cells were evaluated at various SOCs using ARC. Cell A (750 mA h) consisted of Sn-doped $LiCoO_2$ cathode, meso carbon microfiber (MCMF) anode, and EC: EMC + $LiPF_6$ electrolyte. Cell B (790 mA h) consisted of $LiCoO_2$ cathode, graphite anode, and EC: EMC: DMC + $LiPF_6$ electrolyte. Cell A has shown better stability than cell B, which was attributed to the higher thermal stability of MCMF over graphite. The results also showed that the thermal response of both the cathode and anode in an LIB cell was a dynamic process controlled by multiple factors such as SOC, self-heating rates, and total heat generated by each component.

In a more recent work by Feng et al. [45], TR of a 25 A h large format prismatic LIB was studied using the extended volume ARC, which follows the same heating methods as the standard ARC, but with a larger test chamber volume (25 cm diameter and 50 cm depth). The tested LIB sample consisted of two pouch cells that were electrically connected in parallel and kept in an aluminum shell. The two pouch cells had a lithium nickel manganese cobalt oxide cathode. A micro-thermocouple was inserted in between the two pouch cells, and additional thermocouples were attached to the body of the whole battery. The results showed that for the examined LIB cells, the temperature difference between the inner and outer thermocouples was minor (1°C) for most of the test duration. The temperature difference increased as the cell approached TR and reached its maximum difference (520°C) during TR. A maximum internal temperature of 870 °C was recorded during TR. Additionally, the LIB cell voltage was recorded over time; measurements of the voltage showed a predictable delay between the sharp decrease in voltage (corresponding to the onset of self-heating reactions) and the sharp increase in temperature (corresponding to thermal runaway). The authors suggested that quantification of this delay may enable early detection of TR by monitoring the voltage.

VSP2 calorimetry is an adiabatic calorimeter with a pressure/temperature system that balances internal and external pressures as well as temperatures. The adiabatic condition of the VSP2 calorimetry can be used to obtain related profiles of pressure and temperature parameters. Jhu et al. [46, 47] employed VSP2 calorimetry to study the TR reactions in four different commercial LIB cells with an 18650 form factor (cylindrical geometry of 18 mm in diameter and 65 mm in height). All tested cells had

similar cathode chemistry ($LiCoO_2$) and nominal capacity (2600 mA h). Each commercial cell was examined at two different charging voltages of 4.2 and 3.7 V corresponding to (100% SOC) and (50% SOC), respectively. The cells were placed in a 150 ml stainless-steel cylindrical test can that was particularly designed to fit an 18650 LIB cell and surrounded by the heating system. For any of the tested cells, the maximum temperature and pressure of fully charged cells were measured to be 903 °C and 1565.9 psi, respectively. The heat of reaction was estimated to be 26.2 kJ per fully charged cell. Less charged cells showed better thermal stability as expected.

A similar study by Wen et al. [48] utilized the same methodology to examine 18650 $LiFePO_4$ cells charged to voltages of 3.6 V (fully charged) and 4.2 V (overcharged). The recorded exothermic reaction onset and maximum temperatures showed a negligible dependence on the SOC of the cell. The onset and maximum temperatures of TR for the fully charged cell were found to be 199 °C and 243 °C, respectively.

C80 calorimetry is utilized to study the decomposition of individual battery components at different room temperatures up to 300 °C. In a number of studies performed by Wang et al. [28, 30, 34, 49-51], C80 calorimetry was employed to compare the thermal stability of various electrolytes (organic solvents + anion salts) with and without the presence of electrodes. The tested solvent samples showed high thermal stability in an argon environment compared to air. It was found that the addition of $LiPF_6$ reduced the thermal stability of electrolyte mixtures. Also, the results showed that the electrolyte/electrode combination had lower decomposition temperature than either a separate electrolyte or electrode.

Despite the fact that DSC and ARC have been widely used to investigate the thermal stability of electrolytes, yet C80 is the best technique for such studies because it can handle the large pressure waves accompanying the failure reactions. For instance, MacNeil et al. [38] had to replace a typical hermetic DSC sample pan with a custom-welded aluminum sample vessel for their DSC apparatus to prevent leakage of released gases, which complicates the testing process. In contrast, the high-pressure rated stainless-steel vessel utilized in the Setaram C80 calorimeter prevents any leakage of gases and operates at elevated temperatures. As for ARC, it cannot detect endothermic reactions associated with vaporization of the electrolyte, while the C80 calorimetry can.

Lyon and Walters [52] employed an adiabatic bomb calorimeter to investigate thermal failure of four different commercial cathode chemistries with an 18650 form factor. The thermal failure was induced by an electrical resistance heater in a nitrogen-filled bomb calorimeter to preclude combustion of the battery materials. The total energy of the LIB failure was assumed to consist of electrical stored energy in the LIB and the chemical energy produced due to chemical reactions between the LIB materials. The results of this study indicated that the produced energy of an LIB ranged from 1.6-1.9 times its electrical stored energy.

Despite being useful for characterizing failure energetics, none of the aforementioned methods (DSC, ARC, VSP2, C80 or bomb calorimeter) was originally designed for LIB failure analysis; consequently, their application to LIB testing is a subject of several limitations. More specifically, most of these techniques cannot be utilized to test fully assembled commercial cells due to testing chamber size limitation and possible damage to the device. Most of these methods measured the integral

amount of energy resulting from chemical reactions between battery materials but provided no insight into the dynamics of this process. They also were unable to differentiate between the heat generated inside the cell casing and the heat generated from continued reactions between materials ejected from the cell, which is highly important for engineering analysis of failure propagation in LIB arrays (packs). Finally, these methods did not provide a measurement of the energy released from flaming combustion of ejected battery materials.

To overcome the limitations on the aforementioned techniques, Liu et al. [26, 53, 54] developed a new technique that is referred to as Copper Slug Battery Calorimetry (CSBC). This technique enabled careful measurement of the energy generated due to chemical reactions between LIB materials inside the cell casing only. The technique involved inserting an LIB cell into an insulated copper slug. The slug was slowly and uniformly heated to initiate TR. The main assumption invoked in this study was that the temperature inside the tested LIB cell was spatially uniform. A thermocouple was inserted into the copper slug to measure a copper slug time-resolved temperature which was found to be equal to the tested LIB cell temperature. 18650 LIBs with cathode chemistries of lithium cobalt oxide (LCO, 2600 mA h), nickel manganese cobalt oxide (NMC, 2250 mA h), and lithium iron phosphate (LFP, 1500 mA h) were tested, all at SOCs of 0%, 25%, 50%, and 100%. For all cathode chemistries, the internal heat generation increased with increasing SOC up to 50%, but the values for 50% and 100% SOC were comparable for most cathode chemistries due to significantly greater ejected mass at 100% SOC. The fully charged cells produced

total internal heat generations of 37.3 ± 3.3, 34.0 ± 1.8 and 13.7 ± 0.4 kJ per cell for LCO, NMC, and LFP, respectively.

Said et al. [24, 25] modified the CSBC technique to accommodate prismatic LIB cells, Sanyo-UF103450P (LCO, 1880 mA h). The internal heat generation was found to be 33 ± 1.0 kJ per fully charged cell. Quintiere et al. [11, 55] conducted experiments with a similar, custom thermal capacitance calorimeter and expanded their investigation to include other types of batteries (including NiMH, NiCd, and lithium-metal primary cells).

2.1.2 Review of Flaming Combustion Hazard Associated with Failure of Individual LIBs

The flaming combustion hazard of ejected LIB materials have been studied separately from the thermal hazards in experiments which measured the total heat release rate (HRR) associated with flaming combustion of ejected LIB materials. Ribière et al. [56] adopted the fire propagation apparatus [57] (FPA, also called Tewarson calorimeter in the EU) for these measurements. In this study, 2.9 A h commercial pouch cells ($LiMn_2O_4$ cathode and graphite anode) were examined at 0%, 50%, and 100% SOCs. The tested LIB cell was placed in a stainless-steel cage which was laid on a sample holder. The sample holder and its contents were placed atop a weighing sensor to record the mass loss. The cage was enclosed by a combustion chamber while ventilation air, at a volume flow rate of 350 l min^{-1} to simulate outside fire conditions, was injected at the bottom of the chamber. An external heat flux of 35 kW m^{-2} was applied to the chamber to induce thermal runaway into the LIB. Materials ejected during TR were ignited via a pilot-flame placed 30 mm above the LIB cell. For

all the SOCs, the total mass loss was found to be identical (17%, 17% and 16% of initial mass). HRR due to combustion of ejected materials was estimated using the oxygen consumption method. The total heats due to combustion were computed by integrating the HRR profiles over time and found to be 313 ± 37, 383 ± 32, and 361 ± 40 kJ at 100%, 50%, and 0% SOCs, respectively. The maximum effective heat of combustion was estimated to be 4.03 ± 0.34 MJ per kg of a cell.

Liu et al [53, 54] combined the CSBC apparatus with an oxygen-consumption cone calorimeter [58] to measure energy associated with flaming combustion of ejected materials from LIB cells with LCO, LFP, and NMC cathodes. The CSBC apparatus was equipped with an electric coil igniter which was suspended 5 mm above the tested LIB cell. The total heat generated due to combustion of ejected LIB materials varied between 35-63, 27-81, and 36-50 kJ for LCO, NMC, and LFP cells, respectively. The high hydrodynamic strain rates associated with turbulent flow of ejected materials caused intermittency of the flame, prevented significant amounts of ejected materials from burning, and often damaged the igniter, thus resulting in underestimated values of flaming combustion energy.

To resolve this issue, Said et al. [25] modified the manner in which the ejected battery materials were collected and ignited to increase combustion efficiency in comparison to Liu et al.'s studies [53, 54]. More specifically, Said et al. [25] attached a stainless steel collector/burner tube, appended with a perforated plate, to the CSBC apparatus. This attachment enabled homogenizing and reducing the speed of ejected materials and delivered these materials to an electric igniter coil suspended 10 mm above the perforated plate. This new technique resulted in a discernable increase in

combustion efficiency. In this study [25], prismatic, 1880 mA h, $LiCoO_2$ cathode cells were tested. Per failed cell, the effective combustion energy for 100% SOC cells was found to be 113 kJ, compared to just 71 kJ for 50% SOC cells.

Full-scale burning tests were performed by Ping et al. and Wang et al. [59, 60] to investigate the combustion behavior of materials ejected during the failure of a 50 A h lithium iron phosphate ($LiFePO_4$) batteries charged to various SOCs (0%, 50%, and 100 %). Radiative heating of 3 kW was applied to one side [59] or to the bottom surface [60] of the battery to induce thermal runaway. The observed fire behavior was as follows: battery expansion, jet flame, stable combustion, a second cycle of jet flame followed by stable combustion, a third cycle of jet flame followed by stable combustion, abatement, and extinguishment. The number of jet flames was found to be 3, 3, and 2 for 100%, 50%, and 0% SOC, respectively. Additionally, the flaming combustion heat release per failed cell were computed to be 18195, 10396 and 4639 kJ at 100%, 50%, and 0 % SOC, respectively. These values seem to be significantly high for this cathode chemistry when compared to the results of previous studies [25, 53, 54, 56] and current work as well, even if they are normalized by initial mass of the battery pack. This can be attributed to the higher electrical stored energy in this study compared to the previous ones [25, 53, 54, 56].

2.1.3 Review of Chemical Hazard Associated with Failure of Individual LIBs

Other studies have focused on the chemical hazards associated with the hazardous gases that are produced and ejected during cell failure. Maloney [8, 9] measured the concentration of the gases ejected from LIB cells in an inert environment to avoid any impact of combustion. Cells of different cathode chemistries and SOCs

were intentionally failed using external heating inside a 21.7 l pressure vessel equipped with O_2, CO, CO_2, total unburned hydrocarbon (THC), and H_2 analyzers. Results showed that the overall volume of ejected gases increased with increasing SOC. The lower flammability limit of the mixture decreased with increasing SOC up to 40% and then remained fairly constant afterwards.

The ejected gases from cells with $LiFePO_4$ cathodes were also significantly less flammable and smaller in volume than the gases ejected from cells with other cathode chemistries. For $LiCoO_2$ cathode cells of a 2600 mA h nominal capacity, volumetric concentrations of THC and CO_2 were not found to vary significantly with SOC, but concentrations of CO and H_2 were both found to increase from 5-10 vol.% to 20-30 vol.% for SOCs greater than the 50%.

Other studies [56, 61-67] have focused on measuring the concentration of the flaming combustion products. Many toxic products such as CO, hydrogen fluoride (HF), and phosphoryl fluoride (POF_3) were detected when LIBs were tested at high SOCs. Larsson et al. [61] used Fourier-transform infrared spectroscopy (FTIR) technique to detect HF released from 7 A h EIG LFP pouch cells, 3.2 A h K2 LFP cylindrical cells, and 16.8 Lenovo laptop battery packs in an air environment. The HF mass yields of the pouch cells, cylindrical cells, and laptop battery packs were estimated to be 16, 15, and 7.3 mg per g of total mass loss, respectively. Larsson et al. [67] were able to measure POF_3 only for LCO cells at 0% SOC.

2.1.4 Review of Cascading Failure in Lithium Ion Cell Arrays/Packs

All aforementioned hazards (thermal, flaming combustion, and chemical) increase exponentially when LIB cells are assembled into large arrays (battery packs)

to satisfy high power demands in most commercial applications. The failure of an individual cell may induce failure into neighboring cells and then cause TR propagation (alternatively referred to as cascading failure) through the entire pack. This propagating failure is primarily driven by the transport of thermal energy [2, 26] between LIB cells. Multiple studies investigated the effects of cells arrangements [68-70] and active/passive cooling strategies [71, 72] on the thermal behavior of LIB arrays under normal operating conditions (no thermal runaway). Most of these studies were conducted on arrays that consisted of commercial LIB cells.

A limited number of experimental works have investigated cascading failure in LIB cell arrays. Lamb et al. [73] investigated cascading failure of small-scale LIB arrays constructed with either wall-to-wall 18650 cylindrical or wall-to-wall pouch cells. TR was initiated by creating a hard shorting failure in one of the cells via mechanical nail penetration. In the first set of tests, small packs were constructed from 10 Panasonic CGR18650CG cells (cylindrical), with 2200 mA h nominal capacity. The cells were electrically connected either in series or parallel. For the array with cells connected in series, TR of the trigger cell raised the temperature of neighboring cells significantly, triggering safety venting but not TR propagation in the cells. Voltages of some neighboring cells dropped for a short time and then were restored.

Inducing TR in arrays/packs of cells that were connected in parallel resulted in a complete failure propagation into the pack, with significant damage to cells and loss of voltage. It was concluded that failure of any cell in a series configuration would not impact the general ability of LIB pack to continue working, albeit at a lower voltage due to the missing cell. In the second set of tests, the authors examined stacked pouch

cell modules that were constructed from 5 AA Portable Power Corporation model 7035130-10C cells with 3000 mA h nominal capacity. Results from the pouch cell batteries in the series configuration were notably different from the cylindrical cell results. Failure quickly propagated through the pouch cell battery no matter if the cells were connected in parallel or series, which was attributed to the greater conduction heat transfer between pouch cells compared to cylindrical cells. The greater heat transfer is associated with the larger contact area between adjacent pouch cells.

Feng et al. [74] studied TR propagation in a large LIB pack. The examined pack consisted of six prismatic batteries (25 A h each) fixed together with no spacing in between. Each battery was constructed from two pouch cells which were connected in parallel and placed in an aluminum prismatic shell. TR was induced in the first battery of the pack via nail penetration. Failure of the first battery produced large amounts of thermal energy which non-uniformly heated the side wall of adjacent cells, thus initiating TR propagation in the remaining five batteries of the pack. Temperature and voltage histories of each battery were recorded and utilized to determine TR onset times and temperatures. Results showed lower TR onset temperatures and shorter failure onset times than ARC tests on identical single batteries due to the introduction of fast, non-uniform side heating from adjacent cells. A maximum increase in temperature of 792 °C was observed for cells within the pack. Additionally, heat transfer from pole connectors and the developed fire were found to be minimal in comparison to the heat transfer through the battery shell, indicating that conduction was the primary mode of heat transfer.

Ouyang et al. [75] investigated the impact of cell array configuration on the dynamics of cascading failure. Cylindrical LIB cells were arranged in six different geometries: triangular, rectangular, parallelogram, linear, square and hexagon with no inter-cell spacing. The results showed that triangular and linear configurations achieved lower propagation speeds relative to the other configurations. For the same configuration, TR was found to propagate faster for the cells undergoing an electric discharge.

2.1.5 Review of Cascading Failure Passive Mitigation Strategies

Lopez et al. [76] experimentally studied the influence of LIB array design configurations including cell spacing, tabbing style, and vent location on cascading failure. Cells of cylindrical and prismatic form factors were employed in this study. The abuse test consisted of a heat-to-vent setting where a single cell in a module was triggered into TR via a heating element. Results showed that adding 2 mm gaps between cylindrical cells in arrays prevents propagation and alleviates physical damage in the tested arrays. However, this suggestion may not be applicable due to limited space in most practical applications. Branched tabbing improved the voltage retention and array safety compared to serpentine tabbing because the trigger cell was isolated from the array when the tabs were branched. The gap addition did not prevent propagation when testing arrays of prismatic cells with side facing vents. It was also found that installing thermal insulation or intumescent materials between the prismatic cells successfully stopped TR propagation.

Zhong et al. [77] explored the impacts of heating power, SOC, and the cell spacing on cascading failure in the LIB arrays. 18650 LIB cells were employed to

construct two different rectangular arrays: 3 (1 column × 3 rows) or 9 (3 columns ×3 rows) cell arrays without any spacing between neighboring cells. TR was triggered in one of the cells via a cylindrical electric heater with similar dimensions to the cells' dimensions. The failure propagation was tracked using thermocouples (attached at the mid height of side walls of each cell) and visual observations. The fully charged 3 cell arrays were tested at four different heating powers (100, 200, 300, or 400 W). The fully charged 9 cell arrays were only tested at 100 or 200 W. None of the 3 cell arrays experienced cascading failure due to limited contact area between cells, while all the 9 cell arrays underwent cascading failure in all their cells. For the 9 cell arrays, increasing the input power from 100 to 200 W only expedited TR of the cells located in the first row and had a negligible impact on the duration between failures of consecutive rows. Reducing the SOC of the 9 cell arrays to 50% did not stop the failure propagation, but the cells failed slower than the 100% SOC cells. Implementing 4 mm gaps between the cells prevented TR propagation and resulted only in failure of two cells in row 1 and one cell in row 2.

2.1.6 Review of Active Suppression of LIB Fires

A limited number of studies have investigated the efficiency of extinguishing agents to suppress the fires accompanying TR of LIB cells. These studies have focused on using Halon, Novec1230, and water mist as suppressants. Summer [78] investigated the fire safety of lithium ion and lithium polymer batteries and found that these batteries reacted violently when exposed to an external fire. The batteries ejected large amounts of flammable electrolyte, which further fueled the existing fire. A hand-held Halon 1211 fire extinguisher was utilized to suppress the battery fires. Although the Halon

1211 was able to extinguish the flames when applied to the batteries, the temperature of the battery kept increasing, and the ejected gases reignited again.

In a study by Maloney [8], Halon 1301 was utilized to extinguish fires caused by the ignition of gases ejected from LCO cell arrays. Tests were conducted in a well-sealed 10.8 m^3 test chamber. A cell array was placed inside the chamber, and the chamber pressure was brought down to a predetermined pressure. Halon 1301 was then introduced to the chamber at different volumetric concentrations: 3%, 5.28%, and 10.43%. Subsequently, TR was initiated in one cell using a cartridge heater and observed to propagate throughout the cell array by monitoring the temperature at different locations across the tested array. A spark igniter was utilized to initiate combustion of ejected materials. The chamber pressure rise due to combustion was recorded. The test results showed that the volumetric concentrations of 3% and 5.28% were unable to prevent combustion, while a volumetric concertation of 10.43% was able to successfully suppress the combustion.

Wang et al. [79] investigated the efficiency of Novec1230 (C_6F-Ketone) and CO_2 extinguishing agents on suppressing the lithium titanate battery fires. A commercial lithium titanate oxide battery with 50 A h nominal capacity was heated using a 5 kW electric heater to initiate TR. Tests were conducted both in open atmosphere and within and enclosure. The agents were introduced to the battery as soon as TR started. Results showed that CO_2 was unable to completely extinguish the fires, while the Novec1230 agent extinguished the fire within 30 s in all tests.

In another study by Liu et al. [80], the Novec1230 agent was also utilized to suppress the fires accompanying TR of a fully charged prismatic LIB cell with NMC

cathode and 3800 mA h nominal capacity. The tested battery was placed inside an explosion proof module box equipped with a pressure relief vent. A fire detection tube was fixed directly above the safety vent opening; this tube was connected to the Novec1230 agent tank. When the temperature inside the box exceeded a certain threshold, the detection tube melted and the Novec1230 agent was released into the box to extinguish the initiated fire. Suppression experiments were also repeated in an open environment. Different mass doses of Novec1230 agent including 0, 0.5, 1, and 2 kg were examined. The results showed that small mass doses of Novec1230 (below 1 kg) had a negative inhibitory impact on combustion of ejected materials. However, introducing Novec1230 at greater mass doses (above 1 kg) allowed for better suppression of combustion of ejected materials and achieved lower maximum cell temperature.

As an efficient clean fire extinguishing agent, water is widely applied in firefighting because of its outstanding cooling ability. In a study by Ditch [81], it was determined that a sprinkler system can provide protection for a growing or developed LIB rack storage fire. However, the re-ignition remains a potential threat if the water delivery is stopped before temperatures drop to safe levels. Compared with traditional water sprinklers, the water mist technique has shown to provide a better cooling efficiency while consumes less water. Liu et al. [82] investigated the effectiveness of using water mist cooling on TR induced in individual commercial NMC cells. TR was initiated using an electric heater supplied by a 100 W DC power. Tests were conducted inside a chamber of clear walls. A water mist nozzle was placed 0.5 m above the tested battery to introduce the mist into the chamber. The nozzle discharged the water at

pressure and flow rate of 0.5 MPa and 0.79 l min^{-1}, respectively. TR was prevented only when the water mist was applied before the surface temperature of the battery reached a critical value that was 20 °C below the TR onset temperature for the tested cells.

2.2 Review of Numerical Studies

In addition to experimental studies, failure of individual LIBs and failure propagation in LIB arrays has been investigated in numerical simulations. Doughty et al. [83] proposed two general approaches to build such models: calorimetric and chemical reactions approaches. The calorimetric approach requires complete description of the cell design (dimensions and materials), measurement of either materials or whole cell thermal properties (such as heat capacity and thermal conductivity), calculation of materials/cells' thermal response properties, and inclusion of the effect of aging on the thermal response properties. The chemical reaction approach requires identification of the dominant chemical reactions associated with thermal failure events and the evolved chemical species. Reaction rates and activation energies must be measured for all relevant reactions. The studies in this section are divided into two main categories: modeling studies of single LIBs and modeling studies of LIB arrays (packs).

2.2.1 Review of Modeling Studies on Thermal Runaway of Individual LIBs

Several studies focused on modeling LIBs under normal operating conditions. Al Hallaj et al. [44] utilized a one-dimensional thermal model with lumped parameters to simulate temperature profiles under different operating conditions and cooling rates for cylindrical LIB cells of 10 and 100 A h nominal capacity. Results showed that the

cooling rate has a significant effect on the temperature of cells. More specifically, high cooling rates resulted in a significant temperature gradient across the body of the cell. At low cooling rates, however, the LIBs behaved as a lumped capacity body (negligible temperature gradient). Also, the simulation demonstrated a good agreement with temperature measurements at different discharge rates. Pals and Newman [84, 85] produced one-dimensional models that were able to predict the thermal behavior of LIBs. In Part I [84], the authors presented the one-cell model for predicting the thermal behavior of the lithium negative electrode/solid polymer separator/insertion positive electrode cell. In Part II [85], they presented the cell-stack model, a model that used variable heat-generation rates calculated by the one-cell model to predict temperature profiles in cell stacks. Forgez et al. [86] developed a lumped parameter thermal model of a cylindrical $LiFePO_4$/graphite LIB. Heat transfer coefficients and heat capacity were obtained from internal temperature measurements while applying current pulses of different magnitudes at 2 Hz and then inputted them into the model. The developed model enabled estimation of battery internal temperature using the measured current and voltage, and the results were validated with experiments (the model accuracy was within 1.5 °C).

Chen et al. [87] presented a two-dimensional model to simulate the temperature distribution across the layers of spirally wound cells (cylindrical cells) during the discharge process. The temperature in the angular direction was found to be fairly uniform and heat was mainly transferred along the radial direction. Due to natural convection, the hottest temperatures were located in a circular region near the liquid-filled hollow core, not in the exact center. Additionally, air cooling effectively reduced

the surface temperature, yet the inner temperature remained less affected. Radiation contributed to 53.6% of the heat dissipation from the simulated LIB to the surrounding air.

Chen et al. [88] proposed a three-dimensional thermal model to study the thermal behavior of LIBs under various discharge rates. Their model considered the layered-structure of all cell stacks, the case of the LIB pack, and the gap between both elements. Both location-dependent convection and radiation were prescribed at boundaries to demonstrate different heat dissipation performances on all surfaces. The model provided the temperature distribution inside the battery and at the surface as well. Obtained results showed that radiation contributed 43-63% to the overall heat dissipation.

Additional modeling work has been conducted to investigate thermal runaway in single LIBs. Hatchard et al. [89] produced a predictive one-dimensional model for 18650 $LiCoO_2$/graphite cells undergoing TR due to external heat exposure in an oven (oven exposure testing is a standard benchmark abuse test of commercial LIBs). The model predictions of the temperatures of the cells compared favorably with the oven exposure test results. The model was also capable of producing reliable predictions for a variety of extrapolated test conditions such as changing cathode chemistry (i.e $LiMn_2O_4$), increasing the specific surface area of the graphite electrode, varying the diameter of cylindrical cells, or testing cells of prismatic form factor (with different thicknesses).

Kim et al. [90] extended the one-dimensional modelling approach formulated by Hatchard et.al [89] to a three-dimensional model (utilizing finite volume method)

so that geometrical features are considered, allowing for further understanding of the thermal behavior of large format LIBs under oven abuse tests. The model included a list of chemical reactions associated with TR of LIBs; all physical and kinetic parameters utilized in this model were collected from the literature. The model results showed that smaller cells dissipated heat faster than larger cells, which reduces the possibility of TR initiation. In simulations of local hot spots inside large cylindrical cells, the model showed that the reactions initially propagated in the radial and longitudinal directions to form a reaction zone of a hollow cylinder shape. Guo et al. [91] developed a three-dimensional model to simulate the thermal behavior of high capacity prismatic LIBs undergoing oven abuse tests. The model accounted for the effects of geometrical features, heat generation, internal conduction and convection, and external heat dissipation to predict the temperature distribution within a battery. The model predicted favorably the qualitative and quantitative behaviors of a cell in an oven test. The modeling predictions indicated that $LiFePO_4$ active material was more thermally stable in oxidation potential than $LiCoO_2$. The temperature gradient was minimal along the width and length of the LIB and was maximum along the thickness.

Liu et al. [54] utilized COMSOL Multiphysics software to construct a three-dimensional numerical model that predicted the temperature of individual 18650 LIBs undergoing uniform heating in the copper slug battery calorimetry (CSBC) apparatus [53]. In this model, the apparatus was represented by an axisymmetric object with all dimensions equal to those of the actual apparatus. All material properties (density, heat capacity, and thermal conductivity) and heat transfer parameters (heat transfer coefficient and emissivity of surfaces) were obtained from available literature data.

Initial simulations concerned the calibration experiments wherein the LIBs were replaced by a solid copper cylinder [53, 54], without heat generation. In these initial simulations, the thermal conductivity of the insulation (which was an unknown property) was adjusted to achieve good match between the simulated and experimental copper slug temperatures. Subsequently, the thermal conductivity of the LIBs was determined using a similar inverse modelling approach. The thermal conductivity was adjusted until the best agreement between predicted and experimental axial temperature histories (which were collected only up to safety venting since no heat is generated before safety venting). Lastly, the experimental measurements of the volumetric heat generation versus time were fitted with a piecewise-linear function and subsequently coupled with the derived insulation and LIB thermal properties to simulate thermal failure of a LIB. Temperatures obtained from this simulation were validated against experiments and found to be within 5% of the experimental data for all LIB types and SOCs, which indicated that the lumped heat capacity assumption invoked in the analysis of the CSBC experiments was generally valid.

Liu et al. [26] developed a thermo-kinetic model of thermally-induced failure for an LIB using COMSOL Multiphysics software and experimental data measured by CSBC apparatus. The model was proposed for a specific type of LIB (Tenergy ICR18650). CSBC tests were conducted on LIBs to determine the thermal transport parameters and global reaction kinetics associated with the LIBs thermal failure. The model was parametrized via an inverse modeling analysis of the CSBC tests similarly to a previous study by Liu et al. [54]. This model assumed a varying radial thermal conductivity, while it was isotropic in Liu's previous study [54]. Additionally, the

model represented the process of TR by a single first order reaction. The reaction parameters (Arrhenius parameters and heat of reaction) were fitted to be functions of SOC. The model was then validated against CSBC tests that were conducted under conditions not utilized in the parameterization process of the model. The predictions of the model did not always fall within the experimental uncertainty. However, the predicted slug temperatures showed the same qualitative trends and were, on average, within 5% of the mean experimental values, which represents a good overall agreement. The model was also capable of predicting the maximum cell temperature.

2.2.2 Review of Modeling Studies on Thermal Runaway Propagation in LIB Arrays

In addition to experimental studies, a limited number of modeling works has been conducted on LIB array failure as well. In the same work by Liu et al. [26], the generated thermo-kinetic model was applied to predict the thermally induced failure of LIB cells in a more complex scenario: cascading failure of 6 LIB cells in a "billiard rack" configuration. The model predictions showed a good agreement (within 9%, on average) between the simulated and experimentally recorded TR onset times of each failing cell in the tested array.

Feng at al. [92, 93] expanded upon their previous work [74] and built a three-dimensional TR propagation model based on energy balance equations. Empirical equations based on their DSC and ARC data were used to simplify the chemical kinetics calculations and equivalent thermal resistant layers were used to simplify the heat transfer between thin layers with complex geometries. The model determined that TR propagation could be postponed or prevented by modifying the separator to increase failure onset temperatures, discharging the cells to reduce the total energy release,

increasing the convection coefficient to enhance the heat dissipation, or using thermal insulation layers to reduce cell-to-cell heat transfer. Experiments were conducted to validate all of these findings as well.

Wang et al. [94] utilized three-dimensional computational fluid dynamics (CFD) modeling to study the impact of cell arrangement and forced air-cooling strategies on battery pack failure. Results showed that forced air-cooling significantly reduced the temperatures of battery modules and that cooling was most effective when directed at the top of the battery pack. Additionally, a 5 by 5 square arrangement of LIB cells showed the best cooling capability, in comparison to 1 by 24 rectangular, 3 by 8 rectangular, 19 cell hexagonal, and 28 cell circular arrangements. The 19 cell hexagonal arrangement was found to best optimize space utilization, however.

2.3 Objectives and Scope of Current Study

None of the previous studies quantified the speed of TR propagation in LIB cell arrays or packs, measured the composition of gases evolved during the propagation, or determined the thermal energy production. A new experimental setup, therefore, was designed and built for the present study to provide these important data to better understand the processes that govern the cascading failure dynamics. The setup included a sectioned wind tunnel that was used to obtain well-defined boundary conditions for the study of LIB cell arrays.

The first stage of this work was to study the impact of cell array size on the dynamics and hazards of cascading failure. Fully charged Tenergy lithium cobalt oxide (LCO) cells of 18650 form factor and 2600 mA h nominal capacity were used to

construct wall-to-wall 18 (3×6) or 12 (3×4) cell arrays. The arrays were then mounted in the wind tunnel and tested in an N_2 environment.

In the second stage, the focus was to investigate the relation between the cascading failure dynamics and hazards and the LIB cathode chemistry. Lithium cobalt oxide (LCO), lithium nickel manganese cobalt oxide (NMC), and lithium iron phosphate (LFP) cells of 18650 form factor and 2600, 3000, and 1500 mA h nominal capacity, respectively, were utilized to construct wall-to-wall 12 cell arrays. The cascading failure was investigated in an anaerobic environment (N_2) as well as in air to elucidate the impact of flaming combustion.

In the third stage, this work explored passive mitigation strategies to cascading failure using physical barriers between cells. All mitigation experiments were carried out on LCO cells charged at 100% SOC. Due to the fact that battery pack design is typically guided by stringent size and mass limitations, the barriers were introduced between groups of closely spaced cells (rather than between individual cells) and the thickness of the barrier was constrained to 5 mm. The barrier experiments were carried out in an N_2 environment to prevent flaming combustion of ejected materials and thus provide a more controlled environment, where the impact of barriers on failure dynamics could be better quantified. Barrier performance was evaluated by comparing the results of solid barrier experiments with the results obtained for arrays containing empty gaps of the same size and experiments without gaps.

In the last stage, the ability of two extinguishing agents (Novec1230 and water mist) to suppress the fires accompanying cascading failure and prevent failure propagation was investigated. 12 LCO cell arrays were utilized in the suppression

experiments. The experimental setup was equipped with two different systems to enable controlled introduction of the suppressing agents to the system. The Novec1230 agent was introduced at two different concentrations of 8.5 and 15.2 vol.%, while the water mist was utilized at 11.1 and 14.1 wt.%.

For all experiments, the failure was initiated with a small electric heater attached to the side wall of one of the peripheral cells. The setup provided simultaneous measurements of temperature of each cell, and temperatures and volumetric concentrations of gases ejected during cascading failure. The cell temperature measurements allowed calculation of TR propagation speed in the presence and absence of flaming combustion. The gas concentration and temperature profiles, recorded in the anaerobic environment tests, enabled calculation of mass yields and lower flammability limit of the gases ejected by the arrays, as well as the rate of chemical heat generation due to reactions between battery components inside and outside the cell casings. The tests conducted in an air environment were used to evaluate the additional heat produced due to flaming combustion of ejected battery materials.

The main goal of this collection of investigations was to provide previously unavailable, comprehensive assessment of the failure dynamics and energetics in LIB cell arrays or assemblies. These results are expected to serve as a foundation for effective detection, mitigation and prevention of electrical energy storage and electric vehicle fires.

3. Experimental Setup

The objective of this chapter is to present the design criteria and concepts needed to build the experimental facility utilized in this study. Detailed dimensions and descriptions of materials of each component in this setup are provided as well. The designed setup was employed to comprehensively investigate and characterize cascading failure in LIB cell arrays. Additionally, the chapter provides details of the modified CSBC apparatus, originally developed by Liu et al. in [26, 53, 54], which was utilized to measure the heat of nearly complete combustion of ejected materials from individual LIB cells during TR. The test matrices and experimental procedures are added to the last section of this chapter.

3.1 Specifications of LIB Cells

LIB cells with an 18650-form factor, cylindrical geometry of 18 mm in diameter and 65 mm in height, are selected to construct the LIB cell arrays tested in this study. Three different commercial cells were investigated herein: Tenergy ICR18650 [95], LG HG218650 [96], and K2 18650E [97]. Detailed specifications of these cells are listed in Table 3. 1. All uncertainties reported in the table were computed from the scatter of the data as two standard deviations of the mean. The selection of those specific cells was based on the following considerations:

- The 18650 form factor is widely used in a multitude of modern applications such as electric vehicles.
- Different cathode chemistries have different thermal stabilities, which are critical parameters for the fire safety of LIB cells. Therefore, in this study, LIB cells of the

most widely and commercially available cathode chemistries were tested. Based on thermal stability, cathodes can be ranked as follows: LCO < NMC < LFP [38].

Table 3. 1. Factory specifications of the LIB cell samples tested in this study. The uncertainties were computed from the scatter of the data as two standard deviations of the mean.

Specification	Tenergy ICR18650 [95]	LG HG218650 [96]	K2 18650E [97]
Cells with and without packaging			
Cathode	LCO	NMC	LFP
Anode	carbon	carbon	carbon
Safety vent ports number	4	3	5
Nominal capacity [mA h]	2600	3000	1500
Nominal voltage [V]	3.7	3.6	3.2
Minimum cutoff voltage [V]	2.75	2.5	2.5
Maximum cutoff voltage [V]	4.2	4.2	3.65
Discharging current [A]	1.3	0.6	≤ 0.7
Charging current [A]	1.3	1.5	≤ 0.7
Electrical stored energy [kJ]	33.0 ± 0.3	44.3 ± 1.3	17.4 ± 0.2

As shown in Table 3. 1, the positive terminals of each cell are equipped with safety venting ports to release the gases formed inside the cell's enclosure during TR, which helps to avoid cell rupture or explosion caused by pressure build up. Detailed chemical compositions (in mass %) [98-102] of all listed cells are included in Appendix A (Table A. 1, Table A. 2, and Table A. 3). The electrolyte of these LIB cells consists

of organic carbonate mixtures such as EC, DEC, PC, and/or EMC and uses a non-coordinating anion salt of $LiPF_6$. Prior to each experiment, the LIB cells were stripped off their plastic packaging, and their initial masses were recorded.

Prior to the charging process, the cells were electrically cycled according to manufacturer recommendations using an iCharger 208B battery charger controlled by a computer software. The charging process was performed in steps to confirm careful charging of cells to the desired SOC. First, each cell was fully discharged to a minimum cutoff voltage using a constant discharge current. Second, groups of 4 or 6 cells, electrically connected in series, were fully charged to a maximum cutoff voltage, using the constant current/constant voltage balanced charging method [4] until the charge current fell below 0.1 A. Third, the cell groups were then fully discharged to a minimum cutoff voltage. In the last step, the cell groups were charged to the desired SOC of 100%. One exception was the NMC cells that were directly heated by the electric heater to initiate TR; these cells were charged to 50% SOC. The reason for this exception is provided in section 3.5.2. All minimum/maximum cutoff voltages and charging/discharging currents are listed in Table 3. 1. Temporal profiles of the voltage of each cell and the discharge current were recorded during the discharge process. Integrating the product of the voltage and current profiles enabled calculation of the electrical energy stored in each cell, which is also provided in Table 3. 1. This energy was found to be within 1-10 % of the cells' nominal capacities.

3.2 Experimental Setup – Cascading Failure Experiments

A schematic of the experimental facility [103-105] is shown in Figure 3. 1. The setup is composed of three major systems: gas handling system, wind tunnel, and

emitted-gas sampling system. Each system is described in detail in the following subsections. The design process of the experimental setup depended primarily on the dimensions of the cell holder. The discussion, therefore, will start by the design details of the cell holder.

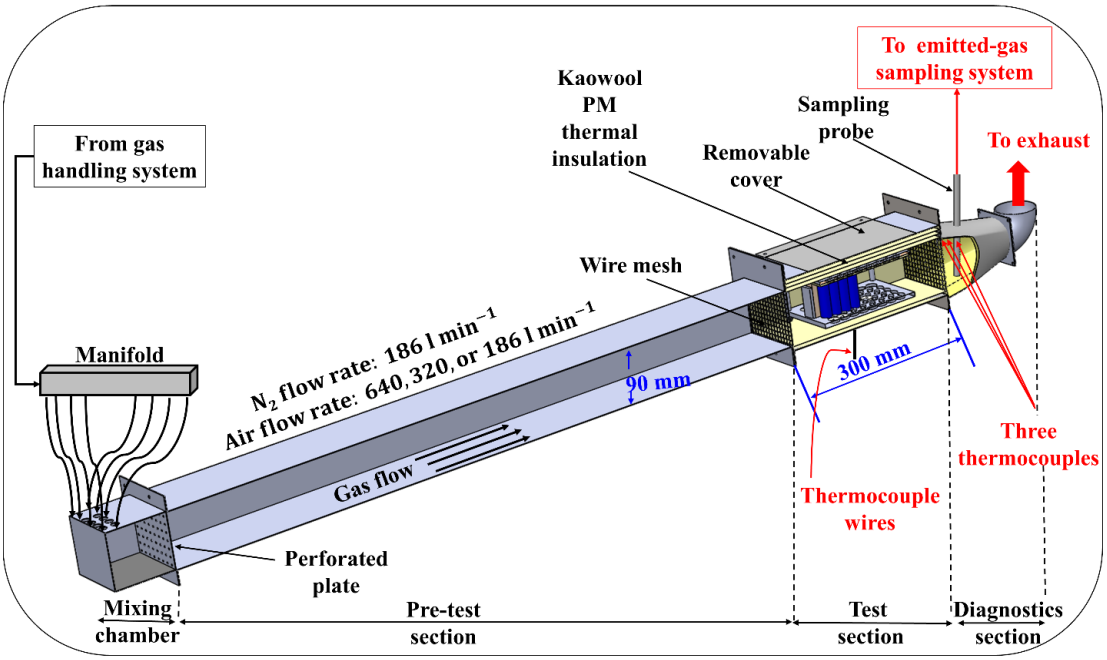

Figure 3. 1. Schematic of the experimental setup (the wind tunnel is drawn to scale).

3.2.1 Cell Holders and Tested Array Configurations

3.2.1.1 Cell Holder without Gaps

The tested cells were arranged in rectangular arrays of either 18 (3 columns × 6 rows) or 12 (3 columns × 4 rows) cells without any spacing in between adjacent cells. A custom-made cell holder, shown in Figure 3. 2, was utilized to maintain the geometry of the LIB cell arrays throughout the cascading failure experiments. The cell holder was made from a stainless-steel frame which consisted of upper and lower plates. This holder was able to support a maximum capacity of 40 LIB cells per test (5×8 rectangular array). 40 depressions of 18 mm diameter and 4.5 mm depth each were machined into the lower plate. The cells were inserted into these depressions in such a

way that each cell was in contact with neighboring cells. The depressions were equipped with Kaowool PM (refractory ceramic fiber) thermal insulation discs (18 mm in diameter and 3.2 mm in thickness). One disc was placed underneath each cell to minimize the heat transfer between the cells' bottom surfaces and the lower plate.

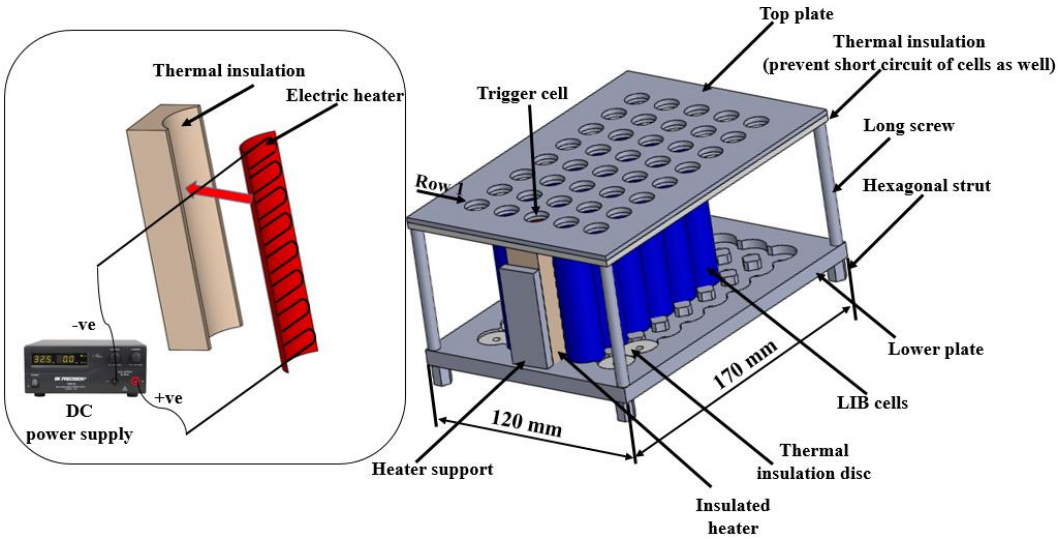

Figure 3. 2. Schematics of the cell holder and electric heater.

A 3.5 mm diameter opening was drilled into the center of each depression and insulation disc, through which silica fiber insulated K-type thermocouple wire (XS-K-24) was extended so that the thermocouple bead was located between the LIB's base and its insulation disc to record the temperature of the bottom surface of each LIB. The top plate, with 40 circular perforations of 12 mm diameter, was placed atop cells in such a way that the safety venting ports were not obstructed by the holder. The contact surface between the upper plate and the top surface of cells was insulated using a perforated Kaowool PM (ceramic fiber) insulation panel to reduce the heat transfer from cells to the plate (thermal isolation purpose) and also to preclude possible short circuit of cells (electrical isolation purpose). The upper and lower plates were secured together using four long screws of 6 mm diameter each. The lower plate was equipped

with four hollow internally threaded hexagonal struts into which the long screws were secured. The wind tunnel test section was designed with an internal open cross section of 90 mm tall by 120 mm wide to house the cell holder.

Thermal failure was initiated into the middle cell (referred to as trigger cell) of row 1 via a surface electric heater depicted in Figure 3. 2. The heater, of 58 mm height and width of 0.45 times the LIB's perimeter (25.4 mm), was made from a nickel resistive heating wire that was wrapped in a coil form and insulated with a high-strength fiberglass cloth tape. The back surface of the heater was insulated using a Kaowool PM (ceramic fiber) thermal insulation piece, as shown in Figure 3. 2, to direct all the supplied energy from the heater to the cell and prevent any significant heat losses from the heater to the environment. The heater assembly was tightly secured between the LIB surface and a stainless-steel support to assure complete contact between the heater and the trigger cell and to prevent any movement of the heater. The heater was powered by a DC power supply, BK Precision 1685B, to initiate the failure.

Figure 3. 3 displays a top view schematic of the tested cell arrays. The 18 cell arrays were only tested in an anaerobic environment (N_2) while the 12 cell arrays were examined in both N_2 and air environments. Further details of the test matrix and procedures are provided in section 3.5.

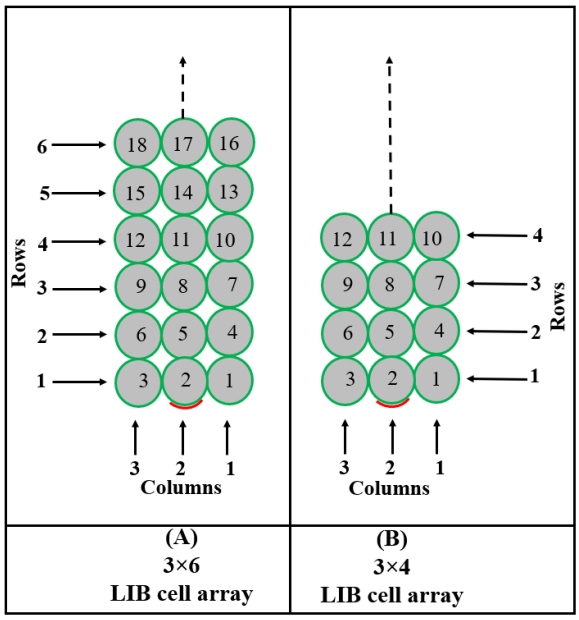

Figure 3. 3. Layout of the studied LIB cell arrays (without gaps). Cell 2 was the trigger cell (the cell that was subjected to localized heating to initiate thermal runaway) in every experiment.

3.2.1.2 Cell Holder with Gaps and Physical Barriers

Several previous studies suggested implementing empty gaps between individual cells of battery arrays/packs to mitigate the cell-to-cell TR propagation, but the gaps would result in a significant increase in the volume of the battery pack. New designs of real battery pack systems are subject to stringent size and mass limitations. Therefore, a different technique [106, 107] was followed in this study where empty gaps were implemented between closely spaced cell groups/clusters rather than between individual cells.

To implement this technique [106, 107], a different custom cell holder was designed and built up for testing closely spaced groups/clusters of cells (with a maximum capacity of 40 cells). Both cell holders (with gaps and without gaps) had similar specifications (such as materials, dimensions, ceramic fiber insulation plates

and discs, heater assembly, and thermocouple locations). The main difference between the two cell holders is the that, in the cell holder with gaps, 5 mm empty gaps were implemented between cell groups/clusters as shown in Figure 3. 4. The electrical heater assembly was attached to the middle cell of the first row of the 9 (3 columns ×3 rows) cell group/cluster. In this cell holder assembly, the top plate perforations were arranged in groups in exactly the same way the cells were grouped so that the safety vent openings were not obstructed and could readily eject the gases during failure conditions.

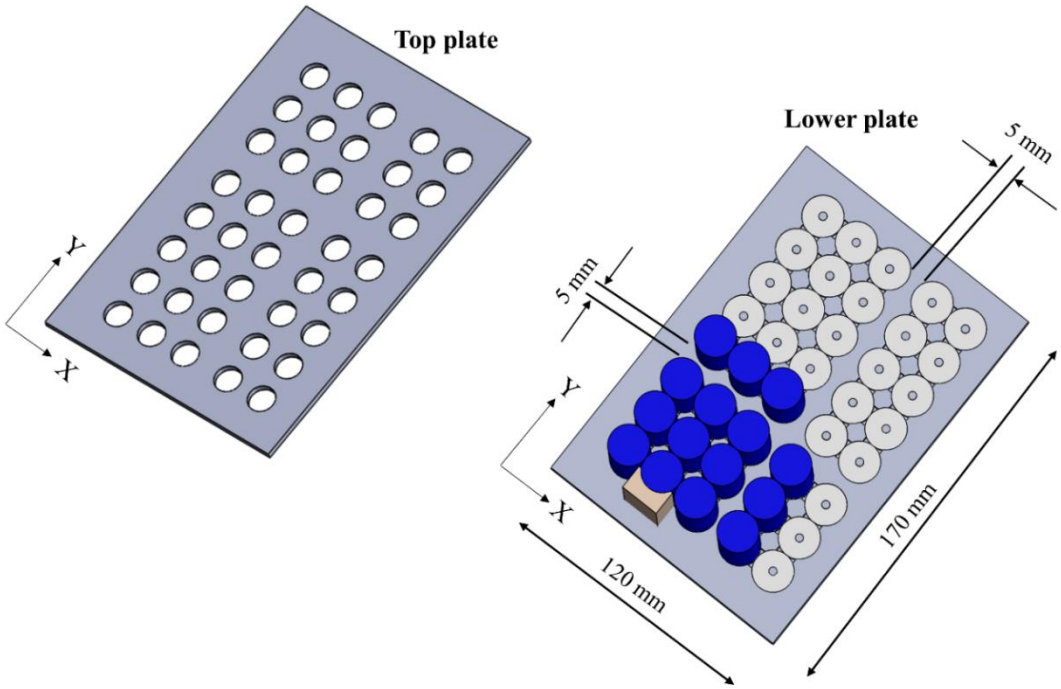

Figure 3. 4. Schematic of the top and lower plates with 5 mm empty gaps.

In further attempts to reduce the heat transfer between cell groups/clusters, the 5 mm empty gaps were equipped with three different types of physical barriers: a double layer of perforated stainless steel plates (referred to as stainless steel barrier), Tecnofire intumescent material [108] supported by a stainless-steel plate (referred to

as intumescent barrier), and Kaowool PM insulation supported by a stainless-steel plate (referred to as ceramic fiber barrier). Figure 3. 5 shows a labeled schematic of the utilized physical barriers. All barrier assemblies were 59.5 mm wide in the direction perpendicular to the gas flow (X-direction), 73 mm long in the direction parallel to the gas flow (Y-direction), and 59 mm in height.

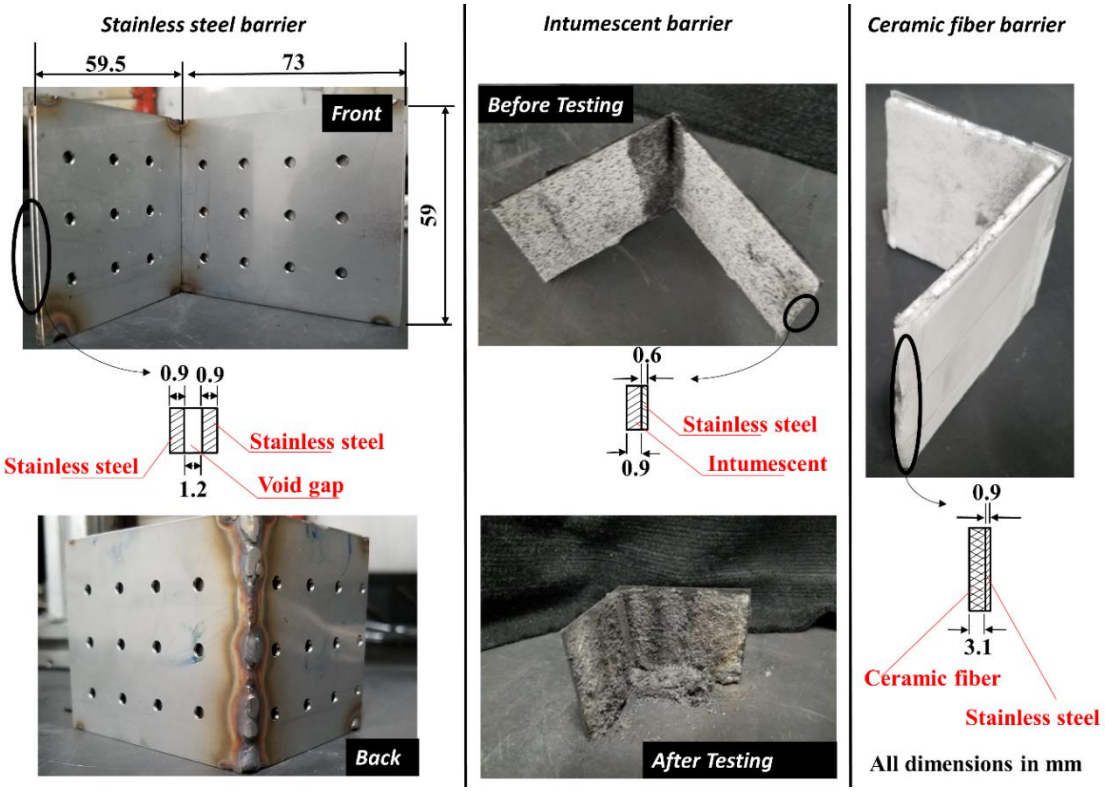

Figure 3. 5. Dimensioned schematics of the tested physical barrier assemblies.

The overall thickness of the stainless steel barrier was 3 mm. The barrier was fabricated from two 0.9 mm thick perforated stainless steel layers. The two layers were separated by a 1.2 mm empty gap. The perforations on the surface of both layers were strategically designed and machined so that they were offset and not aligned with each other. This barrier configuration emulated a typical radiation shield that prevented radiation heat transfer between cells while also allowing for convective cooling of cells by gases flowing through the wind tunnel.

The intumescent material layer was 0.6 mm thick and it was supported on the downstream side by a single layer of 0.9 mm thick stainless steel, resulting in an overall assembly thickness of 1.5 mm. However, the assembly thickness would change during testing because the intumescent material expands at a temperature of approximately 463 K and reaches an expansion ratio of up to 9:1 at 723 K to provide enhanced thermal protection, according to the manufacturer [108].

The overall thickness of the ceramic fiber barrier was 4 mm. The ceramic fiber layer was 3.1 mm thick and supported by a single layer of 0.9 mm thick stainless-steel. Kaowool PM has density, specific heat, and thermal conductivity of 256 kg m^{-3}, 1.07 kJ kg^{-1} K^{-1}, and 0.049 W m^{-1} K^{-1}, respectively, at room temperature [109, 110] and is a thermal insulation product widely used in high temperature (up to 1260 °C) applications. The intumescent and ceramic materials required stainless steel support because initial tests indicated that they would break down during experiments if left unsupported. All barrier assemblies were refurbished after each test except for the stainless steel barrier, which was only cleaned of any carbon particles deposited on the surface.

The tested cells were arranged in three groups/clusters: 9 (3 columns × 3 rows) cell group, 3 (1 column × 3 rows) right-most cell group, and 3 (3 columns × 1 row) back-most cell group. Figure 3. 6 shows a top view schematic of the tested cell arrays. All shown cell arrays were only tested in an anaerobic environment (N_2). Further details of the test matrix and procedures are provided in section 3.5.

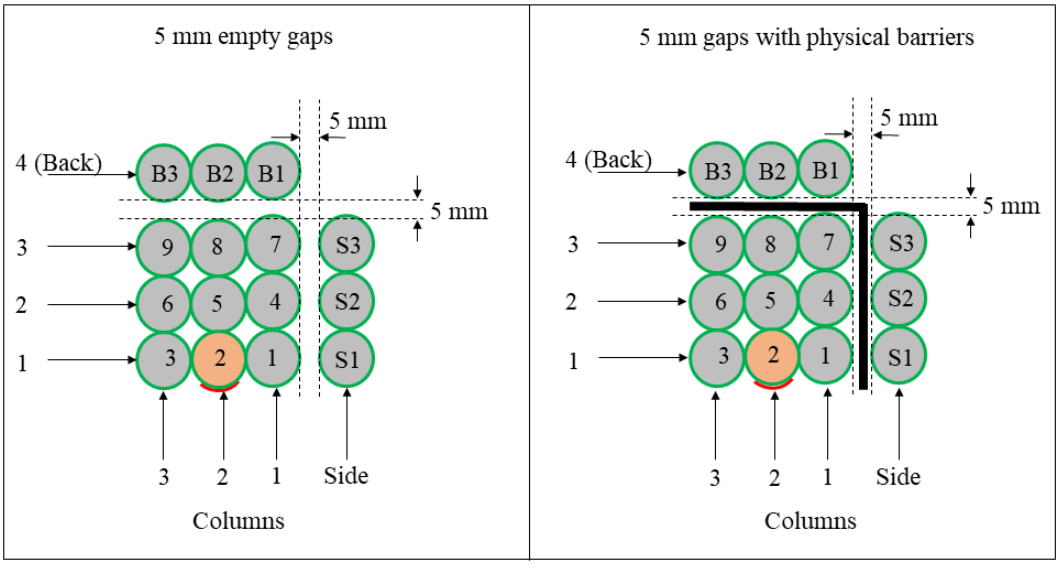

Figure 3. 6. Layout of the studied LIB cell arrays (with gaps). Cell 2 was the trigger cell.

3.2.2 Gas Handling System

The gas handling system presented in Figure 3. 7 was employed to control the gas composition (N_2 or air) and flow rate entering the wind tunnel. N_2 was introduced from a high-pressure nitrogen tank while air was pumped using an air compressor. An Alicat mass flow controller was used to maintain a constant mass flow rate of the introduced gases and was preceded by a pressure regulator in the N_2 line or a filter/dryer in the air line to remove particulates and water vapor.

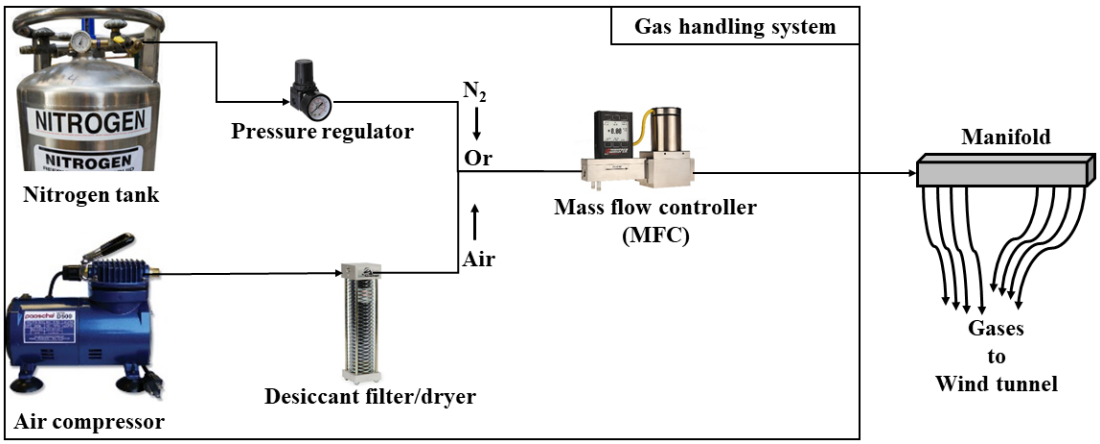

Figure 3. 7. Schematic of the gas handling system.

The N_2 flow rate, 186 l min^{-1} at reference pressure of 14.7 psi and reference temperature of 298 K, was chosen because it was the maximum flow rate that could be maintained constant for the duration of the experiment using the available N_2 storage capacity; this flow rate effectively maintained an anaerobic environment inside the tunnel. When the cell holder was fully loaded with 40 LIB cells, the loaded cell arrays were designed to be ventilated/cooled at an air speed of 4 m s^{-1} (flow is around the array). This speed was within a typical range of ventilation speeds utilized to ventilate/cool LIB packs in most practical applications [68-70, 111]. The air speed, 4 m s^{-1}, corresponded to roughly a 1 m s^{-1} bulk air speed just upstream of the cell array. The air flow rate, 640 l min^{-1} at reference pressure of 14.7 psi and temperature of 298 K, was estimated based on the design speed of air (1 m s^{-1}) and the internal dimensions of the wind tunnel (120 mm × 90 mm). Figure 3. 7 shows that the N_2 or air flow leaving the gas handling system was directed to a rectangular aluminum NITRA pneumatic manifold to provide an even distribution of the flow to the mixing chamber. The manifold received the flow through a single 25.4 mm diameter inlet and discharged it into the mixing chamber through eight 12.7 mm diameter high pressure flexible tubes.

3.2.3 Wind Tunnel

The cell holder was placed inside a wind tunnel to establish well-controlled environment and boundary conditions for cascading failure experiments. Figure 3. 1 shows a three-dimensional rendering of this wind tunnel, which was built using stainless steel ducting. The wind tunnel consisted of four main sections: mixing chamber, pre-test section, test section (containing the cell holder and LIB array), and diagnostics section; photographs of these sections are included in Appendix B (Figure

B. 1 to Figure B. 7). The sections were coupled to each other with bolts and sealed along their flanges with RTV silicon gaskets. The internal dimensions of the wind tunnel, 120 mm width and 90 mm height, were maintained constant throughout the tunnel.

3.2.3.1 Mixing Chamber

The mixing chamber was equipped with eight injectors (12.7 mm in diameter each) that were attached to the flexible tubes coming from the manifold. Detailed dimensions of the mixing chamber are shown in Figure 3. 8. The purpose of the mixing chamber was to hydro-dynamically mix the gas stream before being ejected uniformly into the pre-test section through a perforated aluminum plate. The open area of the perforated plate was 4.6% of the vertical cross-sectional area of the wind tunnel (120 mm × 90 mm). The plate was designed to generate a static pressure larger than the dynamic pressure at the injector exits to produce a nearly uniform flow velocity at the inlet of the pre-test section.

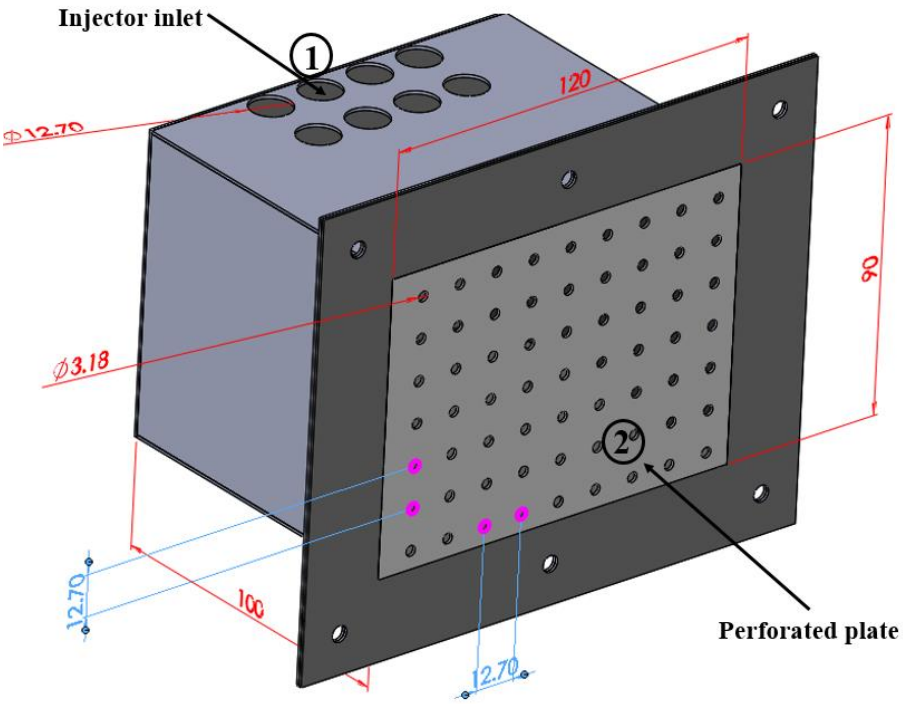

Figure 3. 8. Schematic of the mixing chamber and perforated plate (all dimensions in mm).

Equation 3. 1 assumes that the pressure difference across the perforated plate is greater than the dynamic pressure at the exit of the injectors by a factor of W:

Dynamic pressure at exit of injectors $\leq \frac{1}{W}$ Pressure difference across perforated plate

$$\frac{\rho}{2}V_1^2 \leq \frac{1}{W}(P_t - P_2) \qquad 3.\ 1$$

where ρ is the air density, V_1 is the flow velocity at the exit of injectors, P_t is the total pressure, and P_2 is the static pressure at the exit of the perforated plate.

$$V_1 = \frac{Q}{A_{inj}N_{inj}} \qquad 3.\ 2$$

$$Q = K_{plate}\sqrt{(P_t - P_2)}\,, K_{plate} = A_{open} \times \sqrt{\frac{2}{\rho}} \qquad 3.\ 3$$

where Q is the air flow rate, A_{inj} is the area of the injector, N_{inj} is the number of injectors, K_{plate} is the perforated plate factor, and A_{open} is the open area of the perforated plate. Using Equations 3. 1 to 3. 3, a criterion was determined to compute the pressure factor (W) as a function of injectors and the perforated screen areas as shown in Equation 3. 4.

$$A_{inj}N_{inj} \geq \sqrt{W}A_{open} \quad 3.\ 4$$

For 640 l min^{-1} of air, the plate generated a static pressure drop 4.2 times larger than the dynamic pressure at the injector exits based on the dimensions of the injectors and the open area of the perforated screen.

3.2.3.2 Pre-Test Section

The pre-test section received the gas flow from the mixing chamber as depicted in Figure 3. 1 with the aim of achieving a fully developed flow at the inlet of the test section and providing well-defined flow conditions. To achieve a fully developed flow in the air experiments (which were conducted at a flow rate of 640 l min^{-1}), the length of the pre-test section had to be equal to or greater than the hydrodynamic entry length. The estimation of the hydrodynamic length depended on the nature of air flow (laminar or turbulent). The Reynolds number (Re_D) was computed using the inner dimensions (120 mm × 90 mm) and air speed (u ≈ 1 m s^{-1}) of the pre-test section as described in Equations 3. 5 and 3. 6.

$$Re_D = \frac{uD_h}{\nu} \quad 3.\ 5$$

$$D_h = \frac{4A_c}{P_w} \quad 3.\ 6$$

D_h is the hydraulic diameter of the tunnel (m), ν is the kinematic viscosity of air (m^2 s^{-1}), A_c is the cross-section area of the tunnel (m^2), and P_w is the wetted perimeter of the tunnel (m). The hydraulic diameter and the Reynolds number were estimated to be 103 mm and 6500, respectively. According to the Reynolds number, the air flow was determined to be turbulent, and the hydrodynamic entry length was approximated as 10 D_h [112]. Therefore, the pre-test section was manufactured to be 1.1 m in length as shown in Figure 3. 9. It is noteworthy to mention that the N_2 flow was laminar, and the flow was not fully developed by the end of the pre-test section. However, during the nitrogen experiments, the primary focus was not on achieving a fully developed flow as much as having a near zero oxygen concentration throughout the tunnel.

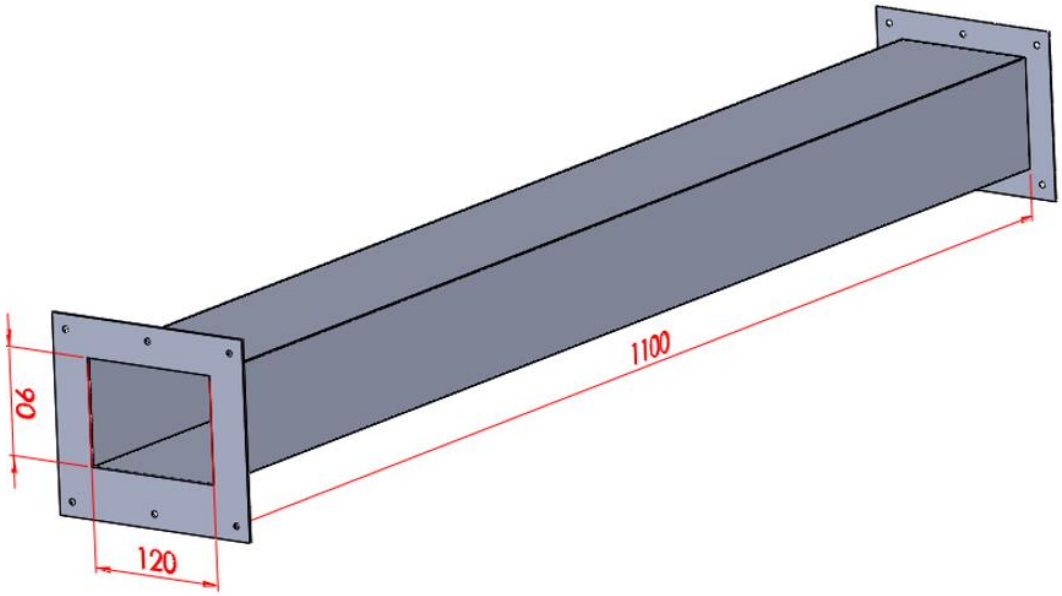

Figure 3. 9. Schematic of the pre-test section (all dimensions in mm).

3.2.3.3 Test Section

The cell holder was fixed with four screws coming through the bottom surface of the test section into the hexagonal struts of the bottom plate, see Figure 3. 10. The center line of the arrays and the symmetry planes of the cell holder and test section

were all aligned. As depicted in Figure 3. 10, the inlet and outlet of the test section were equipped with a wire mesh (8 mm × 8 mm mesh size) to prevent any large debris from travelling either backward or forward through the wind tunnel. The cell holder was accessible via a removable cover. The cover was tightly fixed and sealed during tests to prevent any possible leakage of gases. The top, side, and bottom walls of the test section were lined with panels of Kaowool PM thermal insulation (6.35 mm thickness) to minimize uncontrolled heat loss. One layer of the insulation was used for the side and bottom walls; three layers were used for the top wall because of its direct exposure to materials ejected from the cells. Detailed dimensions of the test section are demonstrated in Figure 3. 10.

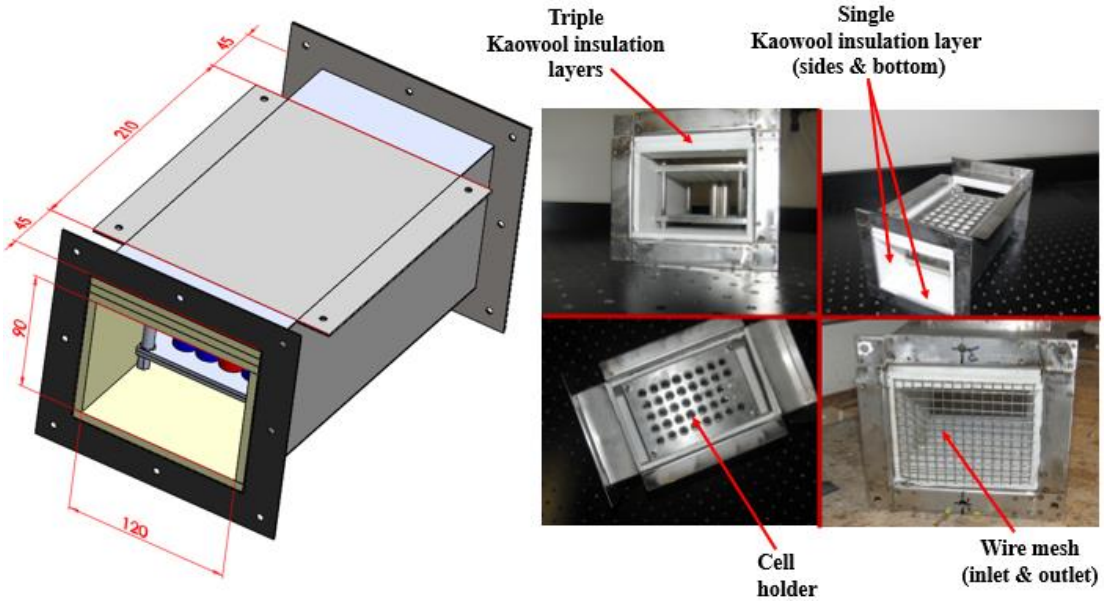

Figure 3. 10. Schematic of the test section duct (all dimensions in mm).

3.2.3.4 Diagnostics Section

As shown in Figure 3. 11, the diagnostic section was designed with a conical shape to increase the momentum of flowing gases, which reduced the boundary layer formation (or thickness) and assisted in achieving representative sampling

temperatures and compositions of the exhaust flow. An elbow was attached to the outlet of the diagnostic section to direct the exhaust flow towards an exhaust hood. The internal walls of the diagnostics section were insulated with a single layer of 6.35 mm thick Kaowool PM thermal insulation.

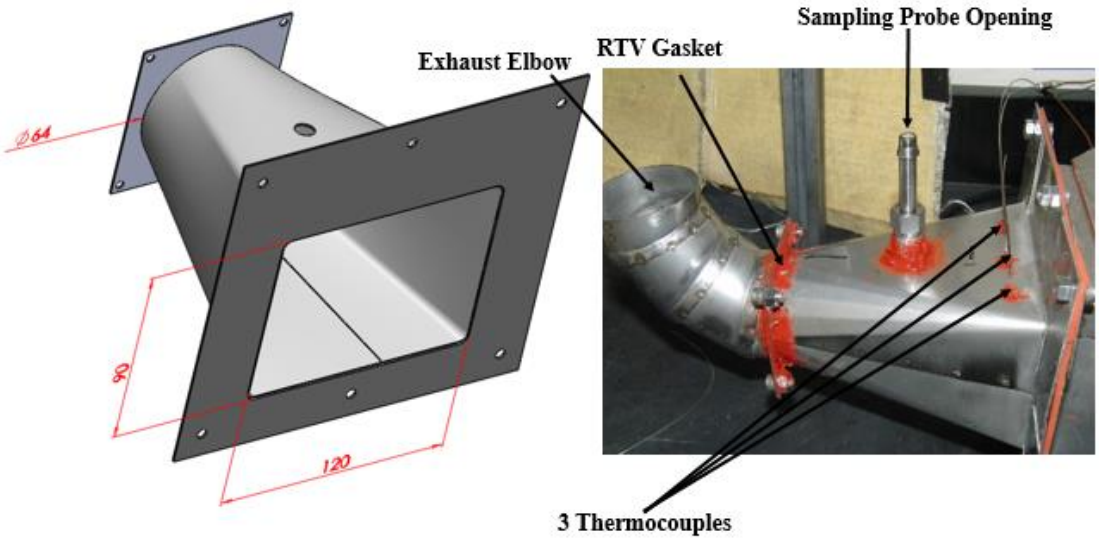

Figure 3. 11. Description of the diagnostics section and exhaust elbow (all dimensions in mm).

This section was equipped with three K-type, stainless steel sheathed, thermocouples (1 mm probe diameter, such large probes were utilized to provide necessary mechanical integrity). Figure 3. 12 depicts the vertical cross section within the diagnostic section along the plane of the exhaust gas thermocouples which were positioned 15 mm back from the section inlet and 46, 36, and 17.5 mm below the bottom surface of the top insulation layer to record the histories of exhaust gas temperature. The thermocouple locations were selected to sample the temperature of the exhaust flow near the bottom, middle, and top of the cross section downstream of the LIB cell arrays.

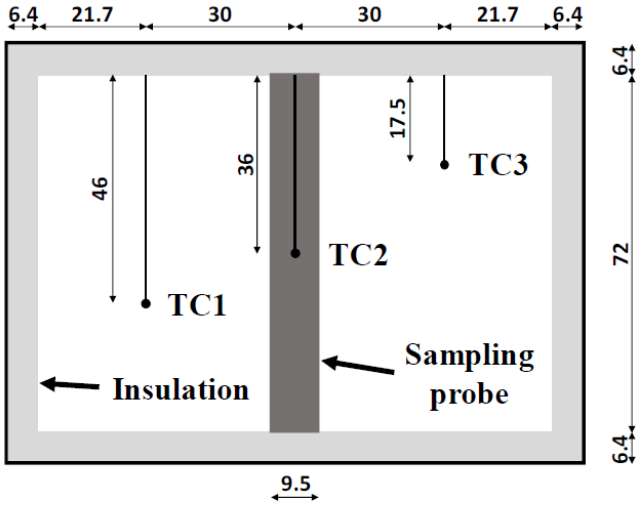

Figure 3. 12. Schematic of the vertical cross section within the wind tunnel along the plane of the exhaust gas thermocouples (all dimensions in mm). The sampling probe is positioned 60 mm behind the thermocouples, TCs.

A sampling probe, made from a hollow stainless steel tube with an internal diameter of 9.5 mm, was vertically inserted into the diagnostic section 60 mm downstream of the thermocouples to sample gases. One end of the tube was blocked, while the other end was connected to the emitted-gas sampling system. The exhaust gas was sampled through two longitudinal columns of perforations, each 1 mm in diameter, located on the tube. The sampling probe was inserted into the section with the perforations facing towards the exhaust elbow of the wind tunnel. The probe was repeatedly purged with an air duster after each test to protect the sampling perforations from clogging and prevent any accumulation of solid particles inside the tube. Additional tests were conducted to check the uniformity of gas sampling location. In these tests, some of the perforations located near the upper or lower end of the sampling probe were temporarily blocked. The results of these tests showed negligible dependence of the sampled gases on the location sampling perforations, indicative of homogenously mixed gases at the position of the sampling probe.

3.2.4 Emitted-Gas Sampling System

The emitted-gas sampling system was responsible for conditioning and analyzing the sampled gas. A schematic of the emitted-gas sampling system is depicted in Figure 3. 13. The gases sampled through the probe were first filtered using a disposable coalescing filter of 95% efficiency at 0.01 microns and subsequently passed through an aluminum adsorption housing containing a desiccant (Drierite) to ensure a complete dehumidification of the sample. A 10KD series diaphragm double head pump, located downstream of the adsorption housing, was utilized to draw samples to the sensors. The pump discharge was divided into four parallel streams, each set to 1.25 l min^{-1} via acrylic rotameters. The distance between the sampling probe and inlet of the pump was designed so that the temperature of the gases entering the pump did not exceed 47°C. The temperature of the gas sample was monitored downstream of the sampling pump to confirm this temperature does not exceed the allowable threshold (47°C) and thus avoid damaging the gas sensors.

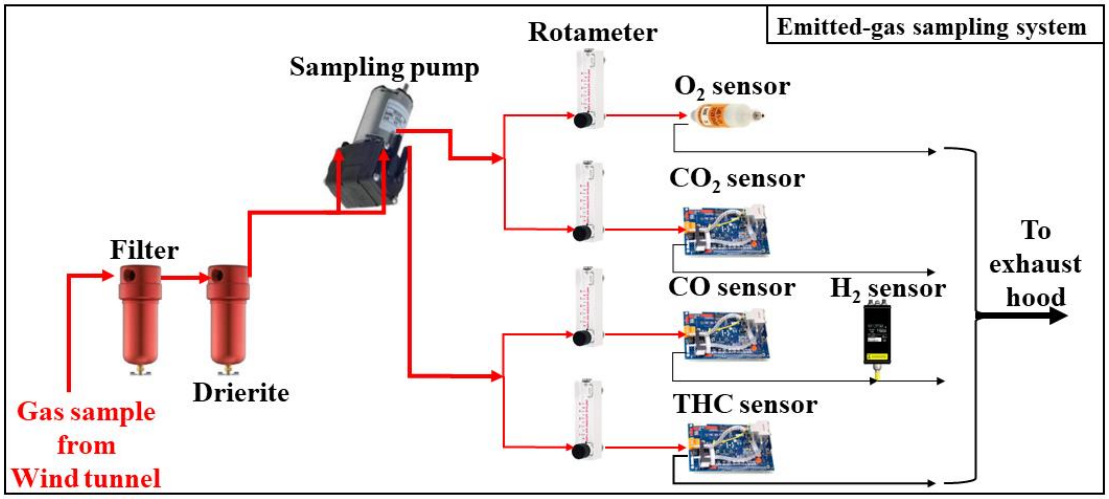

Figure 3. 13. Schematic of the emitted-gas sampling system.

The four streams were connected to gas analyzers which included a fuel-cell type automotive O_2 sensor "Teledyne R17-a", CO/CO_2/total unburned hydrocarbons

(THC) “EDINBURGH Gas-card NG” infrared gas sensors, and a thin film palladium-nickel alloy “HY-OPTIMA 700B Series” H_2 analyzer. All sensors were installed in parallel except for the H_2 sensor which was placed in series downstream of the CO sensor. The H_2 sensor was disconnected from the system when tests were performed in an air environment to avoid exposure to potentially damaging oxygen concentrations. Each sensor received a sample flow rate of 1.25 l min^{-1}, which was within typical ranges recommended by manufacturers.

3.2.5 Data Acquisition and Sensor Calibration

All thermocouple and gas sensors were digitally sampled at a frequency of 2 Hz with National Instruments DAQ modules and LABVIEW software. For the gas sensors, zero and span calibrations were performed by flowing a chemically pure N_2 and gases of certified compositions, respectively, through the sensors before each test. Gas measurements performed by Maloney [8, 9] showed that methane (CH_4) was the dominant THC ejected by LIB cells that are similar to the ones tested in this study. Therefore, the THC sensor was calibrated using methane gas.

Preliminary experiments were conducted to measure the gas transport time to each sensor. In these experiments, the transport time was simply determined by measuring the time period between introducing a gas sample (at the location where the LIB cells are normally fixed in the wind tunnel during actual battery experiments) and observing a shift in the sensor’s signal. The transport times were measured to be 3, 4, 4, 3, and 7.5 s for the O_2, THC, CO, CO_2, and H_2 sensors, respectively. The quantification of transport time aligned the gas and temperature measurements in the data analysis.

In other separate experiments, response times of the gas sensors were estimated by flowing a gas of known concentration through each sensor and then measuring the time required for the sensor output to change from a baseline value to 66% of the steady state value corresponding to the known gas concentration. The response time for all sensors varied between 2 and 4 s. Also, the response time of the exhaust thermocouples was found to be less than 2 s. These times may affect the peaks of the measured gas signals. However, as mentioned in the analysis sections 4.3 and 0, the main focus was on the integral values of gas yields and produced energetics. Therefore, the response time would have negligible effects on the current results.

3.3 Experimental Setup – Active Suppression Experiments

The capability of two common extinguishing agents (Novec1230 and water mist) to suppress LIB fires and prevent TR propagation was also assessed in this study. The cascading failure experimental setup described in section 3.2 was modified to enable well-controlled introduction of the Novec1230 and water mist agents to the test section, where the cell arrays were located. Detailed information on the handling of the extinguishing agents is discussed throughout the following subsections.

3.3.1 Novec130 Suppression

3.3.1.1 Novec1230 Characteristics

Novec1230 (dodecafluoro-2-methylpentan-3-one) fire extinguishing agent features as a next-generation halon alternative and offers a unique combination of large safety margin, outstanding extinguishing performance, and minimal negative impact on environment. The Novec1230 agent normally exists in a liquid form at room temperature. In fire scenarios, however, this agent is dispersed as a gas. The heat of

vaporization of Novec1230 is significantly lower than the heat of vaporization of water, approximately 25 times smaller. Due to the combination of the lower heat of vaporization and the higher vapor pressure of Novec1230 agent compared to water, the liquid Novec1230 evaporates 50 times faster than water [113]. When discharged through a nozzle from a properly designed system, the Novec1230 agent will rapidly vaporize and evenly spread throughout an enclosure. A summary of the Novec1230 physical properties are listed in Table 3. 2.

Table 3. 2. Summary of the Novec1230 agent physical properties. All values were determined at 25 ºC unless otherwise specified [113].

Properties	Novec1230 [$CF_3CF_2C(O)CF(CF_3)_2$]
Molecular weight	316.04 g $mole^{-1}$
Boiling point at 1 atm	49.2 ºC
Freezing point	-108.0 ºC
Critical temperature	168.7 ºC
Critical pressure	18.65 bar
Critical volume	494.5 cc $mole^{-1}$
Critical density	639.1 kg m^{-3}
Density, saturated liquid	1.6 g ml^{-1}
Density, gas at 1 atm	0.0136 g ml^{-1}
Specific volume, gas at 1 atm	0.0733 m^3 kg^{-1}
Specific heat, liquid	1.103 kJ kg^{-1} $ºC^{-1}$
Specific heat, vapor at 1 atm	0.891 kJ kg^{-1} $ºC^{-1}$
Heat of vaporization at boiling point	88.0 kJ kg^{-1}
Liquid viscosity at 0 ºC/25 ºC	0.56/0.39 centistokes
Vapor pressure	0.404 bar
Relative dielectric strength, 1 atm, (N_2=1)	2.3

3.3.1.2 Novec1230 Fire Suppression Mechanism

The Novec1230 agent extinguishes fires principally via removal of heat from the fire zone. When the Novec1230 agent is discharged into a fire zone, it mixes with air forming a gas mixture with a greater heat capacity than air itself. This gas mixture absorbs a significant amount of heat such that the fire zone cools to a limiting

temperature where combustion can no longer be sustained. The amounts of heat lost by the fire is controlled by the concentration of Novec1230 agent in the gas mixture. Additionally, in this work, the agent/air mixture can induce high convective cooling to the body of the cells, which may prevent or mitigate TR propagation through the cell arrays.

3.3.1.3 Novec1230 Handling System

The main objective of the Novec1230 handling system was to convert the Novec1230 agent from liquid to gaseous form and enable controlled delivery of the gaseous agent to the fire zone, which was located in the test section. The current design of the Novec1230 handling system avoids utilizing high pressure nozzle techniques to eliminate the complexity associated with these techniques. A schematic of the Novec1230 handling system is shown in Figure 3. 14; a photograph of this system is also provided in Figure B. 8. The liquid Novec1230 agent was placed into a stainless steel container with a removable top cover (well-sealed during experiments). The top cover was equipped with a thermocouple to monitor the temperature inside the container. The container side surface and top cover were thermally insulated using a blanket ceramic fiber insulation to minimize the heat loss from the container to the surroundings. The container was placed atop an electric induction surface heater which was used to uniformly heat the bottom surface of the container to evaporate the liquid agent.

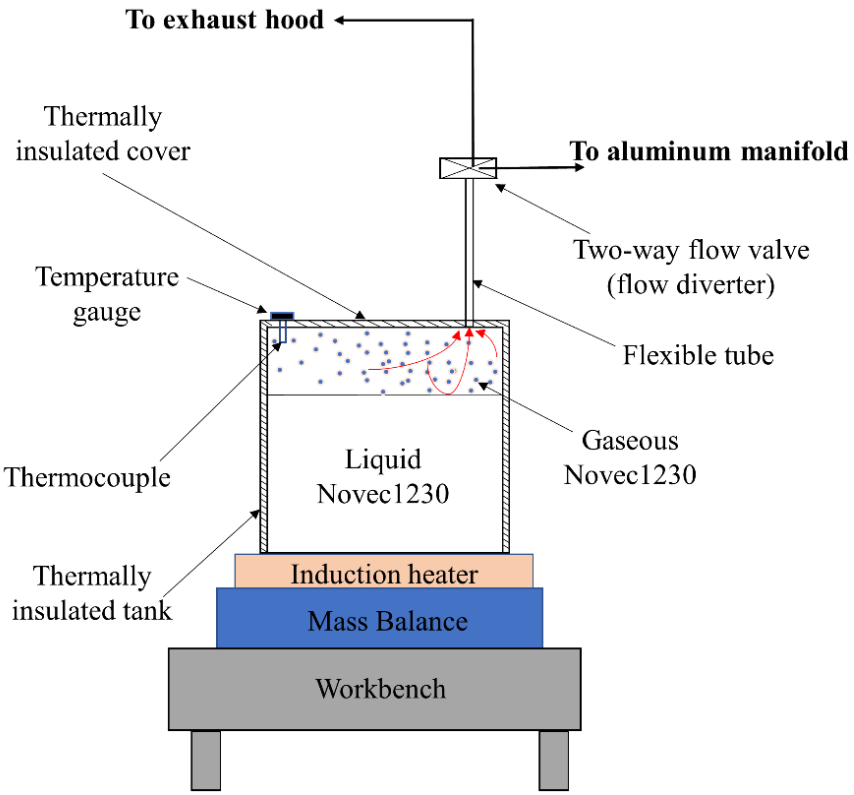

Figure 3. 14. Schematic of the Novec1230 handling system.

The evaporated Novec1230 agent flowed out of the container through a 9.5 mm diameter outlet machined into the top cover. A flexible tube was used to guide the evaporated agent towards a two way valve that directed the gaseous agent either to the exhaust hood (if not used) or to the aluminum manifold (where the gaseous agent was mixed with air and then introduced to the wind tunnel). The destination of the evaporated agent (hood or tunnel) depended on the experimental procedures followed in this study; detailed procedures are presented in section 3.5.4. The container and heater were both placed atop a Mettler Toledo mass balance to record the change in mass of liquid agent with time. This mass change was utilized to compute the volumetric flow rate of vaporized (gaseous) Novec1230 agent.

3.3.1.4 Characterization of the Novec1230 Handling System

Compared to any commercially available halons, the Novec1230 agent has the highest heat capacity, resulting in the lowest extinguishing concentrations for a given fuel. For extinguishing most of fires, the Novec1230 agent is applied at a typical concentration range of 4.5-6 vol.% of the space. No documented information is available about the recommended Novec1230 concentration to extinguish LIB fires. Battery safety experts from Kidde Fire Systems and United Technologies Co. recommended using Novec1230 at a concentration of 9-12 vol.% of the space to effectively suppress the LIB fires. In this study, two concentrations were investigated: ≈ 8.5 vol.% (representing a value that is lower than the maximum safe concentration for humans, 10 vol.%) and ≈ 15.0 vol.% (representing a value that is slightly greater than the maximum value utilized commercially for suppressing battery fires).

The container (shown in Figure 3. 14) was designed to be loaded with 6.1 kg of liquid Novec1230. Theoretical calculations showed that evaporating this amount of liquid Novec1230 over a time duration of 7.5 minutes (approximated cascading failure test duration) needs a heating rate of at least 1.19 kW, assuming adiabatic conditions. For steady state conditions, the rate of change in liquid Novec1230 mass (measured by the balance) is equal to the evaporation rate of Novec1230. The calculations also showed also that the Novec1230 evaporation is 0.0136 kg s^{-1}, which corresponds to 59.8 l min^{-1} of gaseous Novec1230.

Preliminary testing of the Novec1230 handling system indicated that heating the container at a rate of 1.19 kW achieved a slower evaporation rate than the theoretically calculated rate, which is attributed to the inevitable heat loss from the container to the surrounding even with thermally insulting the Novec1230 container.

Therefore, the output heating rate of the induction heater was increased to 1.65 kW to account for the heat loss and thus achieve the design evaporation rate.

In all Novec1230 experiments, the mass change in the liquid Novec1230 was recorded in time and converted to concentrations of the Novec1230 gas in the air/Novec1230 mixture. The Novec1230 handling system produced gaseous Novec1230 at a volume flow rate of 59.2 ± 1.1 l min^{-1}. Also, in these experiments, air was flowed through the tunnel at 640 or 320 l min^{-1}. Mixing this 59.2 l min^{-1} of Novec1230 with 640 or 320 l min^{-1} of air yielded an average Novec1230 concentration of 8.5 ± 0.03 or 15.2 ± 0.04 vol.%, respectively, in the resulting gas mixture.

3.3.2 Water Mist Suppression

3.3.2.1 Water Mist Suppression Mechanism

The water mist system was designed to provide carefully controlled quenching of the flames by introducing a fine water mist into the air stream flowing through the wind tunnel. Water mist is well-known for its efficient performance in suppressing flames primarily via thermal quenching, where evaporation of mist near the flame leads to a direct flame cooling because of the high vaporization enthalpy of water (2260 kJ/kg). Additionally, evaporation of mist upstream of the flame contributes to suppression by increasing the mole fraction of water vapor in the oxidizer (X_{Vapor}), thus diluting the oxidizer. Additional gaseous water vapor in the combustion zone enhances heat dissipation from the reaction zone and reduces the flame temperature. Previous studies [114, 115] have shown that water may exhibit a minimal chemical impact on the kinetics of the combustion reactions. These mechanisms indicate that the

flame is mainly extinguished when its temperature is reduced below the critical value needed to sustain combustion.

3.3.2.2 Water Mist Handling System

The cascading failure experimental setup, described in section 3.2, was equipped with a water mist handling system. The system consisted of a stainless-steel duct piece that was installed downstream of the hydrodynamic mixing chamber as shown in Figure 3. 15. Detailed dimensions of the duct piece are displayed in Figure 3. 16.

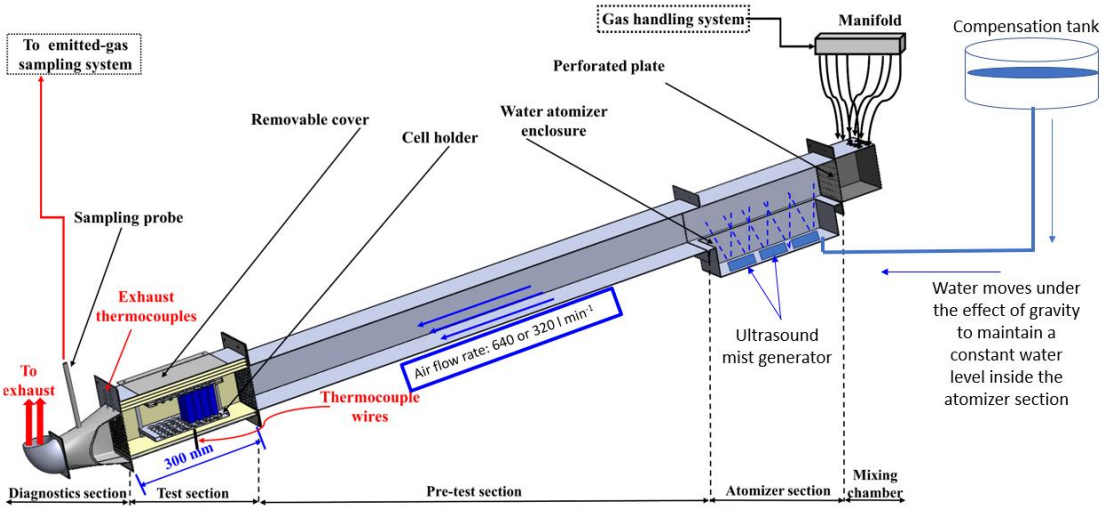

Figure 3. 15. Schematic of the experimental setup with the atomizer section installed.

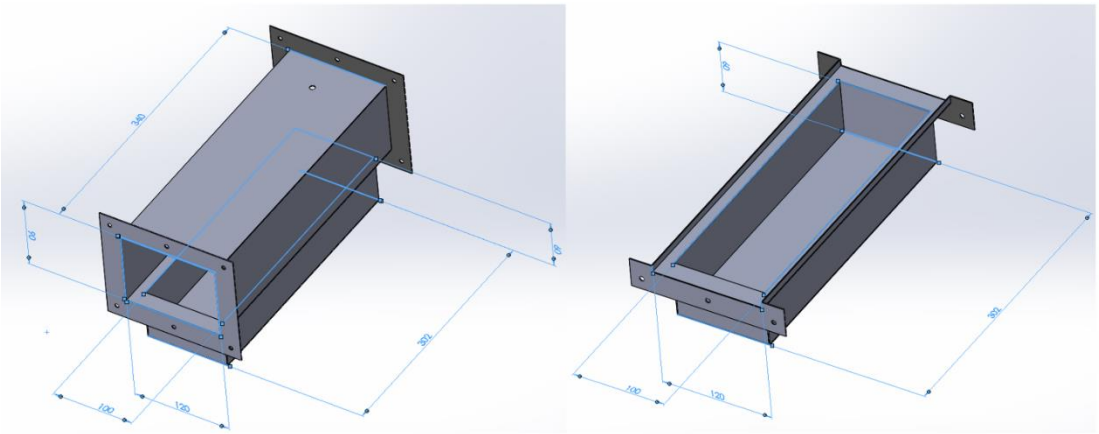

Figure 3. 16. Schematic of the atomizer section (all dimensions in mm).

Water mist was produced using a Vevor ultrasound mist generator submerged in a 60 mm deep layer of water within the base of the atomizer section. The mist generator, shown in Figure 3. 17, included 10 individual piezoelectric atomizers (each is 20 mm in diameter), which vibrate at ultrasonic frequency to produce a plume of fine mist droplets just above the water mist surface. The atomizer section is initially loaded with 1100 ml of liquid water before each experiment. An open top container is located 1.2 m above the base of the atomizer section was employed to compensate for the atomized water so that the water level inside the atomizer section is approximately maintained constant during tests. Water flowed from the compensation container to the atomizer section under the effect of gravity through a short 6.35 mm flexible tube attached to an opening machined into the bottom surface of the atomizer section. The mist produced inside the atomizer section was entrained by the air coming from the hydrodynamic mixing chamber and introduced to the pre-test section and then to the tests section, where the cell array was located.

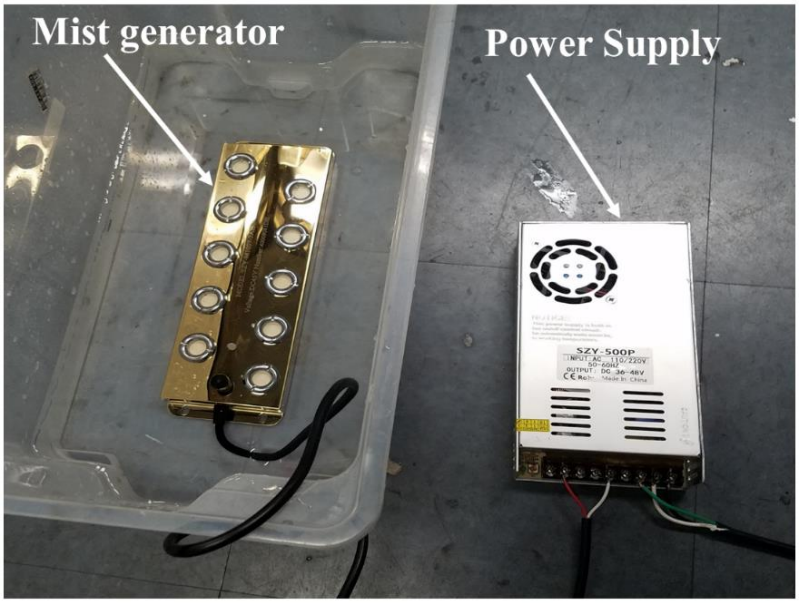

Figure 3. 17. A photograph of a Vevor ultrasound mist generator.

3.3.2.3 Characterization of Water Mist Handling System

Separate preliminary experiments were conducted to characterize the water mist handling system. In these experiments, the set up shown in Figure 3. 15 was utilized, but the test and diagnostics sections were dismantled to facilitate studying the characteristics of generated mist at the outlet of the pre-test section (which is the inlet of the test section). In these preliminary experiments, 640 or 320 l min^{-1} of air was flowed through the installed parts of the wind tunnel, and then the mist generator was operated. The generated mist was entrained by the air flow.

Under steady state conditions, the rate of water mist delivery ($\dot{m}_{WM}$) at the outlet of the pre-test section was calculated as the change in mass of water that was kept in the compensation container during a given time period. The mass fraction of water mist in the air/mist mixture (Y_{WM}) was calculated as follows:

$$Y_{WM} = \frac{\dot{m}_{WM}}{\dot{m}_{air} + \dot{m}_{WM}} \qquad 3.7$$

where $\dot{m}_{air}$ is the air mass flow rate corresponding to an air volume flow rate of 640 or 320 l min^{-1} at the standard atmospheric pressure, P_{std}=101325 Pa, and temperature, T_{std}=298 K. Previous studies [116-118] have estimated that a water mist mass faction (Y_{WM}) greater than 0.1 is sufficient for extinguishing a diffusion flame. In the current study, varying the input voltage to the power supply (which was utilized for powering the mist generator) from 30.8 to 50.7 V enabled controlling the value of Y_{WM} for different air flow rates (640 and 320 l min^{-1}) as shown in Figure 3. 18. In the current study, the generator was always operated at its maximum capacity (an input voltage of 50.7 V was used).

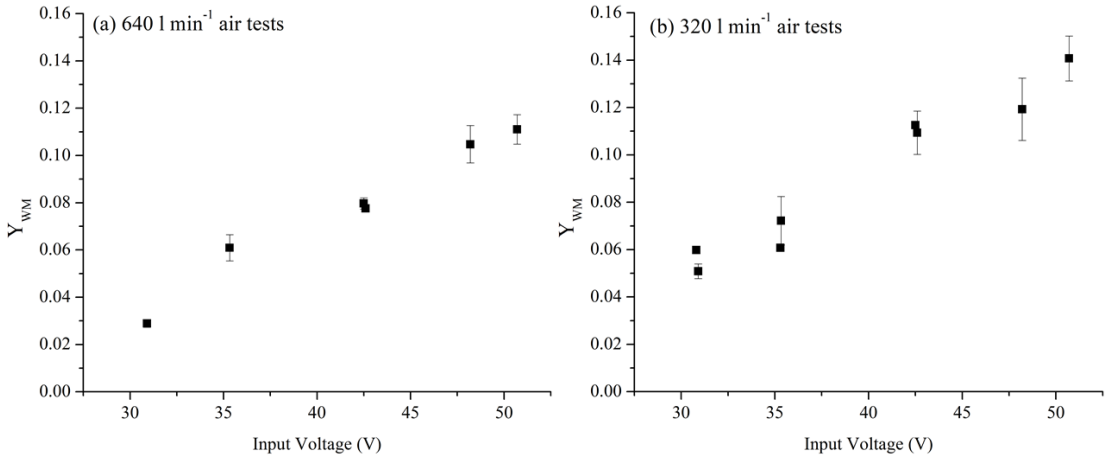

Figure 3. 18. Relation between the input voltage to the power supply operating the water mist atomizer and the mass fraction of mist in the air/mist mixture. All uncertainties were computed from the scatter of the data as two standard deviations of the mean.

The water mist produced by the generator is expected to include liquid water and water vapor. The mass flow rate of water vapor was computed using the saturation pressure (obtained at initial temeprature of the system, T_0) and relative humidity (measured during preliminary testing of the water mist handling system as 77.5 %) of water vapor at the outlet of the pre-test section (which is the inlet of the test section). The water vapor mass flow rate was then utilized to compute the water vapor mass fraction (Y_{WV}) in the air/mist mixture entering the test section. A summary of $\dot{m}_{WM}$, Y_{WM}, and Y_{WV} is reported in Table 3. 3. The table shows that the mass fraction of water vapor was found to be negligible compared to liquid water. Therefore, the mass percentage of water mist including liquid and vapor (11.1 wt.% or 14.1 wt.%) was used in this study to refer to the mist content.

Table 3. 3. A summary of $\dot{m}_{WM}$, Y_{WM}, and Y_{WV} measured during preliminary experiments. The uncertainties were computed from the scatter of data as two standard deviations of the mean.

Air volume flow rate ($l\ min^{-1}$)	$\dot{m}_{WM}$ ($kg\ s^{-1}$)	Y_{WM}	Y_{WV}
640	1.6 ± 0.1	0.111 ± 0.006 (11.1 ± 0.6 wt.%)	0.0094 ± 0.0009
320	1.0 ± 0.1	0.141 ± 0.009 (14.1 ± 0.9 wt.%)	0.0081 ± 0.0011

Figure 3. 19 displays images of the water mist delivery at the outlet of the pre-test section (inlet of the test section) for different mist loading conditions. The figure demonstrates that the mist behaves as a dense gas. The potential of the water mist suppression is primarily characterized by the quantity of Y_{WM}. Variation in this quantity can be obtained by changing the air flow rate (as followed in this study) or by varying the amount of mist loading capacity with a constant air flow rate (through changing the input voltage to the power supply). Another parameter that may affect the suppression potential is the water mist droplet size. The current ultrasonic mist generator did not allow for discernable variation in the droplet size distribution, thus limiting the variation of suppression potential when studying the effects of varied Y_{WM}.

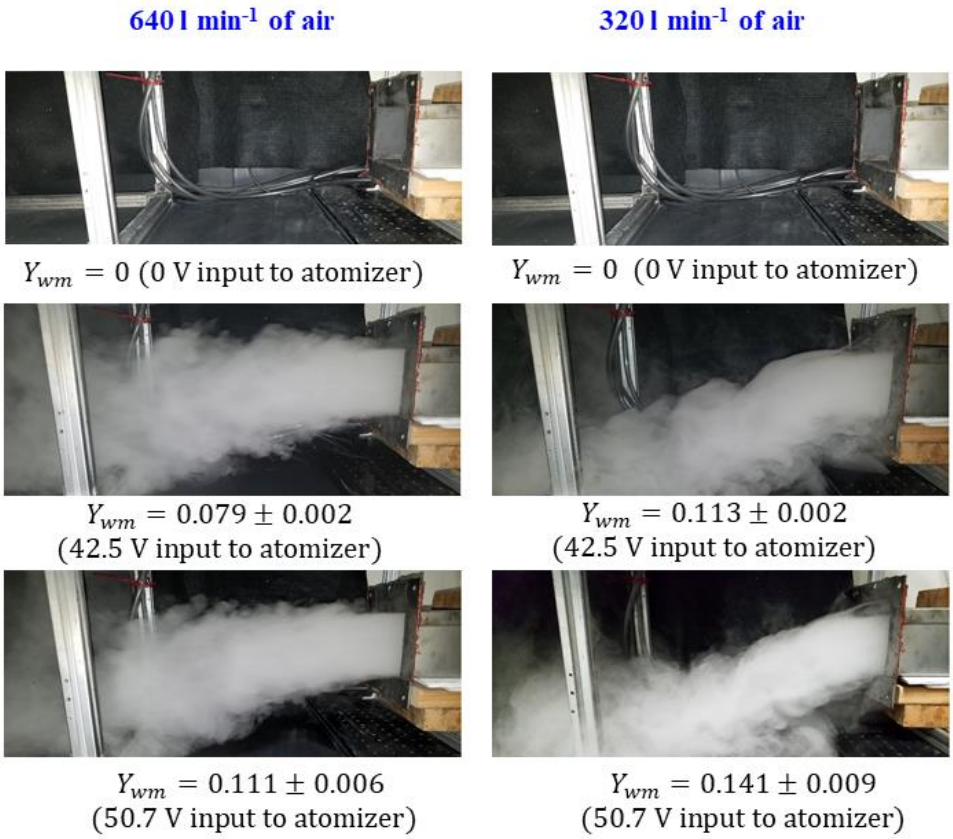

Figure 3. 19. Photographs of water mist delivery at the outlet of the pre-test section for varying Y_{WM}.

The mist droplet size distribution was measured using a Malvern Instruments Spraytec system, which utilizes a laser-diffraction technique [119]. In this technique, a collimated Hellium-Neon laser (632.8 mm) was passed through the mist generated at the outlet of the pre-test section. A multifaceted ring detector collected and analyzed the resulting light scattering patterns produced by the laser-mist interactions. The droplet size distribution was evaluated from the beam scattering patterns. The Spraytec equipment can resolve droplet diameters in a range between 0.1-2000 μm with a measurement accuracy of ± 1%. This accuracy is retained across a wide range of Y_{WM}, which enables up to 95% obscuration of the laser. For mist characterization measurements, the laser source and detector of the Spraytec system were positioned so

that they face each other. The equipment was also positioned in such a way that the laser beam passed horizontally at a distance of 20 mm in front of the outlet of the pre-test section. Based on the measurements obtained by the Spratec system, the characteristic droplet size dv(50) was found to be 8.0 ± 0.6 μm. Results from earlier studies suggested that the mist droplets at this size evaporate well outside the flame sheet and therefore sensible cooling effects are dominant [116].

3.4 Experimental Setup – Copper Slug Battery Calorimeter Experiments

In separate experiments, the original design of the CSBC apparatus [53, 54] was modified according to a study conducted by Said et al. [25], and combined with an oxygen-consumption cone calorimeter [58] to estimate the heat release rate associated with complete combustion of ejected materials from individual LIB cells. Figure 3. 20 depicts a schematic of the original CSBC apparatus. The apparatus consisted of a hollow pure copper cylinder (18 mm in inner diameter, 26 mm in outer diameter, and 65 mm in height) in which the LIB cell was inserted. A resistive heating wire (OMEGA NI80-010) was uniformly wrapped around the copper slug to induce the thermal failure into the LIB cells. The heating wire was supplied with a 40 W DC power via a BK precision power supply. The copper slug was insulated using a cylinder of Gemcolite FG23-112HD ceramic fiber insulation material (200 mm in diameter and 100 mm in height).

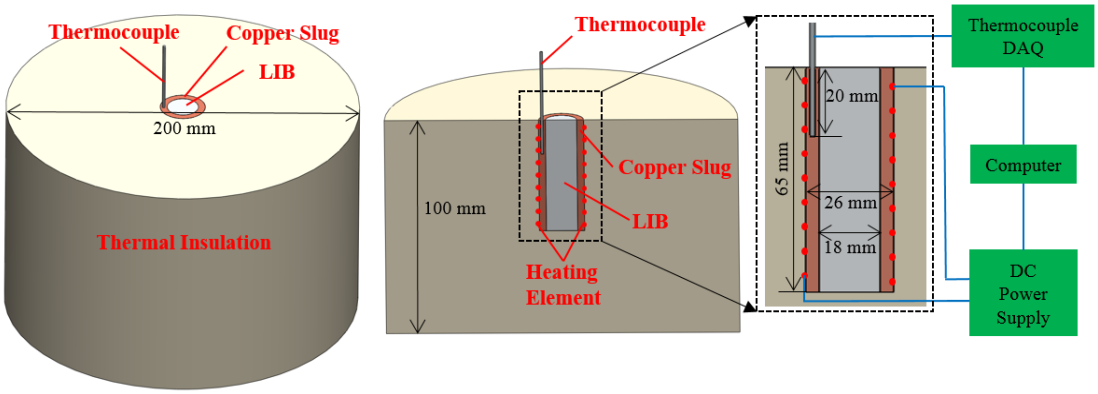

Figure 3. 20. Schematic of the CSBC apparatus [53, 54].

The key difference between previous work done by Liu et al. [53, 54] and the present work was the addition of an ejected battery material collector/burner, developed and outlined by Said et al. [25], as shown in Figure 3. 21. The ejected battery material collector/burner consisted of a 75 mm diameter and 150 mm length stainless steel tube appended with a perforated steel plate. The purpose of the burner/collector was to collect, homogenize, and slow down the flow of ejected battery materials before they were delivered to a hot-wire igniter, which resulted in a significantly enhanced combustion. Additionally, this attachment provided a sufficient separation distance between the coil igniter and the examined LIB cell, which minimized the heating influence from the igniter on the tested cells. The igniter was built using the same resistive heating wire (OMEGA NI80-010) that was wrapped around the copper slug. Two resistive wires were coiled together, arranged into a loop that was suspended 10 mm above the perforated plate, and supplied by 200 W AC power. The igniter was turned on at the beginning of the experiment and kept running up until the end of TR. The oxygen-consumption-calorimetry-equipped exhausted system was designed and operated in accordance with the ASTM E-1354 standard [58]. Sensor outputs from all components of the setup were recorded simultaneously at a frequency of 1 Hz.

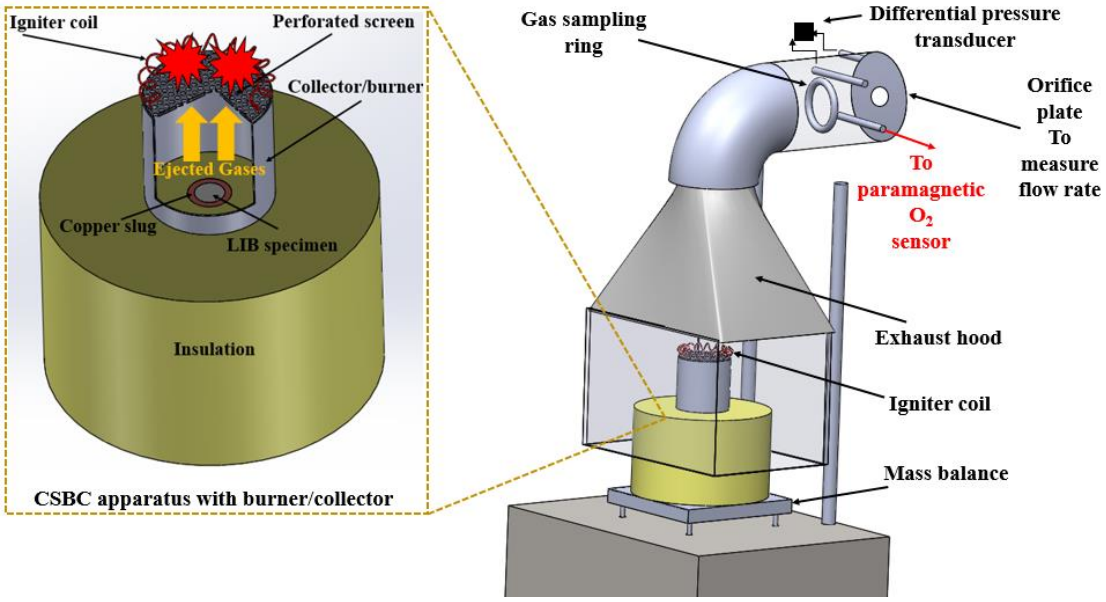

Figure 3. 21. Schematic of the modified CSBC apparatus under the hood of an oxygen consumption calorimeter.

3.5 Test Matrix and Experimental Procedures

3.5.1 Cell Array Size Investigation

Cell arrays of 18 and 12 LCO cells (shown in Figure 3. 22) were employed to investigate the effects of an anaerobic environment (N_2) and cell array size on the dynamics and hazards of cascading failure. If varying the size of an array shows no significant effect on the dynamics of cascading failure, then reducing the size is preferred to limit the setup/lab exposure to extreme heat and high concentrations of hazardous gases. In an N_2 environment, tests on arrays of 18 and 12 cells were repeated five and four times, respectively, to accumulate data statistics. All cells in these experiments were charged to 100% SOC.

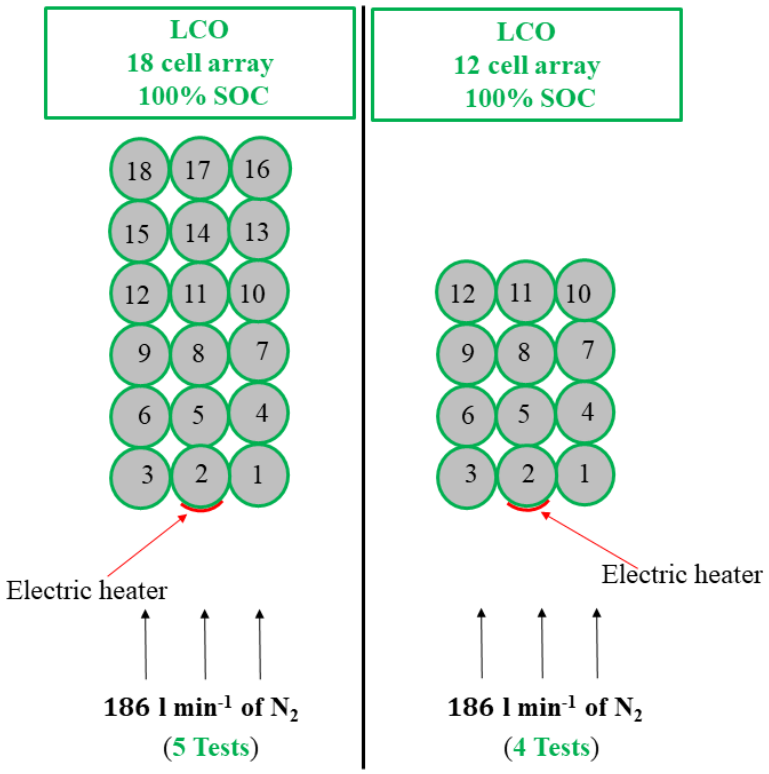

Figure 3. 22. Layout of the 18 and 12 LCO cell arrays tested in N_2. Cell 2 was the trigger cell.

The charged cells were stripped of plastic packaging and weighed individually before and after testing. The cell arrays were inserted into the cell holder and the test section was tightly closed. The wind tunnel was purged with 186 l min^{-1} of pure N_2 for seven minutes before the beginning of tests to ensure complete evacuation of O_2. The electric heater power and data acquisition software were turned on simultaneously.

The electric heater power was set at 115 W and continuously recorded throughout the test duration. This power was initially designed to be applied for the entire duration of the test. However, the heater was partially or completely disabled in early stages of the experiment (between the failure times of the first and third failed cells). Thereby, the integral value of the input power throughout the entire test time

varied between 16-52 kJ from test to test; this range was later found to be 1.5-7.6% of the total chemical energy produced by the cell arrays during cascading failure. Therefore, the variation in input failure power did not have a significant effect on the overall dynamics of failure or the total chemical energy produced from the cell array. Tests were stopped once the temperatures of the cells returned to their initial values.

3.5.2 Cathode Chemistry Investigation

As shown in Figure 3. 23, similarly sized arrays of 12 LCO, NMC, or LFP cells were tested in an N_2 environment to investigate the effect of the cathode chemistry on the dynamics and hazards of cascading failure. Additionally, the cell arrays were tested in an air environment to elucidate the impact of flaming combustion of ejected materials on cascading failure. In an N_2 flow rate of 186 l min^{-1}, tests on all cell arrays (LCO, NMC, and LFP) were repeated four times to accumulate statistics. In an air flow rate of 640 l min^{-1}, tests on LCO and NMC cell arrays were repeated six and four times, respectively. The LFP cell arrays were tested two times in 640 l min^{-1} of air, yet no cascading failure was achieved due to the difficulty of sustaining flaming combustion at such high air flow rate. Therefore, the LFP cell arrays were tested in a reduced air flow of 186 l min^{-1}; tests in the reduced air flow rate were repeated four times.

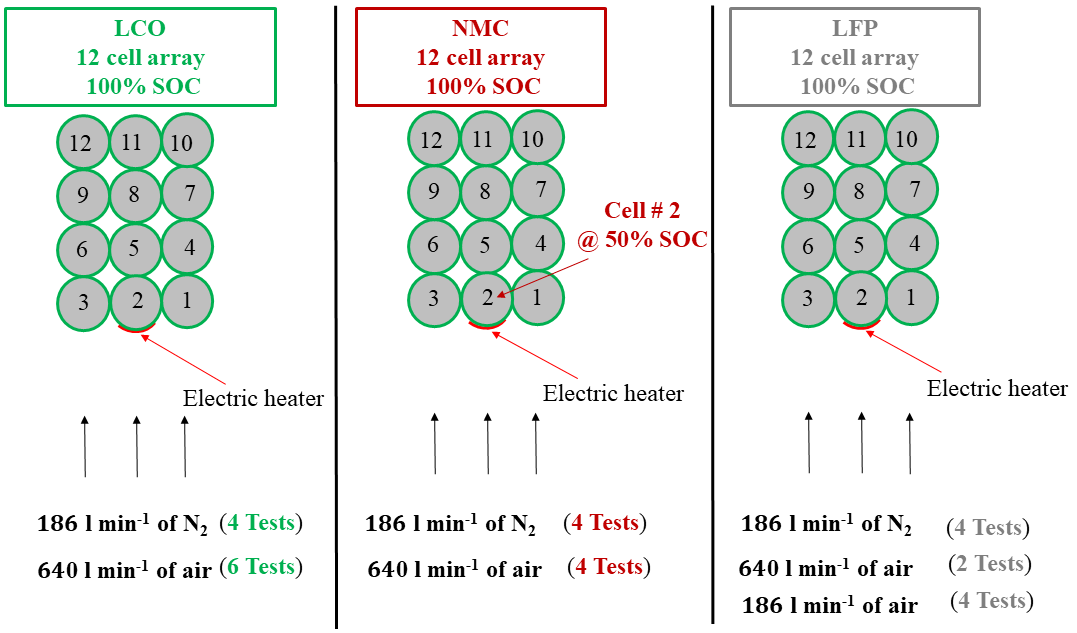

Figure 3. 23. Layout of the 12 LCO, NMC, and LFP cell arrays tested in N_2 and air environments. Cell 2 was the trigger cell.

All the cells in these experiments were charged at 100% SOC. In preliminary experiments on NMC arrays the thermal runaway of the trigger cell (cell 2) dismantled the stainless-steel heater support because of the high energy release rate and frequent rupture of the NMC cell casings. Therefore, it was decided to reduce the SOC of the trigger cell to 50% only for the NMC cell arrays. Tests were conducted in the same manner outlined in section 3.5.1.

The electric heater power was set at 115 W and was continuously recorded throughout the test duration. In the LCO and NMC tests, the heater was partially or completely disabled during early failure stages as was the case in section 3.5.1. The integral value of the input power throughout the entire test time was in a range of 16-52 kJ, and this range represented 1.5-7.6% of the total chemical energy produced by the entire cell arrays during cascading failure. Therefore, the variation in input failure power did not have a significant effect on the overall dynamics of failure or the total

chemical energy produced from the LCO or NMC cell arrays. In LFP tests, the heater stayed intact throughout the entire duration of tests and was manually turned off when the cells' bottom temperatures started to decrease. The significant variation in durations before turning off the heater power between different LFP tests caused the integral value of the input failure power to fluctuate in a wide range from 178-430 kJ. This range was significantly greater than energy produced from the cells that underwent TR, meaning that the heating power was the primary reason of failure advancement from the trigger (cell 2) to some of the cells in the array. The tests were ended once the temperatures of the cells returned to their initial values.

3.5.3 Passive Mitigation Investigation

In this investigation, six different test configurations were compared; each test configuration was repeated three to six times to accumulate statistics. Figure 3. 24 shows schematic diagrams for all analyzed configurations with a summary of the number of test repetitions. The first and second configurations were 12 (3×4) cell arrays with no inter-cell spacing tested in air and N_2 supplied at flow rates of 640 and 186 l min^{-1}, respectively. The first configuration represented the most energetic propagation scenario and included flaming combustion of ejected battery materials. In the second configuration, flaming combustion was suppressed, and thus more controlled experimental conditions were achieved. These two configurations were presented in section 3.5.2 but recalled herein to serve as baseline points to all other test configurations shown in Figure 3. 24.

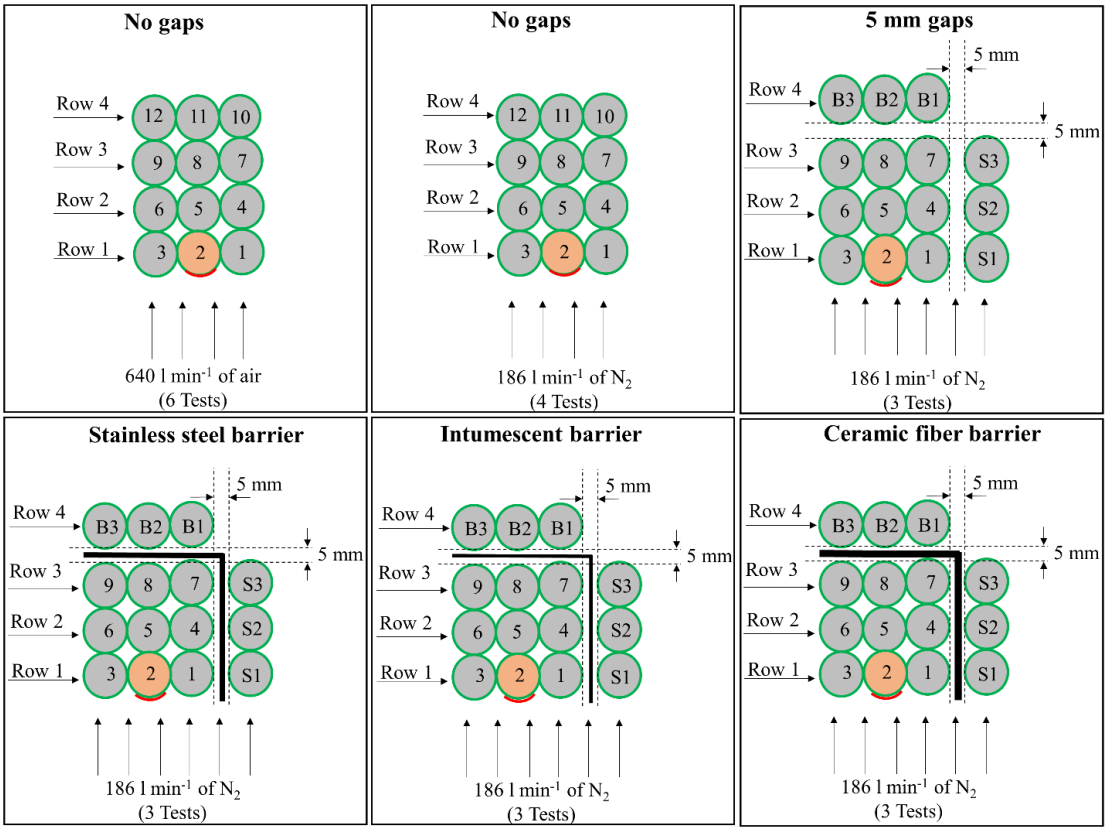

Figure 3. 24. Top view diagrams of cell arrays tested in passive mitigation experiments. Cell 2 was the trigger cell.

In the third configuration, a 3×3 block of cells with no inter-cell spacing was separated from the back row by a 5 mm gap. An additional side column of cells separated by a 5 mm gap was included as well, expanding the total number of cells in the array to 15. The locations of the gaps were selected to examine whether the bulk gas flow direction (parallel or perpendicular to the gap) had any impact on the effectiveness of the gap in slowing down or preventing failure propagation. In the rest of test configurations, various physical barriers were inserted into the 5 mm gaps. The barriers were carefully designed and fabricated from specific materials with the goal of mitigating the failure propagation from between row 3 and row 4; detailed specifications of the physical barriers are found in section 3.2.1.2. In all passive

mitigation experiments, all cells were charged to 100% SOC. Experimental procedures similar to those procedures described in section 3.5.1 were also followed here.

3.5.4 Novec1230 Suppression Experiments

Arrays constructed from 12 LCO cells arranged in rectangular configurations without inter-cell spacing were utilized to investigate the efficiency of Novec1230 agent to suppress the fires accompanying the failure propagation in these arrays and prevent failure propagation. Figure 3. 25 shows that five different tests conditions were compared. Each condition was tested four to six times. The 640 l min^{-1} air tests represent the most energetic scenario in which flaming combustion of ejected battery materials is significant. The 320 l min^{-1} air tests represent a less energetic scenario due to the less air available for burning the ejected battery materials. In the third test condition, the air was completely replaced with N_2 at 186 l min^{-1} to suppress flaming combustion. Note that the 640 l min^{-1} air and 186 l min^{-1} N_2 tests are the same tests reported in sections 3.5.1, 3.5.2, and 3.5.3 but mentioned here to serve as reference points. In the Novec1230 suppression experiments, the Novec1230 agent was utilized at two different concentrations 8.5 ± 0.03 and 15.1 ± 0.04 vol.%.

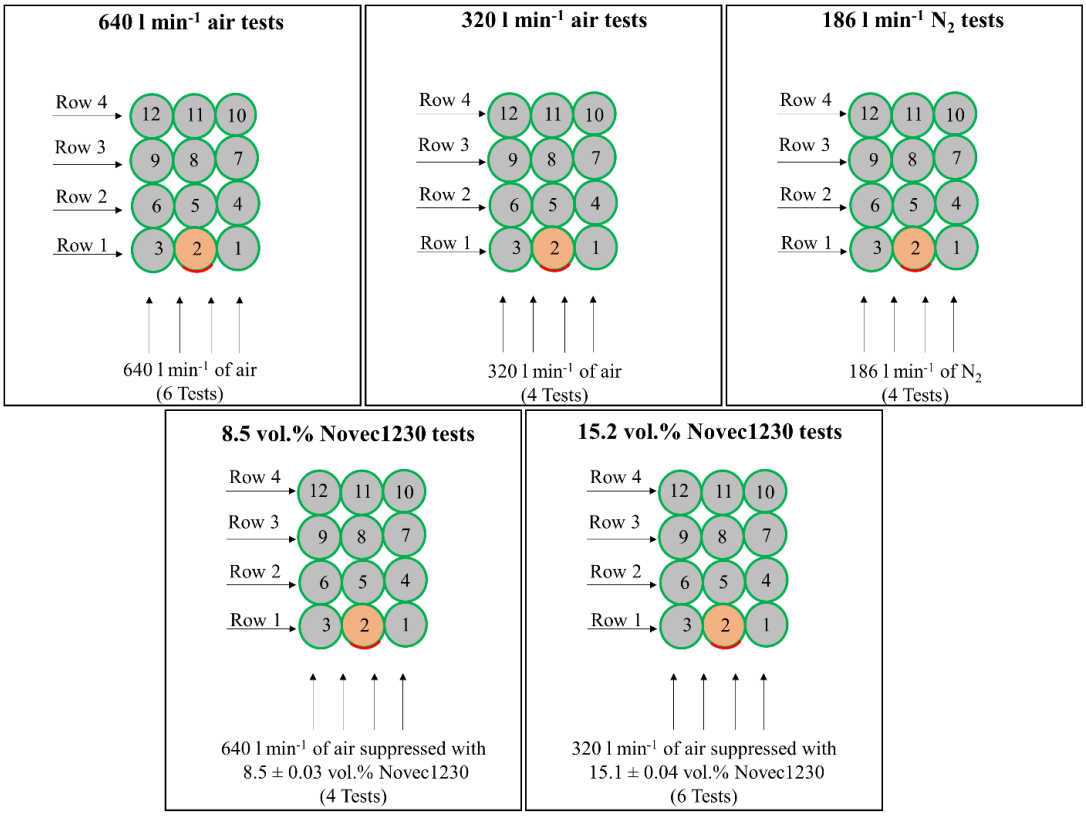

Figure 3. 25. Layout of the LCO cell arrays tested in baseline and Novec1230 suppression experiments. Cell 2 was the trigger cell.

All cells were fully charged (100% SOC), stripped off the plastic packing, and weighed before testing. In a typical air or N_2 experiment, the same experimental procedures presented in sections 3.5.1, 3.5.2, and 3.5.3 were followed. The technique of the Novec1230 suppression experiments, however, was slightly different. A typical Novec1230 test started by fixing the cell array into the cell holder and tightening the removable cover of the test section. Subsequently, 6.1 kg of liquid Novec1230 agent was placed into the container of the Novec1230 handling system. The container was tightly closed to avoid any leakage of Novec1230 agent during the experiment. The wind tunnel was then purged with 640 or 320 l min^{-1} of air for 7 minutes.

The stopwatch and the Novec1230 surface heater were turned on simultaneously. The surface heater power was set at 1.68 kW. The liquid Novec1230 started to evaporate at an unsteady rate. During this unsteady evaporation, the two way valve (installed downstream of the outlet of the Novec1230 container) directed the evaporated Novec1230 to the exhaust hood. After 3.5-4 minutes from starting the experiment, the evaporation rate of Novec1230 started to approach steady state, and the electrical heater adjacent to cell 2 (trigger cell) was enabled and set to a constant rate of 115 W. The two way valve was adjusted to direct all evaporated Novec1230 to the wind tunnel immediately after trigger cell underwent TR. It is important to mention that is not expected to condense inside the tunnel due to its low enthalpy of vaporization and high vapor pressure [113].

Time-resolved profiles of the Novec1230 concentration in an air/Novec1230 mixture obtained from representative Novec1230 tests are portrayed in Figure 3. 26. In these profiles, the gray solid lines represent the times when the vaporized Novec1230 was directed to the exhaust hood, while the black solid lines represent the times when the vaporized Novec1230 was directed to the wind tunnel. The concentration values corresponding to gray lines are theoretical; they were calculated assuming that the vaporized Novec1230 mixes with air. The concentrations corresponding to the black lines are the actual concentration of Novec1230 in the tunnel.

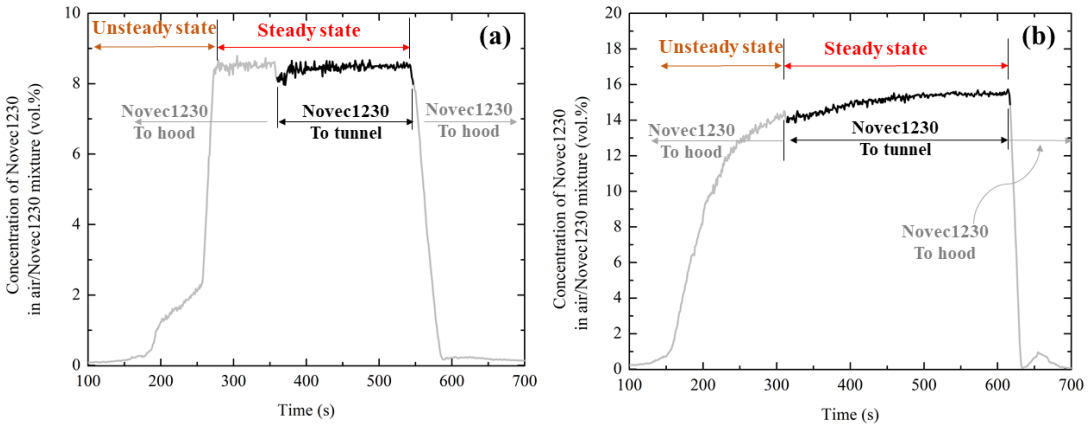

Figure 3. 26. Novec1230 volumetric concentration in an air/Novec1230 mixture obtained from representative (a) 8.5 vol.% and (b) 15.2 vol.% Novec1230 tests.

The Novec1230 flow to the tunnel was stopped shortly after all cell temperatures started to decrease. The test was concluded when all cell temperatures returned to their initial baseline values. Once tests were complete and the entire setup had sufficiently cooled, the cells were removed from the cell holder and weighed to determine the mass loss of each cell.

3.5.5 Water Mist Suppression Experiments

The efficiency of fine water mist to suppress the fires during failure propagation in LIB cell arrays and to prevent or mitigate the failure propagation was examined in this section. Similar LCO cell arrays described in section 3.5.4 are utilized for this investigation as well. Additionally, the baseline points described in section 3.5.4 were also used in this section to compare with the results of water mist suppression tests. All test conditions and repetitions are presented in Figure 3. 27.

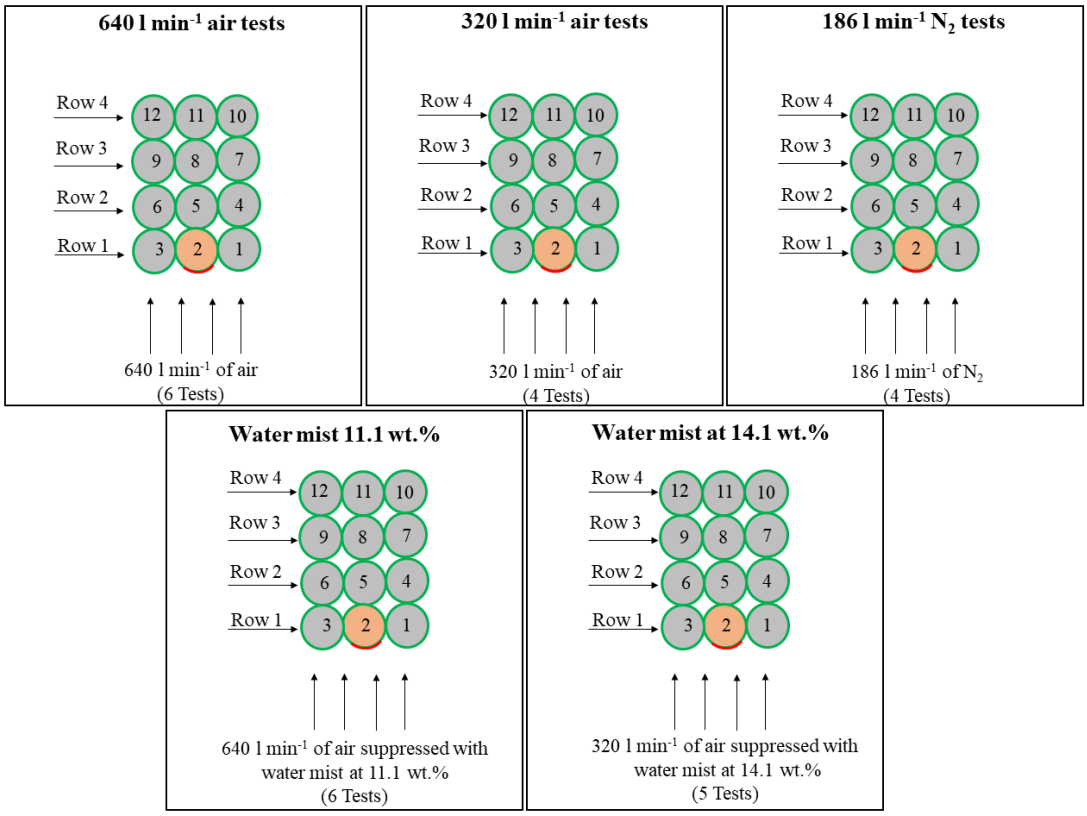

Figure 3. 27. Layout of the LCO cell arrays tested in baseline and water mist experiments. Cell 2 was the trigger cell.

In water mist suppression experiments, all cells were charged at 100% SOC. The cells were prepared and weighed according to the same procedures followed in previous sections. Tests were started by heating cell 2 up to TR, which was directly followed by turning on the water mist handling system to generate the mist at gravimetric concentrations of 11.1 and 14.1 wt.% in 640 and 320 l min^{-1} of air, respectively. The water mist generation was stopped when all temperatures of cells started to decrease continuously. The tests were ended when all cell temperatures returned to the initial values.

3.5.6 CSBC Tests

Single cells were investigated for the CSBC tests. The cells were charged to 100% SOC, weighed, and then placed into the copper slug such that the top surface of the cell was flush with the top surface of the slug and surrounding insulation. With the cell positioned, the collector/burner was attached and the CSBC apparatus was placed under the cone calorimeter with the electric igniter positioned directly above it. Tests were initiated by starting the cone calorimeter data acquisition, power supply, and igniter all at once. The power supply was set to 40 W for all tests. The input power was less in the CSBC tests than in the wind tunnel tests because only the combustion energetics were measured, and the slower heating promoted a more gradual ejection rate allowing for a more complete combustion. The cone calorimeter heater was not used for these tests (nor was the cone calorimeter mass balance). Rather, all heating was supplied by the heating wire wrapped around the copper slug. SV and TR onset times were manually recorded using a stopwatch. Tests were concluded after the cell had fully failed and the heat release rate trend had returned to its baseline value. After each test, the cell was weighed once again to determine its total mass loss.

4. Experimental Data Analysis and Methodologies

The purpose of this chapter is to describe the analysis procedures that were performed on the recorded measurements. The following points summarize the collected measurements and the quantities of interest derived from these measurements.

Measured data:

- Time-resolved temperatures of LIB cells' bottom surfaces (N_2 and air tests).
- Initial and final mass of each cell in a tested cell array (N_2 and air tests).
- Time-resolved concentration of each gas ejected from a tested cell array (N_2 tests).
- Time-resolved concentration of combustion products (air tests).
- Time-resolved temperature of the exhaust gas leaving the wind tunnel (N_2 and air tests).

Derived quantities:

- SV and TR onset temperatures.
- TR propagation speeds.
- Number of failed and ruptured cells in each examined LIB cell array.
- Total mass loss per examined LIB cell array (or per failed cell).
- Yields of gases ejected from the examined LIB cell array (or per failed cell).
- Lower flammability limit of flammable mixture ejected from a single LIB cell.
- Enclosure volume in which failure of an LIB cell array would create a flammable mixture.
- Chemical heat generation due to thermal failure of LIB cell arrays.

- ❖ Flaming combustion heat generation due to combustion of ejected materials in cascading failure experiments.
- ❖ Total flaming combustion heat generation due to combustion of ejected materials in the CSBC experiments.

Figure 4. 1 displays a flow chart that describes the analysis procedures for the data collected in N_2 or air experiments. Application of this analysis procedure to a representative test is presented in the following subsections.

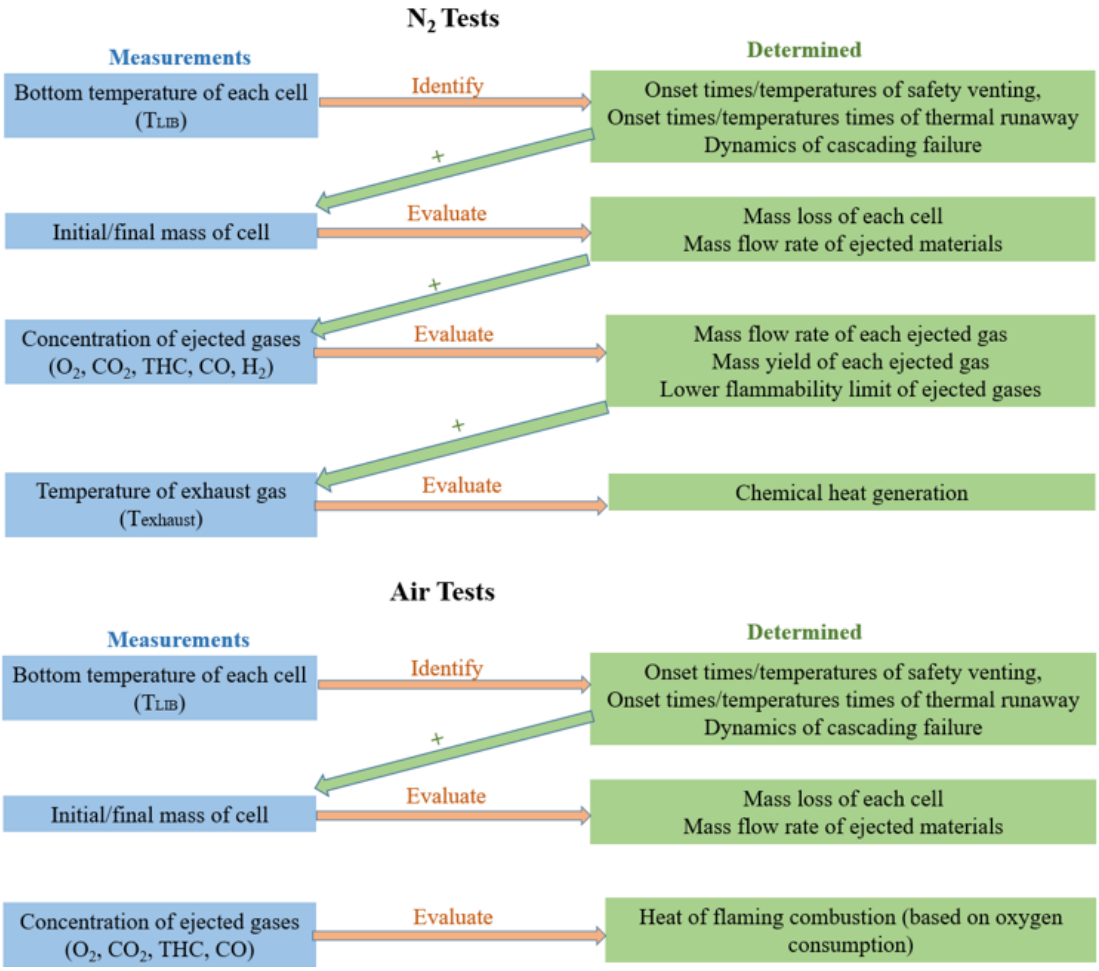

Figure 4. 1. Flow chart demonstrating the analysis procedure for data collected in N_2 and air tests. The same procedures were used to analyze the measured data of the barrier and suppression tests.

4.1 Identification of Safety Venting and Thermal Runaway Onset Times and Temperatures

Figure 4. 2 shows representative cells' bottom temperatures (T_{LIB}) for cells located in the first and last rows of an 18 (3 columns × 6 rows) cell array that was tested in an N_2 environment. Each temperature trend showed a gradual increase followed by a sudden sharp spike, indicative of TR. This behavior was reproducible for all examined cells no matter the array configuration or the test condition (N_2 or air). Measurements of T_{LIB} along with its time derivatives (dT_{LIB}/dt) were employed to provide mathematical criteria for the onset time of SV and the onset and end times of TR.

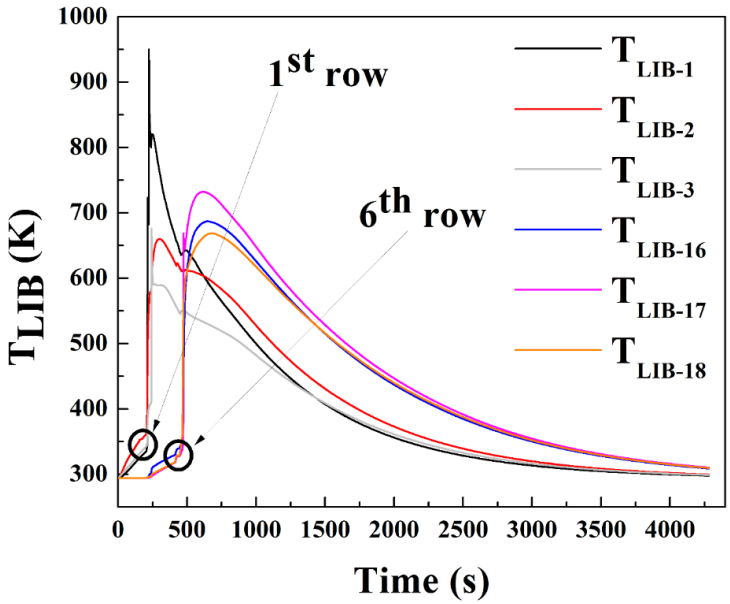

Figure 4. 2. An example of recorded bottom temperatures of cells located in rows 1 and 6 (row numbers are defined in Figure 3. 22) during testing of a fully charged 18 LCO cell array in an N_2 environment.

SV is an endothermic process [2] and therefore was identified by a negative dT_{LIB}/dt peak as shown in Figure 4. 3. The onset time of SV was defined as 0.5 s (which is the measurement's resolution) before dT_{LIB}/dt became negative; this criterion is

applicable for every tested cathode chemistry (LCO, NMC, or LFP). During experiments, the onset of SV was observed by an audible clicking sound accompanied by the appearance of gases at the wind tunnel outlet. The corresponding time was recorded to validate the temperature derivative based criterion ($dT_{LIB}/dt < 0\ K^{-1}$). Temperatures corresponding to the determined onset times were referred to as SV onset temperatures. It is also important to mention that SV was not captured for many cells. This was most likely due to an overlap with TR of neighboring cells.

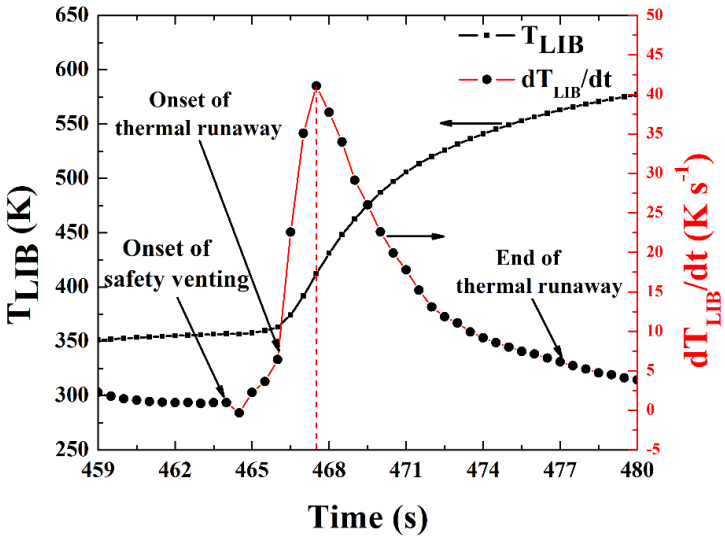

Figure 4. 3. Onset times of safety venting and thermal runaway and end time of thermal runaway for a single representative cell during a test of a fully charged 18 LCO cell array in an N_2 environment.

To identify the onset time of TR, the maximum dT_{LIB}/dt was first determined as shown in Figure 4. 3. The onset of TR was subsequently identified as the point in time preceding the maximum when the dT_{LIB}/dt became greater than 14 K s^{-1} for LCO and NMC cells and 2 K s^{-1} for LFP cells. These particular values for the derivative were selected because it produced TR onset times that closely corresponded to the times of audible explosions, which were also accompanied by a significant increase in the

exhaust flow rate, observed and recorded by the operator during the experiments. Additionally, these derivative values pinpointed the start of the sudden spike in the trend of each LIB's temperature. The TR onset times and corresponding temperatures were identified for every cell in all conducted experiments.

The TR end time was defined as the time that followed the maximum dT_{LIB}/dt when the derivative decreased below 6.5 K s^{-1} for LCO and NMC cells and 1.5 K s^{-1} for LFP cells, as illustrated in Figure 4. 3. These values of dT_{LIB}/dt were selected because the resulting times closely corresponded to the times of return of the gas concentration signals to their respective baselines for individual cells with failure durations that were clearly separated in time from the rest of the cells in the array.

4.2 Thermal Runaway Propagation Speed

In all experiments, advancement of TR appeared to occur sequentially from one row to the next. The cascading failure dynamics, therefore, were analyzed on a row-to-row basis. The TR onset time of each row ($t_{TR}|_{row}$) was computed by averaging the onset times of all cells in the row of interest. The row onset times were subsequently utilized to calculate a row-to-row propagation speed (S_P) in units of s^{-1}. For instance, TR speed of propagation from row 1 to row 2 ($S_{P_{(1\ to\ 2)}}$) is calculated as follows:

$$S_{P_{(1\ to\ 2)}} = \frac{1}{(t_{TR}|_{row\ 2} - t_{TR}|_{row\ 1})} \quad 4.1$$

To enhance clarity, the propagation speed and acceleration can also be introduced as S_P^* in the standard speed and acceleration units mm s^{-1}, respectively. S_P^* are obtained by multiplying S_P by the cells' original diameter (18 mm) for non-spaced rows. Graphical representation of speeds is illustrated in Figure 4. 4.

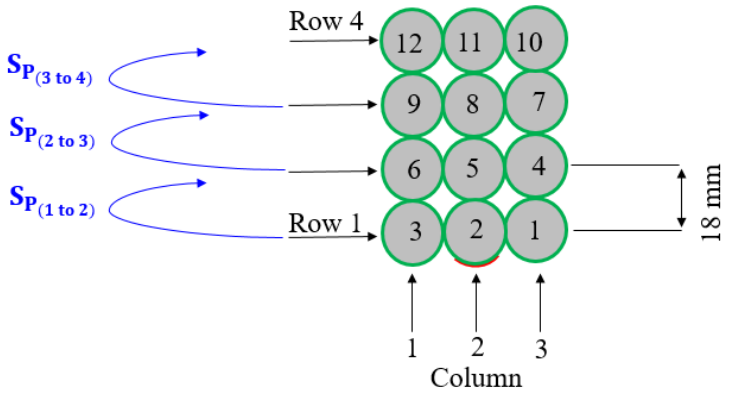

Figure 4. 4. Layout of the cell arrays with the highlighted propagation speeds and the acceleration in these speeds.

Additional analysis was conducted to determine whether the thermal runaway propagation rate had any notable dependence on the column where a cells was located; this dependence was found to be negligible. This analysis was performed by averaging TR onset times for the cells in each individual column (i.e. column 1 of a 12 cell array includes cells 1, 4, 7, and 10). The obtained average time of each column was then normalized by the average time of the middle column (column 2). Representative samples of the normalizations obtained from experiments conducted on 18 and 12 cell arrays in N_2 and air environments are plotted in Figure 4. 5. The normalized onset times approximately approached unity, meaning that the thermal runaway propagation rate had insignificant dependence on the column, but it did depend on the row.

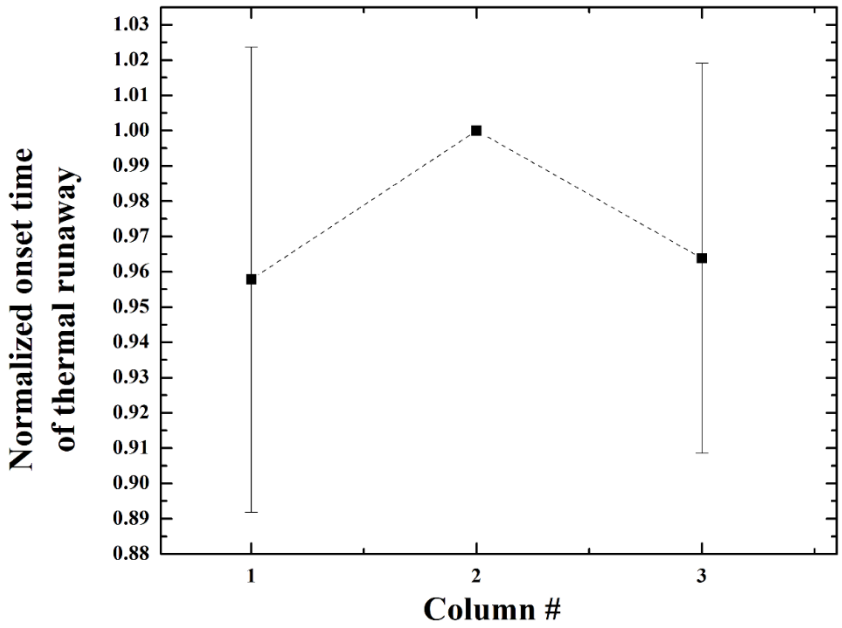

Figure 4. 5. Average thermal runaway onset time of columns normalized by the thermal runaway onset time of column 2. All uncertainties are computed from the scatter of the data as two standard deviations of the mean.

4.3 Ruptured Cells, Cells Mass Loss, and Cells Mass Loss Rate

During experiments, the casings of some LIB cells ruptured. These ruptures are attributed to the safety vent ports' failure to provide sufficiently rapid pressure relief during TR [23], which takes place when the LIB cells are exposed to high heating rates. After each test, the test section was checked, and the number of ruptured cells was counted.

For fully charged LCO and NMC cells, it was assumed that the change in cell mass occurred during TR and the contribution of SV was negligible as reported in earlier studies [25, 53, 54]. For fully charged LFP cells, the contribution of SV to the overall mass loss was more notable, 23% according to [25, 53, 54], and consequently was taken into account. Initial mass ($m_{initial}|_i$) and final mass ($m_{final}|_i$) of individual cells were measured and coupled with the previously determined onset and end times

of TR to approximate the time-resolved mass loss rate for each cell in the array. The total mass loss rate of an LCO or NMC cell array ($\dot{m}_{LIBs}$) was calculated as follows:

$$\dot{m}_{LIBs} = \sum_{i=1}^{N} \frac{m_{initial}|_i - m_{final}|_i}{(TR\ end\ time\ - TR\ onset\ time\ )_i} \quad 4.2$$

where N is the number of cells in the array. The total mass loss rate of LFP cell arrays ($\dot{m}_{LIBs}$) was calculated as:

$$\dot{m}_{LIBs} = \sum_{i=1}^{N} \left[\frac{0.77(m_{initial}|_i - m_{final}|_i)}{(TR\ onset\ time - SV\ onset\ time\ )_i} + \frac{0.23(m_{initial}|_i - m_{final}|_i)}{(TR\ end\ time\ - TR\ onset\ time)_i} \right] \quad 4.3$$

Representative trends of mass and mass loss of individual LIB cells are displayed in Figure 4. 6. The constructed mass loss rates are needed when performing energy analysis in section 4.5.1.

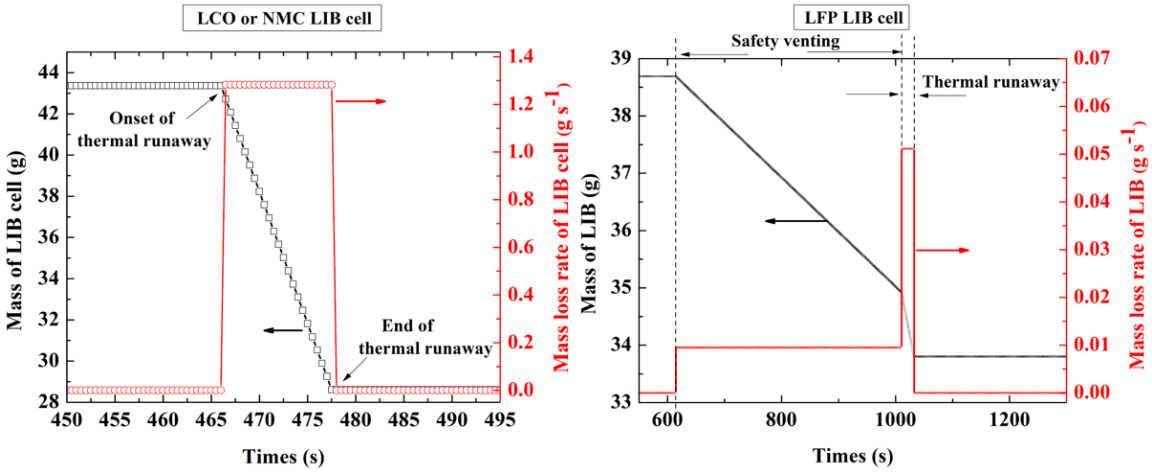

Figure 4. 6. Representative mass and mass loss rate trends of individual LIB cells.

4.4 Ejected Gas Yields and Lower Flammability Limit

The gas yields and lower flammability limit calculations were performed only for N_2 experiments to avoid any impact of combustion on the concentrations of the

gases ejected from the cells. The volume or mole fractions (X_j) of O_2, THC (assumed to be CH_4), CO, CO_2, and H_2 directly measured in the experiments were converted to the corresponding mass flow rates ($\dot{m}_j$) as shown in Equation 4. 4.

$$\dot{m}_j = \frac{X_j \mu w_j}{(1 - \sum_j X_j)\mu w_{N_2}} \dot{m}_{N_2} \qquad 4.\ 4$$

In this equation, μw_j is the molecular mass of species j and $\dot{m}_{N_2}$is the nitrogen flow rate set by the mass flow controller. The underlying assumption utilized in this equation is that the exhaust comprises measured gaseous products and N_2 (which does not participate in chemical reactions), and that the volumetric contribution of unmeasured species is negligible. The total mass of each gas (m_j) was computed by numerically integrating $\dot{m}_j$ over the duration of the whole cascading failure experiment (t_{exp}).

Lower flammability limit (LFL) is defined as the minimum volumetric (or molar) concentration of gases in air that may propagate a flame [120]. In the current study, the lower flammability limit of the gases ejected from an LIB cell ($LFL_{mixture}$) was computed using the Le Chatelier's mixing rule [120] as follows:

$$LFL_{mixture} = \frac{m_{THC}/\mu w_{THC} + m_{CO}/\mu w_{CO} + m_{H_2}/\mu w_{H_2}}{\frac{m_{THC}/\mu w_{THC}}{LFL_{THC}} + \frac{m_{CO}/\mu w_{CO}}{LFL_{CO}} + \frac{m_{H_2}/\mu w_{H_2}}{LFL_{H_2}}} \qquad 4.\ 5$$

Lower flammability limits of 5%, 12.5%, and 4% were used for THC (assumed to be CH_4), CO, and H_2, respectively [121]. The aforementioned limits were obtained at P_{std}=101325 Pa and T_{std}=298 K. Although CO_2 (nonflammable) was produced in large quantities in the ejected gas mixture, its suppressing effects were neglected in the flammability calculation in order to provide the most conservative (lowest) estimate of $LFL_{mixture}$.

To factor in the quantity of combustible gases ejected from the LIB cells into the hazard assessment, the maximum volume of the enclosure (V_{flam}) wherein the failure of a single LIB cell creates a flammable mixture was quantified as follows:

$$V_{flam} = \frac{\frac{(m_{THC}/\mu w_{THC} + m_{CO}/\mu w_{CO} + m_{H_2}/\mu w_{H_2}) \times \overline{R} \times T_{std}}{P_{std}}}{(LFL_{mixture}/100) \times N} \quad 4.6$$

where $\overline{R}$ is the universal gas constant (8.314 J mol^{-1} K^{-1}) and N is the number of cells failed in the cascading failure experiment. The quantity of V_{flam} can be interpreted as the minimum volume above which the ejected gases produced by a single cell must be diluted in order to prevent potential formation of a premixed flame, which may lead to deflagration or detonation. The larger V_{flam}, the higher the detonation hazard of a given cell.

4.5 Energetics of Cascading Failure

4.5.1 Chemical Heat Generation

Testing LIB cell arrays in an inert medium (N_2) allowed for determination of the rate of chemical heat generation (P_{CHG}). This heat generation was a consequence of exothermic chemical reactions occurring between different battery materials inside and outside the cell casings during cascading failure. P_{CHG} was computed from the changes in the enthalpy of the flow entering and leaving the test section. The total chemical heat generation (E_{CHG}) was obtained by numerically integrating P_{CHG} over the total time of the cascading failure experiment (t_{exp}) as follows:

$$E_{CHG} = \int_0^{t_{exp}} P_{CHG}\, dt \qquad 4.7$$

$$= \int_0^{t_{exp}} \left[\left[\dot{m}_{N_2} \bar{C}_{p_{N_2}} + \sum \left(\dot{m}_j \bar{C}_{p_j} \right) + \dot{m}_{sp} \bar{C}_{p_{sp}} \right] (T_{exhaust} - T_0) + P_{loss} - P_{heater} \right] dt$$

Equation 4. 7 comprises five terms: the heat carried by N_2, the heat carried by the gases (j) ejected from the cells, the heat carried by the solid particulates (sp) ejected from the cells, the heat lost through the sidewalls of the test section (P_{loss}) and the heat supplied by the electric heater (P_{heater}). $\dot{m}_{LIBs}$, $\dot{m}_{N_2}$, and $\dot{m}_j$ were discussed in sections 4.3 and 4.4. The mass flow of the solid particulates ($\dot{m}_{sp}$) was computed using Equation 4. 8.

$$\dot{m}_{sp} = \dot{m}_{LIBs} - \sum_j \dot{m}_j \qquad 4.8$$

$\bar{C}_{p_j}$ in Equation 4. 7 represents the mean constant pressure heat capacities of individual species computed from polynomial expressions of specific heat (C_{p_j}), found in the literature data [122, 123], using Equation 4. 9.

$$\bar{C}_{p_j} = \frac{\int_{T_0}^{T_{exhaust}} C_{p_j}\, dT}{T_{exhaust} - T_0} \qquad 4.9$$

In these calculations, THC were assumed to be CH_4 and ejected particulates were assumed to be graphite. The latter assumption was based on the observation that most of the particulates accumulated on the walls of the tunnel exhaust were of apparent graphitic nature. T_0 was the temperature of the system before the start of the experiment (which was also the temperature of the nitrogen continuously injected into the tunnel). As mentioned in section 3.2.3.4, the exhaust temperature ($T_{exhaust}$) was measured using three thermocouples located at the inlet of the diagnostics section. The three

thermocouples, located at different heights, showed comparable histories of exhaust temperature. Therefore, the histories of the three thermocouples were averaged at each time step (0.5 s) to construct a single exhaust temperature profile for every test.

The P_{loss} term in Equation 4. 7 represents the rate of heat loss from the test section through the walls of the tunnel to the surroundings. These losses, which were relatively small due to the presence of the thermal insulation, were estimated using the steady-state version of Fourier's law expression given by Equation 4. 10.

$$P_{loss} = \sum_{n} k_n A_n \frac{T_{exhaust}|_{smoothed} - T_0}{L_n} \qquad 4.\ 10$$

This equation was used to account for the conduction through the insulation and hexagonal stainless-steel struts of the cell holder. Using the thermal conductivity (k_n) of these materials [110, 112] and geometric parameters, including the cross sectional areas (A_n) and thicknesses (L_n), of the heat conducting elements, the total P_{loss} was computed. The internal test section temperature ($T_{exhaust}|_{smoothed}$) is a smoothed version of the $T_{exhaust}$ profile; an example of measured exhaust temperature and its smoothing trends is shown in Figure 4. 7. The Savitzky-Golay second order filter [124] was used to smooth the high rate gas temperature fluctuations and thus account for the thermal inertia of the conducting elements. The key filter constant was the diffusion time scale of the Kaowool PM insulation layer (computed from L_n^2/α, where α is the thermal diffusivity), which was estimated to be 227 s.

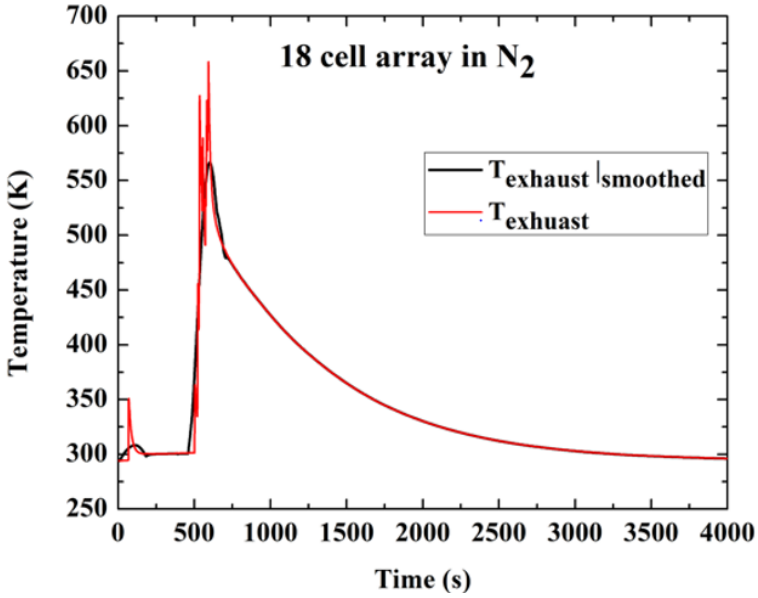

Figure 4. 7. Average exhaust and smoothed exhaust temperatures for an 18 LCO cell array tested in N_2.

Finally, the P_{heater} term in Equation 4. 7 represents the heat supplied by the electric heater, which was determined by recording the voltage and current supplied to the heater during the experiment.

4.5.2 Flaming Combustion Heat Release

As mentioned in 3.2.3.4, the exhaust thermocouples were selected to have a relatively large probe size (1 mm diameter) with the purpose of maintaining necessary mechanical integrity, but this size was too large to provide accurate temperature measurements of the strong intermittent flame jets during air tests. Therefore, the rate of heat release associated with the combustion of materials ejected from the cells ($P_{Flaming}$) was measured using oxygen consumption calorimetry rather than the enthalpy difference technique utilized to calculate P_{CHG}.

The oxygen consumption technique is based on the Huggett's empirical observation [120] that most combustibles release a nearly constant amount of heat per

unit mass of consumed oxygen. Based on this observation, $P_{Flaming}$ can be calculated as follows:

$$P_{Flaming} = E\left(\dot{m}_{O_2}\big|_{in} - \dot{m}_{O_2}\big|_{out}\right) \quad 4.\ 11$$

E is the heat release per unit mass of oxygen (13.1 kJ g^{-1} of O_2); this value of E is an empirically derived constant [120]. $\dot{m}_{O_2}\big|_{in}$ is the mass flow rate of oxygen at the inlet of the wind tunnel; this flow rate was assumed to be constant and calculated from the mass flow controller setting and the air composition (21 vol. % of O_2 and 79% vol. % of N_2). While $\dot{m}_{O_2}\big|_{out}$ is the mass flow rate of oxygen at the outlet of the wind tunnel and was computed using the same technique followed in Equation 4. 4.

Additionally, from the data obtained in the N_2 atmosphere tests, it was determined that the cells produced an amount of oxygen that was negligible with respect to that consumed by combustion in the air tests. Therefore, oxygen production by the cells was ignored in the $P_{Flaming}$ calculation. $P_{Flaming}$ was integrated over the duration of the experiment to yield the total heat produced in flaming combustion of ejected battery materials ($E_{Flaming}$).

An added advantage of this technique is that this measurement is completely isolated from the chemical heat generation by battery materials. If we were to use thermocouples, we would have to subtract heat generated by battery materials, which is a complicated process because it is not clear whether we can completely rely on the N_2 results to perform it.

4.5.3 Flaming Combustion Heat Release in Novec1230 Suppression Experiments

In the Novec1230 suppression experiments, the flaming combustion energy ($E_{Flaming}$) was calculated using the same technique described in section 4.5.2 with the

exception of the way $\dot{m}_{O_2}\big|_{out}$ at the outlet of the wind tunnel was computed. $\dot{m}_{O_2}\big|_{out}$ was calculated via Equation 4. 4, but here the exhaust gases comprised O_2, THC, CO, CO_2, N_2, and Novec1230 gas.

In the current experiments, the Novec1230 gas was initially introduced into the tunnel with a volumetric concentration of either 8.5 or 15.2 % (determined from the mass balance measurements as mentioned in section 3.3.1.4). For simplicity, it was assumed that the Novec1230 gas did not contribute to combustion reactions but only diluted the oxidizer and reduced the temperature of hot gases, meaning the Novec1230 amount was unchanged as it passed through the test section.

Separate preliminary experiments were conducted to study the impact of Novec1230 gas on the gas sensors. In these experiments, the Novec1230 gas was flowed through the tunnel without testing any batteries (no gas production or combustion), and the gases were sampled. The Novec1230 agent was found to cause a systematic reduction in the baseline of O_2, THC, and CO sensors.

Theoretically, introduction of Novec1230 gas into the tunnel should result in the dilution of O_2, reducing its measured concentration. However, the preliminary experiments showed that the measured reduction in O_2 concentration was significantly less than the theoretically calculated reduction. The difference between the measured and theoretically calculated reductions was attributed to the capture or absorption of Novec1230 gas by the filter or the Drierite utilized in the emitted-gas sampling system.

The experimentally measured reduction in O_2 was then utilized to compute the Novec1230 concentration at the location of the sensors (downstream of the filter and Drierite). For 8.5 and 15.2 vol.% Novec1230 tests, the Novec1230 gas concentrations

at the sensors were found to be 2.4 ± 0.004 and 14.9 ± 0.004 vol.%, respectively. These Novec1230 gas concentrations were used in Equation 4. 4 to correctly compute the oxygen mass flow at the outlet of the test section during the suppression experiments.

5. Results and Discussion: Cell Array Size Investigation

This chapter compares the experimental results associated with cascading failure in two different sizes of cell arrays (18 and 12 cell arrays). The arrays were constructed from LCO cells charged at 100% SOC. Both array sizes were tested in an anaerobic environment (N_2). The results presented in this chapter include the impact of array size on the dynamics, failure temperatures, mass loss of cells, mass yields and flammability of ejected gas mixtures, and chemical heat generation of cascading failure.

5.1 Dynamics of Cascading Failure

All LIB cells underwent TR in all cascading failure experiments conducted on 18 and 12 LCO cell arrays in an N_2 environment. Figure 5. 1 shows how TR propagated in time through 18 and 12 cell arrays in representative N_2 experiments. The TR propagation charts for the other test repetitions can be found in Appendix C (Figure C. 1 to Figure C. 3). The dark and light circles represent non-failed and failed cells, respectively. The spacing (which is not drawn to scale) between the cell arrays in the timeline presents a qualitative understanding of the timespan between successive cell failures. The TR onset times of individual cells were not reproducible despite carefully controlled boundary conditions and cell array geometry. The lack of reproducibility was attributed to the physics of the cascading failure, which had a tendency to amplify any minute differences in the geometry of the array (in particular, the physical contact surface area between adjacent cells) or any minor spatial or temporal fluctuations in the boundary conditions.

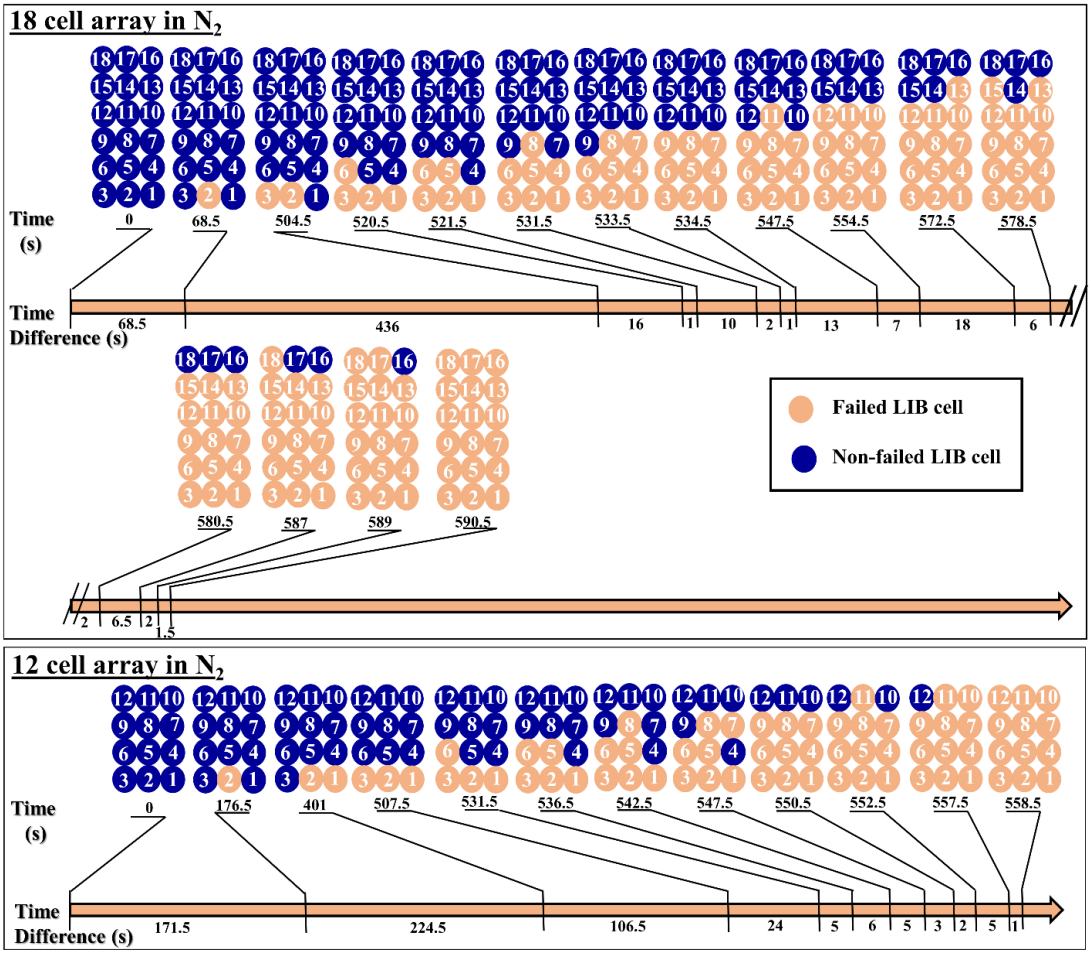

Figure 5. 1. Thermal runaway propagation charts for 18 and 12 cell arrays in N_2 obtained for representative experiments. Cell 2 was the trigger cell.

Unlike individual cell TR onset times, the advancement of TR from one row to the next showed a reasonable degree of reproducibility. The failure dynamics, therefore, were analyzed on a row-to-row basis. The TR onset time of each row was calculated by averaging the onset times of all cells in the row. Figure 5. 2 shows the average TR onset time for each row in all tested 18 and 12 cell arrays. All uncertainties and error bars in this chapter were computed from the scatter of data as two standard deviations of the mean. On average, the TR onset times for similar rows in both array sizes were comparable.

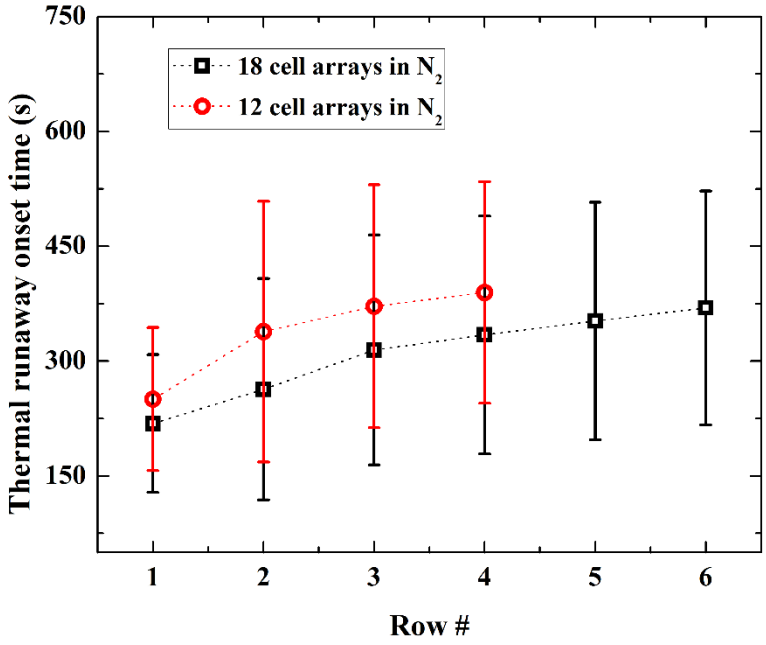

Figure 5. 2. Thermal runaway onset time of each row in 18 and 12 LCO cell arrays tested in an N_2 environment. The error bars were computed from the scatter of the data as two standard deviations of the mean.

Subsequently, the onset times were converted to row-to-row propagation speeds (S_P). An additional analysis was conducted to determine whether the TR propagation rate had any notable dependence on the column where the cells were located; this dependence was found to be negligible as discussed in section 4.2. Figure 5. 3 summarizes the obtained S_P data in units of s^{-1}. To enhance clarity, the row-to-row propagation speed is also presented as S_P^*, in standard units of mm s^{-1}. S_P^* was calculated by multiplying S_P by the diameter of the cells (18 mm). The S_P data plotted in Figure 5. 3 show a relatively steady propagation through the array. 18 and 12 cell arrays yielded essentially the same results. The 18 cell test data suggest that the S_P trend may be sinusoidal (an acceleration followed by deceleration), but it is difficult to establish the presence of this trend with certainty given the significant uncertainties in

the individual data points. The average rate of propagation for all rows and array sizes in N_2 was found to be 0.080 ± 0.025 s^{-1} (or 1.44 ± 0.45 mm s^{-1}).

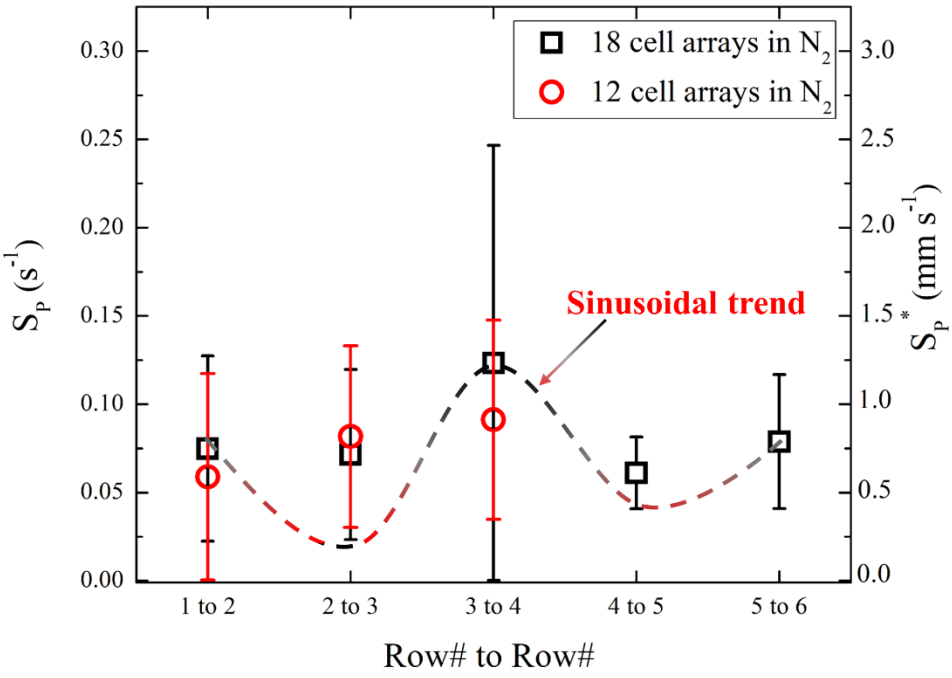

Figure 5. 3. A comparison between row-to-row propagation speeds for 18 and 12 cell arrays tested in an N_2 environment. The error bars were computed from the scatter of the data as two standard deviations of the mean.

5.2 Temperatures of Cascading Failure

Table 5. 1 summarizes the measured onset temperatures of SV and TR as well as the maximum temperatures achieved during cascading failure of 18 and 12 LCO cell arrays in an N_2 environment. These temperatures showed no significant dependence on the cell's position in an array or the size of the array, and therefore the temperatures were averaged over all cells. For 18 and 12 cell arrays together, average values of 354 ± 12 and 370 ± 5 K were obtained for the SV and TR onsets, respectively. The maximum temperatures did show slight dependence on the size of the array. The 18

cell arrays produced somewhat higher maximum temperature values, perhaps due to the higher maximum overall heat generation rates achieved in these experiments.

Table 5. 1. Summary of the cell temperature data. All temperatures were measured at the cell's bottom surface. The uncertainties were computed from the scatter of data as two standard deviations of the mean.

Array size	Atmosphere	SV onset temperature [K]	TR onset temperature [K]	Maximum temperature of cell bottom surface [K]
18 cells	N_2	353 ± 18	364 ± 7	740 ± 19
12 cells	N_2	359 ± 17	381 ± 12	686 ± 23

The SV and TR onset temperatures measured in the current study varied markedly when compared to those reported in a previous work by Liu et al. [54] for the same LIB cells. For fully charged cells, Liu obtained SV and TR onset temperatures of 451 ± 5 and 470 ± 4, respectively. These discrepancies can be attributed to differences in the experimental setups and heating conditions. In Liu's work, the cells were heated slowly (≈ 0.1 K s^{-1}) and uniformly inside of a copper slug by a resistive heating wire wrapped around the slug. While in the current study, each cell in the array was heated rapidly (7 K s^{-1}) and non-uniformly by the neighboring cells. The non-uniform heating resulted in uneven temperature distribution across the body of each cell, meaning that the measured temperature of a cell (measured at its bottom surface) would be less than the temperature corresponding to the failure initiation locations (at side walls of the cell where most of the heat transfer occurred). This observation strongly suggests that temperature-based failure detection thresholds for commercial battery packs must not be determined based on experiments with slow, uniform heating because such

thresholds may fail to provide sufficiently early detection in real failure scenarios (fast, non-uniform heating scenarios).

5.3 Ruptured Cells and Mass Loss

Although 100% of cells underwent TR in the current experiments, only a small fraction of these cells ruptured. Figure 5. 4 (a) shows representative examples of the LCO cells that stayed intact post TR. Some of these cells maintained their original cylindrical geometry, while others were deformed. Figure 5. 4 (b) depicts examples of ruptured cells. Propagation of TR in the 18 and 12 cell arrays resulted in 15.6% and 14.6% of cells rupturing, respectively.

Figure 5. 4. Photograph of LCO cells after testing: (a) non-ruptured (b) ruptured.

The masses of individual cells were recorded pre and post testing to determine the total mass loss. Table 5. 2 provides a data summary for each set of cell array sizes. As the data indicate, the size of the examined array had no impact on the cell mass loss. The obtained mass loss data compare favorably with the mass loss data reported in earlier publications by Liu et al. [54] and Quintiere et al. [11] for the same cells.

Table 5. 2. Initial mass and total mass loss of LCO cells. The uncertainties were computed from the scatter of data as two standard deviations of the mean.

Array size	Atmosphere	Initial mass of a single cell [g]	Mass loss from a single cell [g]
18 cells	N_2	43.40 ± 0.03	16.7 ± 0.9 (≈ 38%)
12 cells	N_2	43.50 ± 0.06	16.7 ± 1.0 (≈ 38%)

5.4 Ejected Gas Yields and Lower Flammability Limit

Figure 5. 5 displays the concentrations of gases ejected from the 18 and 12 cell arrays in representative cascading failure experiments conducted in N_2. The time-resolved gas trends of all other test repetitions conducted on 18 and 12 cell arrays in an N_2 environment are provided in Appendix C (Figure C. 18 and Figure C. 19). The early peaks in the gas signal shown in Figure 5. 5 are associated with TR of the trigger cell (cell 2). The consecutive peaks in gas signals, however, were caused by propagation of TR in the cells of the array. The 18 cell arrays yielded a greater number of peaks in concentration due to the greater number of cells. Figure 5. 5 shows that the most dominant ejected gas in terms of concentration was THC, which reached a maximum concentration of 40 vol.%. Additionally, Figure 5. 5 indicates that the LCO cells produced a small amount of oxygen, with a maximum concentration of 0.40 vol.%.

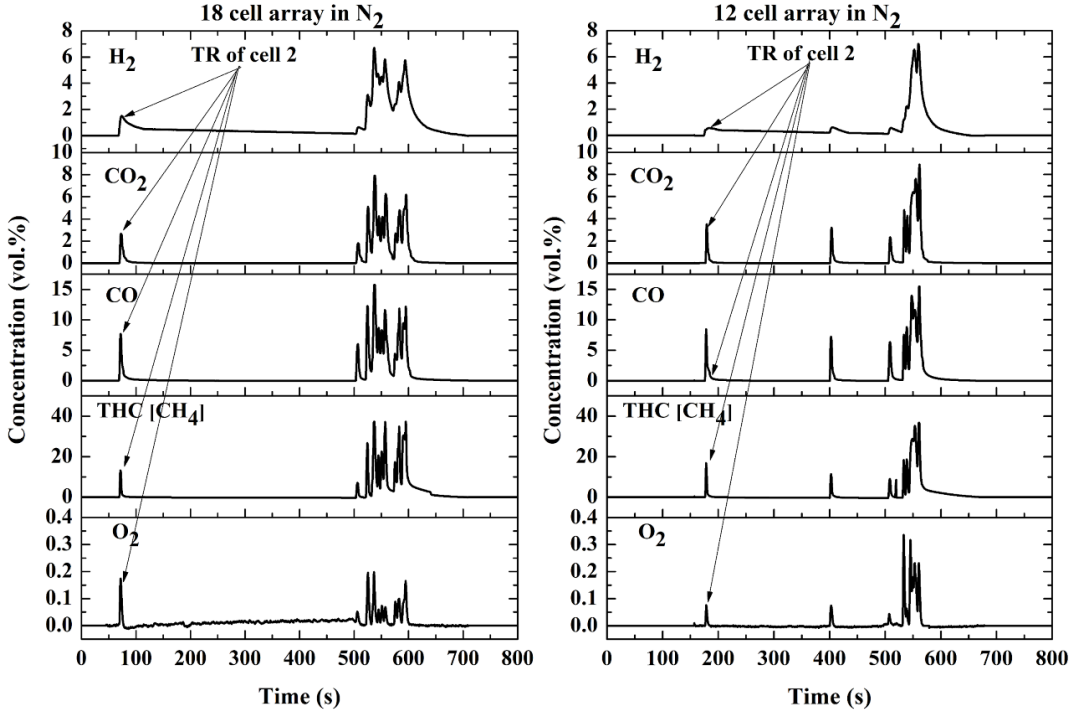

Figure 5. 5. Measured concentrations of gases ejected from 18 and 12 cell arrays during cascading failure in an N_2 environment. Cell 2 was the trigger cell.

The yields of gases calculated from the concentration profiles are reported in Table 5. 3. The obtained yields are normalized either by the total initial mass of all cells or by the number of cells in the array. Within the computed uncertainties, 12 and 18 cell arrays produced the same yields of gases. When averaged over both array sizes, the O_2, THC, CO, CO_2 and H_2 yields per initial cell mass become 0.00059 ± 0.00023, 0.0362 ± 0.0107, 0.0407 ± 0.0049, 0.0324 ± 0.0038 and 0.00201 ± 0.00039, respectively. To better visualize the data listed in Table 5. 3, Figure 5. 6 presents the information on the gas yields in terms of mass and volumetric (or molar) percentages. On volumetric basis, the contribution of H_2 to the overall mixture becomes significant for both array sizes.

Table 5. 3. Summary of computed gas yields for LCO cells. The uncertainties were computed from the scatter of data as two standard deviations of the mean.

Gas	Gas production in 18 cell arrays		Gas production in 12 cell arrays	
	Normalized per initial cell mass [-]	Normalized per failed cell number [g]	Normalized per initial cell mass [-]	Normalized per failed cell number [g]
O_2	0.00064 ± 0.00041	0.028 ± 0.018	0.00052 ± 0.00015	0.023 ± 0.007
THC	0.0368 ± 0.0129	1.60 ± 0.56	0.0355 ± 0.0203	1.55 ± 0.89
CO	0.0431 ± 0.0038	1.87 ± 0.16	0.0377 ± 0.0098	1.64 ± 0.43
CO_2	0.0348 ± 0.0028	1.51 ± 0.12	0.0293 ± 0.0071	1.27 ± 0.31
H_2	0.00207 ± 0.00067	0.090 ± 0.029	0.00193 ± 0.00041	0.084 ± 0.018

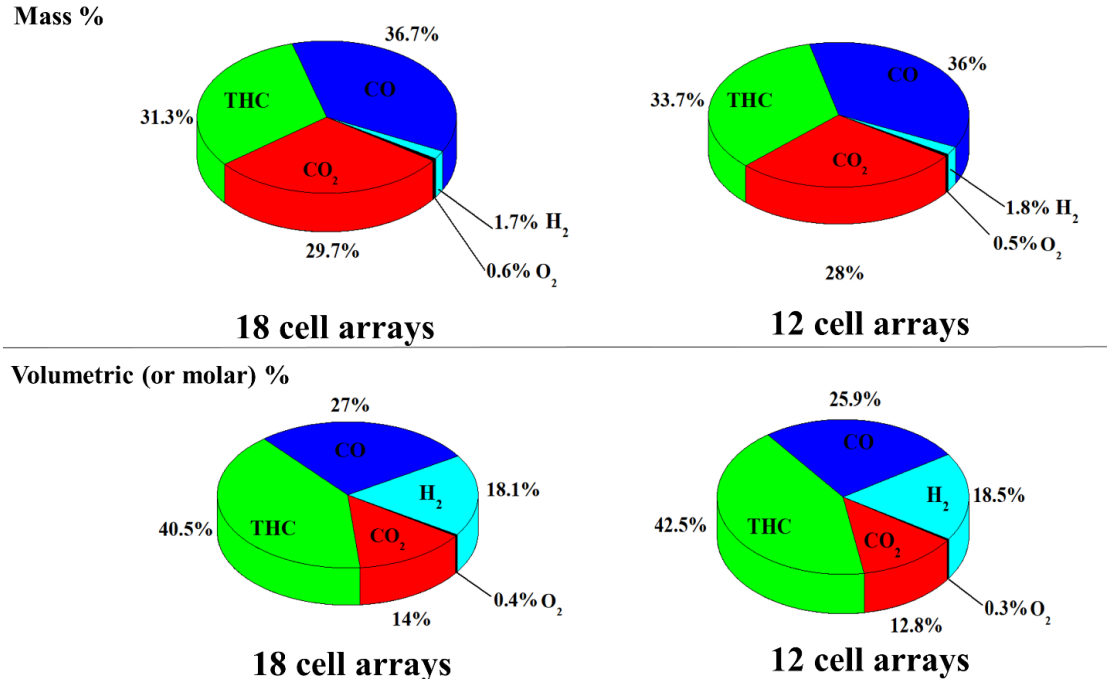

Figure 5. 6. Mass and volumetric percentages of each gas in the ejected gas mixture.

The total masses of ejected gases per cell number from the 18 and 12 cell arrays were calculated as 5.09 ± 0.68 and 4.6 ± 1.6 g, respectively, or a single average value of 4.85 ± 0.76 g. This average value is comparable with the total mass of organic materials in the cell, 6.15 g, which was calculated from the material safety data sheets

[98, 99]. This result is also close to the total gas yield reported by Lyon and Walters [52], 4.46 g, for the same type of LCO cells.

Mass yields of THC [CH_4], CO, and H_2 (shown in Table 5. 3) were utilized to compute the $LFL_{mixture}$ of the flammable mixture. On average, arrays of 18 and 12 cells produced a flammable mixture with $LFL_{mixture}$ of 5.79 ± 0.12 vol.% in air. The maximum volume of an enclosure (V_{flam}) where a failure of a single cell creates a flammable mixture (provided that the enclosure contains air at P_{std} and T_{std}) was calculated to be 0.087 ± 0.017 m^3.

5.5 Chemical Heat Generation

The heat generated due to chemical reactions between cell components was determined from the 18 and 12 cell experiments in N_2. A representative P_{CHG} profile for each array size is plotted as a function of time in Figure 5. 7. The P_{CHG} trends for all other test repetitions are provided in Appendix C (Figure C. 35 and Figure C. 36). In all profiles, the early P_{CHG} peak corresponds to the TR of cell 2 (the trigger cell), while the following significantly larger peaks are associated with the TR propagation through the arrays. Shortly after the end of failure propagation, the rate of energy generation starts to slowly decay until no energy is produced. The positive P_{CHG} observed during the slow decay is associated with the transfer of stored energy (absorbed during cascading failure) from the cells and other test section elements to the nitrogen flowing through the duct.

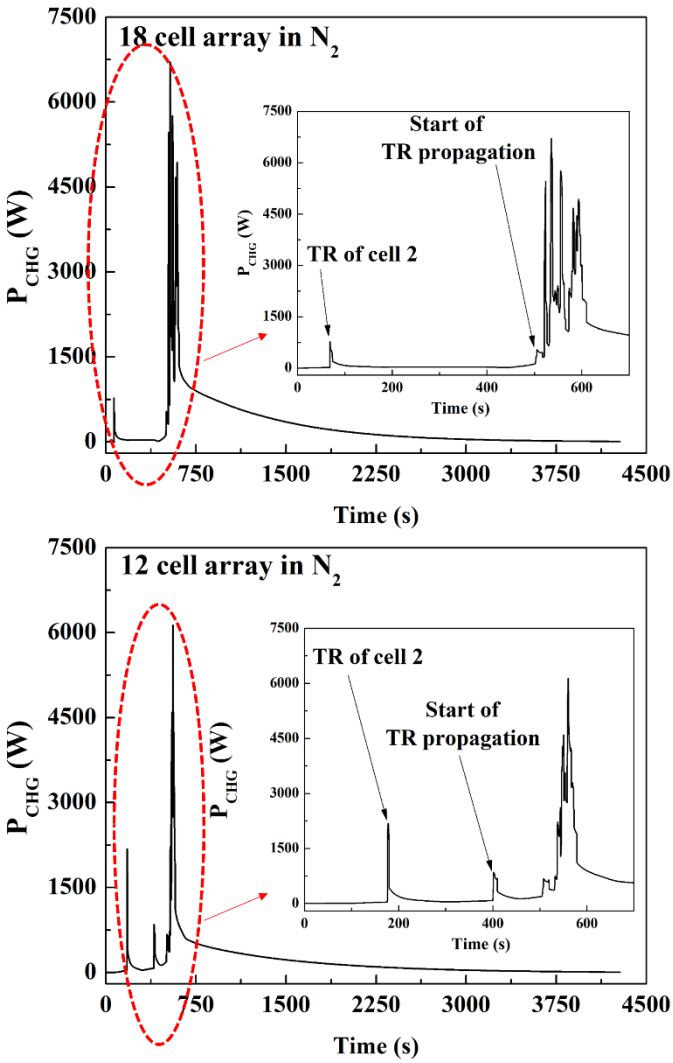

Figure 5. 7. Rates of chemical heat generation computed for representative 18 and 12 cell arrays examined in an N_2 environment. Cell 2 was the trigger cell.

The P_{CHG} curves were numerically integrated to calculate the total heat generated (E_{CHG}). Table 5. 4 provides information on E_{CHG} values that were normalized by the initial mass of all cells, number of cells, or total nominal electrical capacity of all cells. Differences between 18 and 12 cell results were within each other's uncertainties. When averaged over both array sizes, E_{CHG} became 56.6 ± 2.5 kJ per cell, 1.30 ± 0.06 kJ per g of initial cell mass, or 21.8 ± 1.0 kJ per unit electrical capacity in A h.

Table 5. 4. Chemical heat generation during cascading failure of LCO cell arrays in N_2. The uncertainties were computed from the scatter of data as two standard deviations of the mean.

Array size	E_{CHG}		
	Normalized per initial cell mass [kJ g^{-1}]	Normalized per cell number [kJ]	Normalized per electrical capacity [kJ A^{-1} h^{-1}]
18 cells	1.34 ± 0.09	58.0 ± 4.1	22.3 ± 1.7
12 cells	1.26 ± 0.04	54.9 ± 1.8	21.1 ± 0.7

The average E_{CHG} was also normalized by the electrical energy stored and was found to be 1.67 ± 0.05. This means that ≈ 1.7 kJ of energy is released during anaerobic failure per 1 kJ of stored electrical energy. The E_{CHG} obtained in this work was found to be within 14% of that reported by Lyon and Walters [52], 65.7 kJ per cell. Liu et al. [54] reported a chemical heat generation value of 37.3 kJ per cell for LCO cells at 100% SOC. This value represents only the energy generation inside the cell enclosure and does not include energy released by reactions occurring between ejected materials outside the cell body. When Liu et al. [54] extrapolated the chemical heat generation to include the externally produced energy, they obtained 59 kJ per cell, which is within the uncertainties of the current results.

5.6 Summary

Chapter 5 presented the experimental results associated with studying cascading failure in LCO cell arrays of two different sizes: 18 and 12 cell arrays. The main purpose for this study was to determine whether the smaller array size (12 cell arrays) could be used to represent the behavior of larger arrays or not. In both array sizes, the LCO cells were densely packed in rectangular configurations (no gaps

between adjacent cells) and charged at 100% SOC. The cell arrays were mounted in the wind tunnel, where experimental conditions were carefully controlled. TR was initiated in one cell using a small electric heater supplied with 115 W DC power. TR propagation to the other cells was tracked using temperature sensors attached to the bottom surface of each cell in the tested array. Experiments in this chapter were only conducted in an anaerobic environment (N_2).

Tests demonstrated that 18 and 12 LCO cell arrays experienced cascading failure when TR was initiated in one of the cells. Time-resolved measurements of cells' bottom surface temperatures were analyzed to study the dynamics of cascading failure. More specifically, the temperature histories were utilized to identify the onset times of SV and TR. The TR times were then employed to calculate row-to-row propagation speeds. Results showed that the 18 and 12 cell arrays yielded the same propagation speeds. The average TR propagation speeds for both array sizes was found to be 0.08 s^{-1} in N_2.

The SV and TR onset temperatures corresponding to the SV and TR onset times were determined from the temperatures of cells (measured at the cell bottom surfaces). Both SV and TR temperatures showed negligible dependence on the array size. For 18 and 12 cell arrays together, the SV and TR temperatures were found to be 354 ± 12 and 370 ± 5 K, respectively. Additionally, the maximum temperatures of cells (measured at the cell bottom surfaces) were computed for both sizes. The 18 cell arrays achieved maximum temperatures that, on average, were 60 K higher than the maximum temperatures of the 12 cell arrays likely due to higher overall heat generation rates achieved in the 18 cell array tests.

Experiments showed that a small fraction of cells ruptured during cascading failure. Propagation of TR in the 18 and 12 cell arrays resulted in 15.6% and 14.6% of cells rupturing, respectively. Individual cells were weighed before and after tests to measure the total mass loss. Cells of both array sizes essentially lost similar amounts of mass. On average, a single LCO cell lost 38% of its initial mass when tested in N_2.

Time-resolved gas concentrations measured in N_2 were analyzed to calculate the yields of gases ejected from the cell arrays. Results showed insignificant impact of the array size on the gas productions. The arrays tested in N_2 produced O_2, THC, CO, CO_2 and H_2 in average amounts of 0.026 ± 0.009, 1.57 ± 0.47, 1.77 ± 0.21, 1.41 ± 0.16 and 0.087 ± 0.017 g per failed cell, respectively. Thus, carbon monoxide, which is highly toxic, had the largest mass yield. The mass yields THC and CO_2 were comparable and slightly lower than that of CO. Although the mass yield of H_2 was relatively small, the volumetric concentration inside the tunnel reached significant values, exceeding 18 vol.% in some experiments. These measurements also confirmed speculations found in literature [2, 125, 126] regarding formation of O_2 during the thermal runaway of LIB cells. The lower flammability limit of the flammable portion of the ejected gases was found to be 5.79 ± 0.12 vol.% in air. The maximum volume of an enclosure where the gases ejected from a single cell create a flammable mixture was estimated to be 0.087 ± 0.017 m^3.

The heat generation due to chemical reactions between battery materials was determined by computing the enthalpy change of the gases leaving the tunnel. The 18 and 12 cell arrays generated comparable amounts of chemical heat. When averaged over both array sizes, the chemical heat generation was found to be 56.6 ± 2.5 kJ per

cell, 1.30 ± 0.06 kJ per g of initial cell mass, or 21.8 ± 1.0 kJ per unit electrical capacity in A h. The chemical heat generation was also normalized by the electrical energy stored and was found to be ≈ 1.7. Overall, the 18 and 12 cell arrays produced the same results in all measured quantities, which indicates that the 12 cell arrays can be used to represent the behavior of larger scale arrays for any further investigations.

6. Results and Discussion: Cathode Chemistry Investigation

This chapter presents the experimental results associated with the impact of cell cathode chemistry on the dynamics and hazards of TR propagation in 12 cell arrays. The tested arrays were constructed with individual LIB cells of LCO, NMC, or LFP cathode chemistry. All cells were charged at 100% SOC except the trigger cell of the NMC arrays, as previously mentioned in section 3.5.2. The LCO, NMC, or LFP cell arrays were tested in both N_2 and air environments to elucidate the impact of flaming combustion on cascading failure. The chapter presents information on the dynamics of TR propagation, failure temperatures, mass loss of cells, and a flammability assessment of gas mixtures ejected from different cathode arrays. Lastly, heat productions associated with chemical reactions between battery materials (N_2 tests) and flaming combustion of ejected battery materials and aerosols (air tests) were separately quantified.

6.1 Dynamics of Cascading Failure

In cascading failure tests conducted in N_2, TR propagated through the entire LCO or NMC array causing a complete cascading failure. In all LFP cell tests conducted in N_2, however, TR only propagated to the five cells neighboring the trigger cell (cell 2 in the array) causing a partial or incomplete cascading failure. Figure 6. 1 provides TR propagation charts for representative experiments conducted in an N_2 environment. The propagation charts for the other test repetitions are included in Appendix C (Figure C. 3, Figure C. 6, and Figure C. 8).

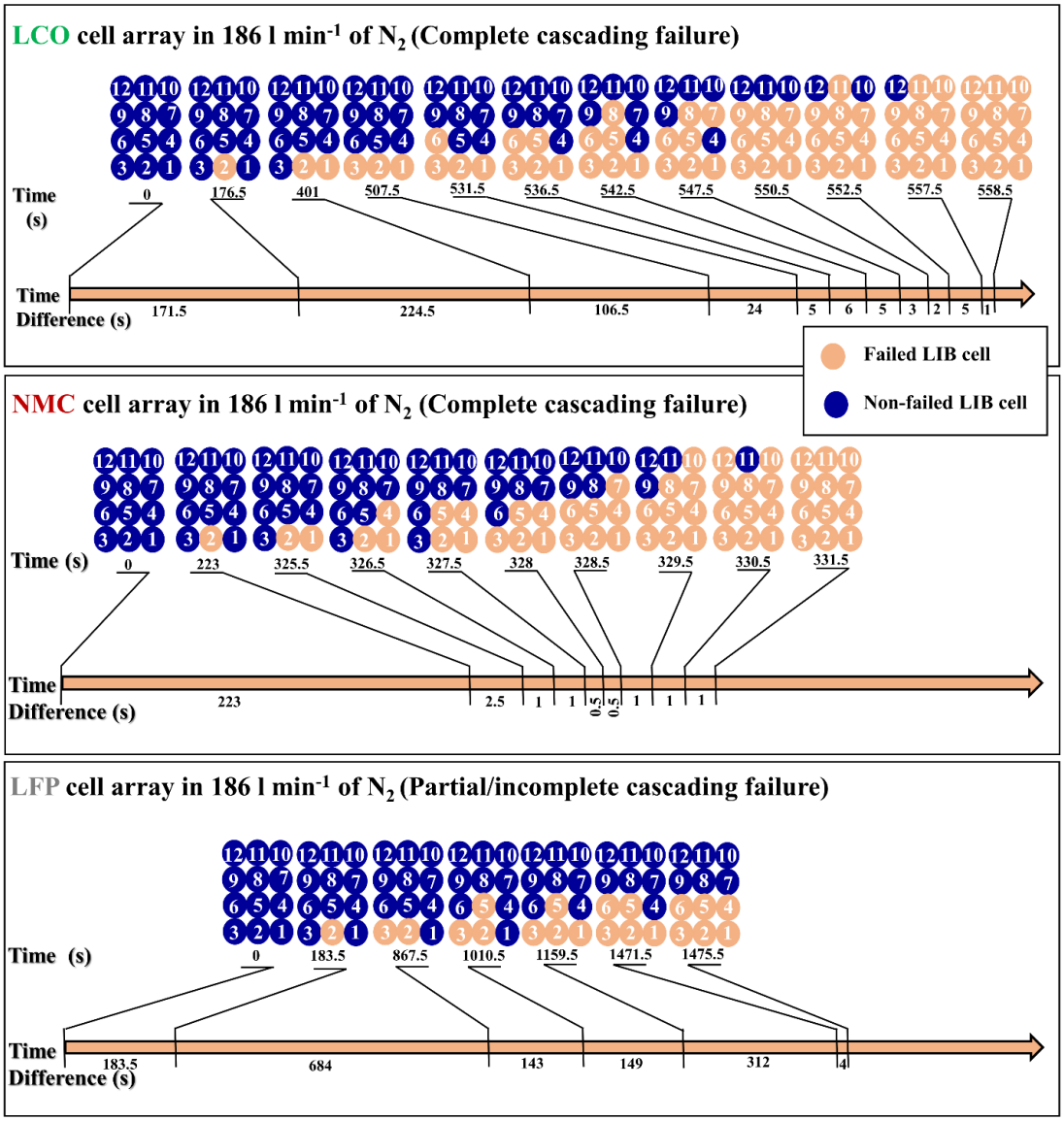

Figure 6. 1. Thermal runaway propagation charts for LCO, NMC and LFP cell arrays obtained for representative experiments conducted in N_2. Cell 2 was the trigger cell. The dark and light circles represent non-failed and failed cells, respectively. The timeline is not drawn to scale.

At 640 l min^{-1} flow rate of air, all LCO and NMC cell arrays experienced a complete cascading failure. The LFP cell arrays were tested twice at the same air flow rate but experienced an incomplete cascading failure where only the maximum of four cells (including the trigger cell, cell 2) underwent TR, perhaps, due to additional

cooling provided by the high air flow. Additional four LFP cell array tests were conducted at a reduced air flow rate of 186 l min^{-1} in an attempt to achieve a complete cascading failure (as described in section 3.5.2). A complete propagation was observed in one of the four tests. In the other three, a maximum of eight cells underwent TR (including the trigger cell). Representative TR propagation charts for the air experiments are provided in Figure 6. 2 (a-c). Figure 6. 2 (d) depicts dynamics of the LFP cascading failure experiment where a complete propagation was observed. The TR propagation charts for all other air test repetitions are included in Appendix C (Figure C. 4, Figure C. 7, and Figure C. 9).

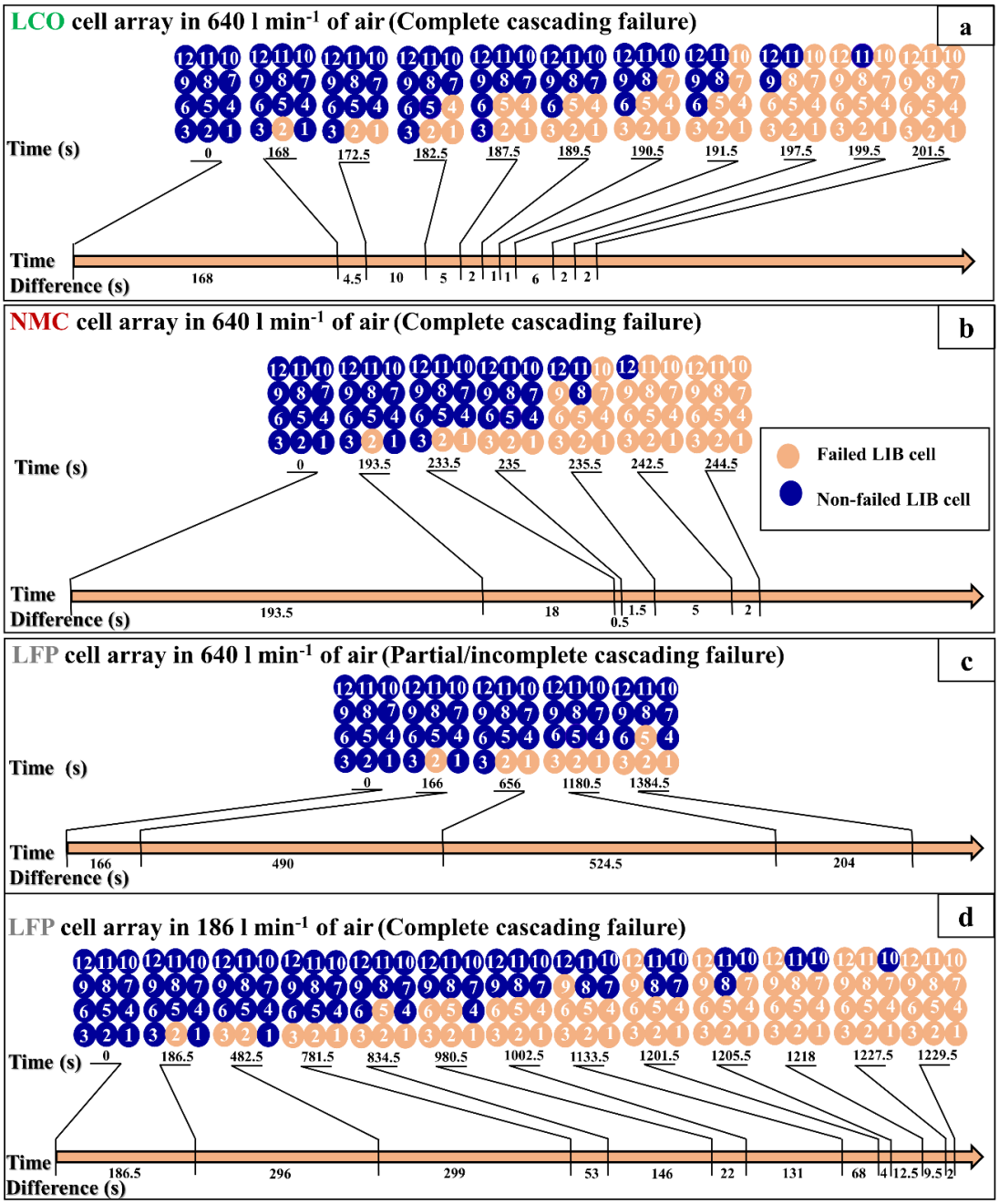

Figure 6. 2. (a-c) Thermal runaway propagation charts for LCO, NMC and LFP cell arrays obtained for representative experiments conducted at 640 l min^{-1} flow rate of air. (d) Chart for the LFP cell array that underwent a complete cascading failure at 186 l min^{-1} air flow rate. Cell 2 was the trigger cell. The dark and light circles represent non-failed and failed cells, respectively. The timeline is not drawn to scale.

As discussed in chapter 5 (section 5.1), the TR onset times of individual cells were not reproducible in any of the experiments even though the heating conditions, atmosphere and initial positioning of the cells in the cell holder were carefully monitored and controlled. This irreproducibility is believed to be related to the changes in the shapes of individual cells that occurred during TR. The shape changes varied widely from cell to cell and from one cathode chemistry to another. These changes significantly affected direct contact areas between adjacent cells, which, in turn, affected the rates of heat transfer. However, the TR advancement from one row to the next row displayed a reasonable degree of reproducibility. Therefore, the dynamics of cascading failure were resolved on a row-to-row basis.

The TR onset time of each row was computed by averaging the onset times of all cells in the row of interest. The row onset times were subsequently utilized to calculate a row-to-row propagation speed, S_P, in units of s^{-1}. The results of these calculations are provided in Figure 6. 3. For better clarity, the row-to-row propagation speed is also presented as S_P^*, in standard units of mm s^{-1}. S_P^* was calculated by multiplying S_P by the diameter of the cells (18 mm).

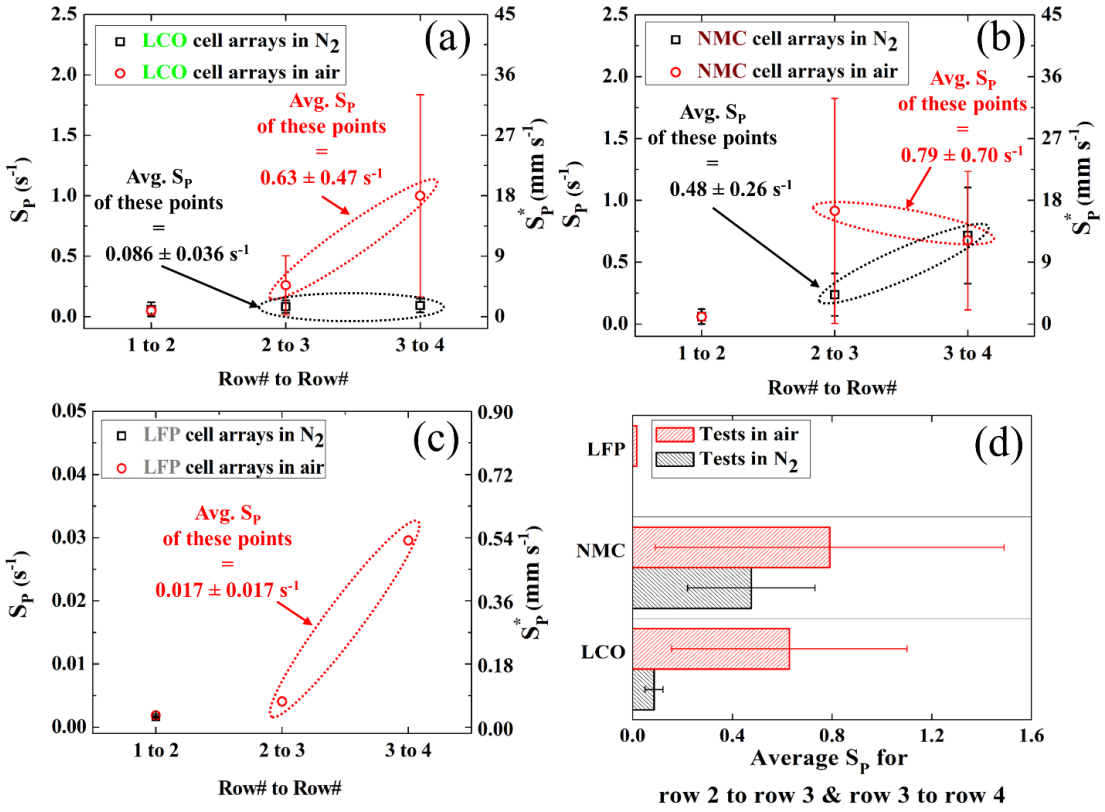

Figure 6. 3. (a-c) Row-to-row TR propagation speeds for LCO, NMC and LFP cell arrays tested in N_2 and air. (d) A comparison of the average S_P of row 2 to row 3 and row 3 to row 4 obtained for different cell chemistries in N_2 and air. Data of non-propagating LFP tests were excluded from the plotted statistics. All error bars were computed from the scatter of the data as two standard deviations of the mean.

The N_2 data presented in Figure 6. 3 (a) show that TR propagates through LCO arrays at a highly steady and reproducible rate. When the LCO experiments are conducted in air, only the early (row 1 to row 2) data are consistent with the results in N_2. In the later stages of the propagation, S_P increases significantly, while also becoming notably less certain. The average S_P for the late stages of the propagation (row 2 to row 3 and row 3 to row 4) was found to be about a factor of 7.3 larger in air than in N_2, as the calculation presented in the figure indicates. This acceleration is likely

attributed to the impact of flaming combustion, which increased heating intensity of the downstream cells.

The NMC cell results presented in Figure 6. 3 (b) display notably different trends. S_P appears to increase and become less certain in the late stages of the propagation in both N_2 and air. The average S_P calculated for air is somewhat higher than that calculated for N_2. However, the impact of air is much less prominent than in the case of LCO cells, suggesting that the heat generated in flaming combustion does not contribute significantly to the failure propagation in the NMC cell arrays. One possible explanation for this observation is the higher rate at which the gases and aerosols are ejected by the NMC cells compared to the LCO cells. This fast ejection causes combustion or ignition to initiate further downstream of the cells near the outlet of tunnel, which, in turn, results in less heat transfer to the cells during TR propagation.

In the case of the LFP cell arrays, only row 1 to row 2 propagation takes place in N_2. This data point is shown in Figure 6. 3 (c). This propagation is believed to be, to a significant degree, driven by the energy input from the electrical heater. The 640 l min^{-1} air data are not presented in the figure because no full propagation to row 2 was achieved in any of these experiments. The only presented air data are from a single test conducted at 186 l min^{-1}, where a complete propagation (through all rows) was achieved. These data also show a late stage acceleration of the propagation rate, which is probably associated with the contribution from the flaming combustion of ejected battery materials.

Figure 6. 3 (d) provides a direct comparison of S_P data obtained from different cathodes at the late stages of the propagation. The LFP cells stand out as the complete

propagation is achieved only in a single air experiment, and, even in that experiment, the measured S_P shown on the figure is significantly lower than that of the other cells in any environment. This performance can be explained by the lower electrical capacity and higher thermal stability of the LFP cells [38]. The comparison also shows that, in an anaerobic environment, the NMC cells propagate TR much faster than the LCO cells. In an air environment, however, their propagation speeds become more comparable.

6.2 Temperatures of Cascading Failure

The SV and TR onset temperatures as well as the maximum cell temperatures showed no dependence on the position of the cell in the array. According to the data summarized in Table 6. 1, the SV and TR onset temperatures were also essentially independent of the atmosphere in which the experiments were conducted, but they did show a notable dependence on the cathode chemistry. The LFP cells had the highest SV and TR onset temperatures, while the NMC onset temperatures were the lowest, which is probably why the NMC showed higher propagation speeds in N_2 and air. The presence of air clearly increased the maximum temperatures for all cells, further supporting the hypothesis that the flaming combustion of ejected battery materials (suppressed in an N_2 environment) contributed to the heating of the cell bodies.

Table 6. 1. Summary of cell temperature data. All temperatures obtained in this table were measured at the bottom surfaces of the cells. The temperature data obtained for the NMC trigger cells (which were charged to 50% SOC) and the non-failed LFP cells were excluded from the presented statistics. All uncertainties were computed from the scatter of the data as two standard deviations of the mean.

Cathode chemistry	Current study			Previous study [54]	
	SV onset temperature [K]	TR onset temperature [K]	Maximum temperature [K]	SV onset temperature [K]	TR onset temperature [K]
LCO in N_2	359 ± 17	381 ± 12	686 ± 23	-	-
NMC in N_2	336 ± 25	354 ± 11	656 ± 17	-	-
LFP in N_2	411 ± 17	447 ± 21	526 ± 27	-	-
LCO in air	350 ± 14	367 ± 8	718 ± 28	451 ± 5	470 ± 4
NMC in air	321 ± 11	355 ± 12	747 ± 31	-	-
LFP in air	412 ± 13	438 ± 16	554 ± 25	471 ± 3	516 ± 2

As reported in Table 6. 1, the onset temperatures obtained for the LCO and LFP cells were found to be 59-103 K lower than the onset temperatures for the same cells tested at the same SOC in a previous study [54]. The differences are believed to be associated with the differences in heating conditions and techniques. In the aforementioned study, the cells were heated slowly, at about 0.1 K s^{-1}, thus achieving a spatially uniform temperature throughout the cell body. In the current study, the rate of heating associated with cell-to-cell heat transfer was substantially high, as high as 7 K s^{-1}, which created a highly non-uniform temperature inside the cells, with the bottoms being notably cooler than the side walls, as indicated in Figure 6. 4. As depicted in the figure, TCs were attached to the side walls (at mid height) of representative cells to record temperature histories of the walls. The temperatures of side and bottom surfaces were compared and found to be significantly different, particularly during TR, confirming temperature non-uniformity. This observation suggests that the onset

temperature information used to detect cell failure should not necessarily be based on slow heating experiments, because this is likely to lead to a late detection in fast heating scenarios such as cascading failure.

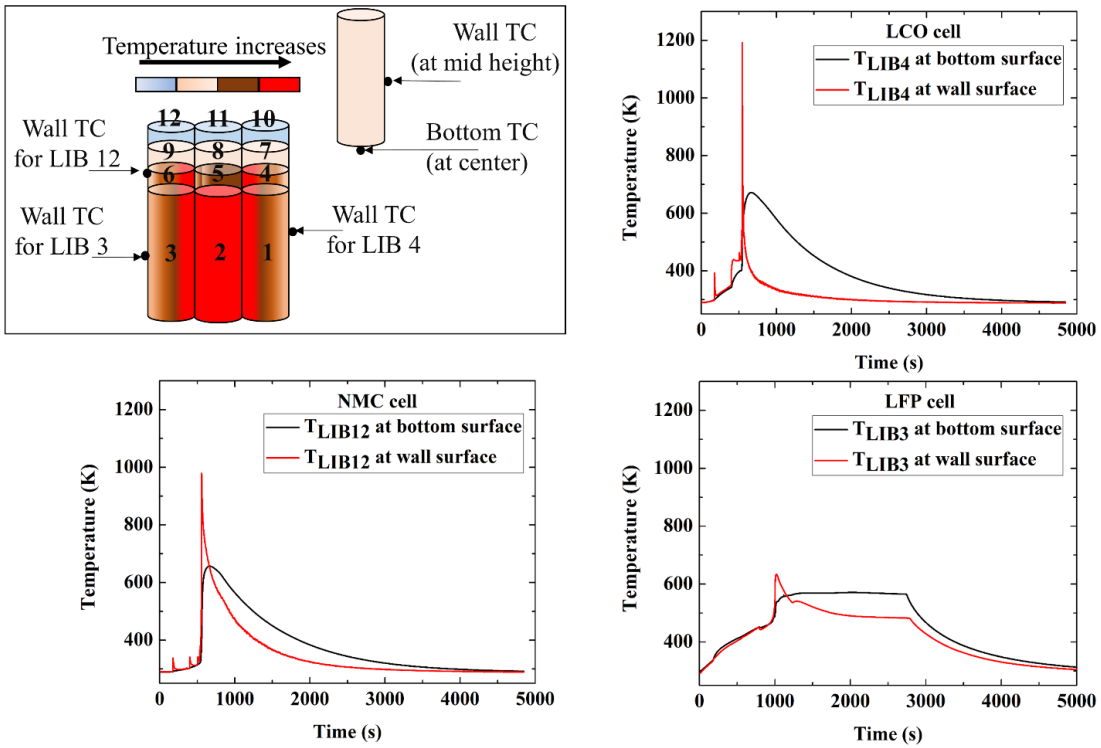

Figure 6. 4. Comparison between temperatures measured at side and bottom surfaces for representative LIB cells in the LCO, NMC, and LFP cell arrays. One TC is placed at the mid height of the cell's side surface in addition to the typical TC which is placed at the center of the same cell's bottom surface of the same cell.

6.3 Failed Cells, Ruptured Cells, and Mass Loss

All cells in the LCO and NMC cell arrays underwent TR, while only 38% and 53% of cells in the LFP cell arrays underwent TR in N_2 and air environments, respectively. Figure 6. 5 displays representative examples of non-ruptured cells (top row) after TR. The figure shows that the intact LCO and NMC cells may maintain their cylindrical geometry or deform, while none of the LFP cells deformed. Additionally,

Figure 6. 5 depicts representative examples of ruptured LCO and NMC cells (bottom row). In some cases, the cell rupture or explosion was so severe that the jelly roll of the LCO and NMC cells was separated from the cell casing. None of the LFP cells ruptured during the experiments.

Figure 6. 5. Photographs of LCO, NMC, and LFP cells after testing: non-ruptured (top row) and ruptured (bottom row).

For the LCO cells, the frequency of obtaining ruptured cells increased from 14% to 23% with the switch from N_2 to air. For the NMC cells, the rupture frequency was significantly lower and just increased from 4% to 6% with the switch from N_2 to air. The cell position did not appear to affect the probability of cell rupture. None of the NMC trigger cells (only charged to 50% SOC) in the current experiments experienced rupture.

Statistics on the cell mass loss are provided in Table 6. 2. The NMC cells lost the highest fraction of their mass upon TR, close to 60%. The LFP cells lost the lowest

fraction, less than 15%. The test environment (N_2 versus air) did not appear to significantly affect the mass loss. The reported mass loss fractions obtained for the LCO and LFP cells are close to those previously measured by Liu et al. [54] for the same cells at the same SOC.

Table 6. 2. Cell initial mass and mass loss data for the cascading failure experiments. The data for the NMC trigger cells (charged to 50% SOC) and non-failed LFP cells were excluded from the reported statistics. All uncertainties were computed from the scatter of the data as two standard deviations of the mean.

Cathode chemistry	Initial mass per tested cell [g]	Mass loss per failed cell number in N_2 [g]	Mass loss per failed cell number in air [g]
LCO	43.56 ± 0.04	16.7 ± 1.0 (38.3%)	17.3 ± 1.1 (39.7%)
NMC	45.30 ± 0.03	26.3 ± 1.1 (58.0%)	26.3 ± 0.9 (58.0%)
LFP	38.50 ± 0.03	5.0 ± 0.2 (13.0%)	5.4 ± 0.1 (13.9%)

6.4 Ejected Gas Yields

Figure 6. 6 (a-c) shows time-resolved volumetric (or molar) concentrations of ejected gases for representative experiments on the LCO, NMC and LFP cell arrays conducted in an N_2 environment. The ejected gas concentration profiles of all other test repetitions are included in Appendix C (Figure C. 19 to Figure C. 21). In all presented trends, the early peak corresponds to TR of the trigger cell (cell 2) or TR of cell 2 and cell 1, which failed nearly simultaneously. These early peaks are followed by larger peaks associated with failure propagation to the other cells in the array.

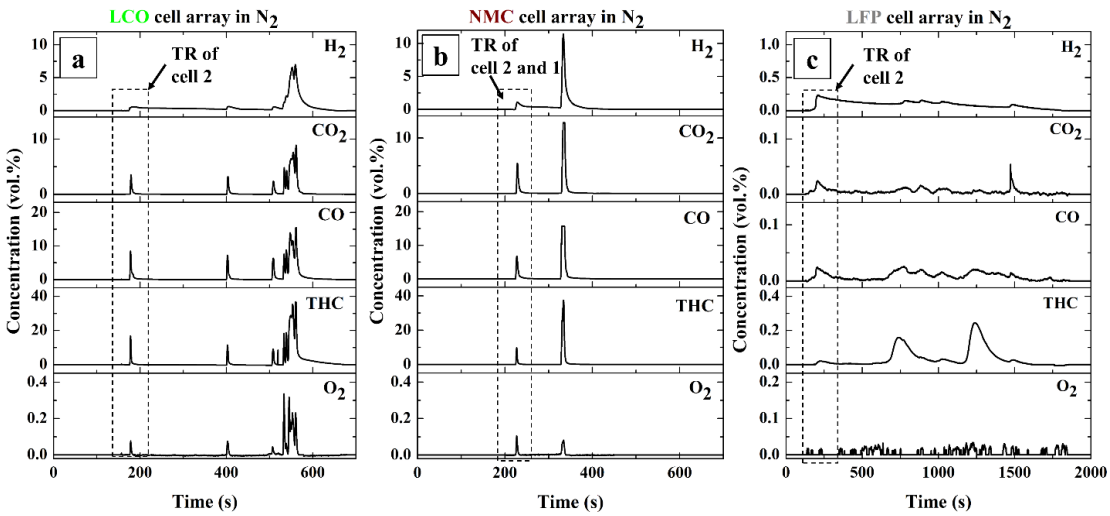

Figure 6. 6. Representative gas concentration profiles obtained from experiments on LCO, NMC and LFP cell arrays tested in N_2. Cell 2 was the trigger cell.

The mass yields of individual gases are provided in Figure 6. 7 (a) and (b). These yields are normalized either by the number of failed cells or initial mass of failed cells in a tested array. The LCO and NMC gas yields are very similar. On a mass basis, THC, CO_2 and CO are produced in high, comparable amounts, while the yields of H_2 and O_2 are an order of magnitude lower. The fact that O_2 is observed in detectable amounts confirms speculations about oxygen production in thermal decomposition of LIBs found in the literature [2, 3]. The total masses of ejected gases per failed cell number were determined to be 4.6 ± 1.6 and 4.6 ± 1.1 g for the LCO and NMC cells, respectively, which are comparable to the total amounts of organic materials in these cells, according to their material safety data sheets [98, 102]. The LFP cell gas yields were found to be approximately an order of magnitude lower than those determined for the LCO and NMC cells for all gases except H_2. The mass yields of H_2 were found to be comparable between all cell chemistries.

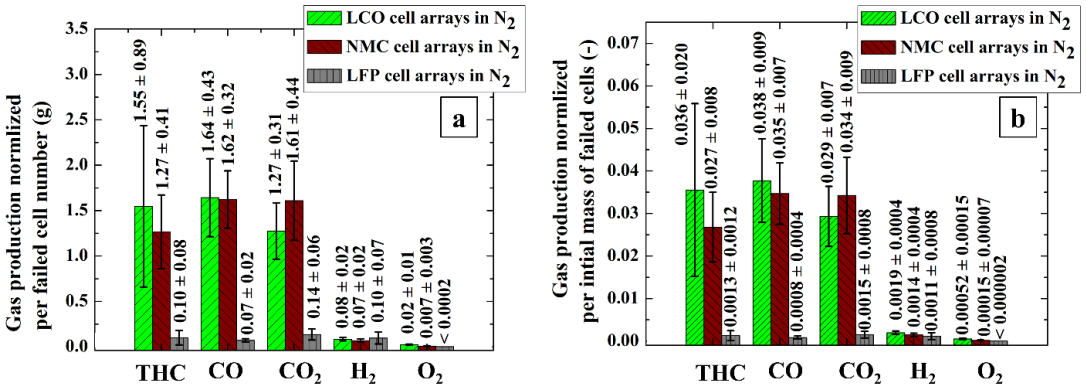

Figure 6. 7. Summary of mass-based gas yields normalized per failed cell number or initial mass of failed cells. All uncertainties were computed from the scatter of the data as two standard deviations of the mean.

Figure 6. 8 presents the information on the gas yields in terms of volumetric (or molar) fractions. The key point of this figure is to demonstrate that, on a volumetric basis, the contribution of H_2 to the overall mixture becomes significant. In fact, in the case of LFP cells, H_2 is by far the most dominant gaseous product.

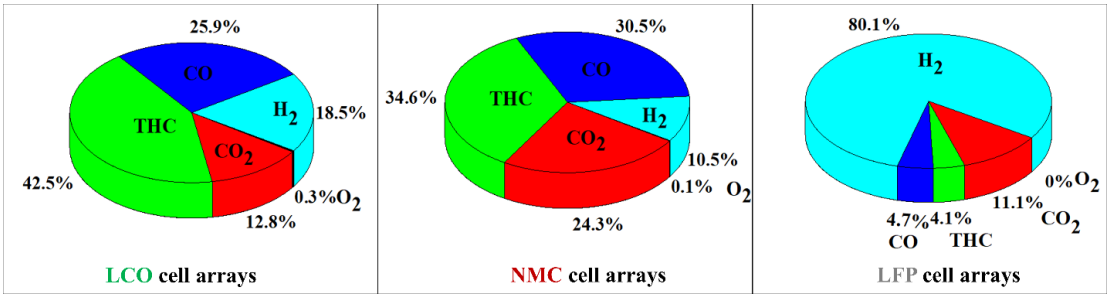

Figure 6. 8. Volumetric (or molar) fraction of each gas in the ejected gas mixture.

6.5 Lower Flammability Limits

The yields of THC, CO and H_2 measured in the cascading failure experiments performed in N_2 were used to calculate $LFL_{mixture}$. The LFL values were determined to be 5.74 ± 0.09, 5.96 ± 0.22 and 4.28 ± 0.15 vol.% in air for the LCO, NMC and LFP cells, respectively. The relatively low $LFL_{mixture}$ obtained for the LFP cells was

associated with the dominant volume faction of H_2 in the ejected gases (see Figure 6. 8).

The maximum volume of an enclosure (V_{flam}) in which failure of a single LIB cell creates a flammable mixture, assuming that the enclosure initially contains air at standard temperature and pressure, was calculated to be 0.084 ± 0.033, 0.071 ± 0.019 and 0.03 ± 0.02 m^3 for the LCO, NMC and LFP cells, respectively. The V_{flam} values were also normalized by the nominal electrical capacity, which resulted in 0.032 ± 0.013, 0.024 ± 0.006 and 0.020 ± 0.013 $m^3\ A^{-1}\ h^{-1}$ for the LCO, NMC, and LFP cells, respectively. These values indicate that the LCO cells represent a substantially greater hazard associated with a potential ignition of the ejected materials mixed with air, despite the LFP cells having a significantly lower $LFL_{mixture}$ value. This is the case because the absolute amounts of flammable gases ejected from the LCO cells upon TR are significantly greater than the amounts ejected from the LFP cells upon TR.

6.6 Energetics of Cascading Failure

6.6.1 Chemical Heat Generation

The rate of chemical heat generation (P_{CHG}) was calculated from the data collected in the N_2 cascading failure tests. Figure 6. 9 provides examples of P_{CHG} profiles obtained for the LCO, NMC and LFP cell arrays; profiles for all other test repetitions are included in Appendix C (Figure C. 36 to Figure C. 38). In these profiles, the earliest peak corresponds to TR of the trigger cell (cell 2) or TR of cell 2 and cell 1, which failed nearly simultaneously. These early peaks are followed by larger peaks associated with failure propagation to the other cells in the array. A slow decay in P_{CHG} is observed after the last TR peak. This decay represents the transfer of energy absorbed

by the cells and other test section components to the N_2 flowing through the tunnel. It is important to note that the maximum P_{CHG} values differed significantly between the cell types. At their maximum, the NMC cells generated energy several times faster than the LCO cells. The P_{CHG} maxima measured for the LFP cells were an order of magnitude lower than those measured for the LCO cells.

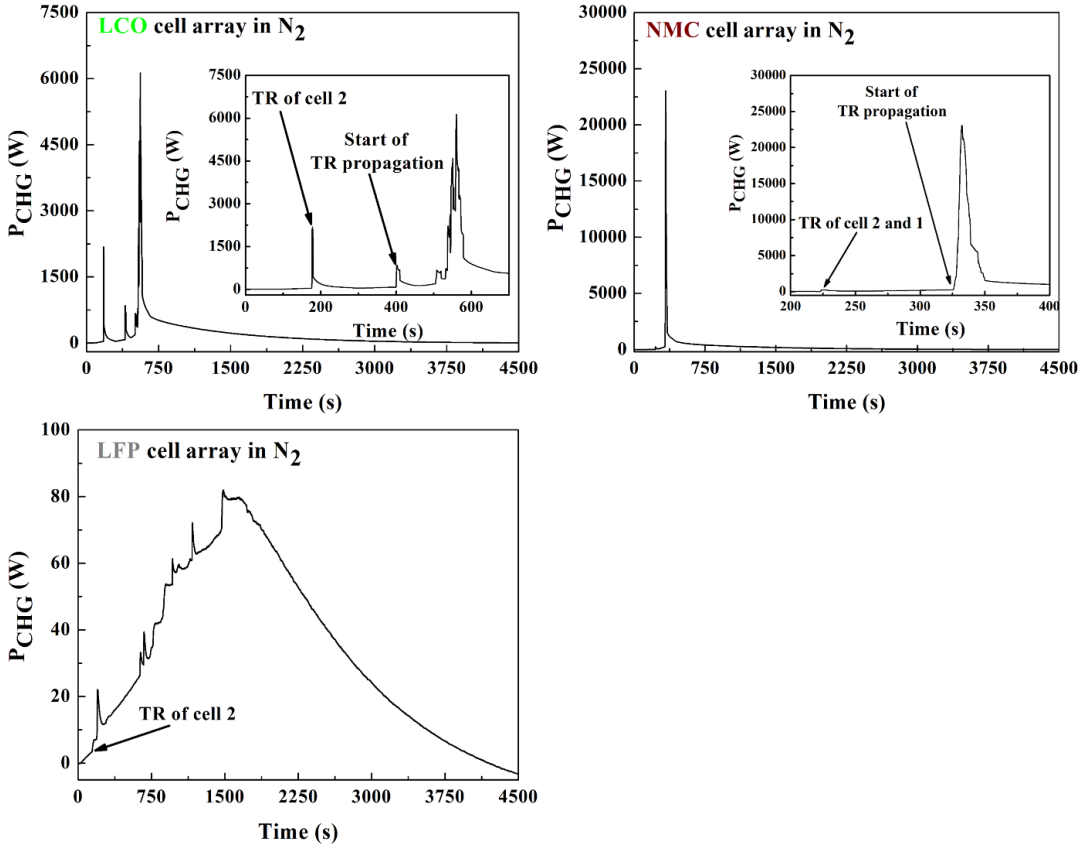

Figure 6. 9. Representative profiles of rate of chemical heat generation obtained from experiments on LCO, NMC and LFP cell arrays tested in N_2.

All P_{CHG} profiles were numerically integrated to compute the total chemical heat generation (E_{CHG}). These values were normalized per failed cell number, initial mass of failed cells, nominal electrical capacity or stored energy of failed cells. In this normalization process, the trigger NMC cell, which was charged to 50% SOC, was counted as half the cell charged to 100% SOC. The normalized quantities are compared

in Figure 6. 10. As shown in the figure, the NMC cells produce the greatest chemical energy upon failure. This energy becomes comparable to that produced by LCO cells when it is normalized either by the stored electrical energy or nominal electrical capacity. The energy produced by the LFP cells is much lower. In fact, this energy is so low that it was at the borderline of the sensitivity of the current measurement method. That is why the E_{CHG} computed for the LFP cells carries a 100% uncertainty.

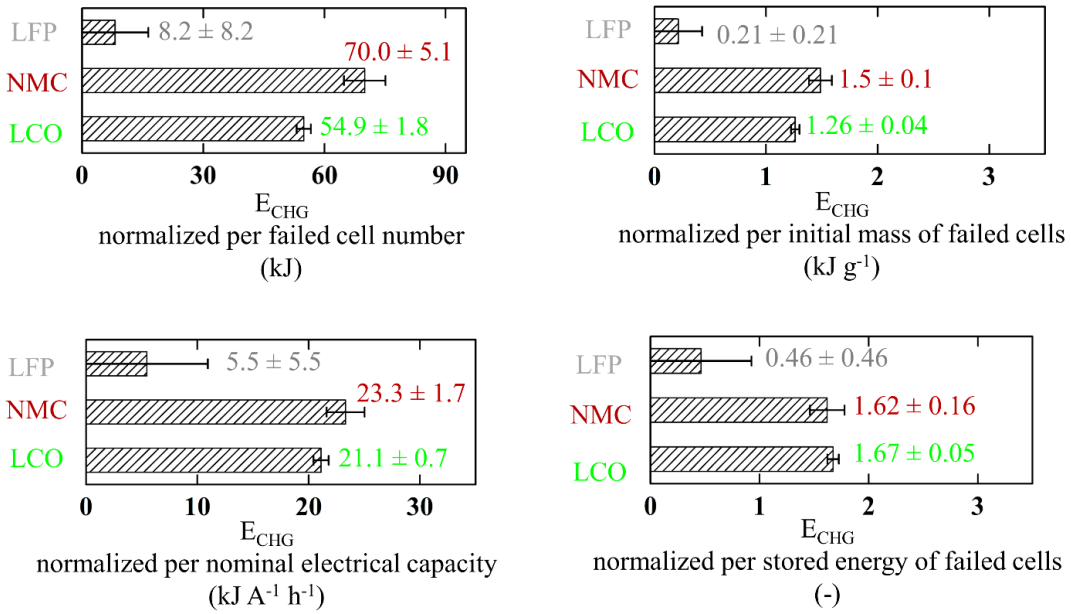

Figure 6. 10. Summary of the total chemical heat generation data normalized in various ways. In this normalization process, the trigger NMC cell, which was charged to 50% SOC, was counted as half the cell charged to 100% SOC. All uncertainties were computed from the scatter of the data as two standard deviations of the mean.

The current E_{CHG} value obtained for the LCO cells was found to be within 14% of that reported by Lyon and Walters [52], 65.7 kJ per cell, for the identical cells at the same SOC. Liu et al. [54] reported chemical heat generation values of 37.3 and 13.7 kJ per cell for the fully charged LCO and LFP cells, respectively. These values represent only the energy generated inside the bodies of the cells and do not include the energy

released by reactions occurring between the battery materials after they are ejected. When these values are extrapolated to include this additional energy release [54], 59 kJ is obtained for the LCO cells, which is consistent with the current results. 15.8 kJ is obtained for the LFP cells, which is within the uncertainties of the current measurement.

6.6.2 Flaming Combustion Heat Release

The data on oxygen consumption obtained in the cascading failure experiments conducted in air were used to calculate the rates of energy production in flaming combustion of ejected battery materials ($P_{Flaming}$). Figure 6. 11 provides examples of the $P_{Flaming}$ profiles obtained for the LCO, NMC and LFP cell arrays; the results of other test repetitions are included in Appendix C (Figure C. 43 and Figure C. 45). It is important to note that, in almost all LFP cell tests conducted in air, no significant oxygen consumption was detected, which means that the materials ejected from these cells did not ignite. The materials ignited and consumed a significant amount of oxygen in only one experiment performed at 186 l min^{-1} of air flow. This is also the only LFP cell test that exhibited a complete cascading failure. The LFP results shown in Figure 6. 11 are from this test. All presented $P_{Flaming}$ profiles contain an early peak corresponding to combustion of the materials ejected from the trigger cell (cell 2) followed by peaks corresponding to the cells that underwent TR at later times. In the case of LFP cells, which exhibited a relatively slow TR propagation, the peaks from individual cells are fairly well resolved in time.

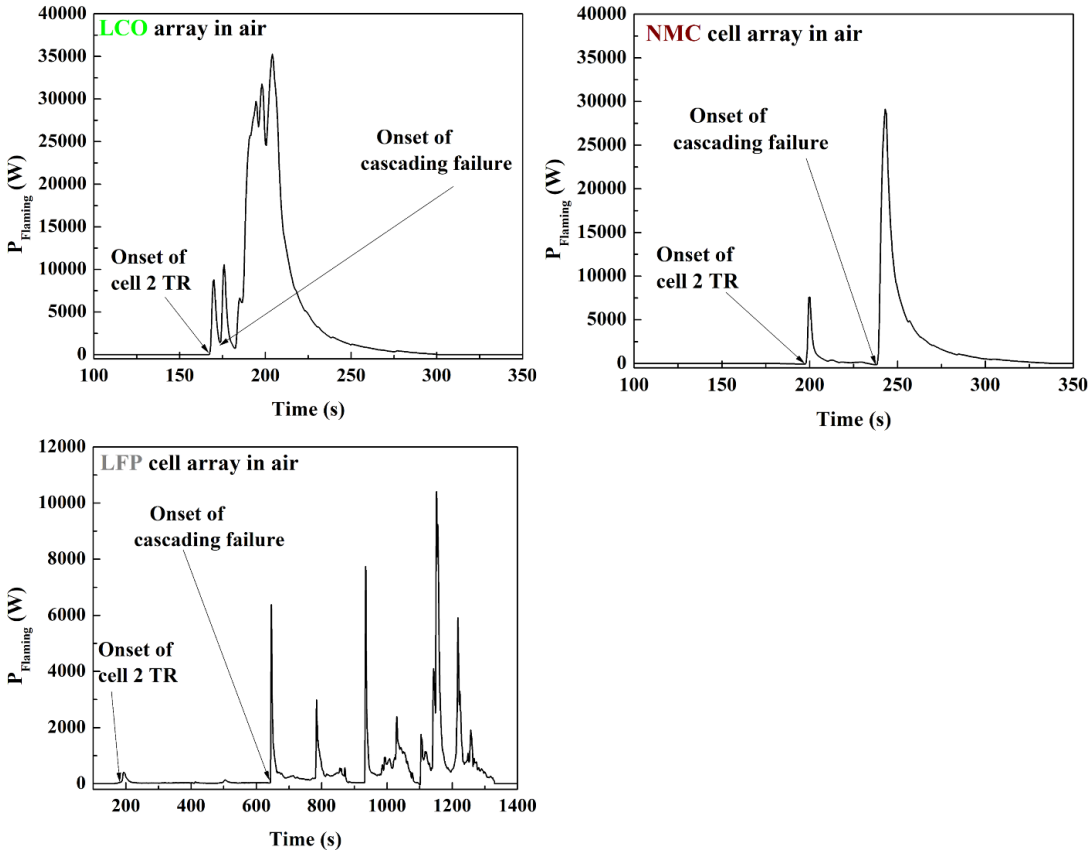

Figure 6. 11. Examples of flaming combustion heat release profiles obtained from experiments on LCO, NMC and LFP cell arrays tested in air. The shown profile for the LFP cells is from the single experiment where a complete TR propagation was achieved.

The profiles of $P_{Flaming}$ were numerically integrated to calculate the total heats of flaming combustion ($E_{Flaming}$). The $P_{Flaming}$ peak associated with the trigger NMC cell, which was charged to 50% SOC, was clearly separated in time and was excluded from the integration to focus on fully charged cells. The $E_{Flaming}$ values normalized per failed cell number, initial mass of failed cells, nominal electrical capacity or stored energy of failed cells are provided in Figure 6. 12. In the case of LFP cells, no uncertainties in $E_{Flaming}$ were computed because the data used were from a single experiment (where ejected battery materials ignited). When normalized by the nominal

capacity or stored electrical energy, the heats of flaming combustion were found to be comparable for all studied cell chemistries.

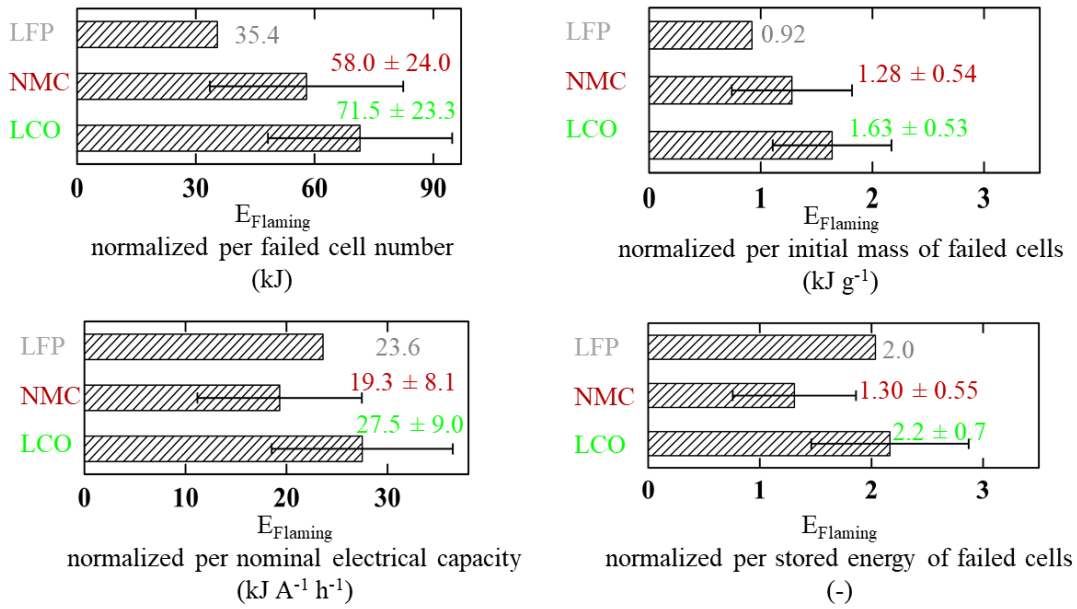

Figure 6. 12. Summary of heats released in flaming combustion during cascading failure normalized in various ways. The data shown for the LFP cells are from the single experiment where a complete TR propagation was achieved. All uncertainties were computed from the scatter of the data as two standard deviations of the mean.

Figure 6. 13 shows the volumetric concentration trends that were collected in the same experiments that were used to calculate the $P_{Flaming}$ profiles given in Figure 6. 11. The volumetric concentration trends for all other test repetitions are included in Appendix C (Figure C. 26 and Figure C. 28 to Figure C. 30). In addition to consumption of oxygen, these trends show significant amounts of CO and THC in the gas steam coming out of the test section, which indicates that the combustion process was incomplete. This observation is further supported by an apparent re-ignition or continued combustion of the gases coming out of the tunnel exhaust captured in the photographs provided in Figure 6. 14.

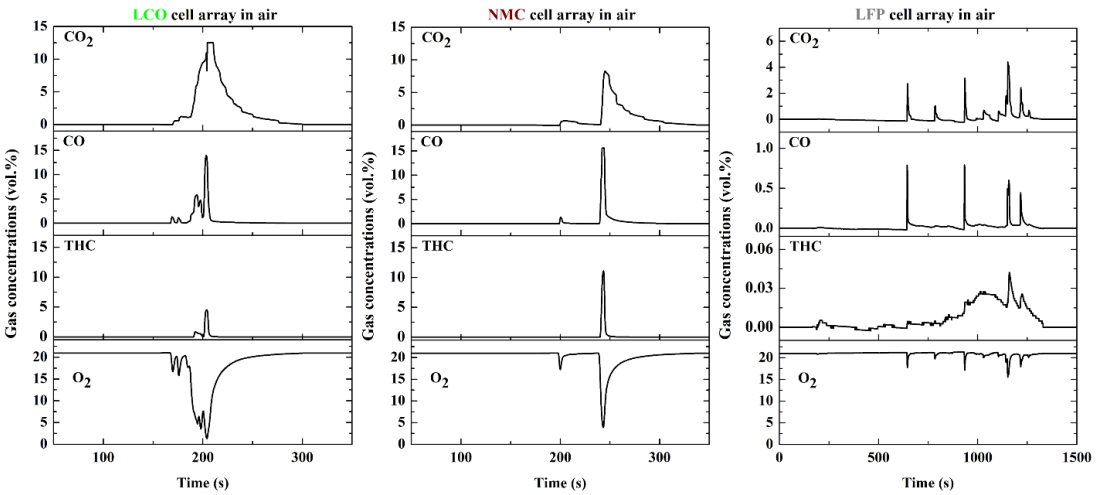

Figure 6. 13. Examples of gas concentration profiles obtained from experiments on LCO, NMC and LFP cell arrays tested in air. The LFP cell data are from the single experiment where a complete TR propagation was achieved.

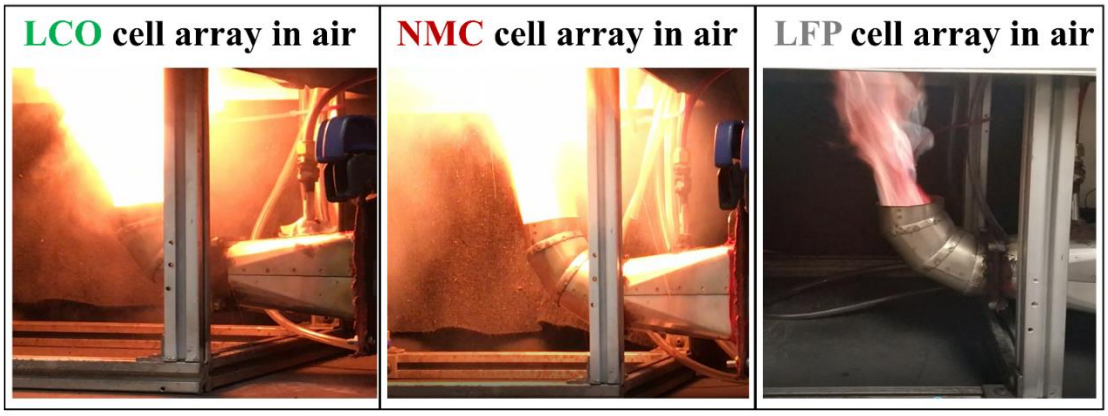

Figure 6. 14. Photographs demonstrating the re-ignition or continued combustion of the exhaust gases observed during the cascading failure experiments conducted in air.

The flaming combustion heat release rates obtained in the CSBC tests (conducted on individual cells as explained in section 3.5.6) were computed and are displayed in Figure 6. 15 for all test repetitions. All plotted profiles were numerically integrated, and the obtained results are listed in Table 6. 3. Assuming these heats correspond to complete combustion, the efficiency of flaming combustion that took place in the cascading failure experiments (conducted in air) can be determined.

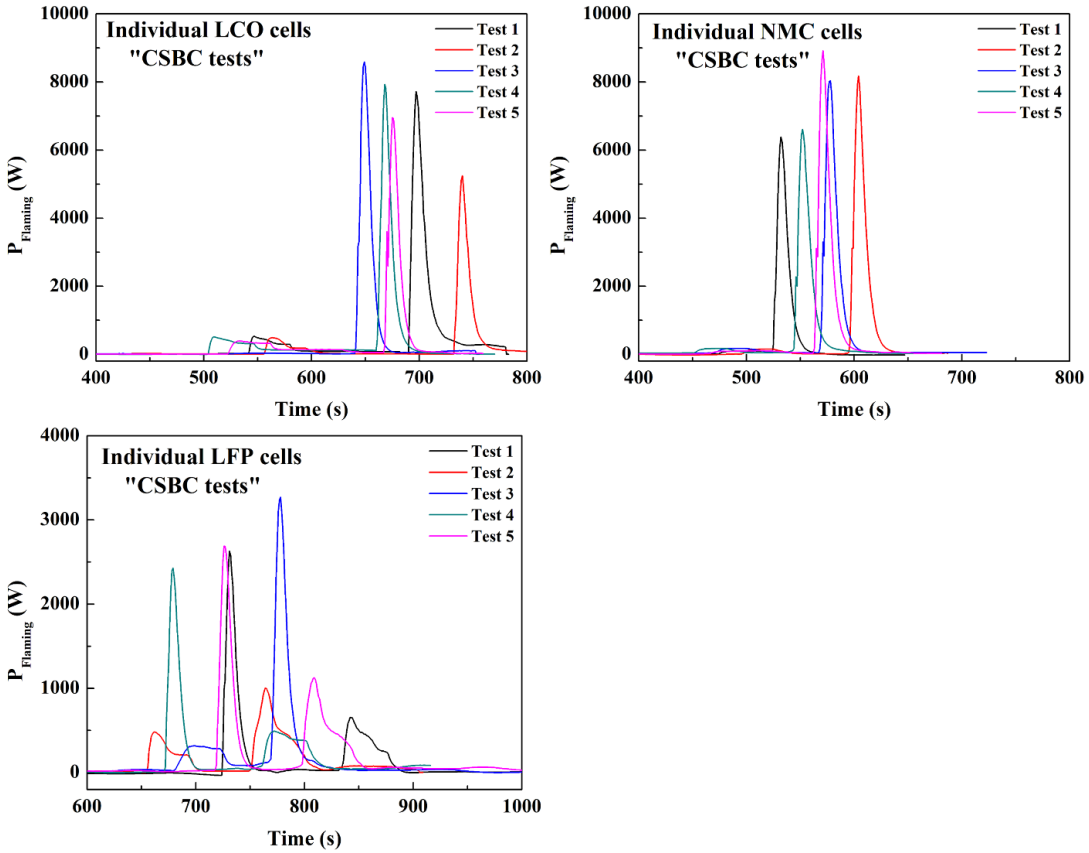

Figure 6. 15. Heat release rates due to flaming combustion of ejected materials from individual LCO, NMC, and LFP cells tested in the modified CSBC apparatus. Results of all test repetitions for each cell chemistry are presented in this figure.

Table 6. 3. The heats of flaming combustion of ejected battery materials measured in the CSBC experiments performed on individual cells. All uncertainties were computed from the scatter of the data as two standard deviations of the mean.

Cathode chemistry	$E_{Flaming}$			
	Normalized per cell number [kJ]	Normalized per initial cell mass [kJ g^{-1}]	Normalized per cell nominal capacity [kJ A^{-1} h^{-1}]	Normalized per stored electrical energy [-]
LCO	107.0 ± 18.0	2.5 ± 0.4	41.2 ± 2.7	3.2 ± 0.5
NMC	103.0 ± 16.0	2.3 ± 0.3	34.2 ± 5.3	2.3 ± 0.4
LFP	51.4 ± 7.5	1.3 ± 0.2	34.3 ± 5.0	3.0 ± 0.4

The combustion efficiency of each cathode chemistry was computed based on the $E_{Flaming}$ data per failed cell and based on the $E_{Flaming}$ data per gram of mass loss. On an $E_{Flaming}$ per failed cell basis, the combustion efficiencies were found to be 67 ± 22%, 56 ± 24%, and 69% for LCO, NMC, and LFP cell arrays, respectively. On an $E_{Flaming}$ per gram of mass loss basis, the combustion efficiencies were found to be 89 ± 31%, 76 ± 32%, and 62% for LCO, NMC, and LFP cell arrays, respectively.

The observed increase in combustion efficiency for the LCO and NMC cascading failure tests when calculated based on $E_{Flaming}$ per gram of mass loss is associated with less mass loss during these tests (reported in Table 6. 2) than the obtained mass loss during the CSBC tests (22 ± 1.5 g per failed LCO cell and 34 ± 3 g per failed NMC cell). The combustion efficiency of LFP tests were approximately the same when calculated based $E_{Flaming}$ per failed cell or per gram of mass loss because the LFP cell mass loss was approximately the same in the cascading failure and CSBC tests.

Overall, the combustion efficiency calculations confirm that the flaming combustion that occurred in the cascading failure experiments was highly incomplete. This is especially true for the LCO and NMC cell arrays, in which combustion was inhibited by a nearly complete consumption of oxygen as indicated by the data shown in Figure 6. 13. It should be noted that the nearly complete consumption of oxygen occurred despite the air flow rate being on the high side of what is typically used for active cooling in commercial LIB packs.

Liu et al. [54] and Quintiere et al. [11] reported $E_{Flaming}$ of 48.7 ± 7.4 and 70 ± 14 kJ per cell for the same LCO cells at 100% SOC. These researchers also pointed

out that the combustion of ejected materials was incomplete. Although these values are close to the $E_{Flaming}$ values measured in the cascading failure experiments (and reported in Figure 6. 12), such comparisons should be made with caution because the combustion efficiency strongly depends on the experimental conditions, which differed significantly between these experiments.

The data reported in Table 6. 3 indicate that, upon complete combustion, the batteries, regardless of the cathode chemistry, produce about three times more heat than the stored electrical energy. It is important to emphasize that this flaming combustion energy is generated in addition to the energy associated with the decomposition of and chemical reactions between cell components (E_{CHG}) measured in the cascading failure experiments performed in N_2. Therefore, in the case of the LCO and NMC cells, the maximum total energy generated upon thermal failure (including reactions between cell components and combustion of ejected materials) may reach close to five times the stored electrical energy.

6.7 Summary

Chapter 6 presented the results associated with investigating cascading failure in cell arrays of different cathode chemistries. Experiments were conducted on 12 LCO, NMC, and LFP cell arrays with cells arranged in rectangular geometry and charged at 100% SOC. All arrays were mounted in a wind tunnel with carefully controlled environmental conditions. TR was induced in one of the cells via an electric heater and observed to propagate through the array using temperature sensors attached to the bottom surfaces of cells. The arrays were tested in N_2 and air environments to study the impact of combustion on the dynamics and energetics of the failure process.

Experiments showed that all LCO and NMC cell arrays were subject to cascading failure in N_2 and air environments. For LCO cell arrays, TR propagated ≈ 8 times faster in air tests than in N_2 tests due to flaming combustion. For NMC cell arrays, the impact of air was much less prominent than for LCO cell arrays, which suggests that the combustion did not contribute to heating the cells. None of the LFP cell arrays tested in N_2 fully propagated TR. A complete propagation (all cells in an array undergoing TR) was observed in one LFP air test (the total of 6 tests was conducted in air). This complete propagation was associated with the ignition of ejected battery materials, which did not occur in any other LFP tests, perhaps, due to a relatively low maximum temperature achieved by these cells during TR.

In N_2, the NMC cells propagate TR much faster than the LCO cells, while their propagation speeds become more comparable in air. The LFP cells stand out as the complete propagation is achieved only in a single air experiment, and, even in that experiment, the measured speeds were significantly lower than those of the other cells in any environment. Such safe performance is attributed to the lower electrical capacity and higher thermal stability of the LFP cells [38].

The LFP cells had the highest SV and TR onset temperatures, while the NMC onset temperatures were the lowest. The TR onset temperatures obtained for the LCO and LFP cells were lower than the onset temperatures for the same cells tested at the same SOC in a previous study [54]. This discrepancy is believed to be associated with the differences in heating rates and techniques. In the previous study, the cells were heated slowly and uniformly. While in the current study, each cell in the array experienced rapid and spatially non-uniform heating from the neighboring cells. This

observation is important as it indicates that temperature-based failure detection thresholds for battery pack systems should not rely on temperature information obtained from experiments with slow uniform heating, otherwise such thresholds may not be able to sufficiently and quickly detect failure in fast non-uniform heating scenarios. The maximum cell temperatures were determined for all tested arrays. The LCO and NMC cells achieved maximum temperatures that were ≈ 100 K more than LFP cells. Also, the air tests substantially increased the maximum temperatures for all cells due to additional heating of cells by flames.

A small fraction of LCO and NMC cells ruptured during cascading failure. None of the LFP cells ruptured during the experiments. On average, the percentage of ruptured LCO cells increased from 14% to 23% when the test environment was changed from N_2 to air. The rupture percentage of NMC cells only increased from 4% to 6% with switching from N_2 to air. On average, the LCO, NMC, and LFP cells lost close to 40%, 60%, and 14% of their initial masses, respectively. The air presence appeared to insignificantly affect the mass loss percentage. The mass loss percentages obtained for the LCO and LFP cells were comparable with those values previously determined by Liu et al. [54] for the same cells charged at 100% SOC.

Gas concentrations measured in N_2 tests were analyzed to compute the yields of gases ejected from all cells. On a mass basis, the LCO and NMC cells produced significant amounts of hydrocarbons, CO and CO_2 (> 1 g per failed cell) and small quantities of H_2 and O_2. In the case of LFP cells, the mass yields of hydrocarbons, CO and CO_2 were found to be approximately an order of magnitude lower than those obtained for the LCO and NMC cells, while the H_2 production was comparable. The

LFP cell O_2 production could not be fully quantified because it was at or below the sensitivity limit of the gas analysis system. On a volumetric basis, the contribution of H_2 to the overall mixture became significant. In fact, in the case of LFP cells, H_2 was the most dominant gaseous product.

Yields of THC, CO, and H_2 were used to calculate $LFL_{mixture}$. On average, LCO, NMC, and LFP cell arrays released flammable gas mixtures with $LFL_{mixture}$ of 5.74 ± 0.09, 5.96 ± 0.22, and 4.28 ± 0.15 vol.% in air, respectively. The maximum volume in which failure of an individual cell creates a flammable mixture was calculated to be 0.084 ± 0.033, 0.071 ± 0.019, and 0.03 ± 0.02 m^3 for the LCO, NMC, and LFP cells, respectively. Despite the LFP cells possessing a lower value of $LFL_{mixture}$, the data still indicate that the LCO cells carry a greater ignition hazard because they produce greater amounts of flammable gases during TR.

In cascading failure tests, the total summation of the chemical heat generation (associated with decomposition of battery components and chemical reactions between these components) and the flaming combustion heat generation (associated with burning of gases and aerosols ejected from the cells) was computed to be 3.5, 2.9, and 2.5 times greater than the electrical energy stored for the LCO, NMC, and LFP cells, respectively. In these experiments the combustion process of ejected materials was substantially incomplete. Additional experiments were conducted to quantify flaming combustion energy when combustion was forced to near completion. Under near complete combustion conditions, the LCO, NMC, and LFP cells generated heats in the amounts of 4.9, 3.9, and 3.5 times greater than electrical energy stored, respectively.

7. Results and Discussion: Passive Mitigation Strategies Investigation – Introduction of Gaps and Physical Barriers

This chapter presents the results associated with the implementation of cascading failure passive mitigation strategies. The strategies included implementing empty gaps or physical barrier-filled gaps between groups/clusters of LCO cells charged at 100% SOC. All empty gaps and barriers experiments were conducted in an N_2 environment to prevent flaming combustion of ejected materials and provide a well-controlled environment to better quantify the impact of barriers on failure dynamics. For comparison, results of tests using LCO cell arrays without gaps (from chapter 5 and 6) are recalled and utilized as reference points for this chapter. The results in this chapter include the impact of different passive mitigation strategies on the dynamics, onset temperatures, cell mass loss, mass yields of ejected gases, and chemical heat generation of cascading failure.

7.1 Impact of Mitigation Strategies on Dynamics of Cascading Failure

Figure 7. 1 and Figure 7. 2 show propagation charts for representative tests of the four passive mitigation strategies; the charts for all other test repetitions are included in Appendix C (Figure C. 10 to Figure C. 14). In most experiments, TR propagated through all the cells of the tested array causing a complete cascading failure. In a few experiments where physical barriers were used, TR only propagated to one or two of the cells in the back row or the right most column leading to an incomplete cascading failure. Although the tested strategies were unsuccessful at preventing failure propagation from the 3 by 3 cell group/cluster to the back row (row 4) or the right most column (side column), the implemented strategies slowed down the rate of propagation,

in particular the use of physical barriers. Across all tests, the effectiveness of the gaps and barriers in the direction parallel to the gas flow were inconclusive. In some tests the propagation to the side column of cells was significantly delayed, but in others the side column cells failed at similar times to the other cells in their respective rows. Therefore, to provide the most direct comparison to the no gap tests, data from the side column of cells are not included in the remaining analysis.

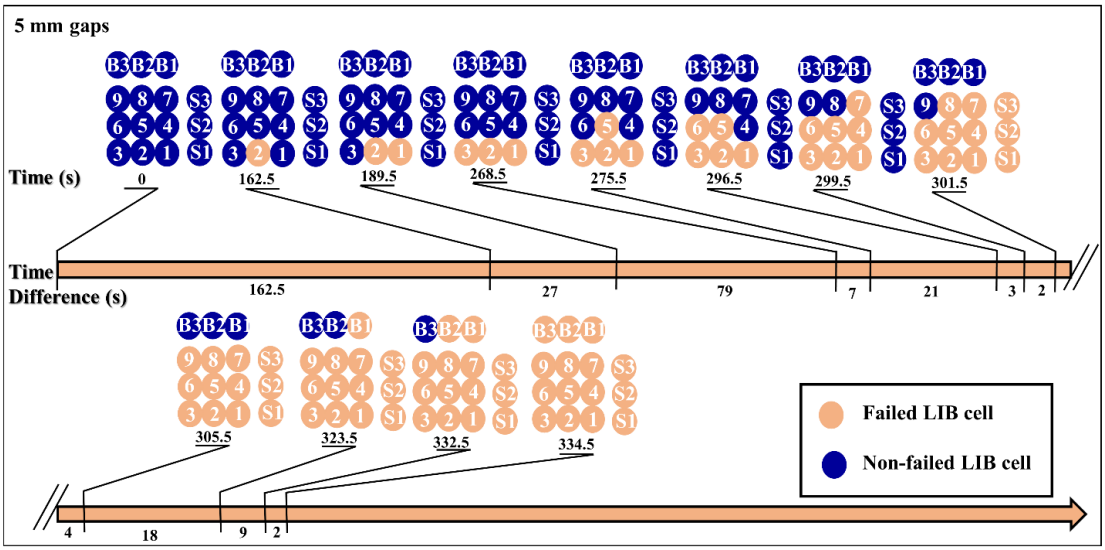

Figure 7. 1. Thermal runaway propagation charts for a representative 5 mm gaps test. Cell 2 was the trigger cell. The dark and light circles represent non-failed and failed cells, respectively. The timeline is not drawn to scale.

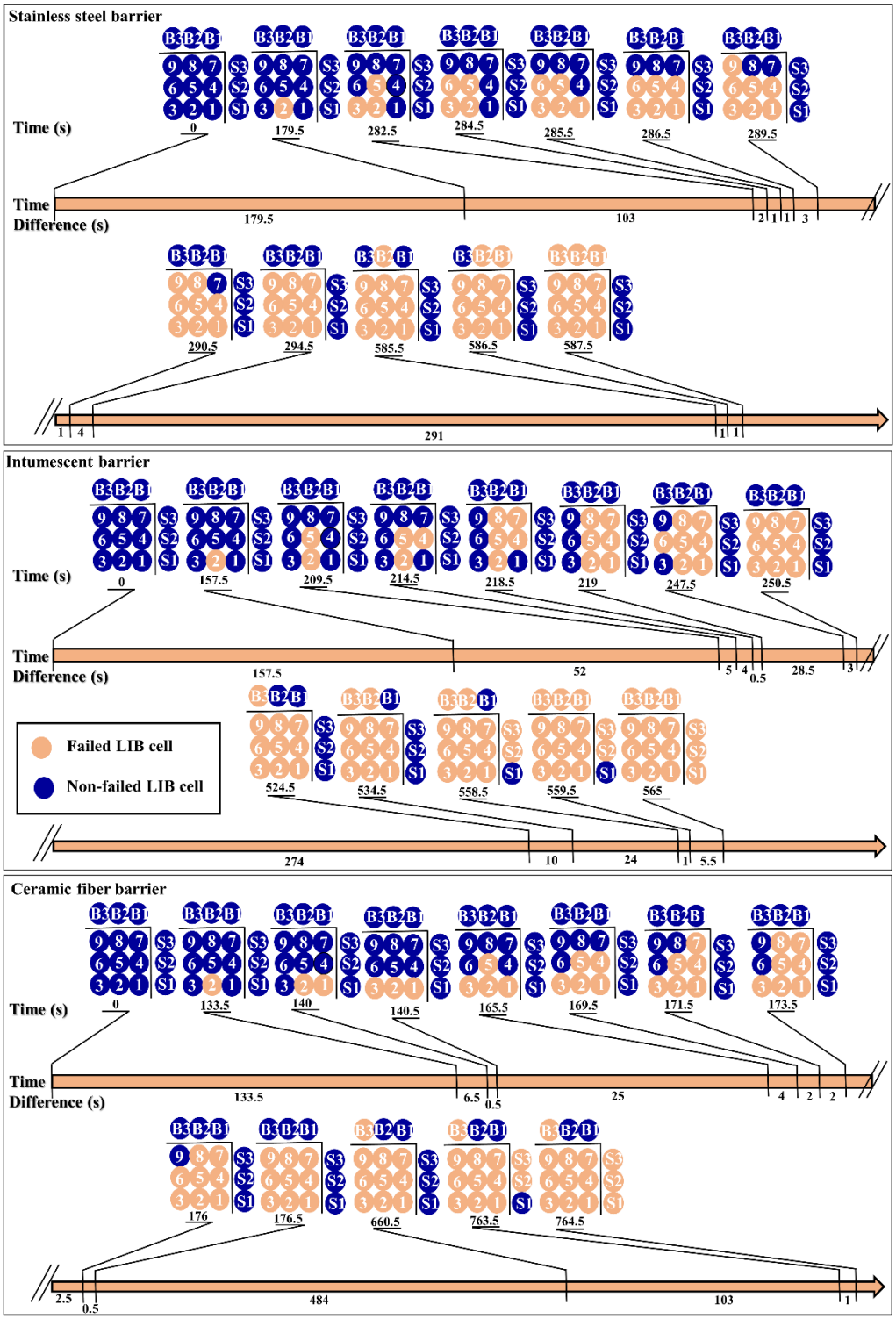

Figure 7. 2. Thermal runaway propagation charts for representative physical barrier tests. Cell 2 was the trigger cell. The dark and light circles represent non-failed and failed cells, respectively. The timeline is not drawn to scale.

Figure 7. 3 shows the average time-resolved temperature histories of row 3 and row 4 for a representative test from each test configuration. Time differences between the average row 3 and row 4 TR onset times are provided as well. As shown in the figure, the physical barriers often increased the row 3 to row 4 propagation durations to over an order of magnitude longer than the no gap tests.

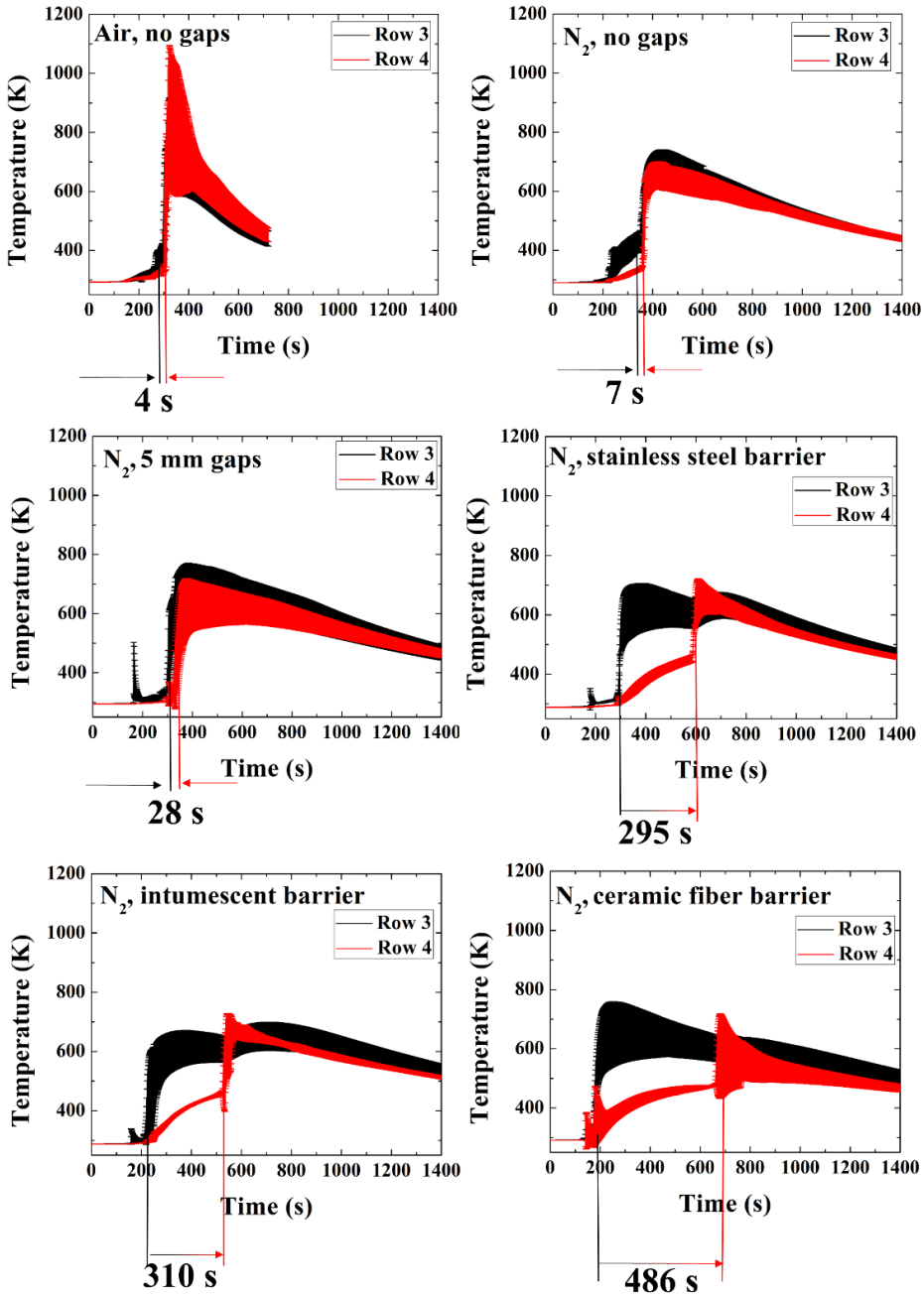

Figure 7. 3. Average row 3 and row 4 temperature versus time data for example tests in all configurations. Time differences between the average row 3 and row 4 TR onset times are also shown. Cells in the separated side column of the tests with gaps were omitted from this analysis to provide a more direct comparison to the tests without any gaps. All error bars were computed from the scatter of the data as two standard deviations of the mean.

To demonstrate the impact of the different mitigation strategies on the dynamics of cascading failure, the time differences were converted into S_P for all tests and averaged for each test configuration. The S_P results are presented in Figure 7. 4. The results show improved mitigation performance of the physical barriers with respect to the no gaps and 5 mm gaps tests. Additionally, among the barriers, ceramic fiber was the most effective, while intumescent was the least effective.

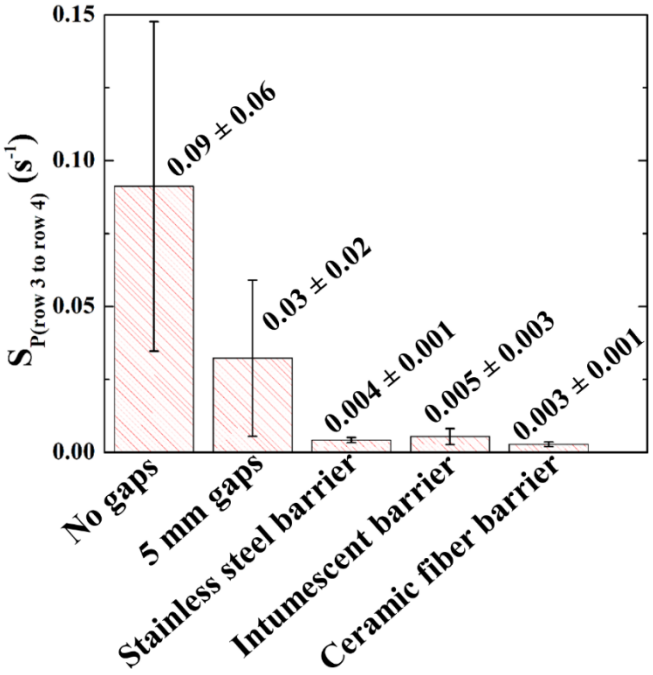

Figure 7. 4. Average row 3 to row 4 thermal runaway propagation speed, $S_{P(row\ 3-\ row\ 4)}$, for each test configuration. All presented data were collected from the experiments in N_2. Cells in the separated side column of the tests with gaps were omitted from this analysis to provide a more direct comparison to the tests without any gaps. All error bars were computed from the scatter of the data as two standard deviations of the mean.

To further quantify the effectiveness of each strategy at mitigating the failure propagation from the 3 by 3 cell group/cluster to the back row cells, a reduction factor

in $S_{P(row\ 3-\ row\ 4)}$ of each strategy was calculated with respect to $S_{P(row\ 3-\ row\ 4)}$ of the no gaps tests conducted in N_2. The reduction factors for all test configurations are computed and compared in Figure 7. 5. The configurations including physical barriers yielded significantly large reduction factors. The reduction factor distinctions between separation panels were not as prominent, but on average the ceramic fiber barrier slowed the TR propagation the most.

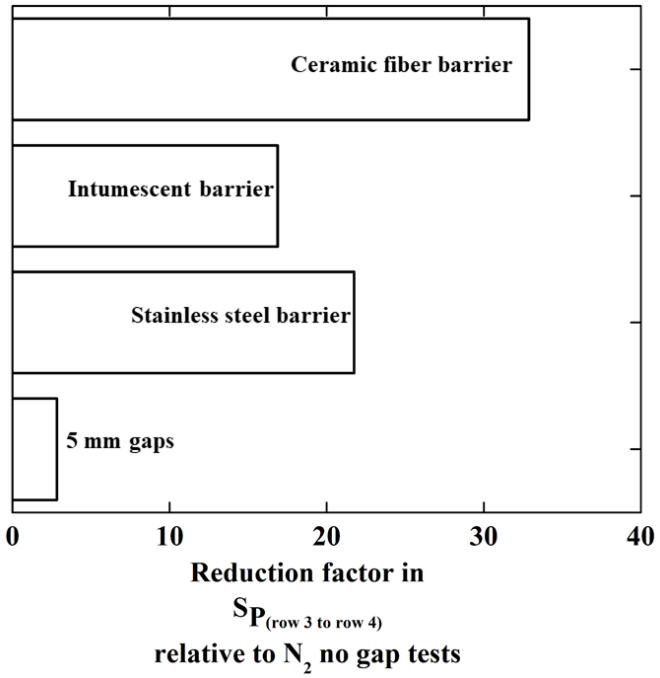

Figure 7. 5. Reduction factor in the average row 3 to row 4 thermal runaway propagation speed, $S_{P(row\ 3-\ row\ 4)}$, for each mitigation strategy. Cells in the separated side column of the tests with gaps were omitted from this analysis to provide a more direct comparison to the tests without any gaps.

7.2 Impact of Mitigation Strategies on Heat Transfer between Cells

In this section, the impact of the mitigation strategies on the heat transfer between cells in row 3 and the back-most row (row4) is examined. The heating rate of each row 4 cell (B1, B2, or B3) in every test was computed by averaging all of the

cell's temperature derivative values (dT_{B1}/dt, dT_{B2}/dt, or dT_{B3}/dt) between the first row 3 TR onset time and the TR onset time of the given cell. The resulting row 4 cell heating rates were further averaged among repeated tests of the same configuration and results are listed in Table 7. 1. The average heating rate was the greatest in air and significantly decreased in N_2. The physical barrier tests showed the slowest heating rate, particularly the ceramic fiber barrier tests.

Table 7. 1. Average row 4 heating rate data for each test configuration. Cells in the separated side column of the tests with gaps were omitted from this analysis to provide a more direct comparison to the tests without any gaps. All uncertainties were computed from the scatter of the data as two standard deviations of the mean.

Test configuration	Heating rate of row 4 [K s^{-1}]
12 cell arrays, 640 l min^{-1} air	8.9 ± 2.9
12 cell arrays, 186 l min^{-1} N_2	4.3 ± 1.4
15 cell arrays, 186 l min^{-1} N_2, 5 mm gap	2.7 ± 0.7
15 cell arrays, 186 l min^{-1} N_2, stainless steel barrier	1.2 ± 0.1
15 cell arrays, 186 l min^{-1} N_2, intumescent barrier	1.6 ± 0.2
15 cell arrays, 186 l min^{-1} N_2, ceramic fiber barrier	1.0 ± 0.2

In a typical cascading failure scenario in an air environment, cells are heated by heat feedback from the developed flames and conduction, convection, and radiation from neighboring cells. The heating rates of the back-most row (row 4) were also analyzed to provide some insight into the contribution percentage of each heat transfer mode to the overall battery pack heat transfer.

The 640 l min^{-1} of air tests included all aforementioned modes of heat transfer, while the tests in 186 l min^{-1} of N_2 without any gaps excluded heat feedback from the flames to the cells. By comparing the heating rates of these two test conditions, it was found that flames contributed 50% of the overall heating of row 4 cells, while the remaining percentage (50%) represented the heat transfer by conduction, convection, and radiation between cells. By instituting 5 mm empty gaps, conductive heat transfer (direct cell-to-cell conduction) from row 3 to row 4 was eliminated. A comparison between heating rates of 640 l min^{-1} air and 5 mm gap tests yielded 30% cumulative convective and radiative heat transfer with 20% remaining for conduction.

7.3 Impact of Mitigation Strategies on Cascading Failure Temperatures

The TR onset and maximum temperatures were determined for each cell in the tested arrays. The onset and maximum temperatures were then separately averaged for the cell group from row 1 to row 3 and for the cell group in row 4. The obtained temperatures for different test configurations are compared in Figure 7. 6.

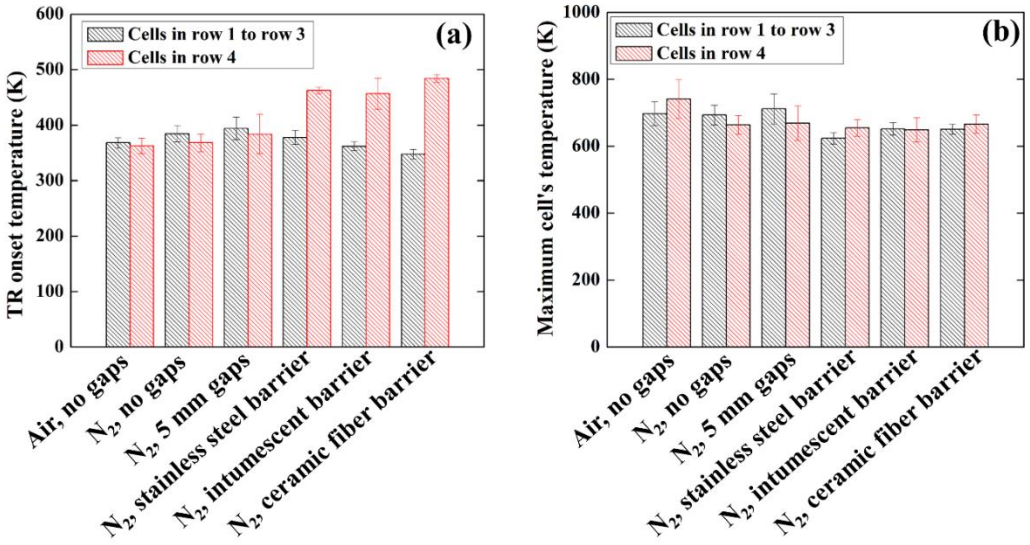

Figure 7. 6. (a) Thermal runaway onset and (b) maximum temperatures for each test configuration. Cells in the separated side column of the tests with gaps were omitted from this analysis to provide a more direct comparison to the tests without any gaps. The cells that just vented small amounts of gases and the non-failed cells were excluded from the statistics reported in this figure. All error bars were computed from the scatter of the data as two standard deviations of the mean.

In Figure 7. 6 (a), the TR onset temperatures for the no gaps and 5 mm empty gaps tests showed negligible dependence on the position of cells within the cell array. With the introduction of physical barriers, the TR onset temperatures for the downstream cells (in row 4) were 80-140 K greater than the onset temperatures for the upstream cells (in row 1 to row 3), which was attributed to the slower rates at which the downstream cells were heated before failure. The relation between the heating rate and onset temperature was further discussed in sections 5.2 and 6.2.

Figure 7. 6 (b) shows that the position of the cell had no considerable impact on the maximum temperature achieved by the cells in all the test configurations. Overall, the maximum cell temperatures achieved in the air tests were greater than the

maximum temperatures in all other test configurations (conducted in N_2) due to the additional heating from the flames during air tests. The N_2 tests with no gaps and 5 mm empty gaps achieved relatively greater maximum temperatures than the physical barrier tests but with larger uncertainties as well.

7.4 Impact of Mitigation Strategies on Mass loss Percentage

Cells were weighed via a mass balance before and after each experiment to determine the mass loss of each cell. The mass loss of each failed cell was utilized to compute the mass loss percentage of the cell with respect to its initial mass. The mass loss percentages were then separately averaged for the cell group in row 1 to row 3 and for the cell group in row 4. Figure 7. 7 provides the mass loss percentage per failed cell for each test configuration. The mass loss percentages showed almost no dependence on the position of the cell in the no gaps and 5 mm empty gaps test configurations, meaning mass loss percentages for cells in row 1 to 3 and cells in row 4 were comparable. In the barrier tests, however, the cells located downstream of the barriers (in row 4) lost greater mass than the upstream cells (in row 1 to row 3). The more uniform and prolonged heating of the cells located in row 4 during the barrier tests enhanced decomposition and chemical reactions inside each cells' enclosures and thus resulted in larger mass losses.

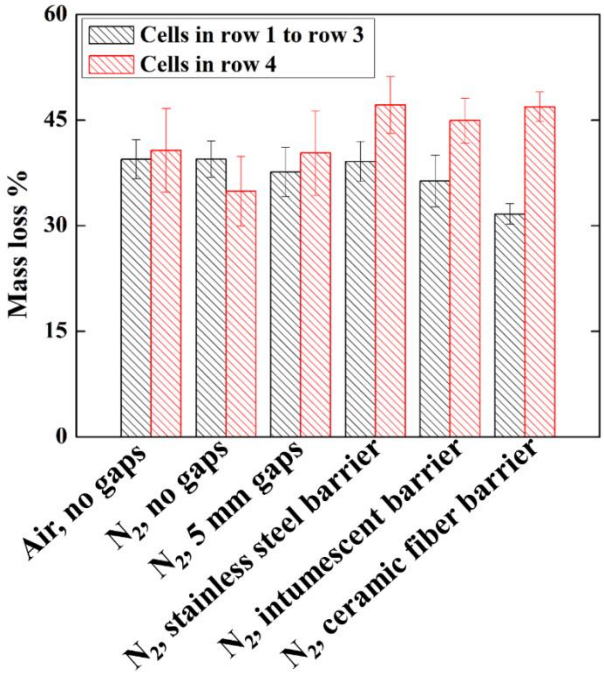

Figure 7. 7. Mass loss percentage with respect to initial cell mass for each test configuration. Cells in the separated side column of the tests with gaps were omitted from this analysis to provide a more direct comparison to the tests without any gaps. The cells that just vented small amounts of gases and the non-failed cells were excluded from the statistics reported in this figure. All error bars were computed from the scatter of the data as two standard deviations of the mean.

7.5 Impact of Mitigation Methods on Gas Productions

Analysis of gaseous product yields was performed only for tests conducted in N_2 to focus on the gases produced in reactions between LIB cell components (rather than in flaming combustion). The volumetric concentration measurements were converted to mass production rates and integrated over each test time to obtain mass yields, as described in detail elsewhere [103]. Figure 7. 8 shows volumetric gas concentration profiles obtained from representative mitigation tests. The results of

other test repetitions for all test configurations are included in Appendix C (Figure C. 22 to Figure C. 25).

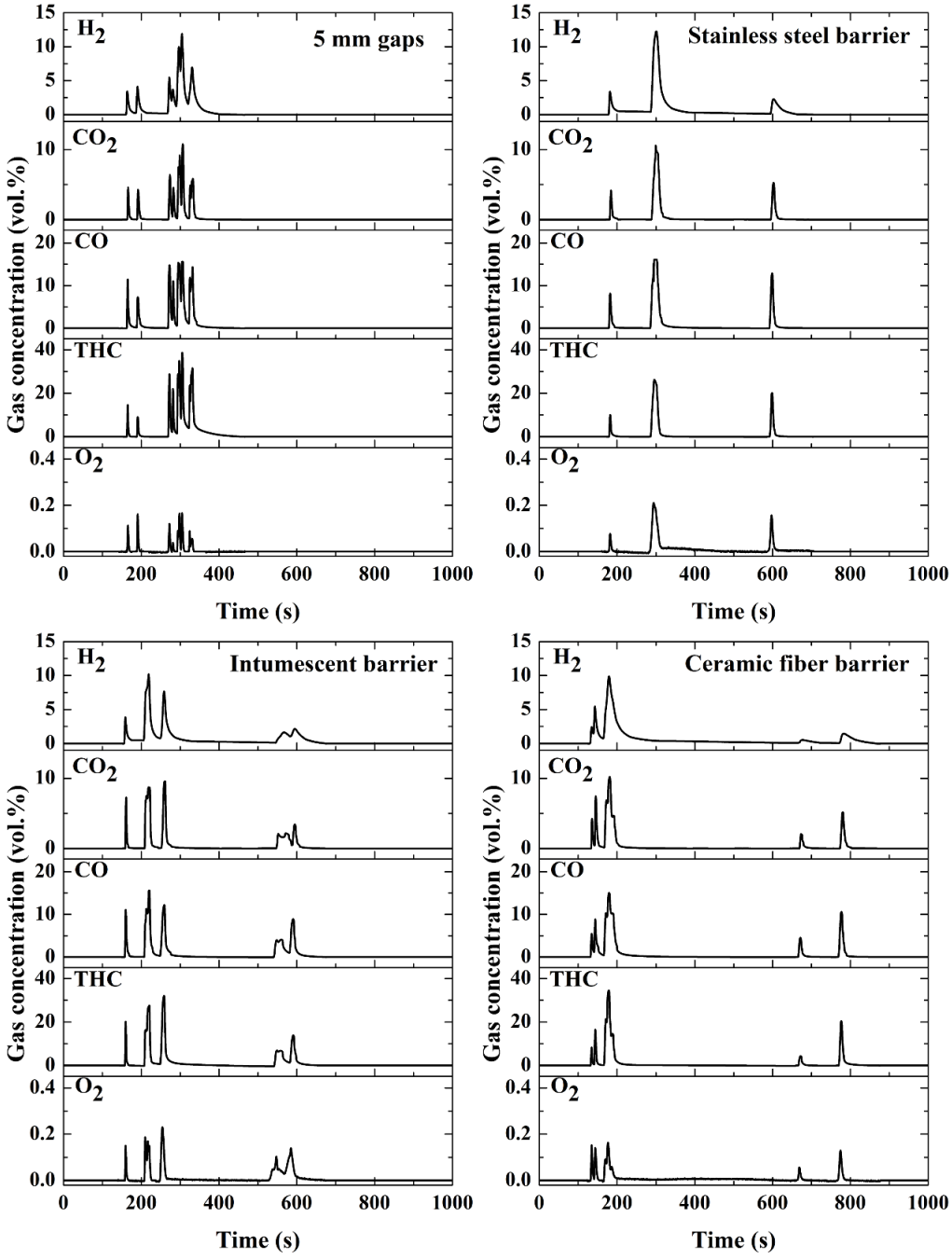

Figure 7. 8. Gas concentration profiles obtained from representative 5 mm gaps and barrier tests conducted in an N_2 environment.

The first peak on each of the gas concentration profiles corresponds to the failure of the trigger cell (cell 2). The following peaks correspond to the TR propagation through the remaining cells. The mass yields presented in Figure 7. 9 were normalized by the number of cells in each array that underwent TR. Overall, these data indicate that, on a mass basis, THC, CO and CO_2 were the dominant products, while H_2 and O_2 were produced in notably smaller but still non-negligible quantities. The test configurations including gaps and/or barriers (all barrier data were lumped together due to their similarity) were found to produce THC, CO and CO_2 and H_2 in notably higher yields than the configuration without gaps. This difference was attributed to a longer duration of the propagation process in the gap and barrier configurations, which caused longer exposure of the tested cell arrays to the elevated temperatures and thus enhanced thermal decomposition of ejected and retained battery materials.

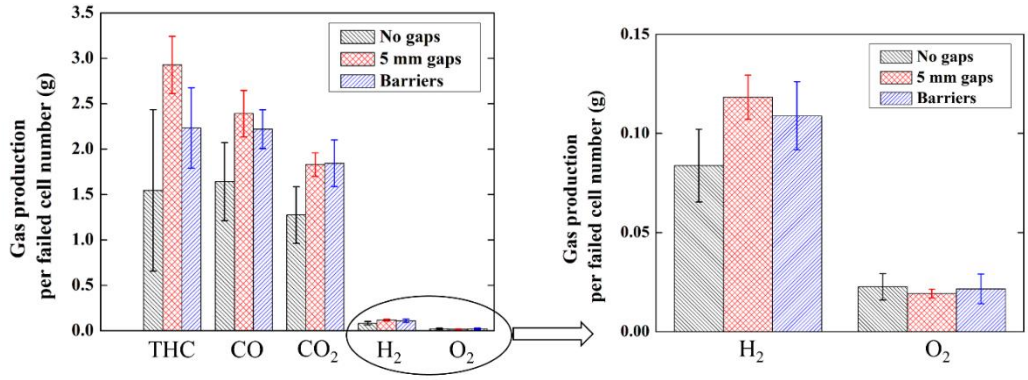

Figure 7. 9. Summary of the gas yield data for all LIB array configurations studied in N_2. All barrier data were combined into a single set due to similarity in values. All error bars were computed from the scatter of the data as two standard deviations of the mean.

7.6 Energetics of Cascading Failure

The rate of chemical heat generation, P_{CHG}, from cell arrays (due to chemical reactions between battery components) were computed for all tests conducted in N_2 to investigate the impact of the presence of gaps or barriers on the total amount of heat production. Figure 7. 10 provides P_{CHG} profiles obtained from representative 5 mm gaps and barrier tests; the profiles for other test repetitions are included in Appendix C (Figure C. 39 to Figure C. 42). The first P_{CHG} peak shown in all profiles corresponds to TR of cell 2 (the trigger cell). The latter spikes are related to TR propagation to the 9 cell groups, back rows (row 4), and side columns.

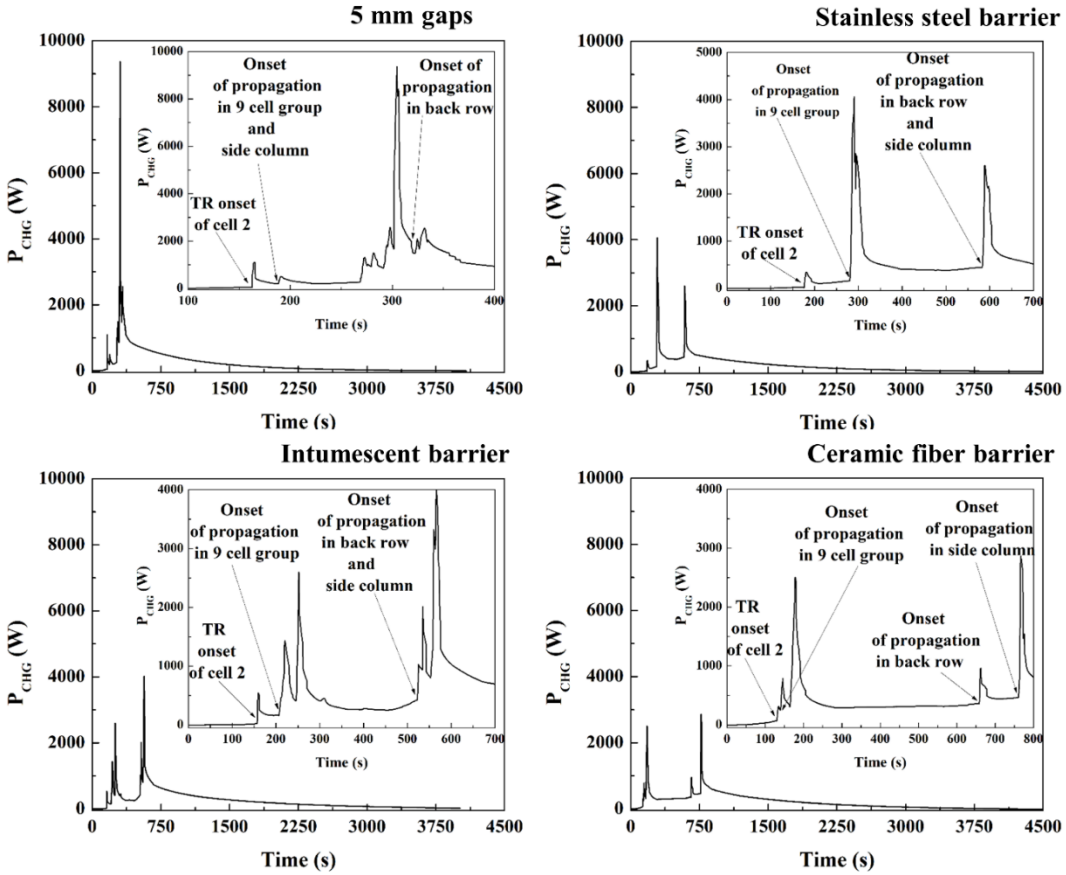

Figure 7. 10. Rates of chemical heat generation obtained from representative 5 mm gaps and barrier tests conducted in an N_2 environment.

All P_{CHG} profiles were numerically integrated to compute the total chemical heat generation (E_{CHG}). Table 7. 2 presents the E_{CHG} data with four different normalizations: per cell, per initial cell mass, per nominal electrical capacity, and per stored electrical energy. On a per failed cell basis, the figure shows that the heat generated in the 5 mm gap and barrier tests (61.4 ± 2.8 kJ, on average) were slightly higher than in the tests without gaps (54.9 ± 1.8 kJ). The observed difference, however, was not sufficiently great to claim that any of the mitigation strategies had a considerable influence on the failure energetics.

Table 7. 2. Average chemical heat generation data from each nitrogen atmosphere test configuration. Data is presented normalized per cell, per initial cell mass, per nominal electrical capacity, and per stored electrical energy.

Test configuration	E_{CHG}			
	Normalized per initial cell mass [kJ g^{-1}]	Normalized per cell number [kJ]	Normalized per electrical capacity [kJ A^{-1} h^{-1}]	Normalized per electrical stored energy [-]
No gaps	1.26 ± 0.04	54.9 ± 1.8	21.1 ± 0.7	1.70 ± 0.05
5 mm gaps	1.40 ± 0.10	61.1 ± 4.2	23.5 ± 1.6	1.85 ± 0.13
Stainless steel barrier	1.36 ± 0.27	59.3 ± 11.7	22.8 ± 4.5	1.80 ± 0.35
Intumescent barrier	1.44 ± 0.06	62.7 ± 2.8	24.1 ± 1.1	1.90 ± 0.09
Ceramic fiber barrier	1.44 ± 0.07	62.9 ± 3.0	24.2 ± 1.2	1.90 ± 0.09

7.7 Summary

Chapter 7 discusses the results associated with implementing different passive mitigation strategies to prevent or lessen TR propagation through LCO cell arrays. The strategies examined include introduction of 5 mm gaps between wall-to-wall groups/clusters of cells and addition of double layer perforated stainless steel plates,

intumescent solid or ceramic fiber board into these gaps. TR was initiated into one cluster using an electric heater and propagation was tracked using cell bottom temperature histories.

None of the implemented techniques were able to completely prevent TR propagation between spaced cell groups. However, some of these strategies were able slow down TR propagation to different extents. While empty gaps were found to be the least effective strategy, the configurations including physical barriers showed considerable reductions (more than a factor of 17) in the propagation speed between different cell groups. These reductions in speed provide additional time for detection and suppression of battery pack fires.

Among the physical barriers, the ceramic fiber board supported by a stainless steel plate was able to slow propagation the most. The main drawback of this type of barrier is that it may interfere with active suppression thermal management of the battery pack. The perforated stainless steel barrier showed the second best performance in terms of the mitigation effectiveness. This stainless steel barrier is not expected to interfere with the battery thermal management but is heavier than the ceramic fiber and intumescent barriers. The intumescent material supported by a stainless steel plate was the least effective among all barrier assemblies.

The collected cell temperatures were utilized to calculate the cell heating rates. The heating rates were subsequently analyzed to determine the contributions of individual processes to heat transfer driving cascading failure in air experiments on LIB arrays without gaps – the most energetic failure scenario examined in the current study. The analysis indicated that flaming combustion of ejected battery materials contributed

50% to the heating of downstream cells, direct cell-to-cell conduction contributed 20%, and the rest was associated with convective and radiative heat transfer between cells. It is important to note that this breakdown is specific to the studied LIB cell form factor, chemistry and array geometry and may not be generalized to all LIB module designs.

Additional analyses were conducted, including determining cell TR onset temperatures, cell mass loss, gas yields of different species ejected from the cells, and chemical heat generation for all mitigation configurations. The average row 4 cell TR onset temperatures appeared to be proportional with the heating rates. In the physical barrier tests, the average row 4 cell TR onset temperatures were approximately 100-150 K greater than the average row 1-3 cell TR onset temperatures. In the barrier tests, the row 4 cells lost greater mass than cells in rows 1-3. The uniform prolonged heating of the cells located in row 4 during the barrier tests enhanced decomposition and chemical reactions inside each cell's enclosure and thus resulted in larger mass loss. Across all test configurations, THC, CO, and CO_2 were the predominant measured gas species produced through cell decomposition, and smaller mass yields of H_2 and O_2 were measured as well. Both barriers and gaps were found to increase the production of THC, CO, CO_2, and H_2 by the cells undergoing TR. None of the tested mitigation strategies significantly impacted the chemical heat generation associated with the cell decomposition; all configurations produced approximately 61 kJ per failed cell on average.

8. Results and Discussion: Novec1230 Suppression Investigation

In this chapter, the results of the tests using the Novec1230 agent to extinguish the flames accompanying cascading failure in cell arrays are presented. Due to its high molecular heat capacity relative to air or N_2, the Novec1230 agent is an excellent coolant that may additionally help to dissipate the heat generated during early failures in cell arrays, potentially slowing down or preventing any subsequent failure propagation.

All Novec1230 experiments were conducted on LCO cell arrays of similar size and SOC to those LCO arrays tested in chapter 6 (12 cells with no gaps and 100% SOC). Herein, the Novec1230 experiments were initially started in an air environment. 59.2 ± 1.1 l min^{-1} of gaseous Novec1230 agent was generated using the Novec1230 handling system and then introduced to the wind tunnel immediately after TR of the trigger cell occurred. In 640 and 320 l min^{-1} air experiments, the Novcec1230 gas was utilized at concentrations of 8.5 vol.% and 15.2 vol.%, respectively. More details on the experimental procedures and test matrix are communicated in section 3.5.4.

The results presented in this chapter demonstrate the impact of Novec1230 suppressing agent on different key quantities such as the dynamics, temperatures, cell mass loss, and flaming combustion energy of cascading failure. The results of the 640 l min^{-1} air, 320 l min^{-1} air, and 186 l min^{-1} N_2 tests are utilized as baseline points in this chapter for comparison and evaluation of the performance of Novec1230.

8.1 Cascading Failure Dynamics of Baseline Tests

This section provides a direct comparison between the failure dynamics of the reference point tests (640 l min^{-1} of air, 320 l min^{-1} of air, and 186 l min^{-1} of N_2).

Complete TR propagation was not prevented in any cell array tested in the three test conditions. Figure 8. 1 displays TR propagation charts for a representative test of each baseline test condition. The propagation charts for the other test repetitions are included in Appendix C (Figure C. 3 to Figure C. 5). The propagation charts obtained from all baseline tests exhibited similar behavior. Detailed discussions on these behaviors were mentioned in section 6.1.

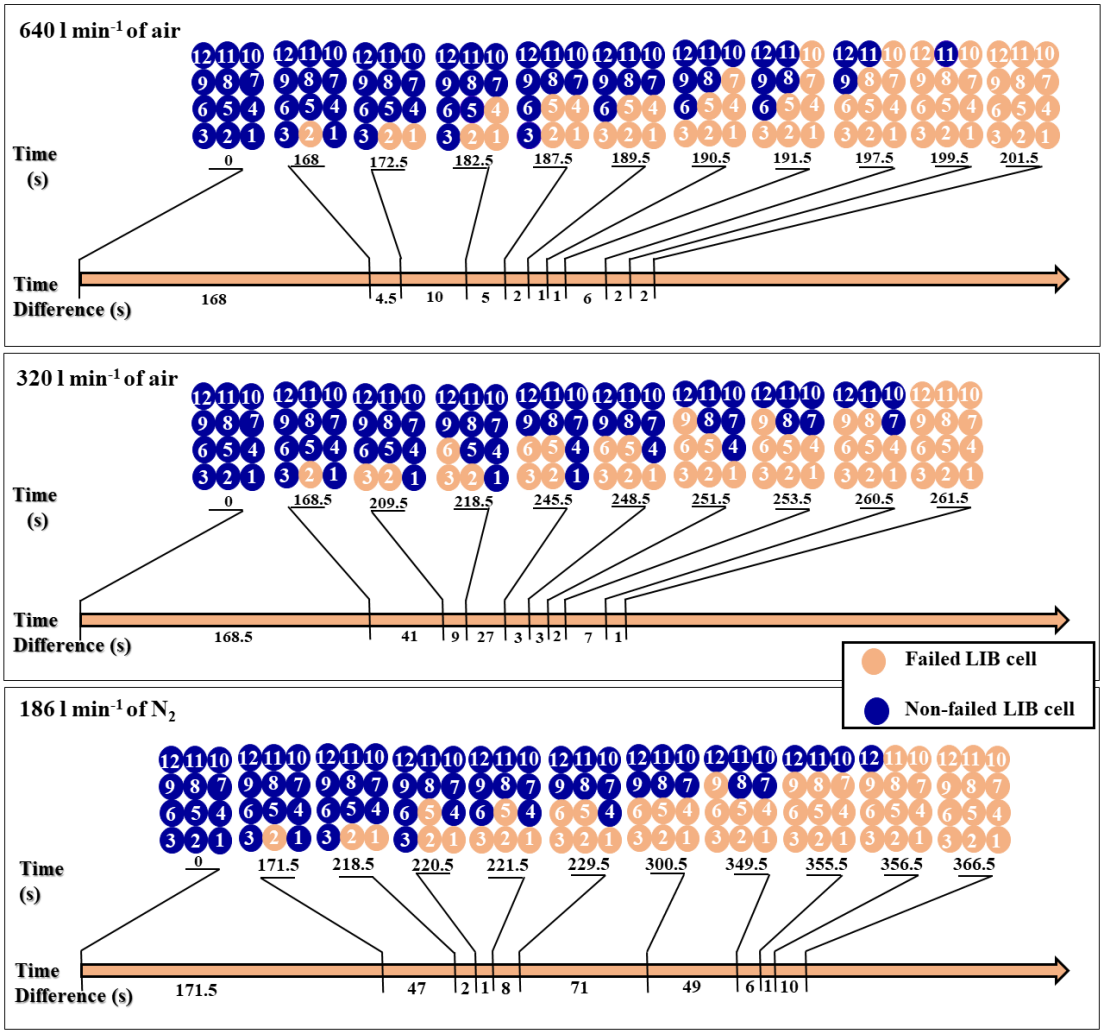

Figure 8. 1. Thermal runaway propagation charts for representative baseline tests. Cell 2 was the trigger cell. The dark and light circles represent non-failed and failed cells, respectively. The timeline is not drawn to scale.

The S_P data were calculated on a row-to-row basis, and the obtained results are plotted in Figure 8. 2. All three test conditions achieved similar TR propagation speeds during the propagation from row 1 to row 2 due to the absence of flaming combustion. While the propagation speed in nitrogen remained relatively constant throughout the entire cell array, the propagation speeds in air appeared to accelerate as TR propagated throughout the array. This acceleration was much more pronounced at 640 l min^{-1} air flow rate than at 320 l min^{-1}, likely due to enhanced combustion with greater amounts of oxidizer.

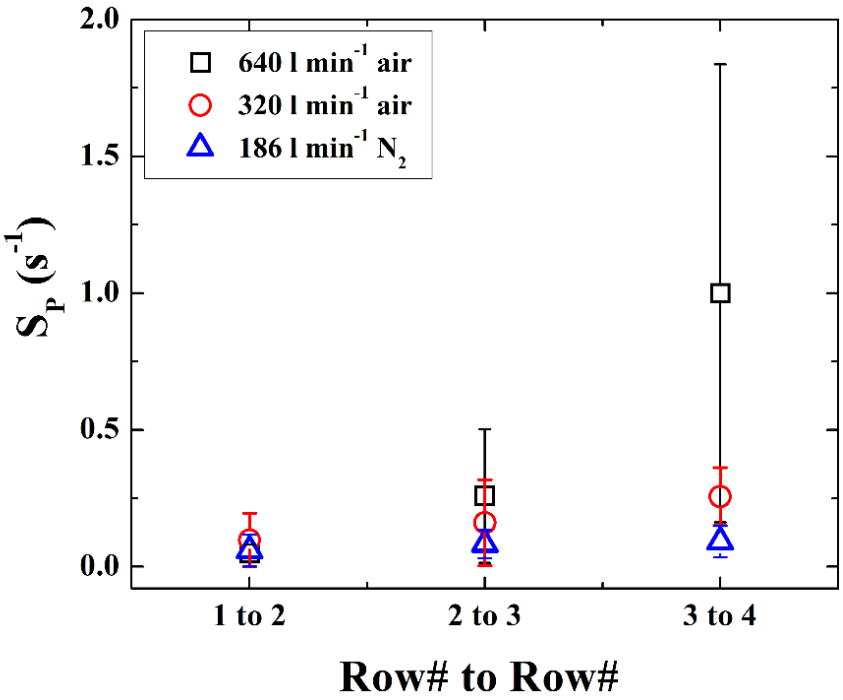

Figure 8. 2. Thermal runaway propagation speeds computed for baseline tests. The error bars for this plot were calculated from the scatter of the data as two standard deviations of the mean.

8.2 Impact of Novec1230 on Dynamics of Cascading Failure

In all four cascading failure experiments where Novec1230 was used at 8.5 vol.% concentration, TR propagated through all cells in the examined array, which

resulted in a complete cascading failure. Six cascading failure tests conducted with Novec1230 at 15.2 vol.% concentration. In four tests, TR either did not propagate from the trigger cell (cell 2) to any cell or did propagate to only one cell of the three cells that were in direct contact to the trigger cell causing a partial or incomplete cascading failure. On average, ten cells out of twelve cells did not fail in the 15.2 vol.% Novec1230 experiments. In the other two tests, the cell arrays experienced a complete cascading failure.

TR propagation charts for representative Novec1230 tests are shown in Figure 8. 3; the propagation charts for all other test repetitions are included in Appendix C (Figure C. 14 and Figure C. 15). In these figures, the dark and light circles represent the non-failed and failed cells, respectively. Also, the dark and light arcs adjacent to cell 2 (trigger cell) correspond to enabled and disabled heaters, respectively. As mentioned in section 3.5.4, the experiments began with heating the liquid Novec1230 using the surface heater employed in the Novec1230 handling system and the vaporized Novec1230 is directed to the exhaust hood. The heater adjacent to cell 2 was not enabled until the evaporation rate of Novec1230 reached steady state conditions. Similarly to the baseline data, the TR propagation from one cell to another was not always repeatable, while the row-to-row TR advancement displayed more reproducibility to a reasonable degree.

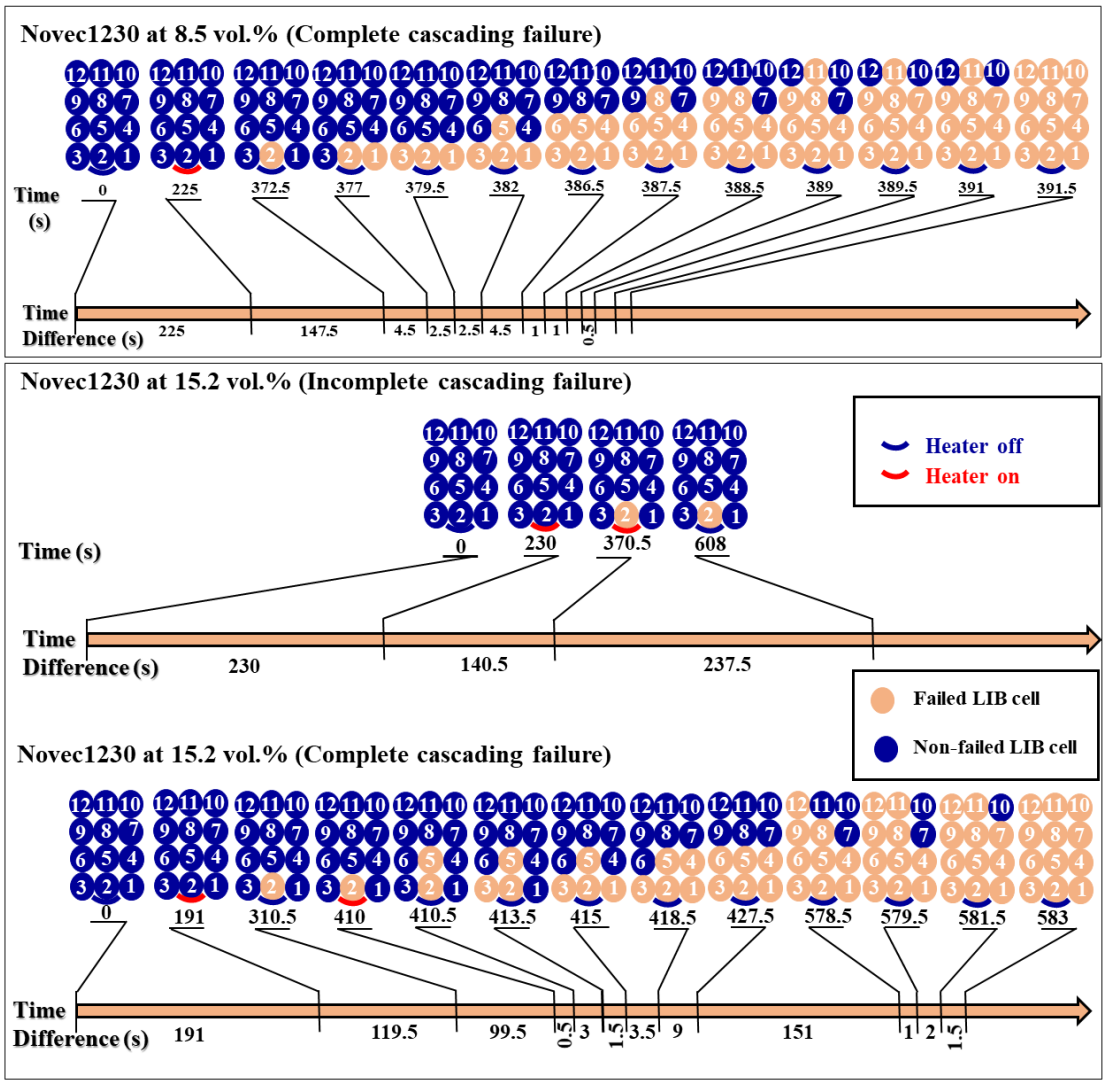

Figure 8. 3. Thermal runaway propagation charts for representative Novec1230 tests. Cell 2 was the trigger cell. The dark and light circles represent non-failed and failed cells, respectively. The dark and light arcs adjacent to cell 2 (trigger cell) correspond to disabled and enabled heaters, respectively. The timeline is not drawn to scale.

The TR onset times were utilized to compute S_P for all baseline and Novec1230 tests in units of s^{-1}. The propagation speed can also be introduced as S_P^* in standard units of mm s^{-1}, respectively. S_P^* data were obtained by multiplying S_P by the cells' original diameter (18 mm). The results of propagation speeds are compared in Figure

8. 4. For the tests where propagation between particular rows did not occur, the S_P value of zero was entered into the calculation of the average.

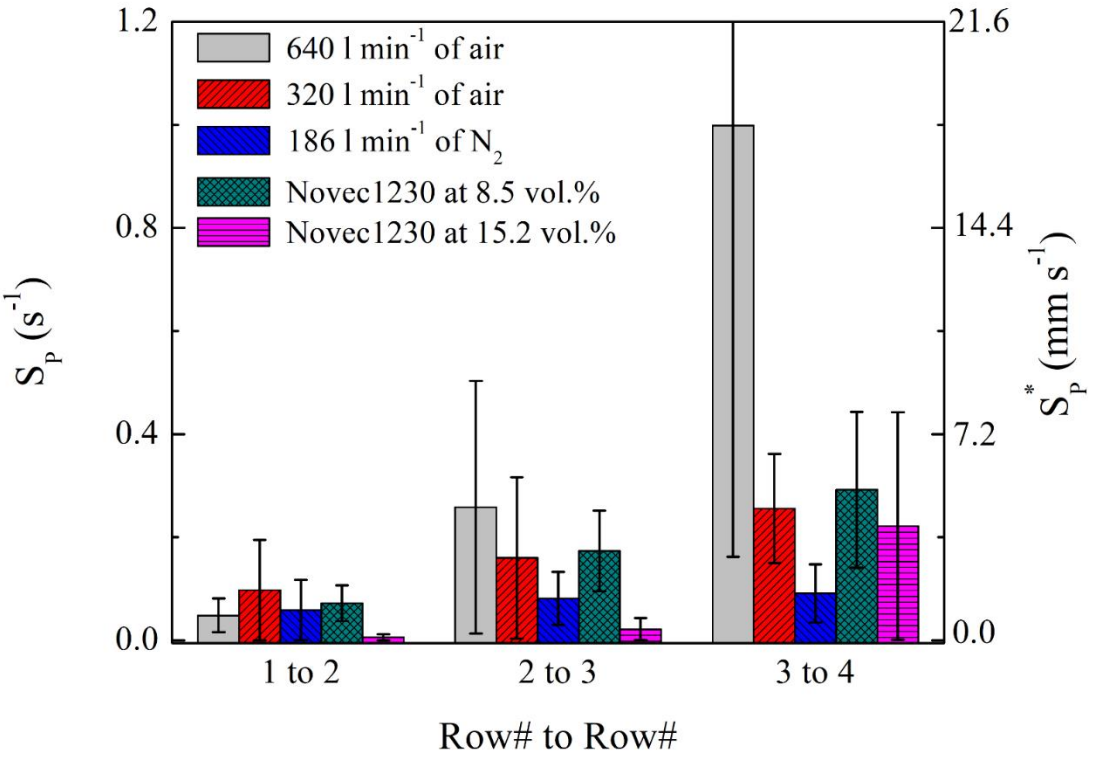

Figure 8. 4. Thermal runaway propagation speeds computed for baseline and Novec1230 tests. The error bars for this plot were calculated from the scatter of the data as two standard deviations of the mean.

Overall, the S_P data show a relatively steady propagation through the array in N_2 and a monotonic increase in the air or Novec1230 tests. This increase is associated with the additional heating of cells by the flames. The 640 l min^{-1} air tests yielded the greatest speeds among all tests. Compared to the 640 air l min^{-1} tests, testing the cell arrays in 320 l min^{-1} of air and using Novec1230 at 8.5 vol.% reduced the TR propagation speeds by 56% and 52%, respectively, during the late failure stages (row 2 to row 3 and row 3 to row 4). The N_2 and 15.2 vol.% Novec1230 tests yielded the greatest reductions in speeds during later failure stages: 80% and 85%, respectively,

but additionally using Novec1230 at such concentration stopped TR propagation in 67% of the tests. Additionally, the results showed that using Novec1230 at 15.2% reduced the speeds of propagation by 50% compared to speeds of the 320 l min^{-1} air tests during later failure stages.

8.3 Impact of Testing Conditions on Heating Rates and Temperatures of Cascading Failure

The heating rate of each cell was computed by taking the average of heating rate values corresponding to 20 s before this cell underwent TR. The computed heating rates of all cells were then averaged for each test condition. Additionally, the TR onset temperatures were also determined for each test condition. The cell heating rates and the TR onset temperatures for all test conditions are plotted in Figure 8. 5. It is important to mention that the data of the non-failed cells were excluded from these calculations.

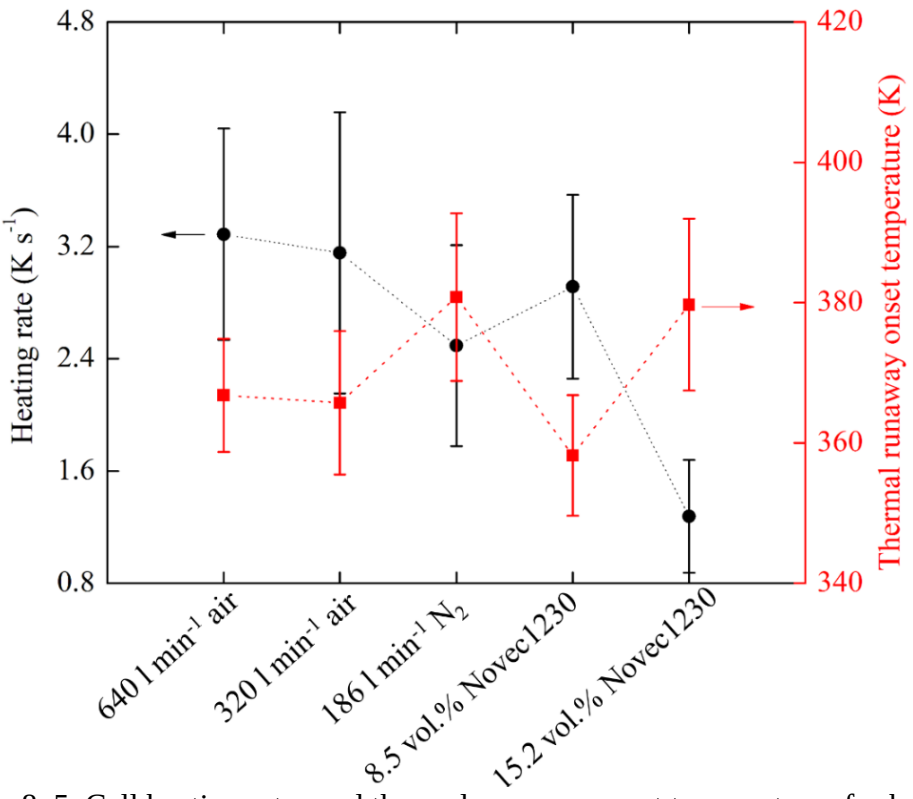

Figure 8. 5. Cell heating rates and thermal runaway onset temperatures for baseline and Novec1230 tests. All temperatures obtained in this figure were measured at the bottom surface of cells. The error bars were computed from the scatter of the data as two standard deviations of the mean.

The figure shows that the 640 and 320 l min^{-1} air tests achieved the largest cell heating rates likely due to large amounts of heat added to the cells by the flames. The average heating rate of the cells tested in N_2 was ≈ 30% less than the heating rate achieved in the air tests due to the absence of flames. Using Novec1230 at 8.5 vol.% showed a minimal decrease in the heating rate compared to the air tests. The slowest heating rate was obtained in the 15.2 vol.% Novec1230 tests. This high concentration of the Novec1230 agent suppressed the flames and cooled down the body of the cells during failure, which caused discernible reductions in the heating rates of cells.

The TR onset temperatures of the 640 l min^{-1} air, 320 l min^{-1} air, and 8.5 vol.% Novec1230 tests were almost comparable (within each other's uncertainty). The 186 l min^{-1} N_2 and 15.2 vol.% Novec1230 tests had the greatest TR onset temperatures due to their slower heating rates. The observed relation between the cell heating rate and onset temperature is consistent with similar observation discussed in section 7.3.

Figure 8. 6. shows the maximum cell temperature for different test conditions. The maximum temperature data obtained for the non-failed cells were excluded from the presented statistics. The 640 l min^{-1} air, 320 l min^{-1} air, and 8.5 vol.% Novec1230 tests yielded comparable maximum temperatures; these test conditions resulted in greater maximum temperatures compared to N_2 tests due to the impact of flaming combustion. The maximum temperatures achieved in the 15.2 vol.% Novec1230 tests were ≈ 100 K less than the maximum temperatures for air tests due to high convective cooling impact of Novec1230 at this concentration.

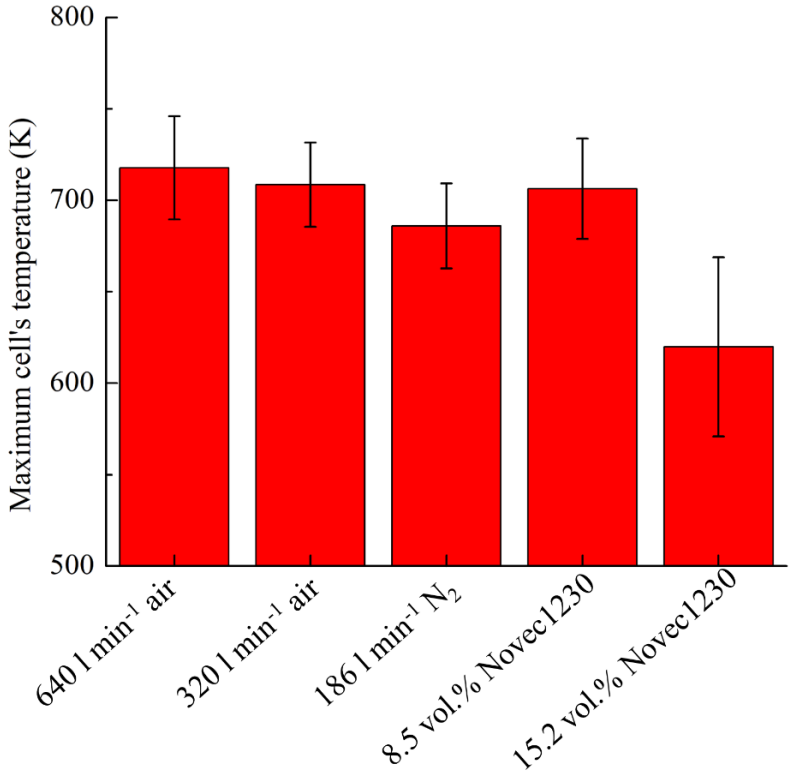

Figure 8. 6. Maximum cell temperature for baseline and Novec1230 tests. All temperatures obtained in this figure were measured at the bottom surface of cells. The error bars were computed from the scatter of the data as two standard deviations of the mean.

8.4 Impact of Testing Conditions on Ruptured Cells and Mass loss

The position of a cell within an array did not appear to influence its probability of rupture. The number of ruptured cells was utilized to calculate the percentage of ruptured cells with respect to the total number of cells in 12 cell arrays; the obtained results are compared for different test conditions in Figure 8. 7. The lower cell rupture probabilities in the N_2 and 15.2 vol.% Novec1230 tests are associated with slower heating rates.

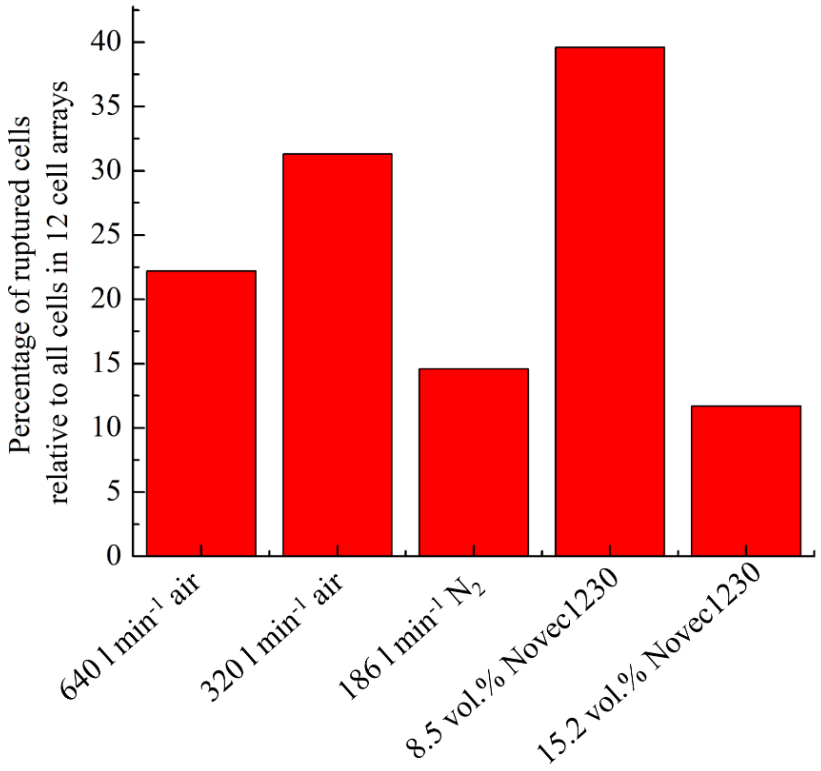

Figure 8. 7. Percentages of ruptured cells for baseline and Novec1230 tests.

The total mass loss was fairly constant for each cell within a particular test, meaning the cells' positions had a negligible impact on mass loss. Therefore, the average values of mass loss and mass loss percentage per failed cell were computed for all cells in each test condition and reported in Table 8. 1. The mass data of non-failed cells were excluded from the presented statistics. The mass loss data also showed no dependence on the test condition.

Table 8. 1. Summary of initial cell mass, cell mass loss, and mass loss percentage for baseline and Novec1230 tests. The mass data obtained for the non-failed cells were excluded from the presented statistics. The uncertainties were computed from the scatter of the data as two standard deviations of the mean.

Test condition	Initial Mass per cell [g]	Mass loss per failed cell [g]
640 l min^{-1} Air	43.60 ± 0.06	17.3 ± 1.3 (39.8 ± 2.5%)
320 l min^{-1} Air	43.50 ± 0.05	17.2 ± 1.4 (39.5 ± 3.2%)
186 l min^{-1} N_2	43.50 ± 0.06	16.7 ± 1.0 (38.4 ± 2.3%)
Novec1230 at 8.5 vol.%	43.50 ± 0.06	16.1 ± 1.3 (37.0 ± 3.0%)
Novec1230 at 15.2 vol.%	43.50 ± 0.04	16.5 ± 2.2 (38.0 ± 5.1%)

8.5 Suppression Effects of Novec1230

8.5.1 Flaming Combustion Heat Release

The rate of energy production due to flaming combustion was calculated for the baseline and Novec1230 tests. Figure 8. 8 shows $P_{Flaming}$ profiles obtained from representative baseline and Novec1230 tests. The presented examples for the 15.2 vol.% Novec1230 tests include tests with incomplete and complete cascading failure. The $P_{Flaming}$ profiles for all other test repetitions are included in Appendix C (Figure C. 43, Figure C. 44, Figure C. 46, and Figure C. 47).

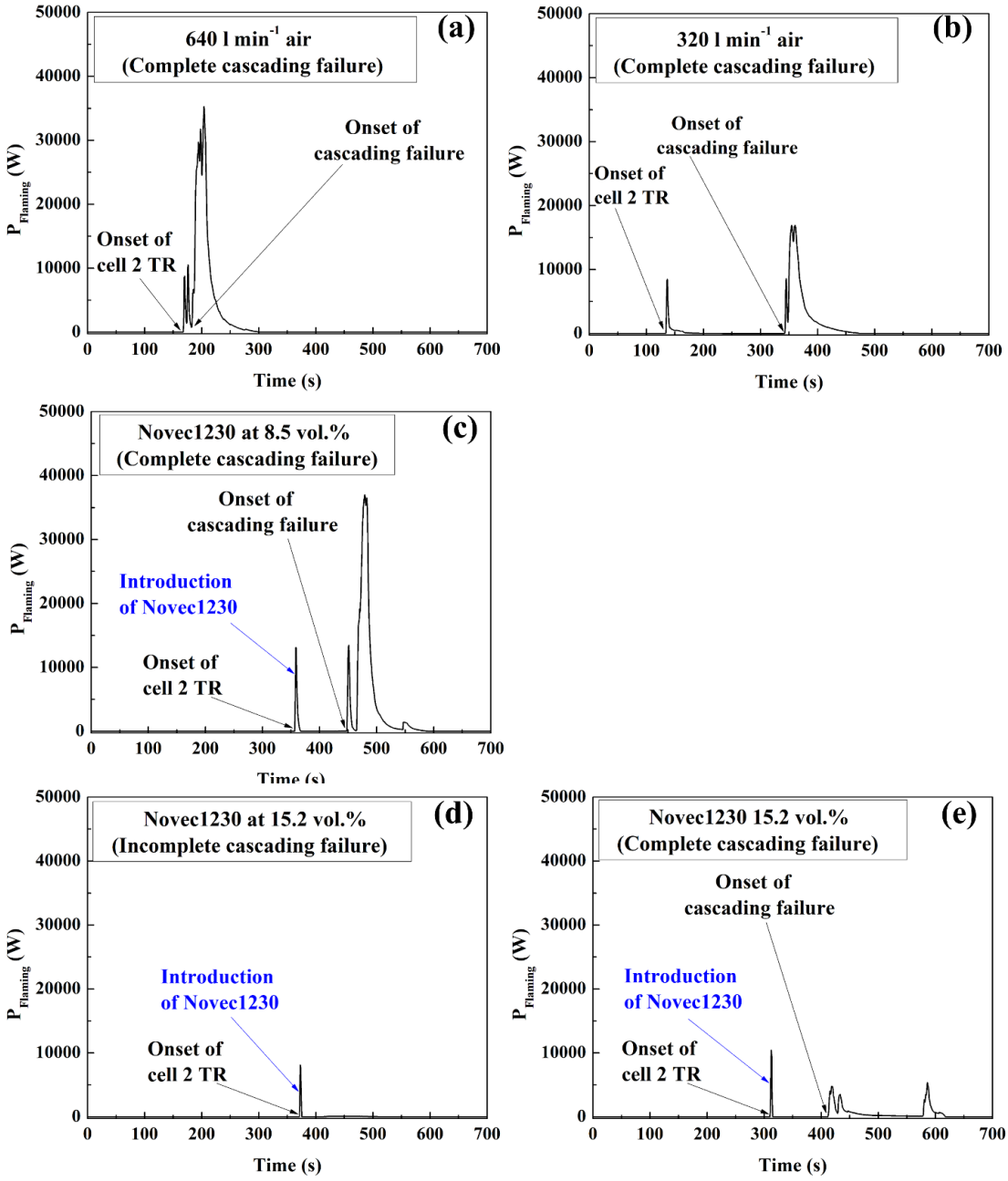

Figure 8. 8. Heat release rate due to flaming combustion of ejected battery materials obtained for representative (a) 640 lmin^{-1} air, (b) 320 l min^{-1} air, (c) 8.5 vol.% Novec1230, (d) non-propagated 15.2 vol.% Novec1230, and (e) propagated 15.2 vol.% Novec1230 tests.

In all presented profiles, the earliest peak is associated with energy production due to combustion of gases and aerosols ejected from the trigger cell. When a complete

cascading failure was achieved, this peak was followed by multiple peaks corresponding to combustion of the gases ejected from the other cells during failure propagation. Figure 8. 8 (a-b) show that the $P_{Flaming}$ maxima obtained in the 640 l min^{-1} air and 8.5 vol.% Novec1230 tests are similar in magnitude (≈ 35 kW), but both were found to be two times greater than those measured in the 320 l min^{-1} air tests. In all 15.2 vol.% Novec1230 tests, the $P_{Flaming}$ maxima did not exceed ≈ 10 kW.

All obtained $P_{Flaming}$ profiles were integrated in time to compute the effective heat of flaming combustion ($E_{Flaming}$). The resulting integral values were normalized by the number of failed cells or total mass loss of all cells and are compared in Figure 8. 9. A reduction in $E_{Flaming}$ was achieved when cell arrays were tested in an air flow rate of 320 l min^{-1} rather than 640 l min^{-1} likely due to less oxygen available for combustion. The 640 l min^{-1} and 8.5 vol.% Novec1230 tests essentially yielded the same $E_{Flaming}$ results, which indicates that the Novec1230 at this concentration was completely ineffective. The 15.2 vol.% Novec1230 tests achieved the lowest $E_{Flaming}$, which indicates efficient suppression of flaming combustion achieved in these tests.

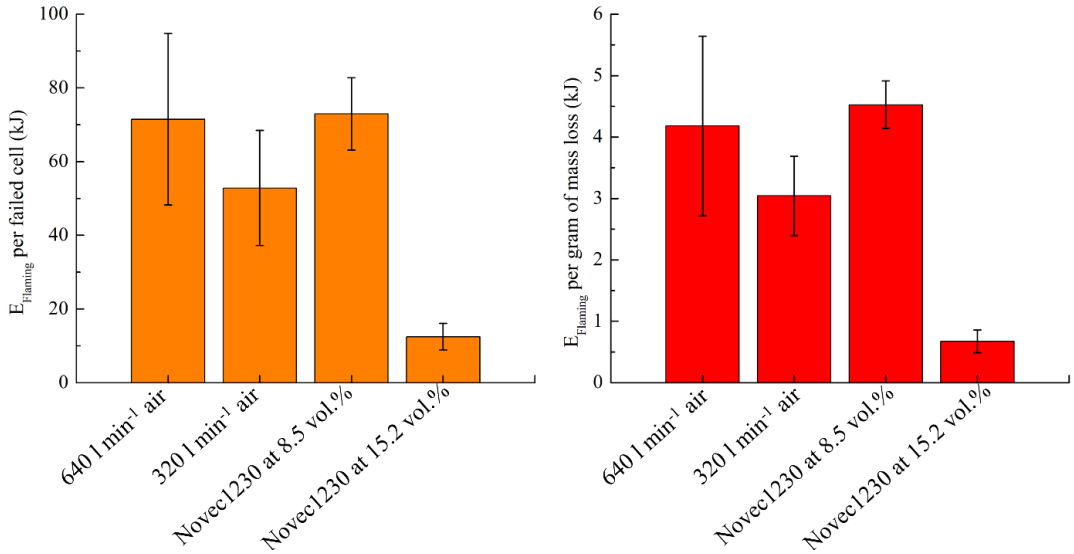

Figure 8. 9. Heats released in flaming combustion normalized per failed cell or per gram of mass loss for baseline and Novec1230 tests.

8.5.2 Combustion Efficiency

Figure 8. 10 displays gas concentration profiles obtained for the same representative experiments that were utilized to compute $P_{Flaming}$ in Figure 8. 8; the gas profiles of all other test repetitions are included in Appendix C (Figure C. 26, Figure C. 27, Figure C. 31, and Figure C. 32). The main feature of all gas profiles is the significant production of CO and THC during failure propagation accompanied by almost complete consumption of available oxygen (concentrations below 1 vol.%). The exception is that the oxygen consumption during the 15.2 vol.% Novec1230 tests was much smaller than the case in the other test conditions. Also, the observed decrease in the oxygen baseline is associated with the dilution impact of Novec1230 on the concentration of oxygen. This baseline shift is restored when the Novec1230 flowing into the tunnel was stopped.

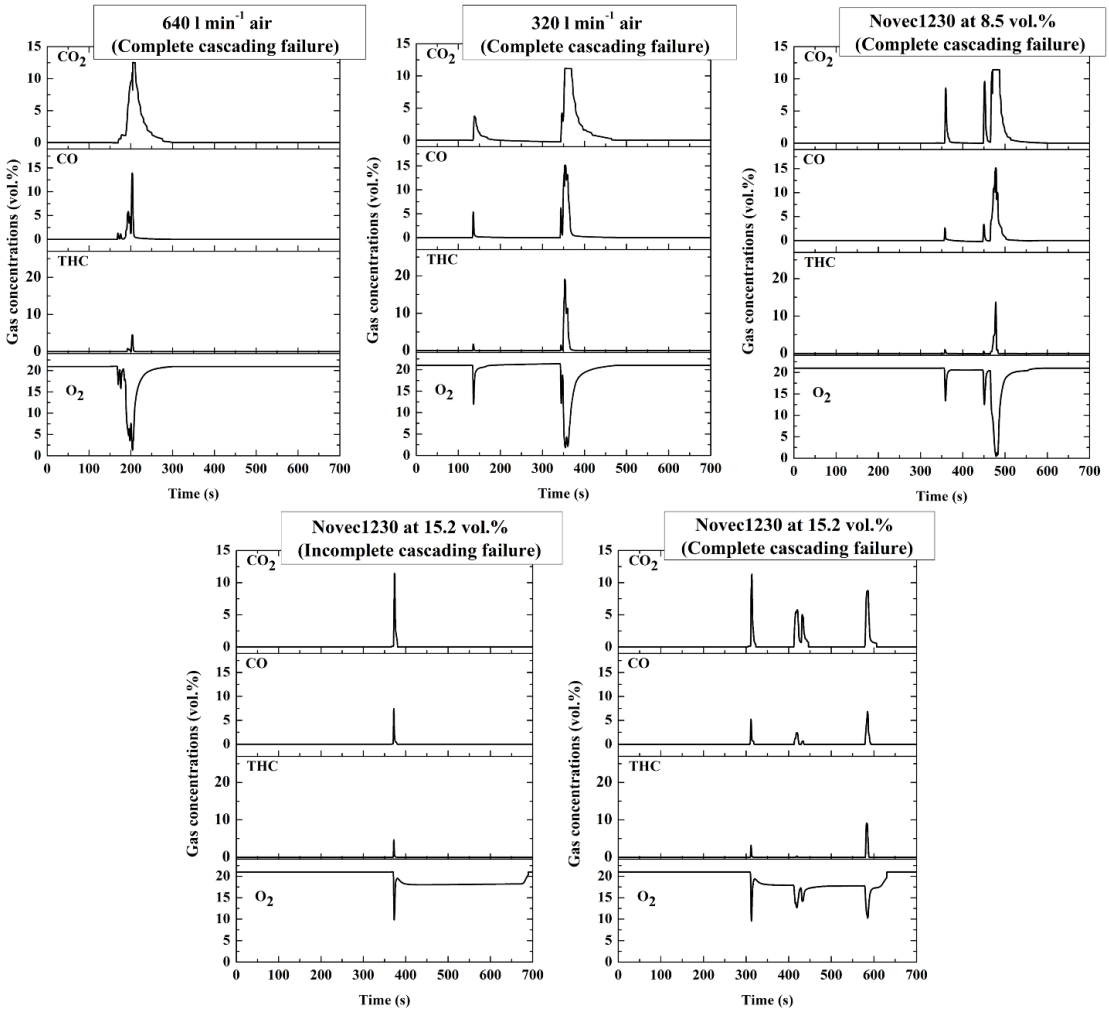

Figure 8. 10. Gas concentration profiles obtained from representative 640 l min^{-1} air, 320 l min^{-1}, 8.5 vol.% Novec1230, and 15.2 vol.% Novec1230 experiments.

Cascading failure was accompanied by combustion of ejected battery materials inside the tunnel. However, as identified from the gas measurements, most of the oxygen available inside the tunnel was consumed before all ejected materials combusted to completion. Figure 8. 11 shows that the combustion products re-ignited (or continually combusted) again when left the wind tunnel, where the oxygen gas becomes available in the atmosphere, in all tests but the 15.2 vol.% Novec1230 tests.

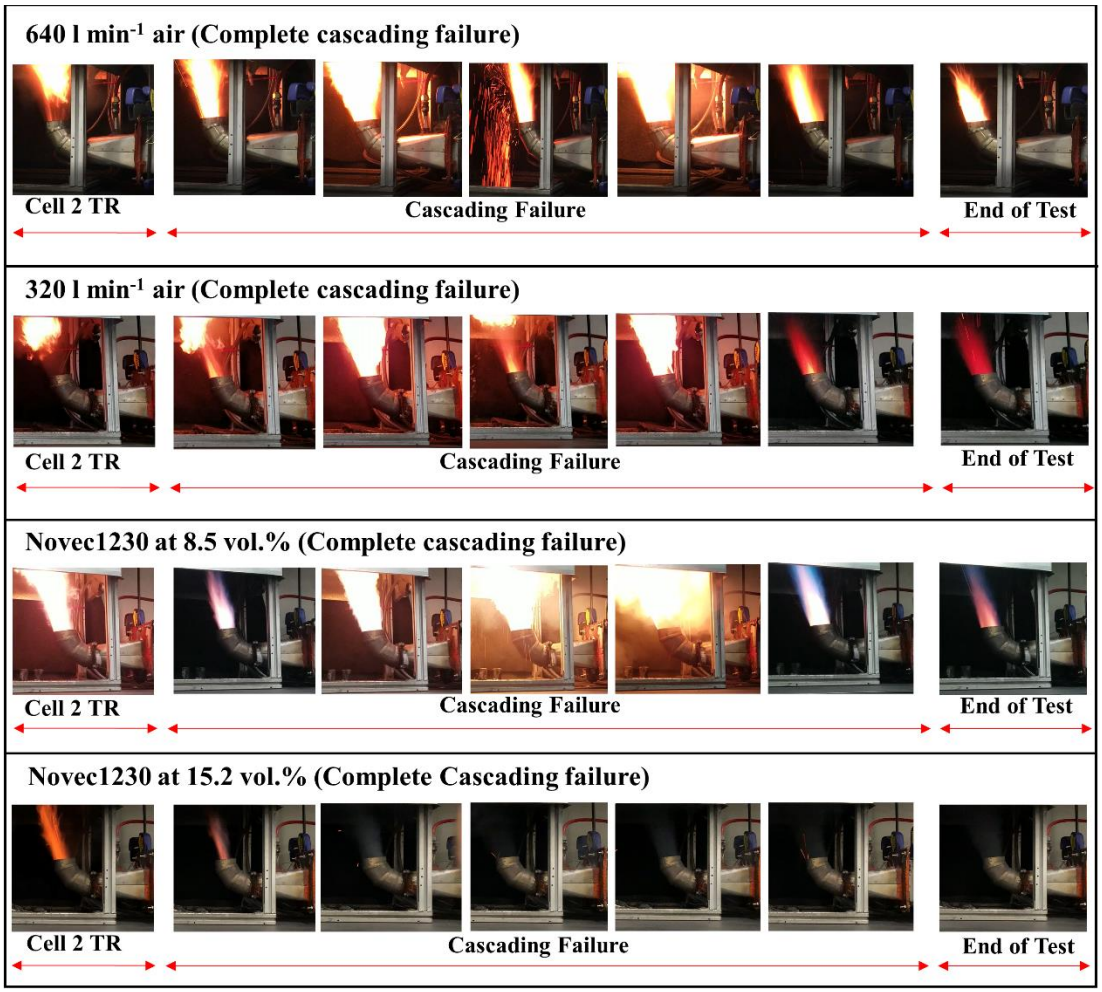

Figure 8. 11. Photographs demonstrating the re-ignition or continued combustion of the tunnel exhaust gases during representative air and Novec1230 suppression experiments.

In the 640 and 320 l min^{-1} air tests, the observed yellow flame regions indicate the local dominance of soot incandescence. In the 8.5 vol.% Novec1230 tests, introduction of Novec1230 agent immediately after TR of cell 2 resulted in dilution of oxygen concentration throughout the wind tunnel and reduction in the average temperature of the hot gases leaving the tunnel, which in turn caused the cessation of soot production and the flame color to alter from yellow to blue (the luminescence of

CH radicals), see Figure 8. 11. In the 15.2 vol.% Novec1230 tests, no flames were observed at the outlet of the tunnel after the Novec1230 was applied.

Detection of discernable amounts of CO and THC, almost complete consumption of O_2 inside the tunnel, and observation of a flame at the tunnel exhaust suggest that the combustion inside the tunnel is incomplete. To further investigate the incompleteness of combustion, the $E_{Flaming}$ data obtained in the cascading failure experiments were compared with the $E_{Flaming}$ obtained in the CSBC experiments. The combustion efficiency was computed based on $E_{Flaming}$ per failed cell or per gram of cell mass loss; the obtained results are shown in Figure 8. 12.

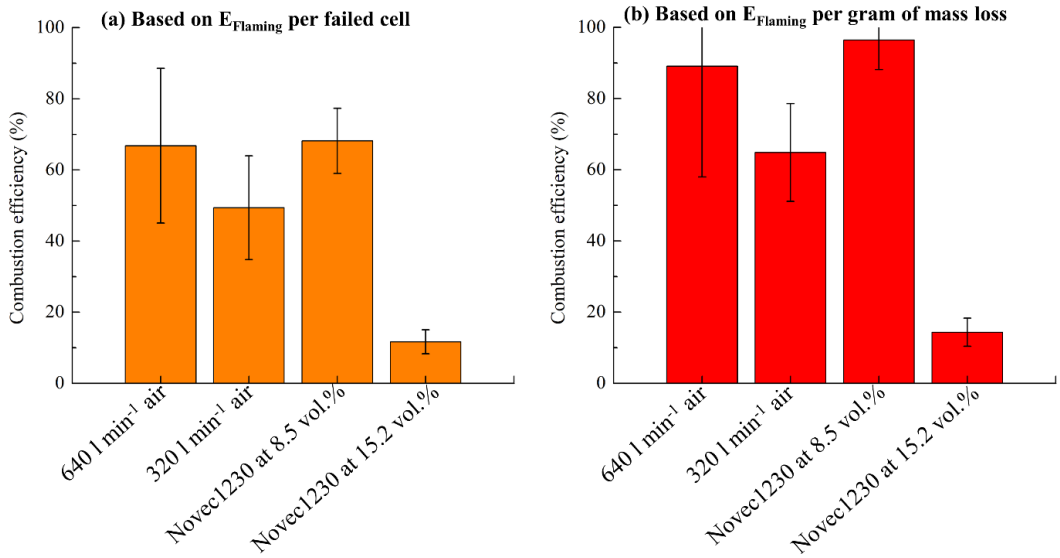

Figure 8. 12. Combustion efficiency for baseline and Novec1230 tests computed based on (a) $E_{Flaming}$ per failed cell and (b) $E_{Flaming}$ per gram of mass loss.

On per a failed cell basis, the results shown in Figure 8. 12 (a) confirm that the combustion in the 640 l min^{-1} air tests is indeed highly incomplete. Testing cell arrays in a reduced air flow rate (320 l min^{-1}) lessened the combustion efficiency, which is explained by less available amounts of oxygen. When the Novec1230 agent was introduced at 8.5 vol.%, the combustion efficiency slightly increased compared to the

640 l min^{-1} air tests. The increase in efficiency indicates that the Novec1230 agent at this concentration contributed to the combustion process. Overall, this observation matches with findings reported in previous studies [80, 127, 128] regarding combustion enhancement with the addition of Novec1230 agent at similar concentrations. The 15.2 vol.% Novec1230 tests achieved the smallest combustion efficiency (below 12%), indicative of highly extinguished flames.

To factor in the variation in cell mass loss in different test conditions, the combustion efficiency was also calculated based on $E_{Flaming}$ per gram cell mass loss and the results are shown Figure 8. 12(b). The combustion efficiency in Figure 8. 12(b) was greater than in Figure 8. 12(a) by ≈ 2%-22% for different test conditions. These changes in efficiencies are attributed to less cell mass loss achieved in the cascading failure experiments (listed in Table 8. 1) compared to the CSBC experiments (23 ± 2 g).

8.6 Suppression Mechanism of Novec1230

Cascading failure is primarily driven by the transport of thermal energy [26]. The mechanism of the thermal transport includes heats added to the cells by the flames and by conduction, convection, and radiation from neighboring cells. The mechanism of preventing or mitigating the TR propagation through cell arrays using Novec1230 agent depends on suppressing the flames (to reduce heat transfer from the flames to cells) and cooling the body of cells (to reduce the conduction, convection, and radiation heat transfer between the cells).

In the current study, the Novec1230 agent was introduced to the wind tunnel immediately after cell 2 underwent TR. The Novec1230 and air gases were hydro-

dynamically mixed in the mixing chamber, forming a gas mixture with a heat capacity that is greater than the heat capacity of air only. The air/Novec1230 mixture was delivered uniformly to the test section, where the examined cell arrays were located.

The air/Novec1230 mixture enhanced the convective cooling of the body of the cells, which reduced the cells heating rates and maximum temperatures. These impacts reduced the heat transfer between neighboring cells, which, in turn, prevented TR propagation (for tests with incomplete cascading failure) or mitigated the speed of propagation (for tests with complete cascading failure). The lack of reproducibility (incomplete/complete cascading failure) was attributed to the physics of the cascading failure, which had a tendency to amplify any minute differences in the geometry of the array (in particular, the physical contact surface area between adjacent cells) or any minor spatial or temporal fluctuations in the boundary conditions. In all tests with an incomplete TR propagation, each cell was found to be in its location after the test, meaning that the physical contact surface areas between adjacent cells were maintained constant during these tests. However, in all tests with complete cascading failure, changes in contact between cells were observed after tests.

The Novec1230 agent extinguishes fires via removal of heat from the flame reaction zone. In this study, the air/Novec1230 mixture absorbed significant amounts of heat from the flames and hot gases, which limited the temperature necessary to sustain the combustion process. The amounts of heat extracted from the flames and hot gases depended on the concentration of Novec1230 agent in the gas mixture.

8.7 Summary

Chapter 8 presented the results associated with investigating the impact of using Novec1230 suppressing agent on the dynamics and hazards associated with cascading failure in lithium ion cell arrays. Tests were conducted on cell arrays consisting of 12 fully charged LCO cells arranged in a rectangular configuration without any gaps between adjacent cells. All arrays were mounted in a specially designed wind tunnel with well-controlled environmental conditions. Experiments were initially conducted in an air environment by inducing TR in one of the cells (trigger cell) via a small electric heater. Immediately after the trigger cell underwent TR, 59.2 ± 1.1 l min^{-1} of gaseous Novec1230 was generated by the Novec1230 handling system and then introduced to the wind tunnel. In the wind tunnel, the Novec1230 was mixed with 640 or 320 l min^{-1} of air at a concentration of 8.5 ± 0.2 or 15.20 ± 0.04 vol.%, respectively. TR propagation was tracked using temperature sensors attached to the bottom surface of cells. The results of the 640 l min^{-1} air, 320 l min^{-1} air, and 186 l min^{-1} N_2 tests were utilized as baseline points in this chapter.

In all the 640 l min^{-1} air, 320 l min^{-1} air, and 186 l min^{-1} N_2, 8.5 vol.% Novec1230 tests, TR propagated through all cells of the tested array (12 cells), resulting in a complete cascading failure. Six experiments were conducted with Novec1230 at 15.2 vol% concentration. Four tests were subject to incomplete cascading failure (where less than 12 cells underwent TR) with an average number of ten non-failed cells per test. In the remaining two tests, the cell arrays experienced complete cascading failure.

The analysis of the cascading failure dynamics showed that the 640 l min^{-1} air tests yielded the greatest speeds among all test conditions. Compared to the 640 air l min^{-1} tests, testing the cell arrays in 320 l min^{-1} of air and using Novec1230 at 8.5 vol.% reduced the TR propagation speeds by 56% and 52%, respectively, during the late failure stages (row 2 to row 3 and row 3 to row 4). The N_2 and 15.2 vol.% Novec1230 tests yielded the greatest reduction in speeds during later failure stages: 80% and 85%, respectively, but additionally using Novec1230 at such concentration stopped TR propagation in 67% of the tests.

The TR onset temperatures of the 640 l min^{-1} air, 320 l min^{-1} air, and 8.5 vol.% Novec1230 tests were comparable (within each other's uncertainty) likely due to the comparable rates at which the cells are heated in these tests. The N_2 and 15.2 vol.% Novec1230 tests had the greatest TR onset temperatures due to slower heating rates of cells during these tests. The cell maximum temperatures achieved in the 640 l min^{-1} air, 320 l min^{-1} air, and 8.5 vol.% Novec1230 tests were greater than the maximum temperatures achieved in the N_2 tests due to impact of flaming combustion. The maximum temperatures achieved in the 15.2 vol.% Novec1230 tests were lower (by more than 80 K) than the maximum temperatures achieved in other test conditions because of the high convective cooling impact of Novec1230 at this concentration.

The oxygen consumption calorimetry calculations indicated that the 640 l min^{-1} and 8.5 vol.% Novec1230 resulted in the highest $E_{Flaming}$, which indicates that the Novec1230 at this concentration was completely ineffective in preventing combustion. The 15.2 vol.% Novec1230 tests generated the lowest flaming combustion energy, which indicates efficient suppression of flaming combustion achieved in these tests.

Using Novec1230 at 15.2 vol.% reduced the combustion efficiency by a factor of 5 compared to the 640 l min^{-1} tests.

9. Results and Discussion: Water Mist Suppression Investigation

In continuation of the exploration of effective active strategies to tackle the cascading failure phenomenon, water mist was examined as another fire suppressing agent. 12 LCO cell arrays at 100% SOC without gaps were used in this set of tests. Upon TR of cell 2 (trigger cell), the water mist was generated inside the tunnel and mixed with 640 or 320 l min^{-1} of air initially flowing through the tunnel, resulting in a mist concentration of 11.1 ± 0.6 wt.% or 14.1 ± 0.9 wt.%, respectively. Details on the experimental procedures and test matrix can be found in section 3.5.5. The results of this chapter focus on the impact of using water mist on the dynamics, temperatures, cell mass loss, and flaming combustion of cascading failure. Some of the results presented in chapter 8 are presented again in this chapter to provide points of reference.

9.1 Impact of Water Mist on Dynamics of Cascading Failure

The water mist experiments conducted at 11.1 wt.% were repeated six times. Incomplete cascading failure was observed in 50% of these tests. The water mist experiments conducted at 14.1 wt.% were repeated five times. 40% of the tests were subject to incomplete cascading failure. On average, eleven and five cells per test did not undergo TR during the 11.1 wt.% and 14.1 wt.% water mist experiments, respectively. TR propagation charts for representative water mist tests are displayed in Figure 9. 1 and Figure 9. 2. Propagation charts for all other test repetitions are included in Appendix C (Figure C. 16 and Figure C. 17).

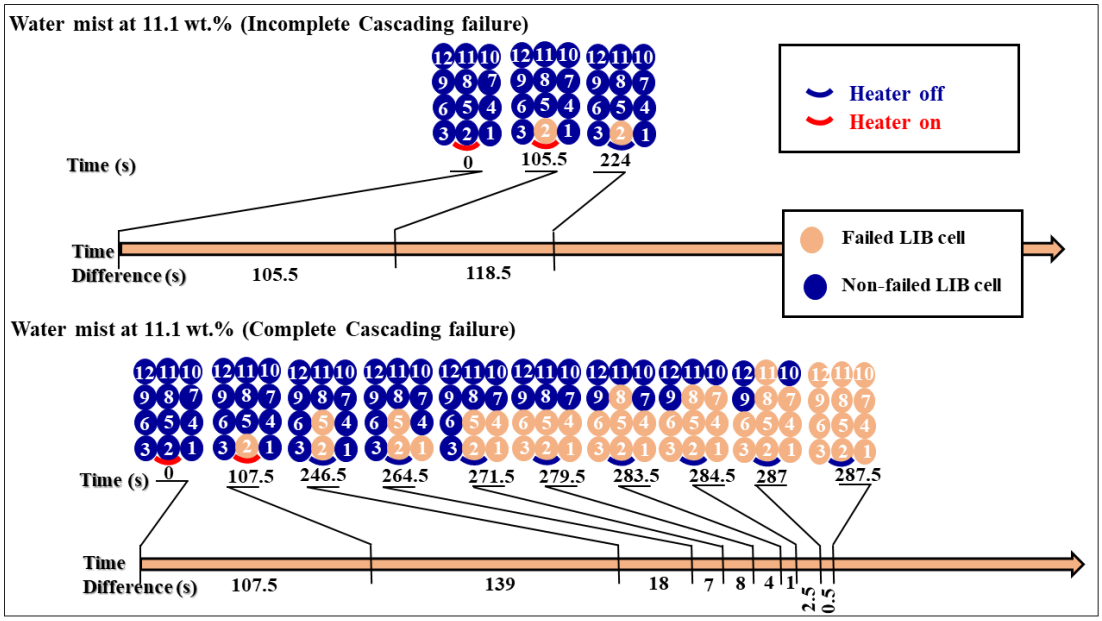

Figure 9. 1. Thermal runaway propagation charts for representative 11.1 wt.% water mist tests. Cell 2 was the trigger cell. The dark and light circles represent non-failed and failed cells, respectively. The dark and light arcs adjacent to cell 2 correspond to disabled and enabled heaters, respectively. The timeline is not drawn to scale.

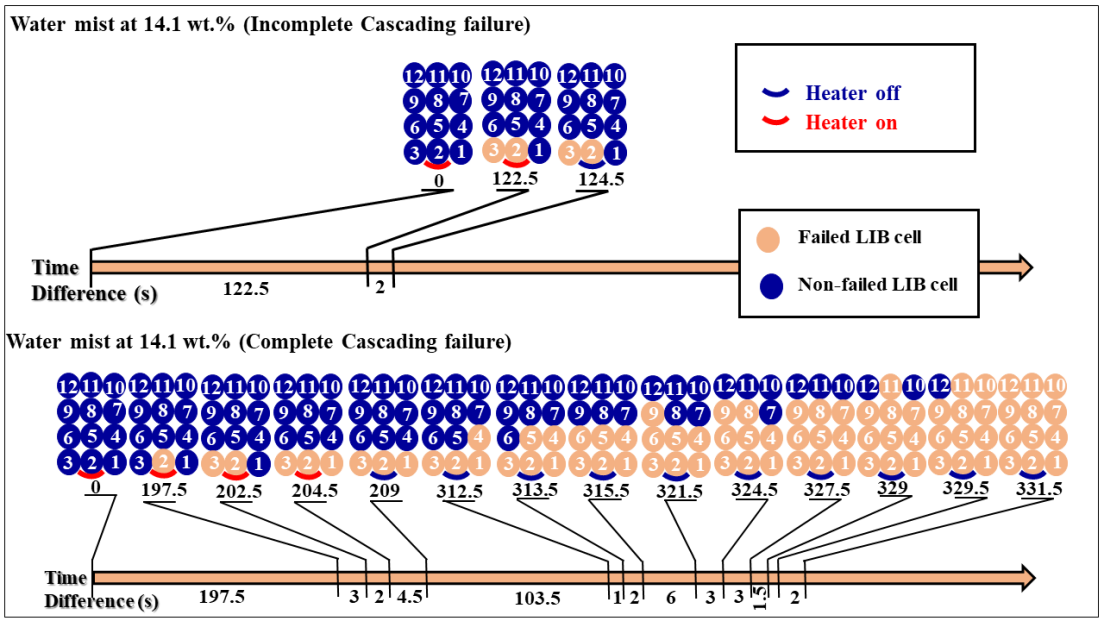

Figure 9. 2. Thermal runaway propagation charts for representative 14.1 wt.% water mist tests. Cell 2 was the trigger cell. The dark and light circles represent non-failed and failed cells, respectively. The dark and light arcs adjacent to cell 2 correspond to disabled and enabled heaters, respectively. The timeline is not drawn to scale.

The S_P data were computed for all baseline and water mist tests in units of s^{-1} or mm s^{-1}, and the results are plotted in Figure 9. 3. For the tests where propagation between particular rows did not occur, the S_P value of zero was entered into the calculation of the average. The figure shows that the 640 l min^{-1} air tests had the greatest S_P data among all tests, while testing the arrays in a reduced air flow rate (320 l min^{-1}) achieved smaller speeds due to less impact of flaming combustion. Using N_2 or water mist achieved a significant reduction in the propagation speeds compared to the air tests, particularly during the late stages of failure (row 2 to row 3 and row 3 to row 4).

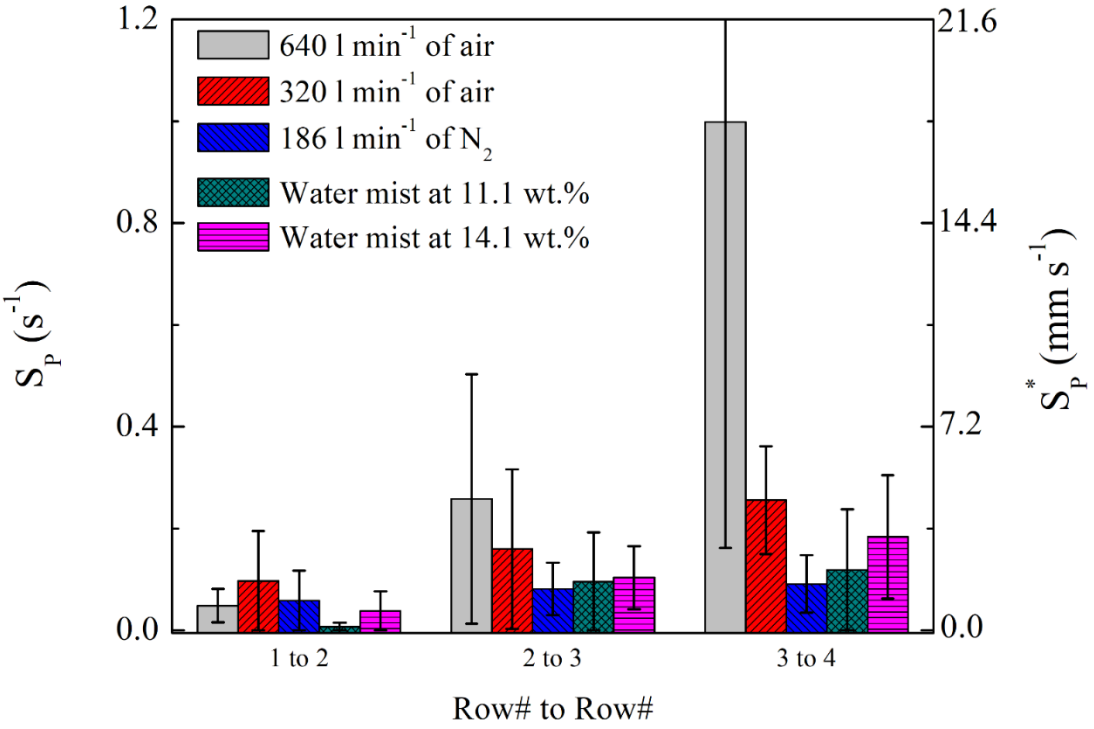

Figure 9. 3. Thermal runaway propagation speeds computed for baseline and water mist tests. The error bars for this plot were calculated from the scatter of the data as two standard deviations of the mean.

The 11.1 wt.% and 14.1 wt.% water mist tests achieved propagation speeds that were slightly higher than the speeds in the in N_2 tests. However, the introduction of water mist was more effective in preventing failure propagation in more than 40% of the tests. Also, using water mist at 11.1 wt.% achieved relatively slower propagation speeds than at 14.1 wt.% due to better convective cooling induced by the higher water mist delivery during the 11.1 wt.% water mist tests.

The introduction of water mist at concentrations of 11.1 wt.% and 14.1 wt.% reduced the TR propagation speeds during the late failure stages (row 2 to row 3 and row 3 to row 4) by 75% and 71%, respectively, compared to the propagation speeds

obtained in the 640 l min^{-1} air tests. Additionally, using water mist at 14.1 wt.% achieved 32% reduction in speeds compared to 320 l min^{-1} air tests.

9.2 Impact of Testing Conditions on Heating Rates and Temperatures of Cascading Failure

The heating rate of each cell was computed by averaging the heating rates during 20 s before this cell underwent TR. Also, the TR onset temperature was determined for each cell. The heating rates and TR onset temperatures of all cells were then averaged for baseline and water mist tests; the obtained results are plotted in Figure 9. 4. The data of non-failed cells were excluded from the presented calculations.

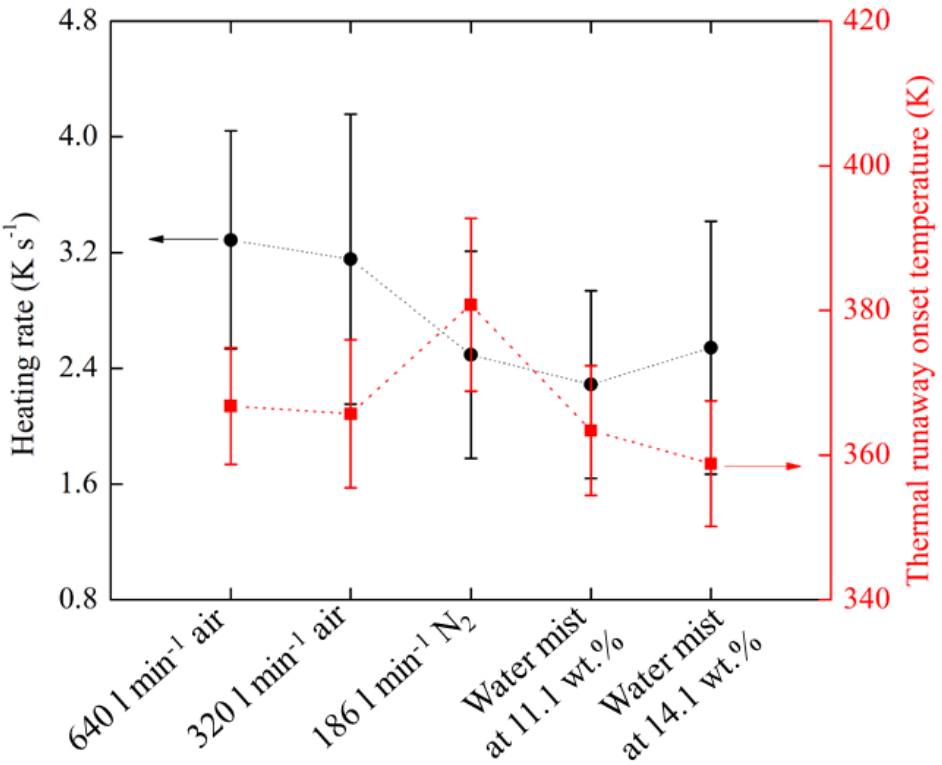

Figure 9. 4. Cell heating rates and thermal runaway temperatures for baseline and water mist tests. All temperatures obtained in this figure were measured at the bottom surface of cells. The error bars were computed from the scatter of the data as two standard deviations of the mean.

The cell heating rates obtained in the N_2 and water mist tests were less than the heating rates in the air tests due to suppressed flames. The data also indicate that the 11.1 wt.% water mist tests achieve less heating rates compared to 14.1 wt.% water mist tests, which is attributed to better convective cooling of cell surfaces with higher water mist delivery during the 11.1 wt.% water mist tests.

The TR onset temperatures of all air tests and water mist tests were comparable (within each other's uncertainties), but both were somewhat lower than N_2 tests. Unlike the Novec1230 test results, the slow heating rates achieved during the water mist tests showed almost no impact on the TR onset temperatures. This observation may be explained by more temperature non-uniformity across the body of the cells when water mist was used.

Figure 9. 5 presents the maximum cell temperature for baseline and water mist tests. The data of the non-failed cells were excluded from the presented averages. The water mist tests yielded maximum temperatures that were ≈ 100-200 K less than the maximum temperatures achieved during the air and N_2 tests due to better cooling achieved by the water mist.

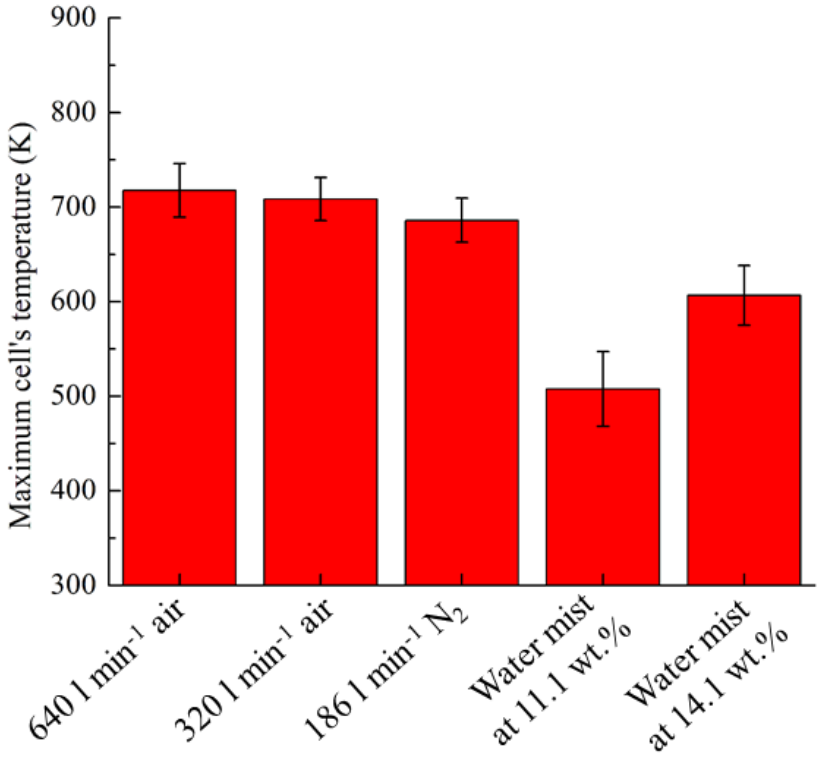

Figure 9. 5. Maximum cell temperature for baseline and water mist tests. All temperatures obtained in this figure were measured at the bottom surface of cells. The error bars were computed from the scatter of the data as two standard deviations of the mean.

9.3 Impact of Testing Conditions on Ruptured Cells and Mass loss

The percentage of ruptured cells relative to the total number of cells in 12 cell arrays was calculated for each test condition. The obtained results are compared for different test conditions in Figure 9. 6. Slower heating of cells in the N_2 and water mist tests lessened the cell rupture probabilities compared to the air tests.

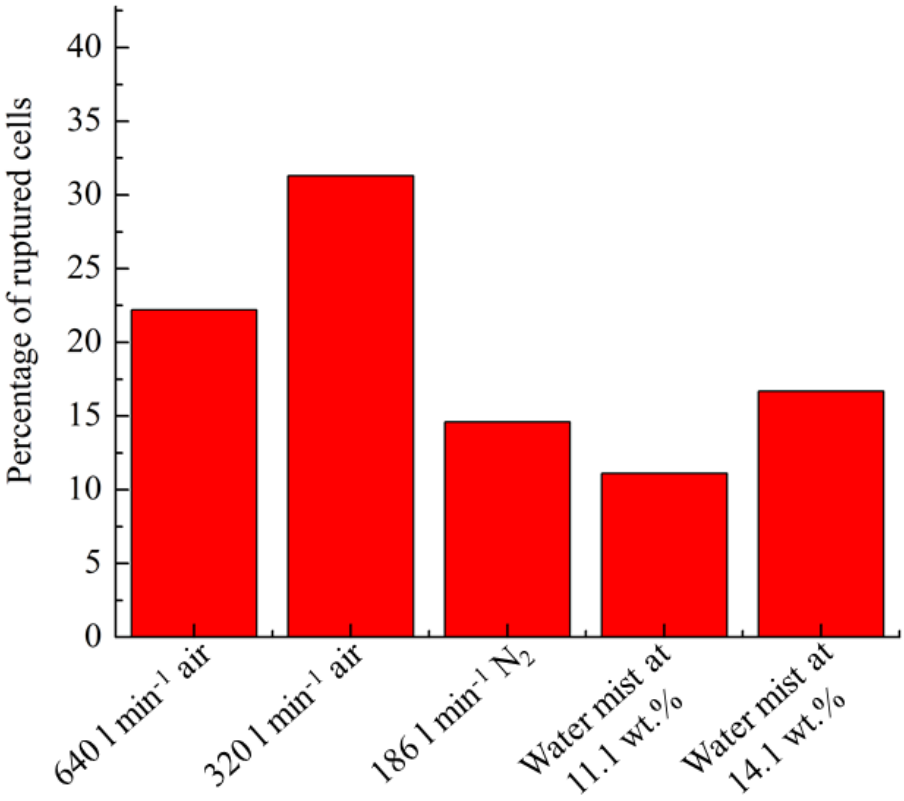

Figure 9. 6. Percentages of ruptured cells for baseline and water mist tests.

The initial and final masses of each cell were recorded before and after testing. The cells tested using water mist were dried in a desiccant box after testing to ensure complete removal of water from the outer surfaces of cells and then were weighed. The data of mass loss and mass loss percentages per failed cell are listed in Table 9. 1. When compared to N_2 and 15.2 vol.% Novec1230 tests, the water mist tests showed less mass loss percentages, which is attributed to possible chemical reactions between the water mist and some of the materials ejected from the cells. The products of those reactions deposit on the surfaces of the cells, increasing the mass of cells.

Table 9. 1. Cell initial mass and mass loss data for air and water mist experiments. The mass data obtained for the non-failed cells were excluded from the presented

statistics. The uncertainties were computed from the scatter of the data as two standard deviations of the mean.

Test condition	Initial Mass per cell [g]	Mass loss per failed cell [g]
640 l min^{-1} Air	43.60 ± 0.06	17.3 ± 1.3 (39.8 ± 2.5%)
320 l min^{-1} Air	43.50 ± 0.05	17.2 ± 1.4 (39.5 ± 3.2%)
186 l min^{-1} N_2	43.50 ± 0.06	16.7 ± 1.0 (38.4 ± 2.3%)
Water mist at 11.1 wt.%	43.70 ± 0.03	12.8 ± 1.2 (29.3 ± 2.7%)
Water mist at 14.1 wt.%	43.50 ± 0.04	13.8 ± 1.4 (31.6 ± 3.2%)

9.4 Suppression Effects of Water Mist

9.4.1 Flaming Combustion Heat Release

The rate of energy generation due to combustion of ejected battery materials ($P_{Flaming}$) was calculated for all water mist tests and compared with the $P_{Flaming}$ data for the 640 and 320 air tests (reference points). Representative examples of $P_{Flaming}$ for baseline and water mist tests are shown in Figure 9. 7. The $P_{Flaming}$ results of all other test repetitions are included in Appendix C (Figure C. 43, Figure C. 44, Figure C. 48, and Figure C. 49). As previously discussed in chapters 6 and 8, the $P_{Flaming}$ trends display an early peak (corresponding to energy release during TR of cell 2) followed by consecutive peaks (corresponding to energy release during failure propagation). To a large degree, this behavior was reproducible in every test. The main difference observed in the trends of water mist tests compared to baseline tests is that the consecutive peaks are mostly equal to or smaller than the early peak, which is due to the suppressing effects of water mist on combustion of ejected battery materials. Overall, the $P_{Flaming}$ maxima observed in the 640 l min^{-1} air tests were the largest (≈

35 kW), and the 14.1 wt.% water mist test results showed the smallest $P_{Flaming}$ peaks (below 10 kW).

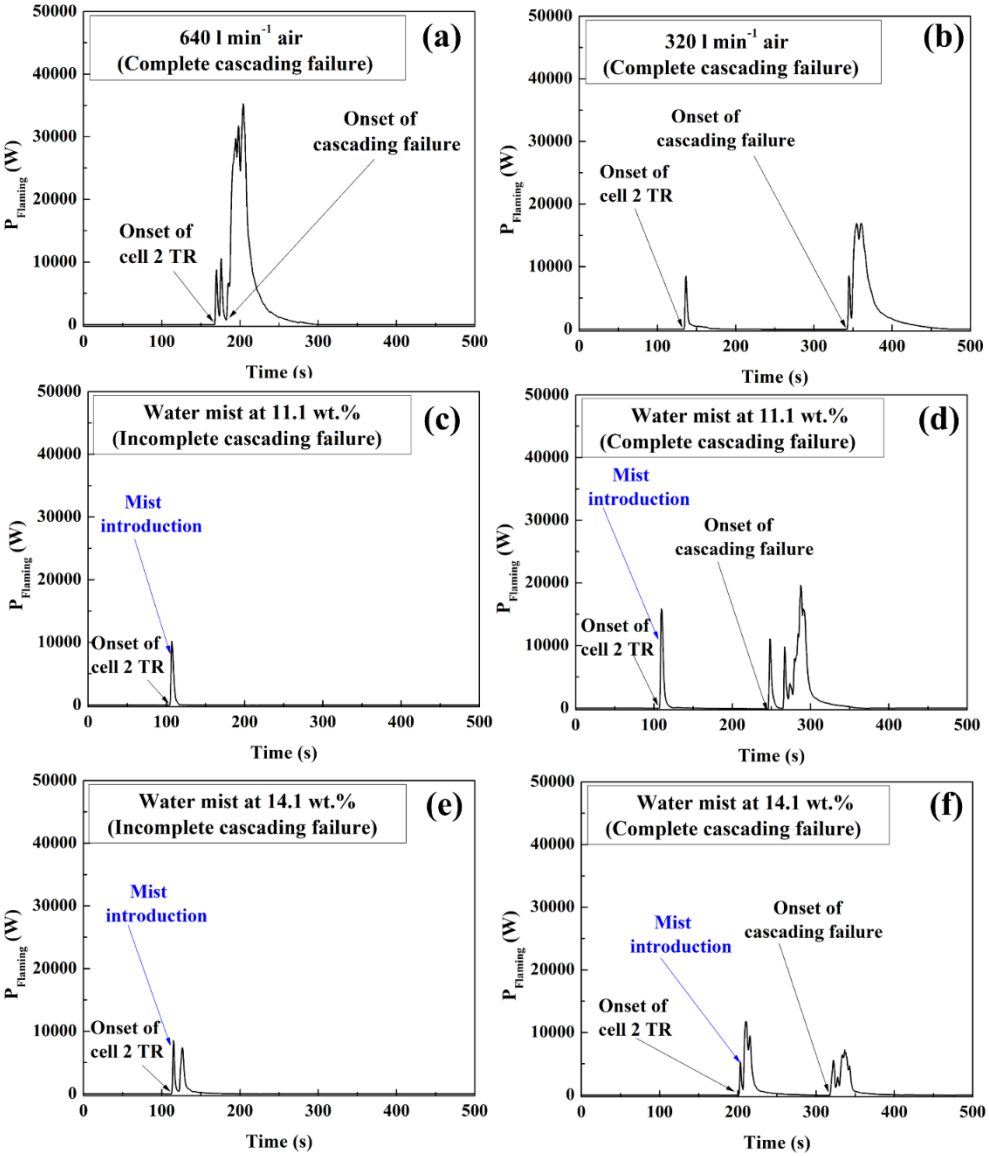

Figure 9. 7. Heat release rate due to flaming combustion of ejected battery materials obtained for representative (a) 640 lmin^{-1} air, (b) 320 l min^{-1} air, (c-d) non-propagated and propagated 11.1 wt.% water mist, and (e-f) non-propagated and propagated 14.1 wt.% water mist tests.

All $P_{Flaming}$ profiles were numerically integrated to calculate $E_{Flaming}$ in each test condition. The calculated integrations were normalized by the number of failed cells or total mass loss. The results are graphically compared in Figure 9. 8.

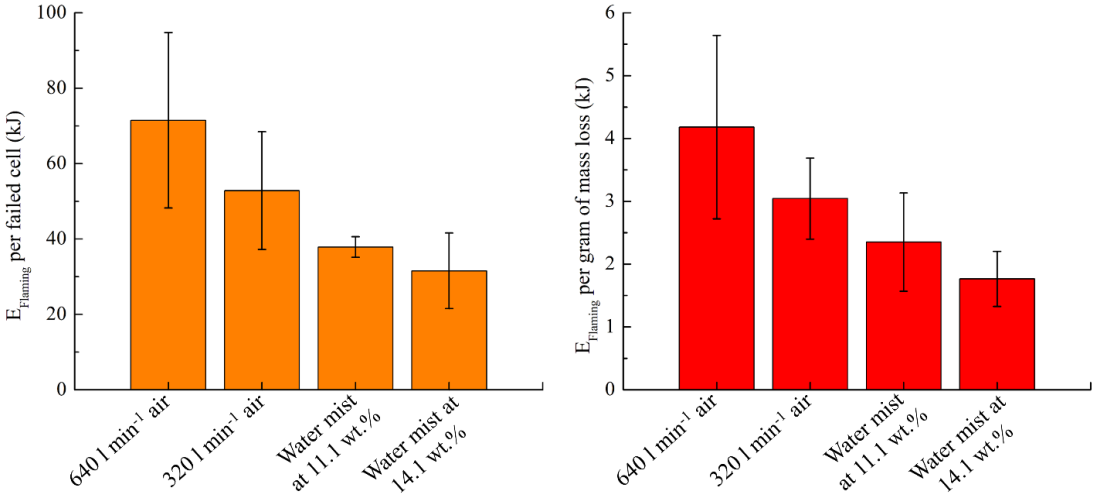

Figure 9. 8. Heats released in flaming combustion normalized in per failed cell or per gram of mass loss for baseline and water mist suppression tests.

The data show a monotonic decrease in $E_{Flaming}$ with the increase in the water mist percentage, which is attributed to the thermal quenching and oxidizer dilution impacts of the water mist on the flames. More specifically, evaporation of the mist existing near the flame leads to direct flame cooling due to high vaporization enthalpy of water. Additionally, evaporation of mist upstream from the flame contributes to suppression by increasing the water vapor mole fraction in the oxidizer and thus reducing the mole fraction of oxygen. The water vapor then dissipates heat from the reaction zone and lowers the flame temperature, which ultimately results in significant reductions in $E_{Flaming}$. The figure also shows that $E_{Flaming}$ for 11.1 wt% and 14.1 wt.% water mist tests were ≈ 2.5-3 times $E_{Flaming}$ for the 15.2 vol.% Novec1230, indicative

of better suppression effects of Novec1230 at such concentration compared to water mist.

9.4.2 Combustion Efficiency

Histories of O_2, THC, CO, and CO_2 volumetric concentrations are plotted in Figure 9. 9 for representative baseline and water mist tests. All gas profiles for all other test repetitions are included in Appendix C (Figure C. 26, Figure C. 27, Figure C. 33, and Figure C. 34). For tests that underwent a complete cascading failure, the combustion products contained large amounts of THC and CO. Less amounts of oxygen were consumed during the water mist tests compared to the baseline tests.

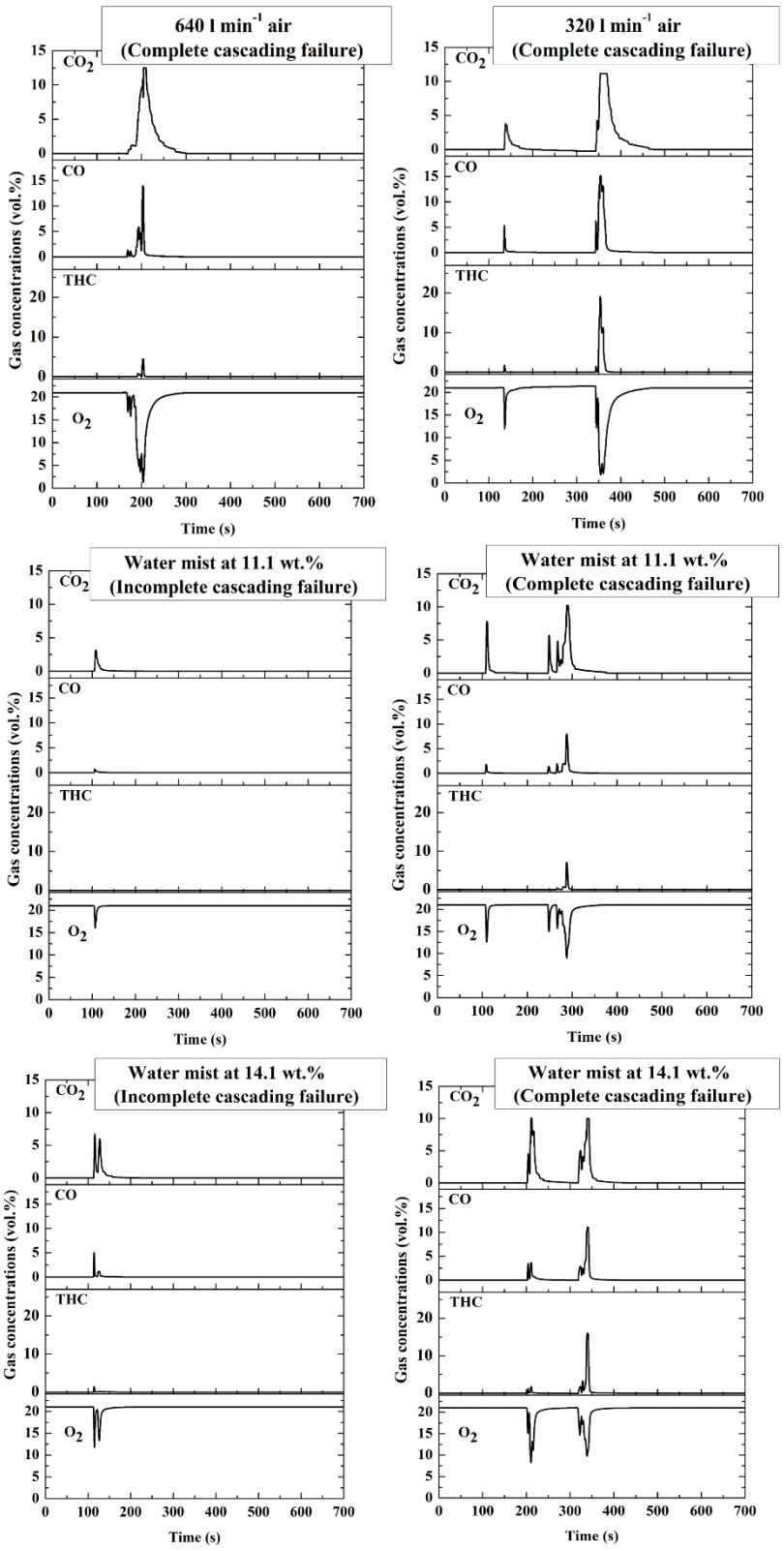

Figure 9. 9. Gas concentration profiles obtained from representative 640 l min^{-1} air, 320 l min^{-1}, 11.1 wt.% water mist, and 14.1 wt.% water mist tests.

Figure 9. 10 indicates that the exhaust gases reignited after leaving the exhaust elbow for all examined scenarios in this chapter. In the 640 and 320 l min^{-1} air tests, the photographs show that strong turbulent flames tend to anchor at the rim of the exhaust elbow during cascading failure. The flames observed during the 11.1 wt.% water mist tests were of less turbulent nature and more tendency to initiate downstream of the exhaust elbow (lifted flames). The 14.1 wt.% water mist tests showed highly intermittent flame, where a flame could not continue for more than a second or two each time it ignited. The flames also experienced reductions in luminosity with the introduction of mist due to flame cooling, where temperature is no longer high enough to produce soot on the fuel rich side of the flame.

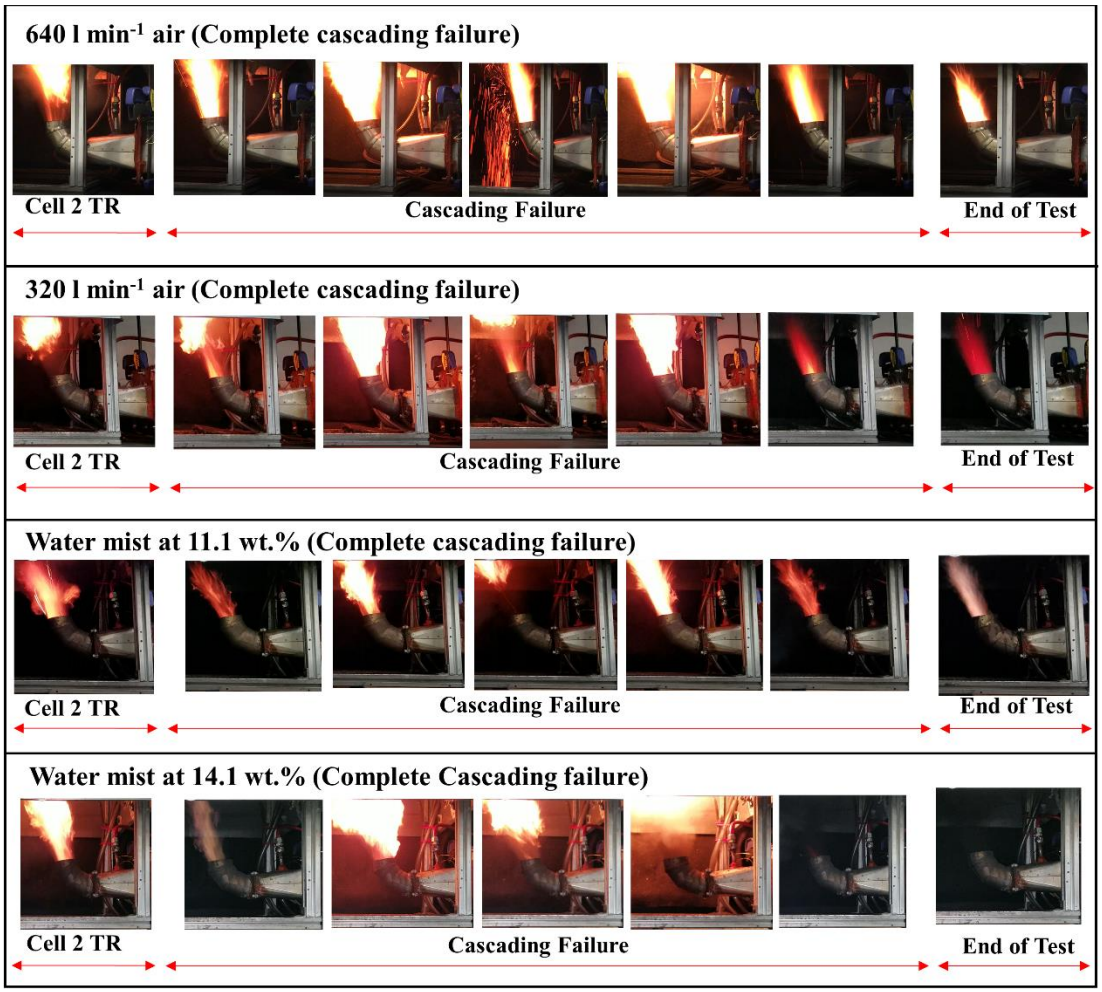

Figure 9. 10. Photographs demonstrating the re-ignition or continued combustion of the exhaust gases observed during representative baseline and water mist experiments.

The detected THC and CO, oxygen consumption, and re-ignition of gases all indicate that the combustion inside the wind tunnel was likely incomplete. Therefore, further analysis was performed to calculate the combustion efficiency. This analysis also helped to better assess the efficiency of mist to suppress the battery fires. The combustion efficiency was calculated by comparing the $E_{Flaming}$ obtained from the cascading failure experiments (shown in Figure 9. 8) and the CSBC experiments (listed in Table 6. 3); the results are presented in Figure 9. 11.

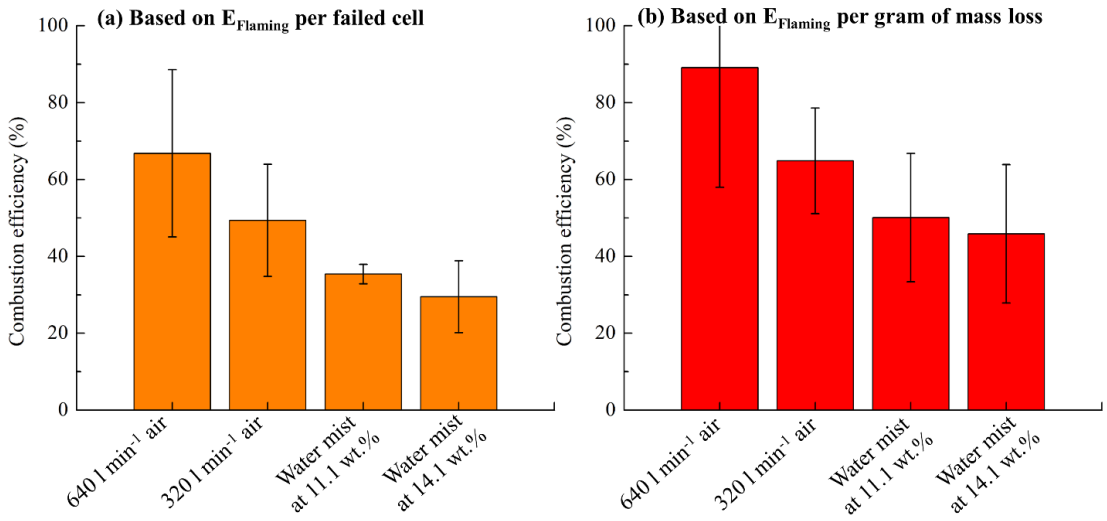

Figure 9. 11. Combustion efficiency for baseline and water mist tests computed based on (a) $E_{Flaming}$ per failed cell and (b) $E_{Flaming}$ per gram of mass loss.

Figure 9. 11 (a-b) show that the combustion efficiency somewhat decreased with the increase in the mass percentage of introduced water mist. In all test conditions, the combustion efficiencies computed based on $E_{Flaming}$ per gram of mass loss were found to be greater than the combustion efficiencies computed based on $E_{Flaming}$ per failed cell. As discussed in section 8.5.2, the increase in the combustion efficiencies is associated with greater mass loss achieved during the cascading failure experiments compared to the CSBC experiments.

9.5 Suppression Mechanism of Water Mist

Cascading failure is primarily driven by the transport of thermal energy [26]. The mechanism of the thermal transport includes heats added to the cells by the flames and by conduction, convection, and radiation from neighboring cells. The mechanism of preventing or mitigating the TR propagation through cell arrays using Novec1230 agent depends on suppressing the flames (to reduce heat transfer from the flames to

cells) and cooling the body of cells (to reduce the conduction, convection, and radiation heat transfer between the cells).

In the current study, water mist was generated in the atomizer section of the wind tunnel immediately after cell 2 underwent TR. The generated water mist was entrained by the air flowing through the tunnel and delivered to the test section, where the examined cell arrays were located. The high heat capacity of water mist helped to reduce the cells heating rates and maximum temperatures, which, in turn, prevented TR propagation (for tests with incomplete cascading failure) or mitigated the speed of propagation (for tests with complete cascading failure). The lack of reproducibility associated with obtaining incomplete or complete cascading failure was believed to be related to the changes in the shapes of individual cells that occurred during TR. The shape changes varied widely from cell to cell, which directly affected the contact area between adjacent cells.

Water mist is well-known for its efficient performance in suppressing flames primarily via thermal quenching and oxidizer dilution. In this study, evaporation of mist near the flame resulted in a direct flame cooling due to the high vaporization enthalpy of water (≈ 2260 kJ/kg). Additionally, evaporation of mist upstream of the flame contributed to suppression by increasing the mole fraction of water vapor in the oxidizer, thus diluting the oxidizer. Additional gaseous water vapor in the combustion reaction zones enhances heat dissipation from the reaction zone and also reduces the flame temperature. Previous studies [114, 115] found that water may exhibit a minimal chemical impact on the kinetics of the combustion reactions. These mechanisms

indicate that the flame is mainly extinguished when its temperature is reduced below the critical value needed to sustain combustion.

9.6 Summary

Chapter 9 presented the results associated with investigating the impact of using water mist suppressing agent on the dynamics and hazards of cascading failure in lithium ion cell arrays. Tests were conducted on fully charged 12 LCO cell arrays. All arrays were mounted in the wind tunnel, where environmental conditions were carefully controlled. Experiments were initially conducted in an air environment by inducing TR in one of the cells (trigger cell) via a small electric heater.

Immediately after the trigger cell underwent TR, the ultrasound mist generator located in the atomizer section was enabled to start water mist generation. The generated water mist was entrained by the air flowing through the tunnel and delivered to the test section. An air flow rate of 640 or 320 l min^{-1} (at reference pressure of 14.7 psi and temperature of 298 K) was able to deliver 1.6 ± 0.1 or 1.0 ± 0.1 g s^{-1} of water mist to the test section, resulting in a water mist mass concentration of 11.1 ± 0.6 wt.% or 14.1 ± 0.9 wt.%, respectively. TR propagation was tracked using temperature sensors attached to the bottom surface of cells. The results of the 640 l min^{-1} air, 320 l min^{-1} air, and 186 l min^{-1} N_2 tests are utilized as baseline points in this chapter.

The 11.1 wt.% water mist experiments were repeated six times. Incomplete cascading failure (where less than 12 cells underwent TR) was obtained in 50% of these experiments. The 14.1 wt.% water mist experiments were repeated five times. 40% of the experiments were subject to incomplete cascading failure. On average, eleven and five cells per test did not undergo TR in the 11.1 wt.% and 14.1 wt.% water mist

experiments, respectively. The higher possibility of obtaining incomplete cascading failure during the 11.1 wt.% water mist tests compared to the 14.1 wt.% water mist tests is associated with the higher amount of water mist delivered to the cells during the 11.1 wt.% water mist tests, which induced enhanced convective cooling of the cells and prevented the propagation.

The introduction of water mist at concentrations of 11.1 wt.% and 14.1 wt.% reduced the TR propagation speeds during the late failure stages (row 2 to row 3 and row 3 to row 4) by 75% and 71%, respectively, compared to the propagation speeds obtained in the 640 l min^{-1} air tests. Using the Novec1230 at 15.2 vol.% was more effective in preventing TR propagation in 67% of the tests and also in reducing the speeds of TR propagation during the late failure stages (for the tests that propagated) by 85% compared to the speeds obtained in the 640 l min^{-1} air tests.

The analysis of the collected temperature measurements showed that the TR onset temperatures of the 640 and 320 l min^{-1} air tests were comparable (within each other's uncertainty) likely due to the comparable rates at which the cells are heated in these tests. Switching the test environment to N_2 resulted in slightly higher TR onset temperatures due to exposure of cells to slower heating rates in these tests. The introduction of water mist reduced the cells heating rates, however, unlike the N_2 and 15.2 vol.% tests, the reduction did not increase the TR onset temperatures, which can be explained by substantial temperature non-uniformity across the body of cells tested with water mist.

The water mist tests achieved maximum temperatures that were 100-200 K less than the temperatures achieved in the N_2 and air tests. The achieved maximum

temperatures during the water mist tests were slightly less than the temperatures achieved in the 15.2 vol.% Novec1230 tests, which again can be explained by the temperature non-uniformity across the cells tested in water mist conditions.

$E_{Flaming}$ was computed for the different test conditions. The 640 l min^{-1} air tests resulted in the highest $E_{Flaming}$. The introduction of water mist at concentrations of 11.1 wt.% and 14.1 wt.% reduced the amounts of $E_{Flaming}$ by 37% and 47.5%, respectively, in comparison to $E_{Flaming}$ of the 640 l min^{-1} air tests. Additionally, the 11.1 wt.% and 14.1 wt.% water mist tests were found to generate 3 and 2.5 times $E_{Flaming}$ of the 15.2 vol.% Novec1230 tests, indicative of better suppression effects of Novec1230 at such concentration compared to water mist.

10. Conclusions

10.1 Summary

A new experimental setup was developed to allow for a detailed analysis of the dynamics of thermal runaway propagation (referred to as cascading failure) in LIB cell arrays. Individual LCO cells of a widely used 18650 form factor (cylindrical geometry of 18 mm diameter and 65 mm height) were employed to construct two different sizes of cell arrays. 18 and 12 LCO cells were arranged in two rectangular configurations with no gaps between adjacent cells (3 columns × 6 rows) and (3 columns × 4 rows), respectively; all cells were charged at 100% SOC. The cell arrays were mounted in a specially designed wind tunnel with a carefully controlled environment throughout. Tests were conducted in an N_2 environment to quantify the impact of array size on the dynamics and hazards associated with cascading failure.

Experiments showed that both of the examined cell array sizes experienced cascading failure when one of the cells was intentionally forced to undergo thermal runaway. Time-resolved measurements of the cells' bottom temperatures were analyzed to provide information on the onset times and temperatures of safety venting and thermal runaway. The onset times of thermal runaway were subsequently employed to compute a row-to-row thermal runaway propagation speed. The propagation speed displayed negligible dependence on the size of the arrays. On average, for both arrays sizes, the propagation speed was found to be 0.08 s^{-1} in an N_2 environment. Additionally, several other quantities (cell mass loss, yields of gases ejected from cells, flammability assessment of ejected gases, and chemical heat generation) obtained from 18 and 12 LCO cell arrays were found to be comparable.

Given the similarity of results obtained from different array sizes and also the safety limitations of the experimental facility, the 12 cell array was utilized as the typical array size in this study for subsequent experiments.

The experimental setup was also used to study and compare thermally induced cascading failure in arrays of 12 fully charged cells containing LCO, NMC, or LFP cathode. The failure propagation was studied in N_2 and air environments to elucidate the impact of flaming combustion of materials ejected from the batteries on the dynamics and energetics of the failure process.

LCO and NMC cell arrays experienced a complete cascading failure in all N_2 and all air experiments. For the LCO cells, the air propagation rate was significantly ($\approx$ 8 times) greater than the N_2 propagation rate. The LFP cell arrays tested in N_2 did not fully propagate thermal runaway. The complete propagation (where all cells in the array underwent thermal runaway) was observed in a single LFP test in air (six tests were conducted in an air environment). This complete propagation was associated with the ignition of ejected battery materials, which did not occur in any other LFP tests, perhaps, due to a relatively low maximum temperature achieved by these cells during the thermal runaway (as mentioned in Table 6. 1).

The fully charged LCO, NMC and LFP cells lost about 40, 58 and 13% of initial mass upon thermal runaway, respectively. As was measured in the N_2 experiments, on a mass basis, the LCO and NMC cells produced significant amounts of hydrocarbons, CO and CO_2 (> 1 g per cell) and minor quantities of H_2 and O_2. In the case of LFP cells, the mass yields of hydrocarbons, CO and CO_2 were found to be approximately an order of magnitude lower than those obtained for the LCO and NMC cells, while the H_2

production was comparable. The LFP cell O_2 production could not be fully quantified because it was at or below the sensitivity limit of the gas analysis system.

The maximum volume of an enclosure wherein the gas ejection from a single cell creates a flammable mixture in an air environment was calculated from these measurements to be 0.084 ± 0.033, 0.071 ± 0.019 and 0.03 ± 0.02 m^3 for the LCO, NMC and LFP cells, respectively. As was already pointed out in section 6.5, this quantity can be interpreted as the minimum volume above which the ejected gases produced by a single cell must be diluted in order to prevent potential deflagration or detonation. The larger this volume is, the higher the detonation hazard associated with a given cell.

In the cascading failure experiments, the sum of the chemical heat (associated with the decomposition of cell's components and chemical reactions between these components) and flaming combustion heat (associated with burning of ejected battery materials) was found to be about 3.5, 2.9 and 2.5 times greater than the electrical energy stored for the LCO, NMC, and LFP cells, respectively. The flaming combustion observed in these experiments was highly incomplete. Under the conditions where the flaming combustion is nearly complete, the LCO, NMC, and LFP cells are expected to generate heat in the amount 4.9, 3.9 and 3.5 times greater than the electrical energy stored, respectively.

The experimental setup was also employed to study passive mitigation of cascading failure in LCO cell arrays. Various mitigation strategies have been investigated including the introduction of 5 mm empty gaps between clusters of wall-to-wall cells and the insertion of double layer perforated stainless steel plates,

intumescent solid, or ceramic fiber board into the gaps. None of the mitigation strategies was able to fully prevent thermal runaway propagation. However, while empty gaps were found to be ineffective, the configurations including physical barriers showed a large, more than a factor of 17, reduction in the propagation speed, thus providing significant additional time for detection and suppression of potential LIB fires.

Among the barriers, the ceramic fiber board supported by a steel plate slowed propagation the most. However, one drawback associated with the introduction of such barrier is that it may interfere with active thermal management of the battery pack. Perforated steel plates were found to be the second best in terms of mitigation effectiveness. Additionally, these plates are not expected to significantly interfere with the battery pack thermal management but are heavier than the ceramic fiber or intumescent barriers. The intumescent material supported by a steel plate was found to be the least effective among all barriers. Both barriers and gaps were found to notably increase the production of THC, CO, CO_2, and H_2 by the cells undergoing thermal runaway, while the chemical heat generation was found to be essentially unaffected. Cells located behind the barriers showed markedly increased thermal runaway onset temperatures due to prolonged exposure to high temperatures.

The collected data also provided insight on the contributions of individual processes to the heat transfer driving cascading failure in air experiments on LIB arrays without gaps – the most energetic failure scenario examined in the current study. The data indicates that flaming combustion of ejected battery materials contributed 50% to the heating of downstream cells, direct cell-to-cell conduction contributed 20%, while

the rest is associated with convective and radiative heat transfer between cells. It is important to note that this breakdown is specific to the studied LIB cell form factor, cathode chemistry, and array geometry and may not be generalized to all LIB module designs.

Based on the results obtained from the passive mitigation strategies, flaming combustion was found to be the most impactful factor on the dynamics of cascading failure as flames contributed 50% to the heating of cells. Therefore, two of the most common fire extinguishing agents (Novec1230 and water mist) were utilized to suppress the LIB fires and possibly prevent failure propagation through cell arrays. Suppression experiments were started by thermally inducing failure into one of the cells followed by applying the extinguishing agents.

The Novec1230 agent was introduced into the tunnel in a gaseous form at a concentration of 8.5 or 15.2 vol.%. Complete cascading failure was observed in all 8.5 vol.% Novec1230 tests. However, the Novec1230 agent was more effective in preventing thermal runaway propagation through the array (four tests did not propagate out of six) when used at a concentration of 15.2 vol.%. Even in the propagated 15.2 vol.% Novec1230 tests, the thermal runaway propagation speeds were found to be less or comparable with the speeds obtained in the N_2 tests. The Novec1230 agent resulted insignificant reductions in cell heating rates, which caused the cells to undergo thermal runaway at higher temperatures compared to typical air tests.

At low Novec1230 concentration (8.5 vol.%), the flaming combustion energy calculations displayed an increase in the combustion efficiency, which was likely attributed to Novec1230 contribution to the combustion process, thus increasing the

energy released; similar observation was reported in previous studies [127, 128]. Applying the Novec1230 at 15.2 vol.% inhibited the combustion inside the test section and achieved combustion efficiency below 12%, indicative of highly extinguished flames. Additionally, the exhaust products did not reignite at the outlet of the wind tunnel occurred when Novec1230 was used at 15.2 vol.% concentration.

Water mist was generated using an ultrasound atomizer and mixed with 640 or 320 l min^{-1} air flowing inside the tunnel, resulting in water mist concentrations of 11.1 or 14.1 wt.%, respectively. Experiments showed that the number of tests which were prevented from achieving complete cascading failure was greater for the 11.1 wt.% (three tests did not propagate out of six tests). At 14.1 wt.%, failure propagation was prevented in two tests out of five tests. Overall, the two mist concentrations applied in this study achieved propagation speeds that are slightly higher than the N_2 tests. Based on flaming combustion energy calculations, introducing the water mist allowed for suppression of the flames. The 11.1 and 14.1 wt.% water mist tests essentially yielded comparable combustion efficiencies of ≈ 35%, on average, meaning the mist reduced the combustion efficiency by a factor of ≈ 2 compared to the 640 l min^{-1} air tests.

10.2 Contributions and Recommendations for Industry

This work presents comprehensive information on cascading failure in lithium ion cell arrays—the information is unprecedented in terms of completeness and detail. The results of this research provide an insight into the physics causing failure propagation. Additionally, the study was able to distinguish and quantify the various hazards associated with this phenomenon, which ultimately can help to lay foundation

for effective methodologies for early detection and mitigation of electrical energy storage fires.

Overall, the current results show that cells of any cathode chemistry (LCO, NMC, or LFP) are more hazardous in an air environment than in N_2. Not only was the heat production during failure more than double its value (due to flaming combustion), but also the rate at which this failure propagated was dramatically increased and had a great tendency to accelerate throughout the rows of the array.

Maintaining an inert environment around lithium ion battery packs can be an effective strategy to mitigate the rate of propagation but costly, particularly for large battery packs. Therefore, it is suggested that the battery systems should be equipped with automated systems that allow for the introduction of inert gas into the system based on experimentally measured temperature thresholds of cells to reduce the severity of cascading failure. It is also recommended that those thresholds are designed and selected on the basis of fast heating scenarios as mentioned in section 6.2.

The Novec1230 agent has shown a promising performance in reducing the probability of failure propagation when used at a concentration of 15.2 vol.%, meaning the Novec1230 can be an efficient alternative for completely purging the system with an inert gas. Water mist also showed a reasonable performance; however, one disadvantage is that the mist may damage the battery management system or any electronics in contact with it.

The introduction of physical barriers between closely spaced cell groups/cluster also reduces the rates at which failure may propagate between those clusters albeit at the cost of increased volume occupied. The ceramic fiber barrier examined in this study

showed the best performance in terms of mitigating the failure propagation; the ceramic fiber materials also had low density which eliminates the issue of increased weight of the battery pack. Combining active suppression strategy (Novec1230 or inert gas) with passive suppression strategy (introduction of physical barriers) may be able to completely prevent thermal runaway propagation. These hybrid, passive/active mitigation methodologies should be further examined in the future.

Lastly, it is important to point out that, while from the perspective of the chemical heat, the LFP cells stand out as significantly less energetic than the LCO or NMC cells, when flaming combustion heat is included, the LFP cell failure energetics becomes comparable to the cells of the other cathode chemistries. This observation indicates that a qualitative improvement in the safety of the LFP cells can be achieved by reducing the combustibility of the electrolyte and/or separator utilized in these batteries. The LFP cell cascading failure is also much more likely to be prevented through traditional means of fire suppression, such as dispersion of CO_2 or halocarbons, which inhibit flaming combustion; this can be a potential future work.

11. Future Work

In continuation of the contributions and progress achieved in this research work, select recommendations for future work are summarized herein.

1. The current study focuses only on studying cascading failure in cell arrays constructed from individual cells of 18650 form factor. It is recommended that the cell holder is modified to test other form factors such as prismatic and pouch cells.
2. It is recommended that the emitted-gas sampling system is equipped with more gas sensors (such as HF and H_2O) to provide more accurate estimates of the gas yields and flow rates.
3. LFP cells showed the almost no tendency to propagate failure. However, the utilized cells were of relatively low nominal electrical capacity. It is recommended to test LFP cells with greater capacities to confirm that the failure dynamics will not change with capacity.
4. It is recommended to investigate how the dynamics of cascading failure change if the cells in the tested array are electrically connected (series/parallel) and under charging or discharging conditions.
5. It is recommended to study the impact of cell aging on the failure energetics.
6. Combining passive mitigation strategies with the introduction of a fire extinguishing agent is recommended to prevent cascading failure.
7. It is recommended to study the efficiency of the current passive mitigation and active suppression techniques in preventing cascading failure in NMC cell arrays.

8. Based on visual observations during cascading failure, large amounts of graphite powder were observed at the outlet of the tunnel. It is recommended to study how the graphite may influence the failure propagation process.
9. It is recommended to test other suppressing agents such as CO_2 or halocarbons.

Appendix A: Chemical Compositions of Tested LIB Cells

Table A. 1. Chemical composition of Tenergy ICR18650 LIB cell [98, 99].

Chemicals	Composition (wt.%)
Lithium metal oxide (Co, Mn, Ni)	37
Graphite powder	23
Polypropylene	4
Electrolyte ($LiPF_6$+EC:DEC:PC)	13
Polyethylene	0.8
Copper	7
Aluminum	8
Polyvinylidene fluoride	0.9
Silicon	1.4
Epoxy resin	1.6
PVC	0.4
Nickel	2.5
Gold	0.3
Tin	0.1

Table A. 2. Chemical composition of LG HG218650 LIB cell [101, 102].

Chemicals	Composition (wt.%)
Lithium metal oxide (Co, Mn and Ni)	20-50
Carbon	10-30
Electrolyte (EC [102])	10-20
Polyvinylidene fluoride	<5
Aluminum foil	2-10
Copper foil	2-10
Stainless steel, nickel and inert materials	Remainder

Table A. 3. Chemical composition of K2 18650E LIB cell [100].

Chemicals	Composition (wt.%)	Classification and hazard labeling
Lithium iron phosphate ($LiFePO_4$)	25-35	Eye, skin, respiratory irritant
Carbon (graphite powder)	12-18	Eye, skin, respiratory irritant
Polypropylene	2-3	Inert
Electrolyte:		Mixture: flammable, reactive, sensitizer, eye, skin & respiratory irritant
Ethylene carbonate (EC)	3-5	
Diethyl carbonate (DEC)	3-5	
Ethyl methyl carbonate (EMC)	3-5	
Lithium hexafluorophosphate	1-3	
Aluminum metal	3-7	Inert
Copper metal	5-9	Inert
Mild steel can & cap	18-22	Inert

Appendix B: Experimental Setup

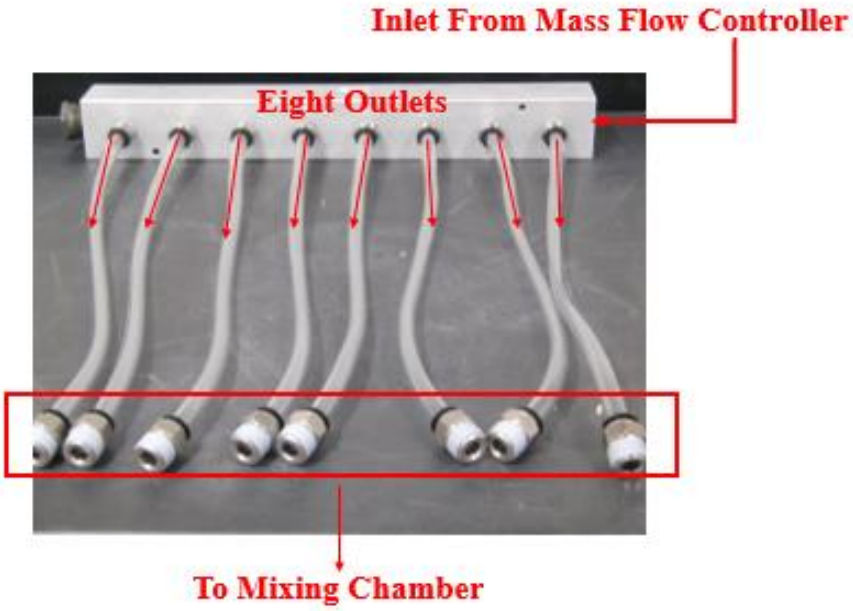

Figure B. 1. An aluminum NITRA pneumatic manifold with attached flexible tubes.

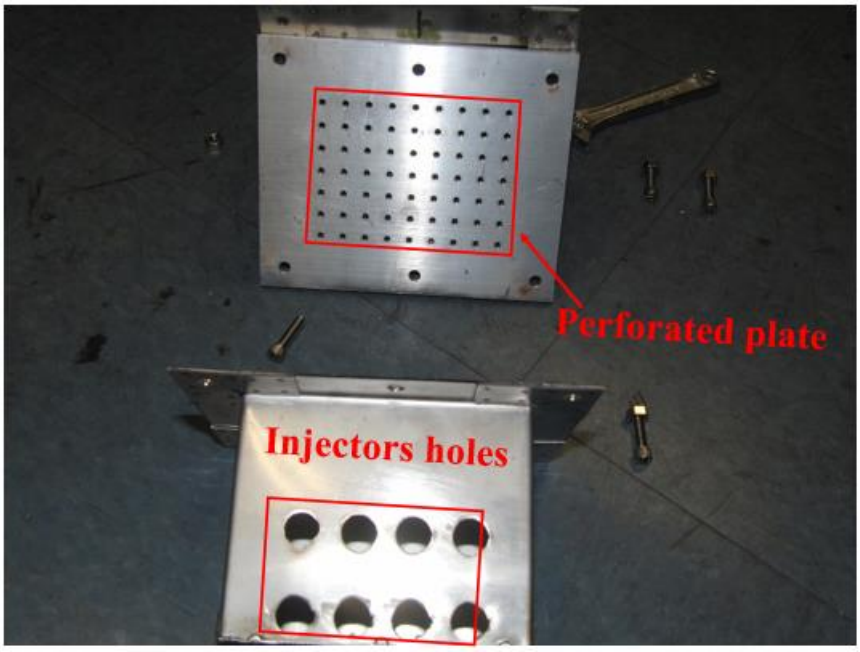

Figure B. 2. Images of the hydrodynamic mixing chamber and perforated plate.

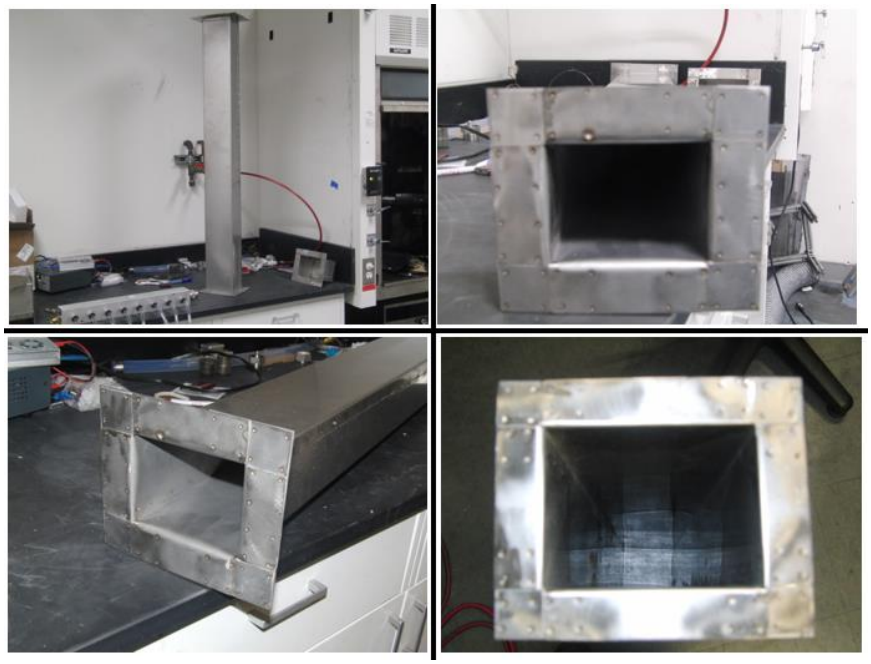

Figure B. 3. Images of the pre-test section.

Figure B. 4. Images of the test section.

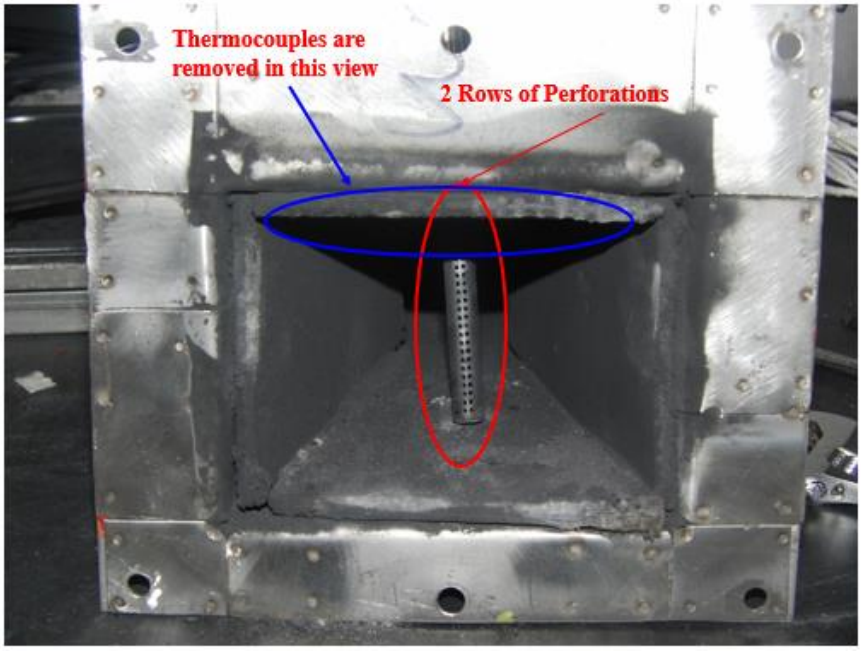

Figure B. 5. The sampling probe after a set of experiments (during cleaning).

Figure B. 6. Images of the diagnostics section.

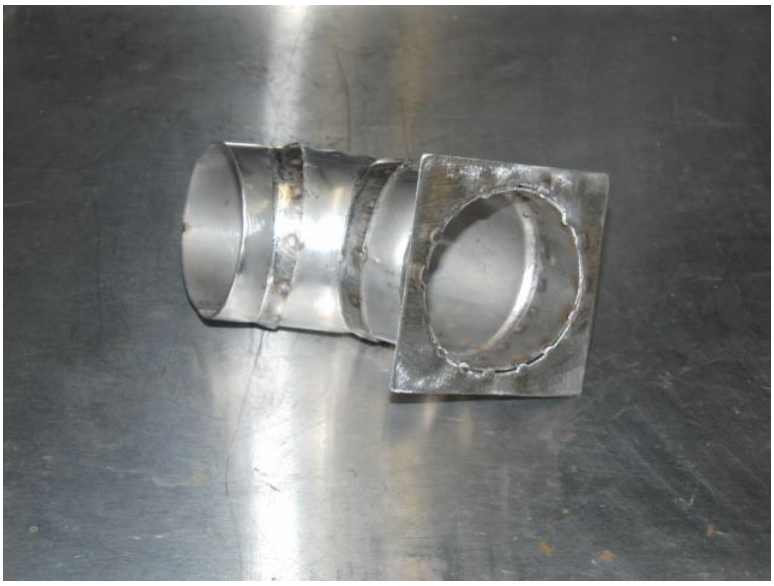

Figure B. 7. An image of the exhaust elbow.

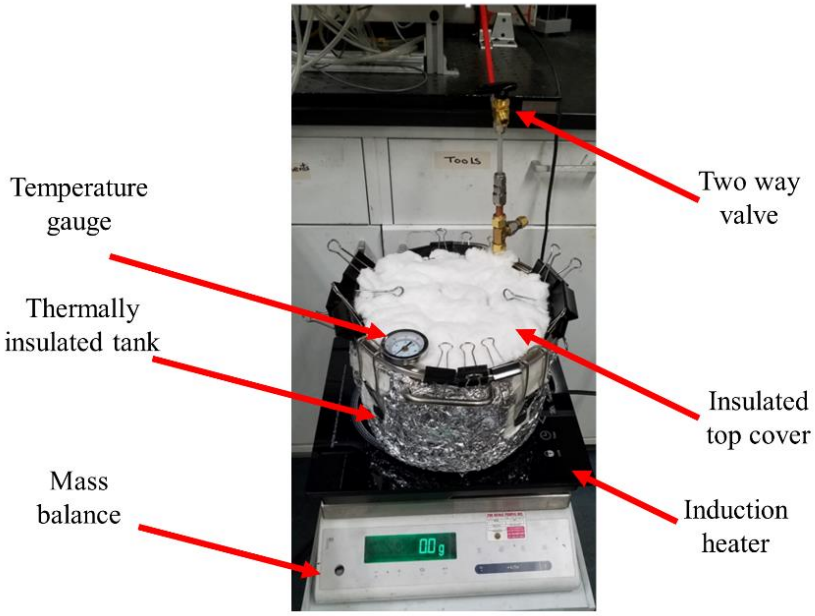

Figure B. 8. A photograph of Novec1230 handling system.

Appendix C: Results of Test Repetitions

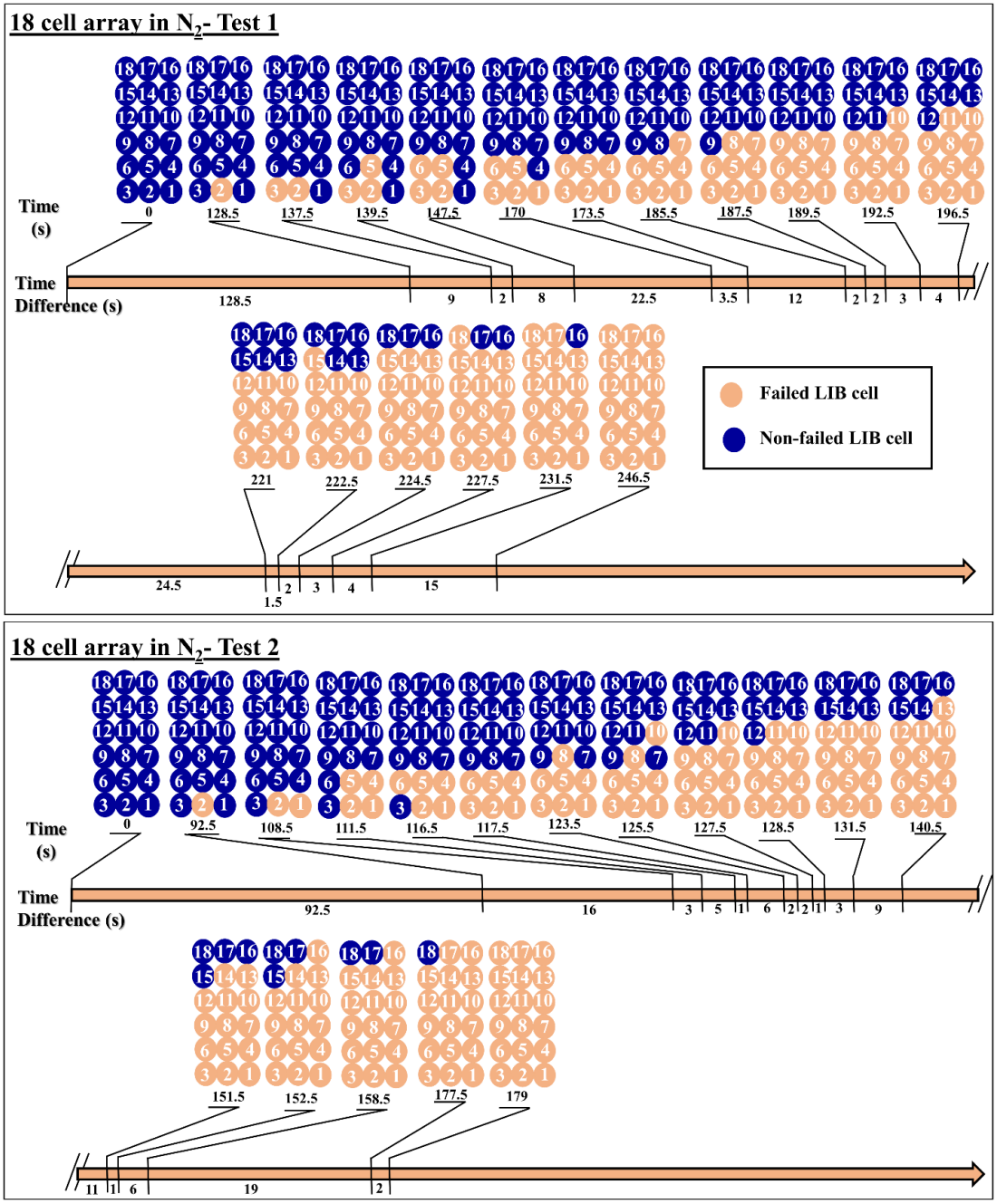

Figure C. 1. Thermal runaway propagation charts for 18 LCO cell arrays in N_2 (186 l min^{-1}). Test repetitions 1 and 2.

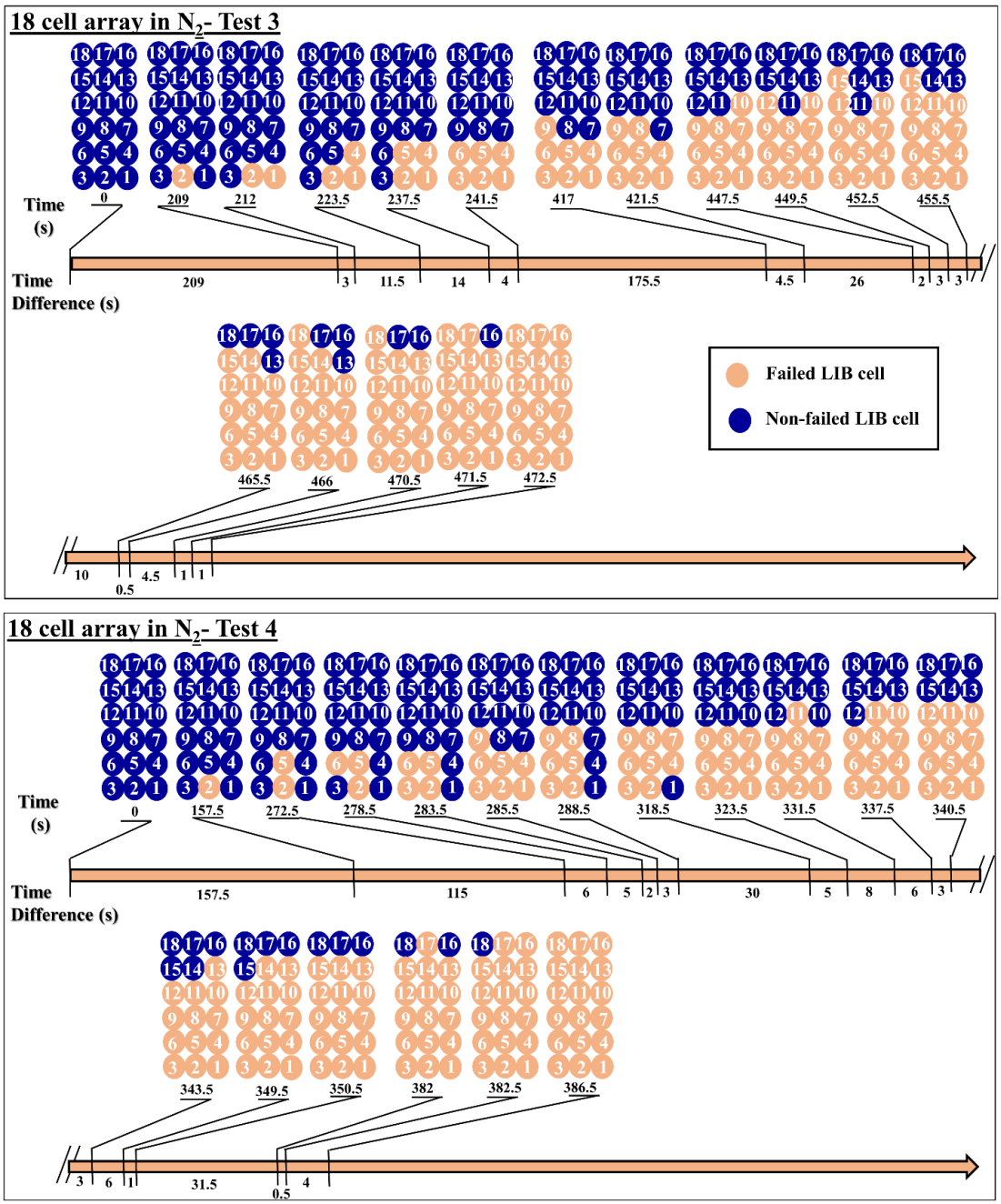

Figure C. 2. Thermal runaway propagation charts for 18 LCO cell arrays in N_2 (186 l min^{-1}). Test repetitions 3 and 4.

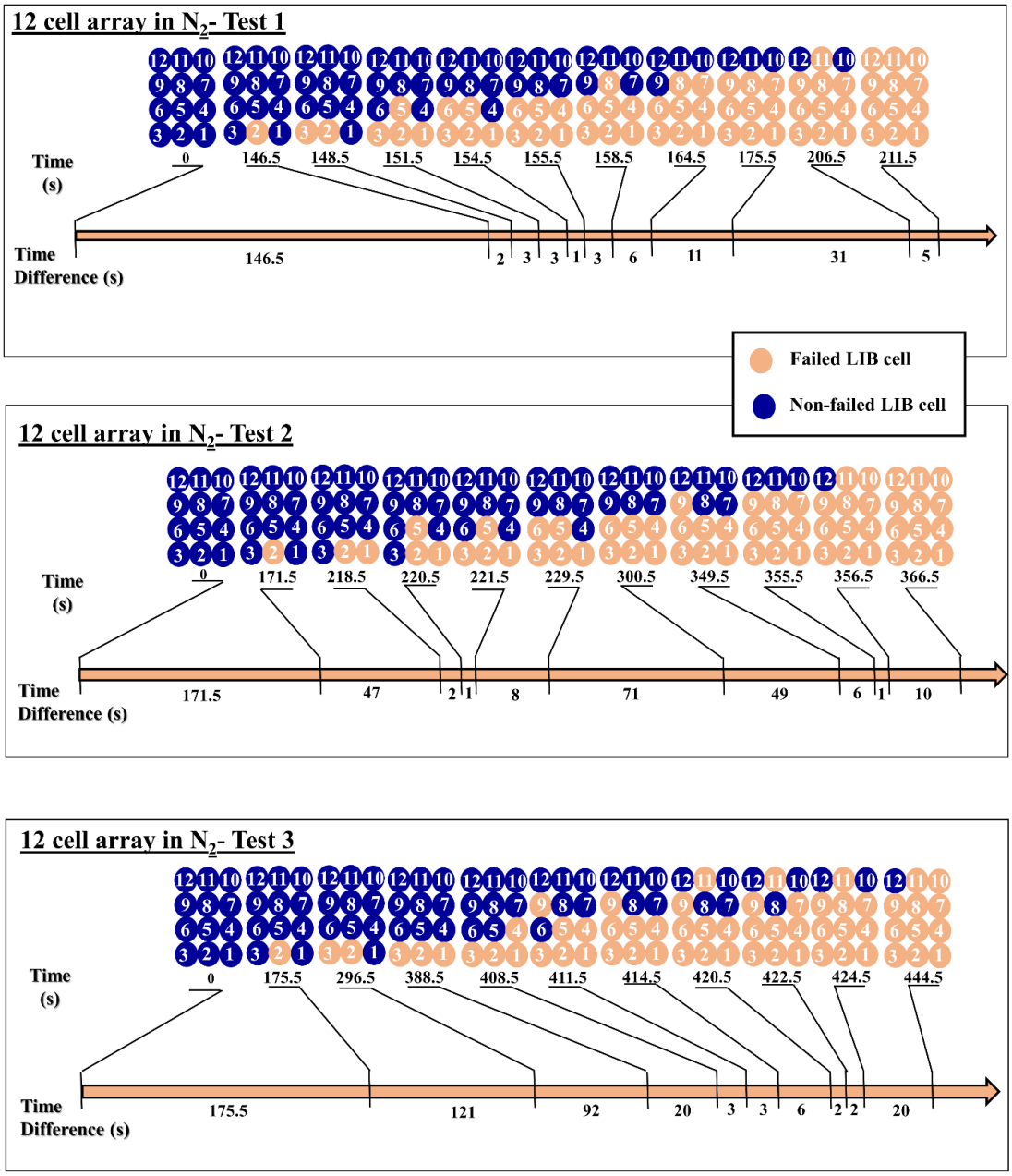

Figure C. 3. Thermal runaway propagation charts for 12 LCO cell arrays in N_2 (186 l min^{-1}). Test repetitions 1, 2, and 3.

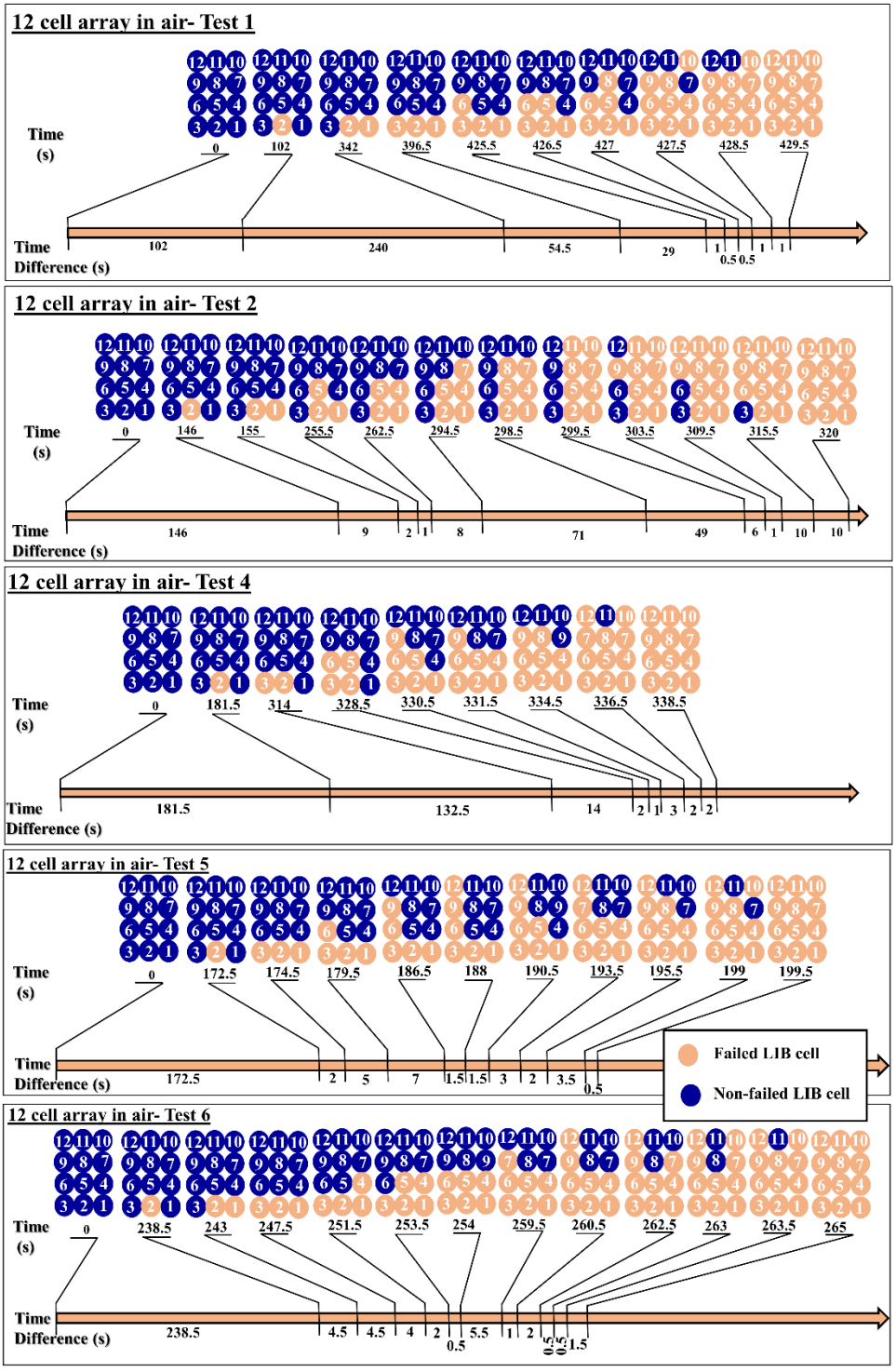

Figure C. 4. Thermal runaway propagation charts for 12 LCO cell arrays in air (640 l min^{-1}). Test repetitions 1, 2, 4, 5 and 6.

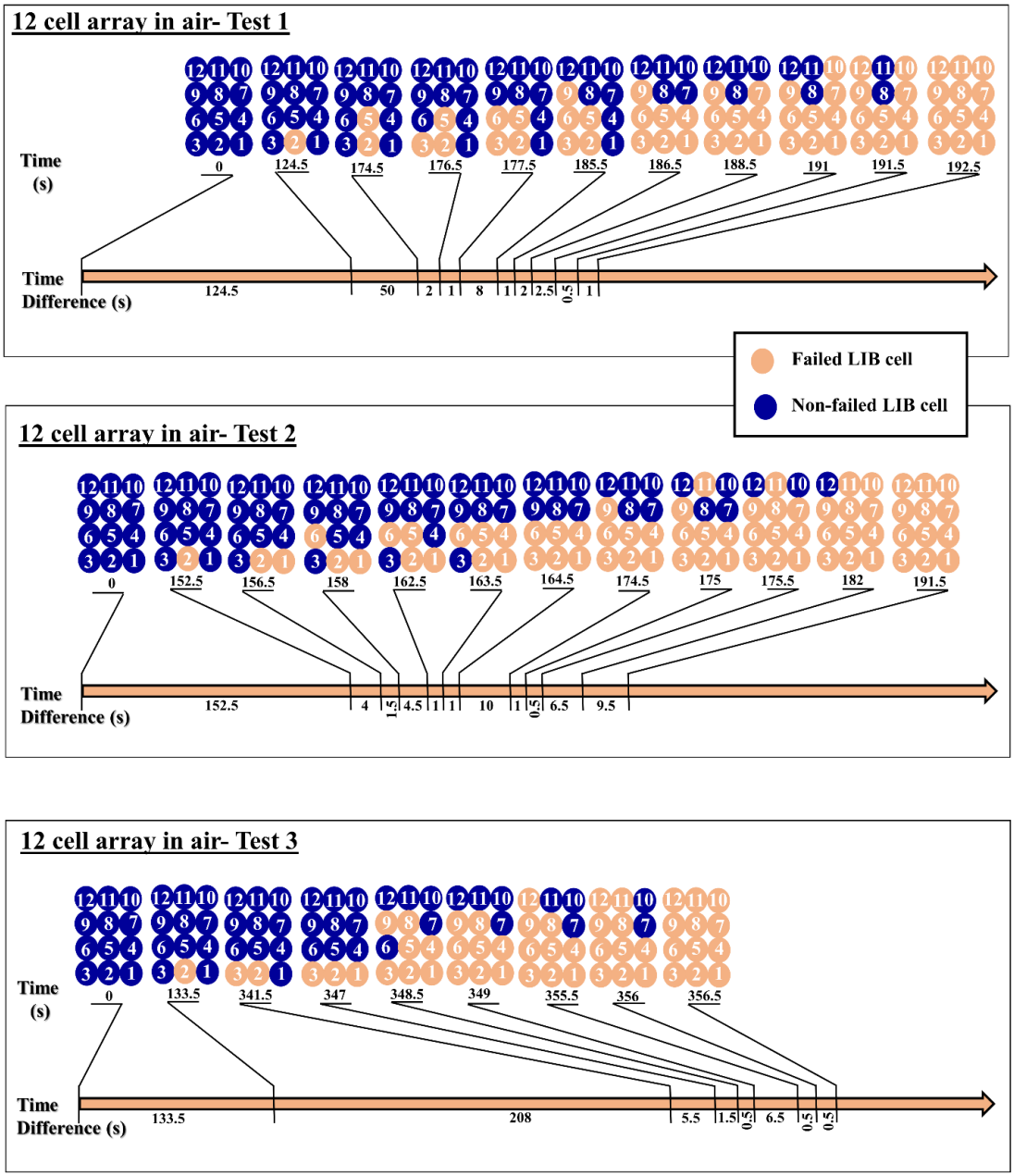

Figure C. 5. Thermal runaway propagation charts for 12 LCO cell arrays in air (320 l min^{-1}). Test repetitions 1, 2, and 3.

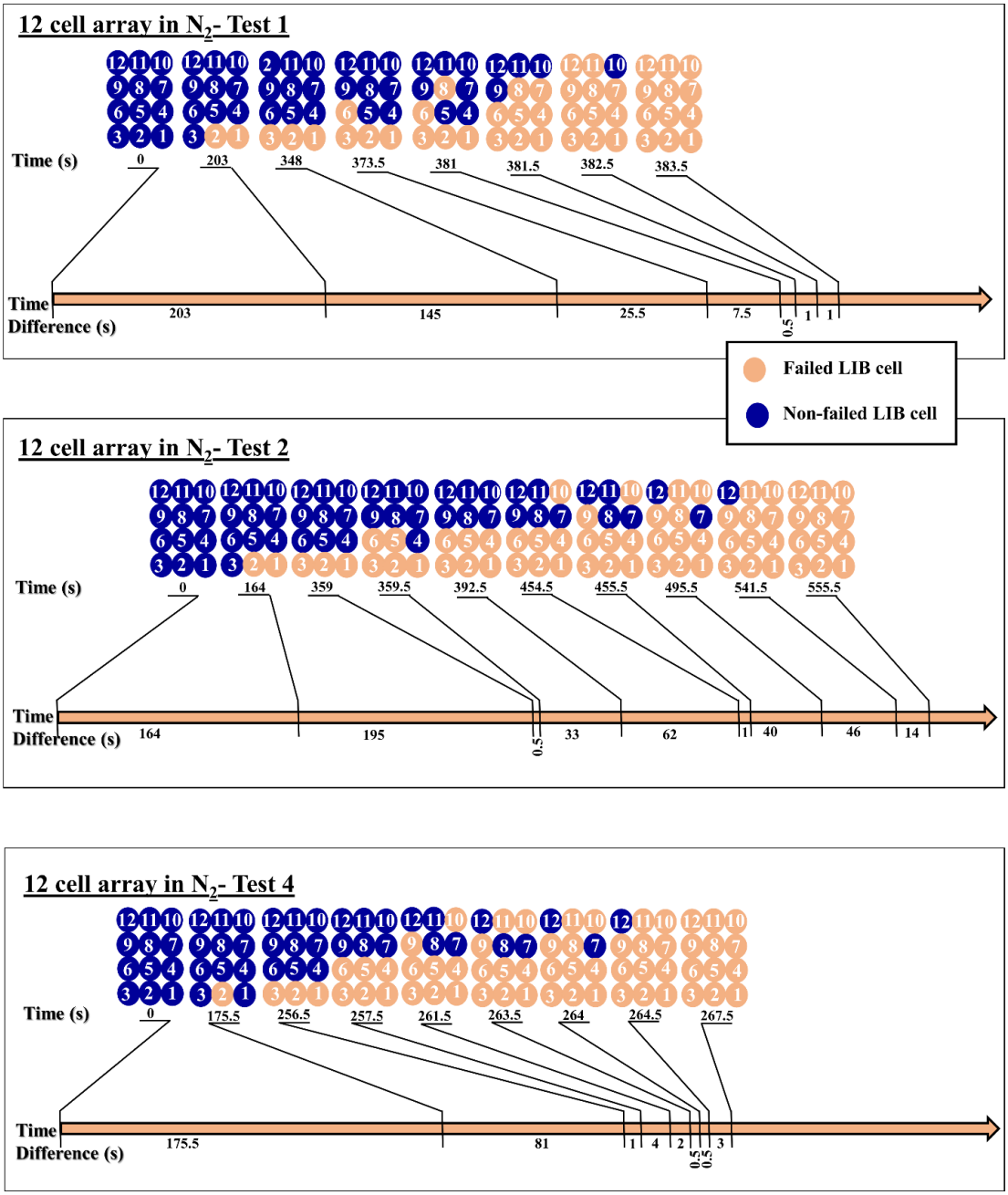

Figure C. 6. Thermal runaway propagation charts for 12 NMC cell arrays in N_2 (186 l min^{-1}). Test repetitions 1, 2, and 4.

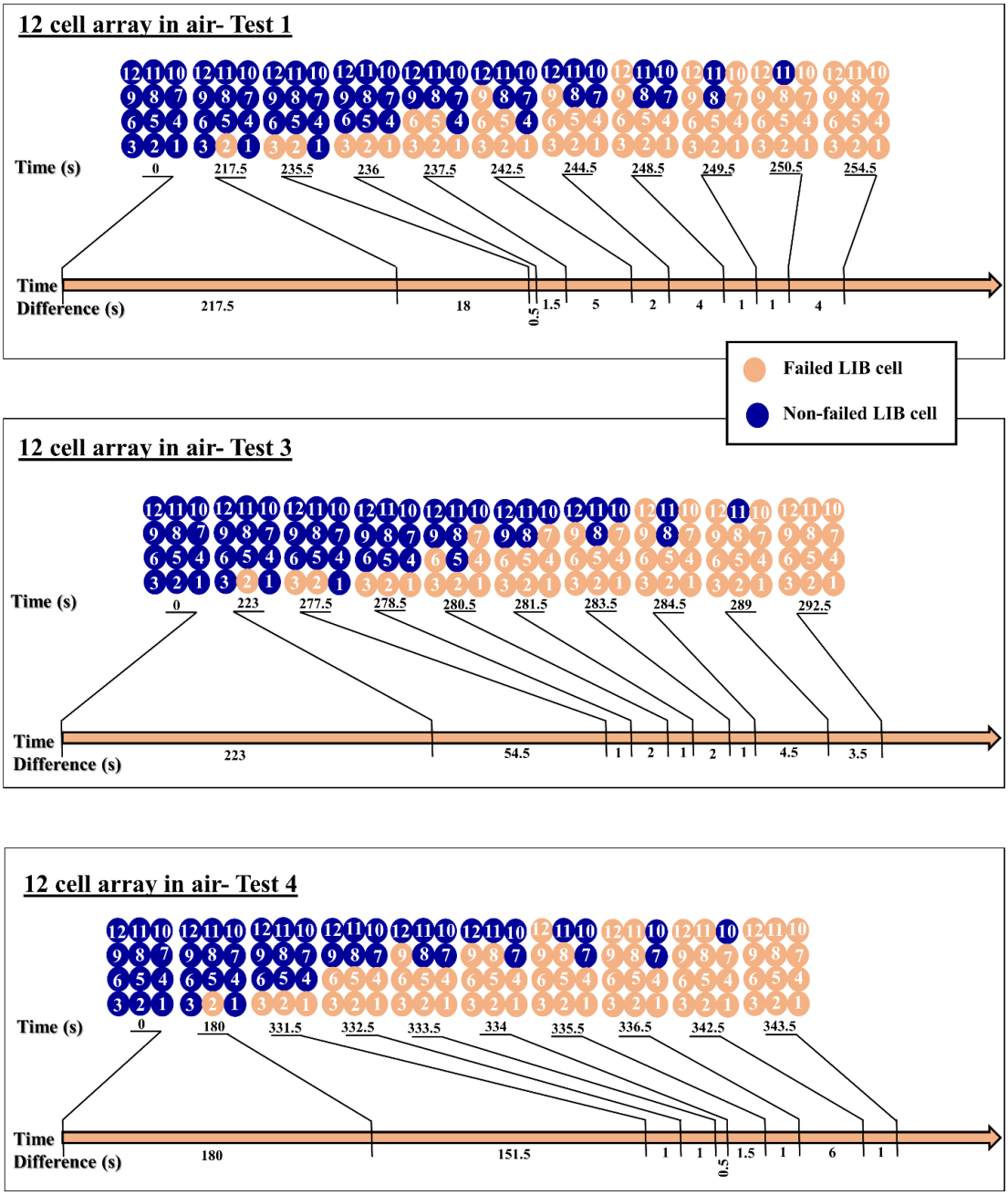

Figure C. 7. Thermal runaway propagation charts for 12 NMC cell arrays in air (640 l min^{-1}). Test repetitions 1, 2, and 4.

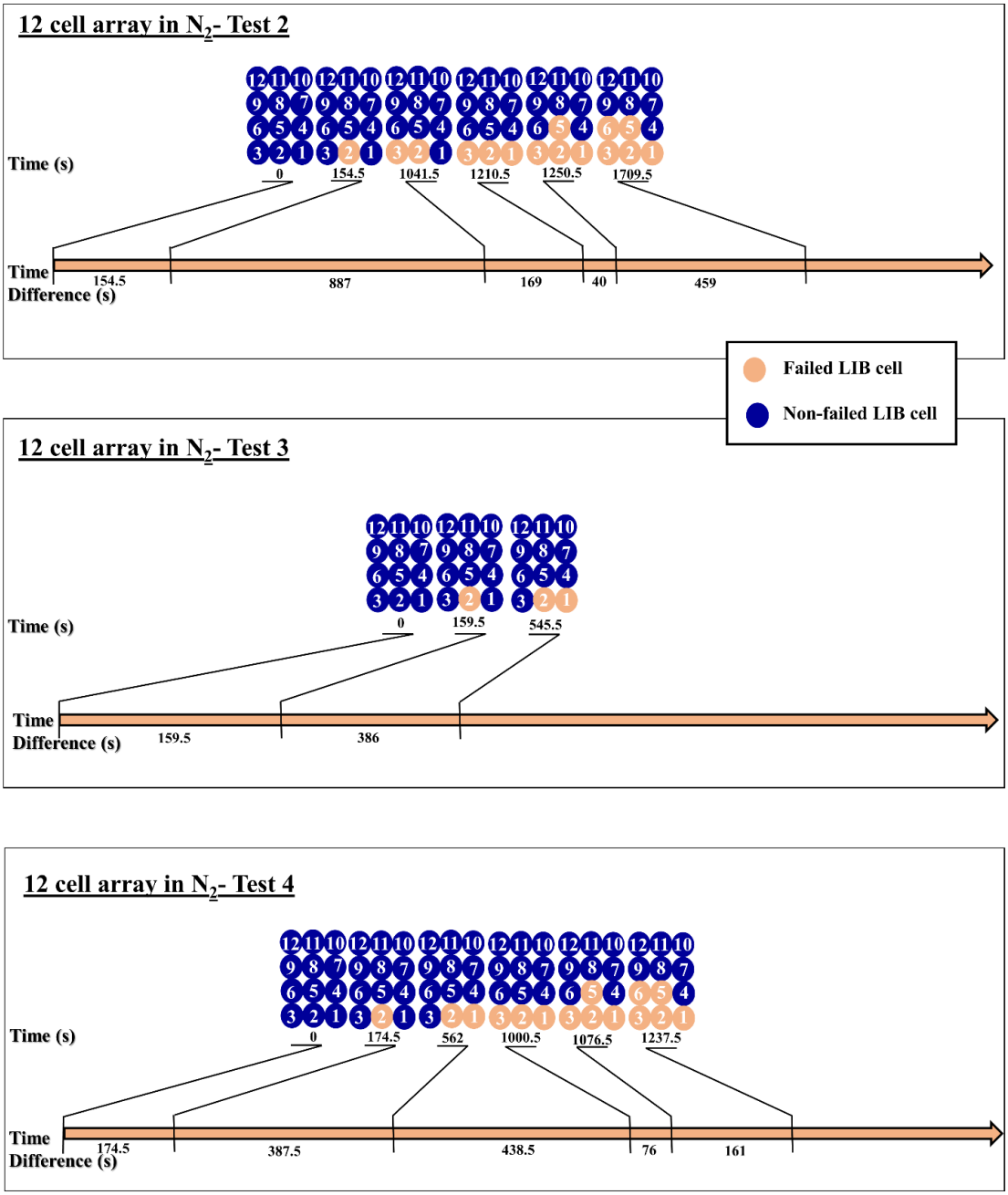

Figure C. 8. Thermal runaway propagation charts for 12 LFP cell arrays in N_2 (186 l min^{-1}). Test repetitions 2, 3, and 4.

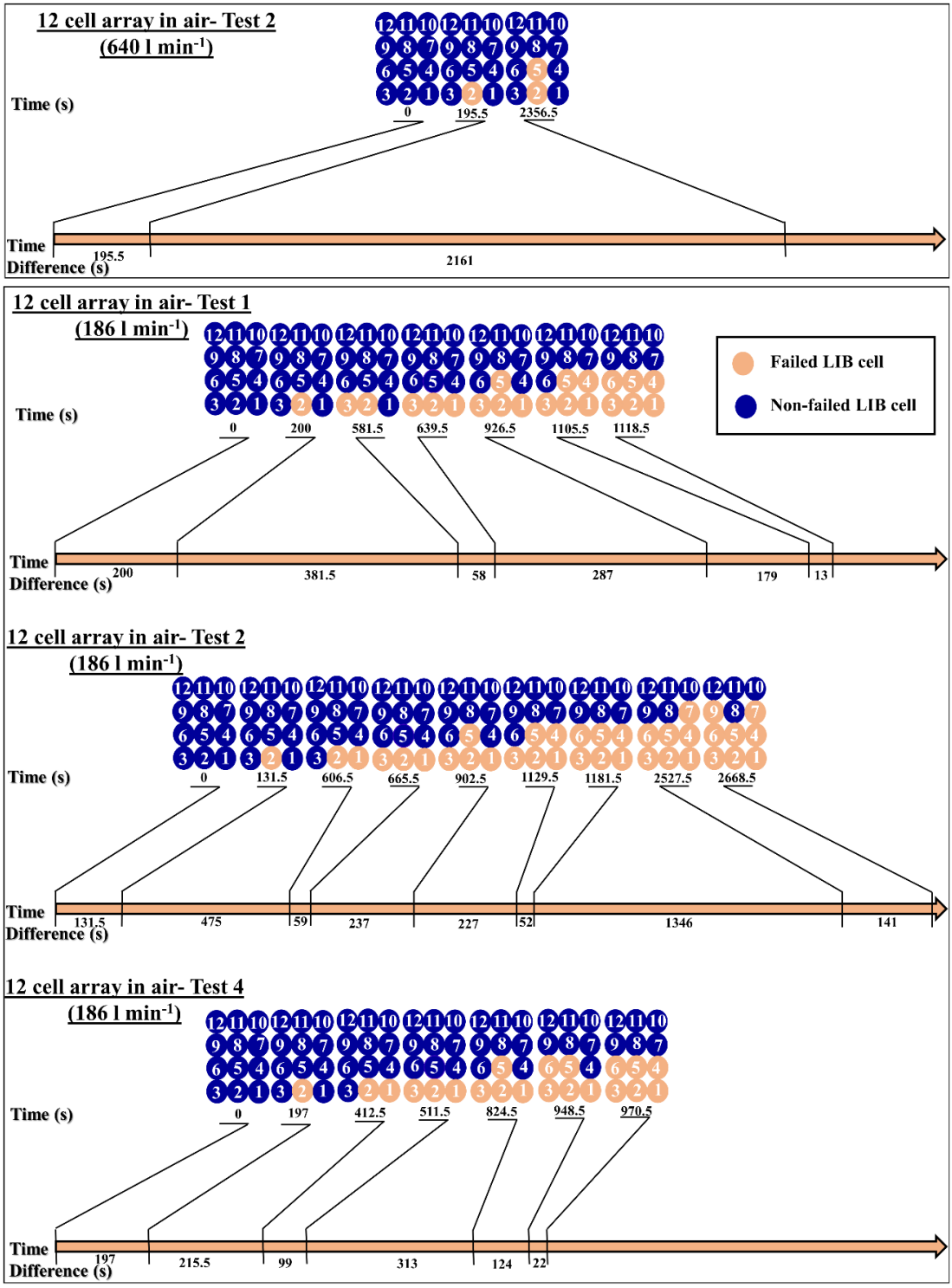

Figure C. 9. Thermal runaway propagation charts for 12 LFP cell arrays in air (640 l min^{-1}); test repetition 2. Thermal runaway propagation charts for 12 LFP cell arrays in air (320 l min^{-1}); test repetitions 1, 2, and 4.

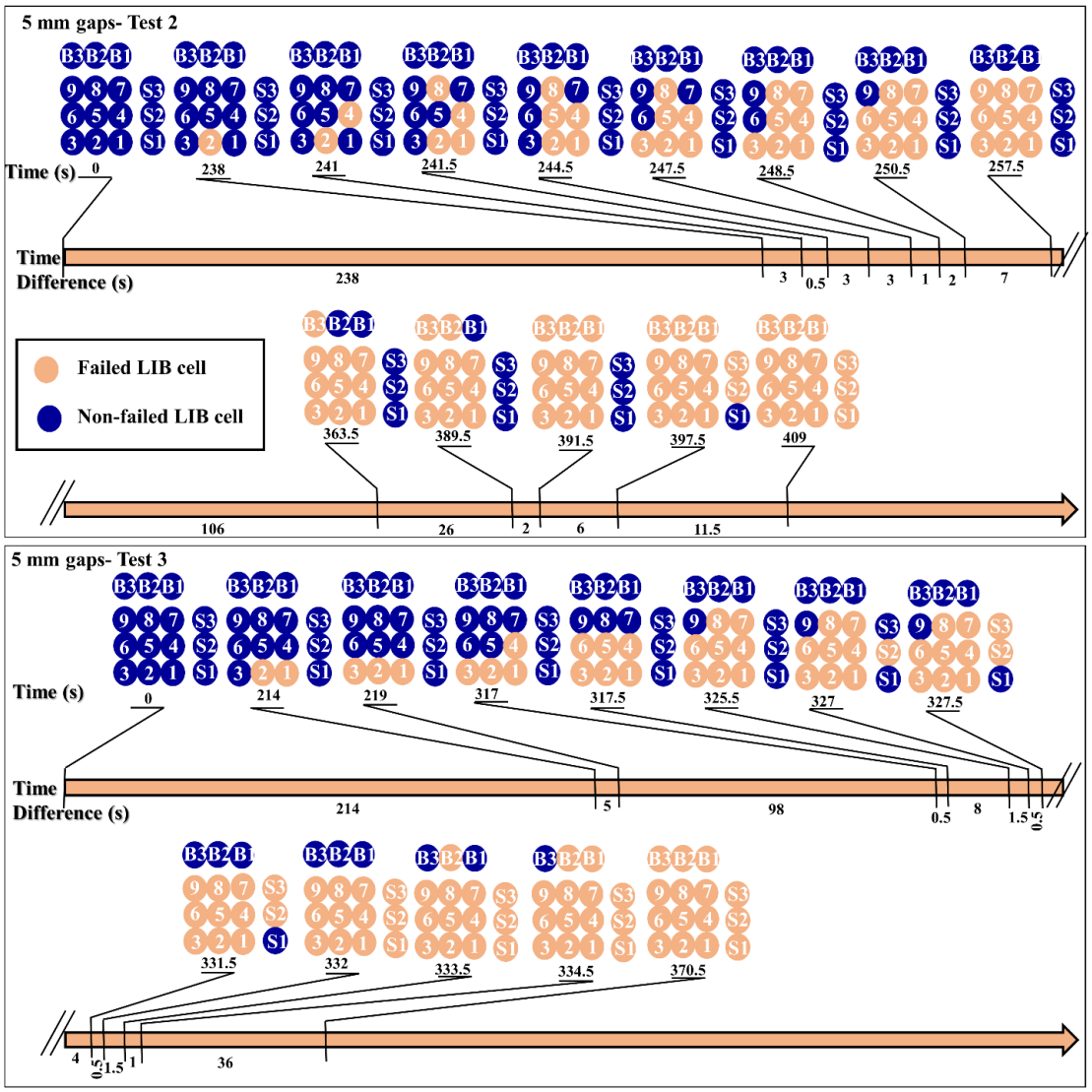

Figure C. 10. Thermal runaway propagation charts for 5 mm gaps tests. Test repetitions 2 and 3.

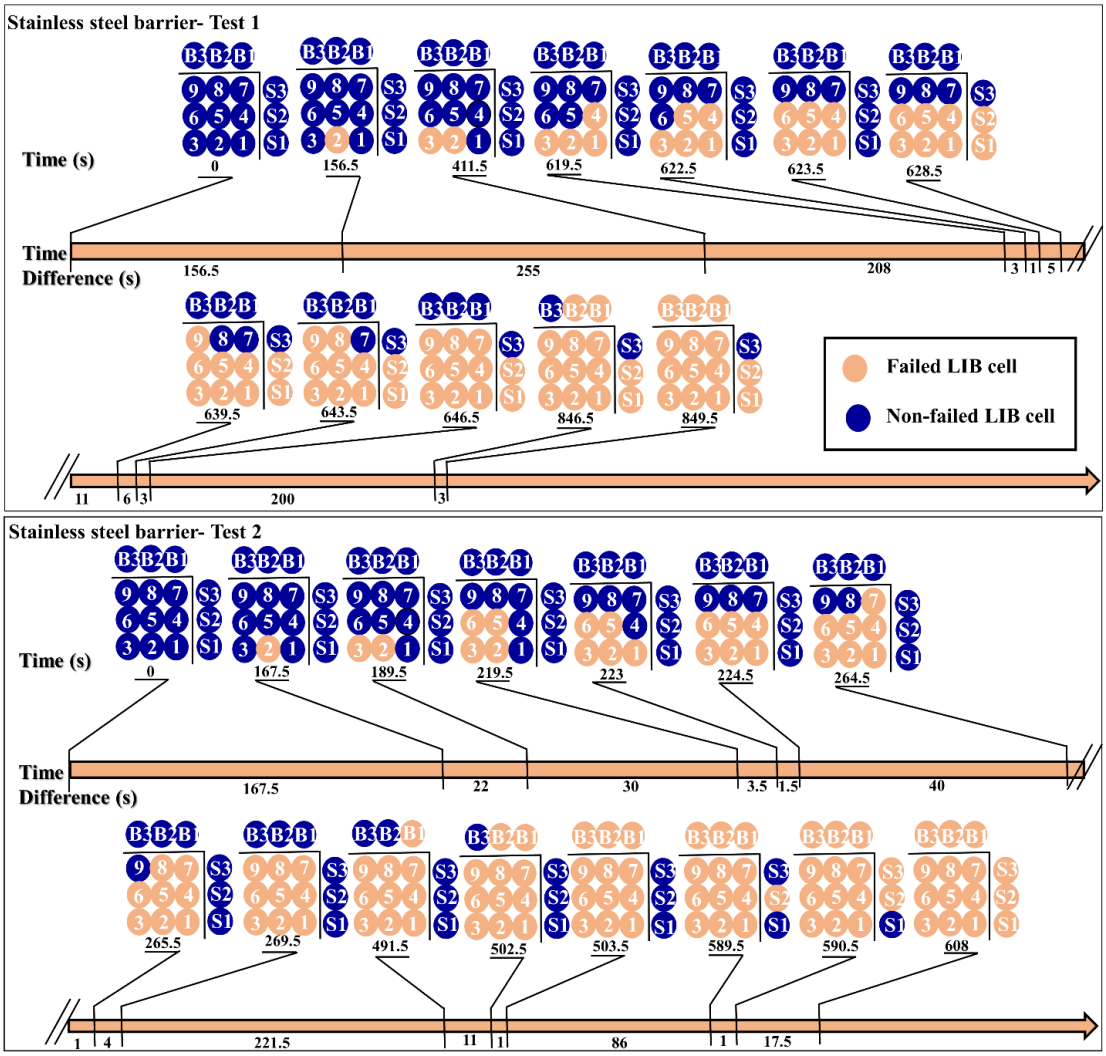

Figure C. 11. Thermal runaway propagation charts for stainless steel barrier tests. Test repetitions 1 and 2.

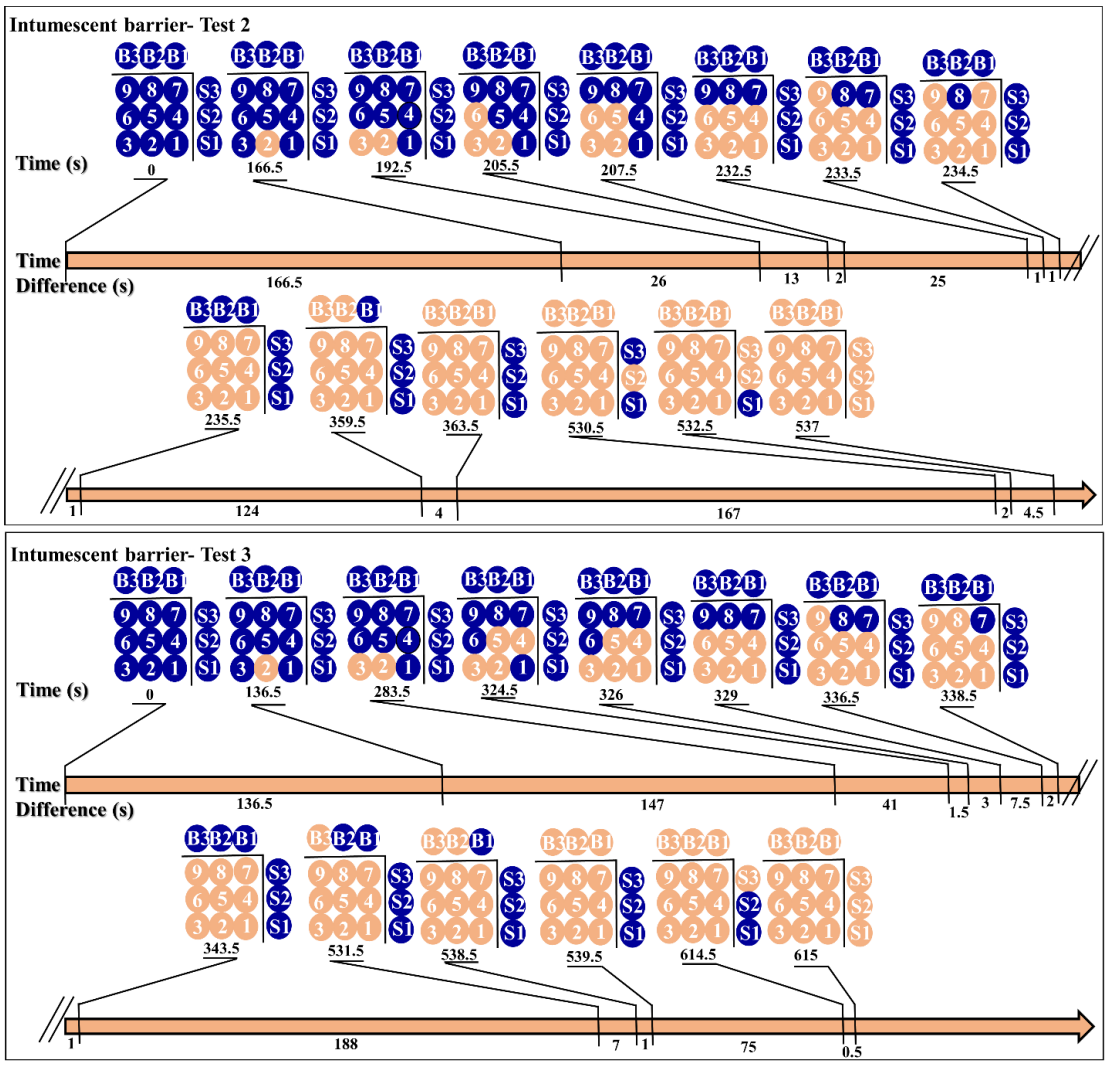

Figure C. 12. Thermal runaway propagation charts for intumescent barrier tests. Test repetitions 2 and 3.

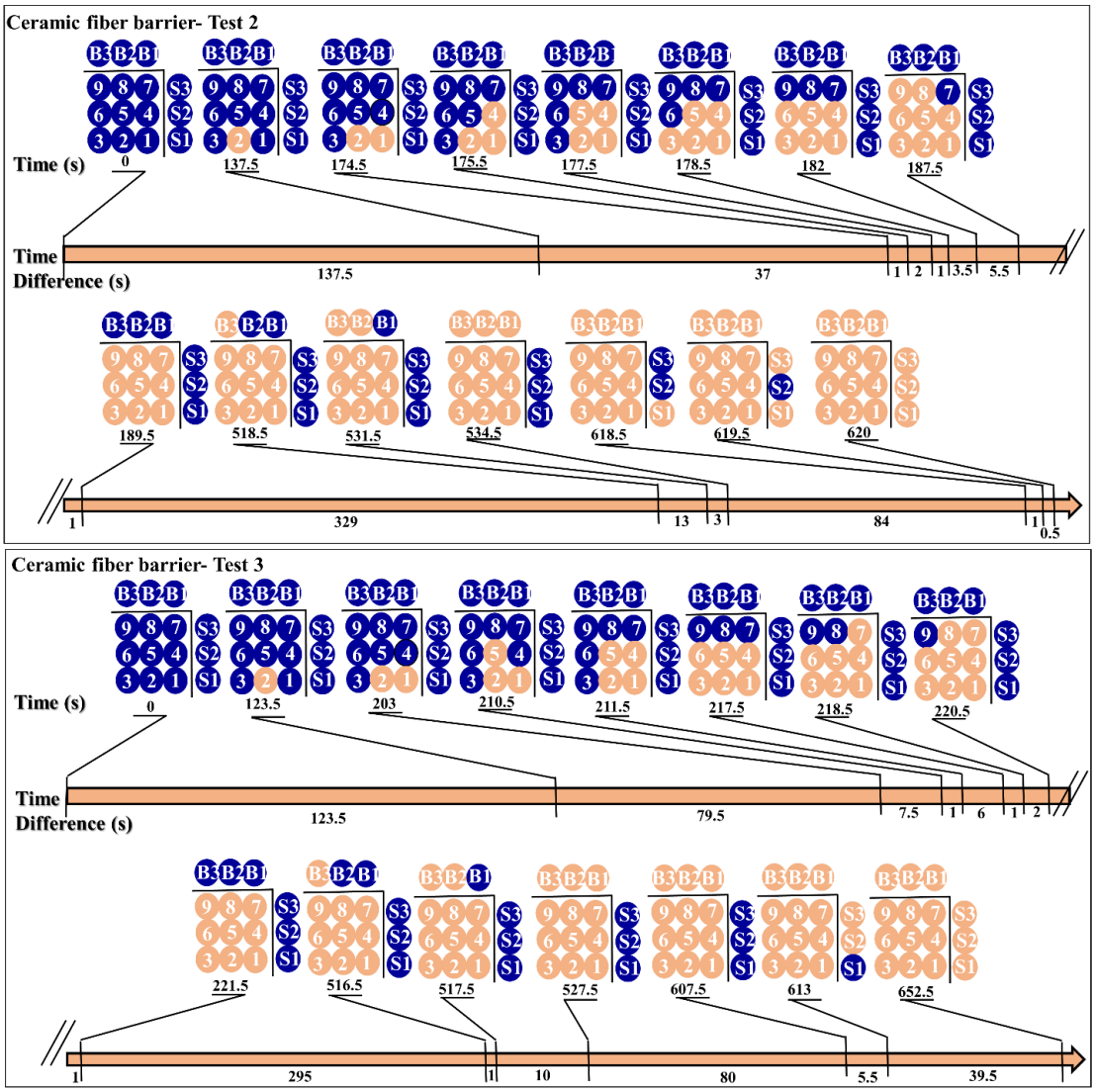

Figure C. 13. Thermal runaway propagation charts for ceramic fiber barrier tests. Test repetitions 2 and 3.

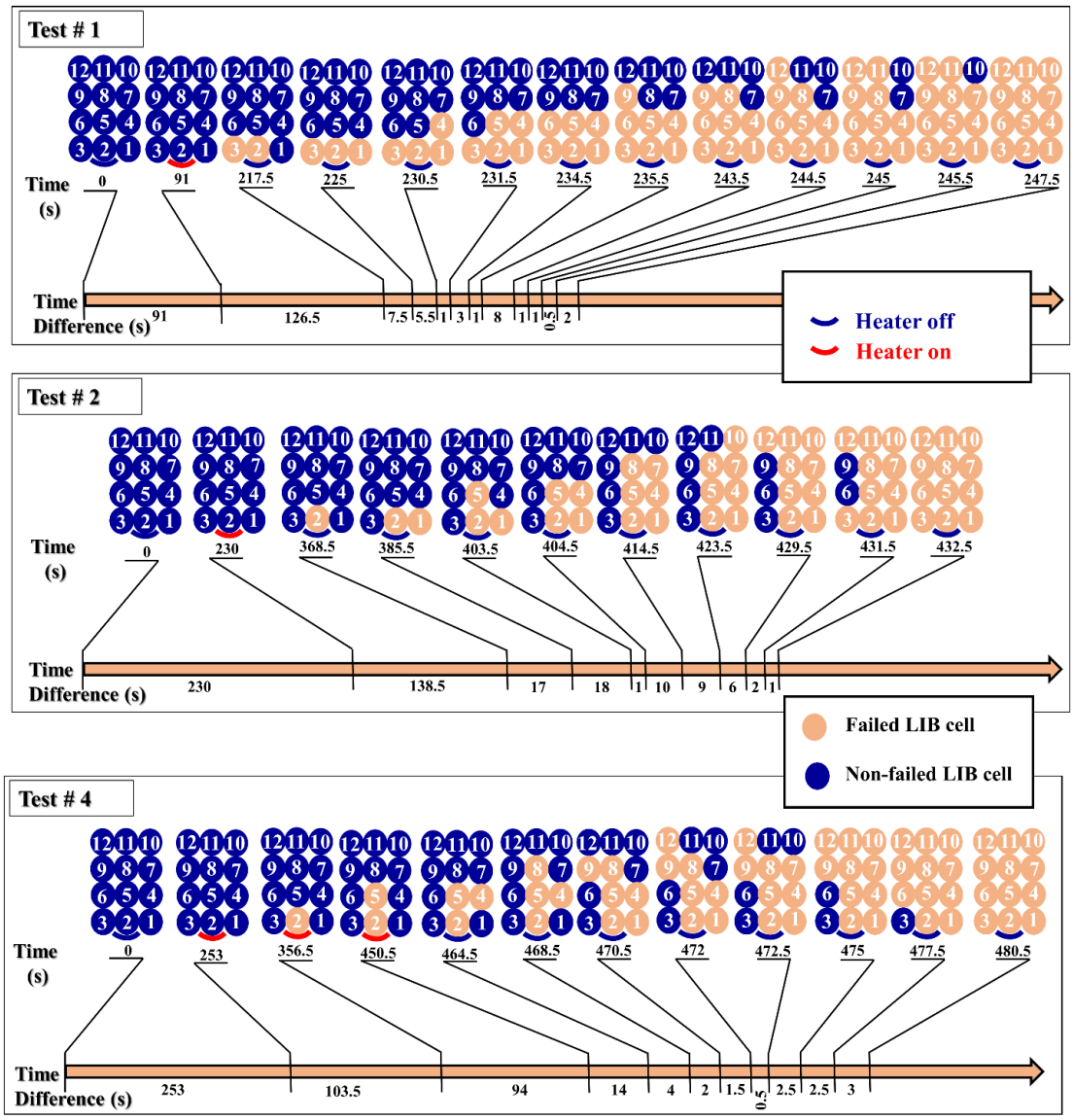

Figure C. 14. Thermal runaway propagation charts for 8.5 vol.% Novec1230 tests. Test repetitions 1, 2 and 4.

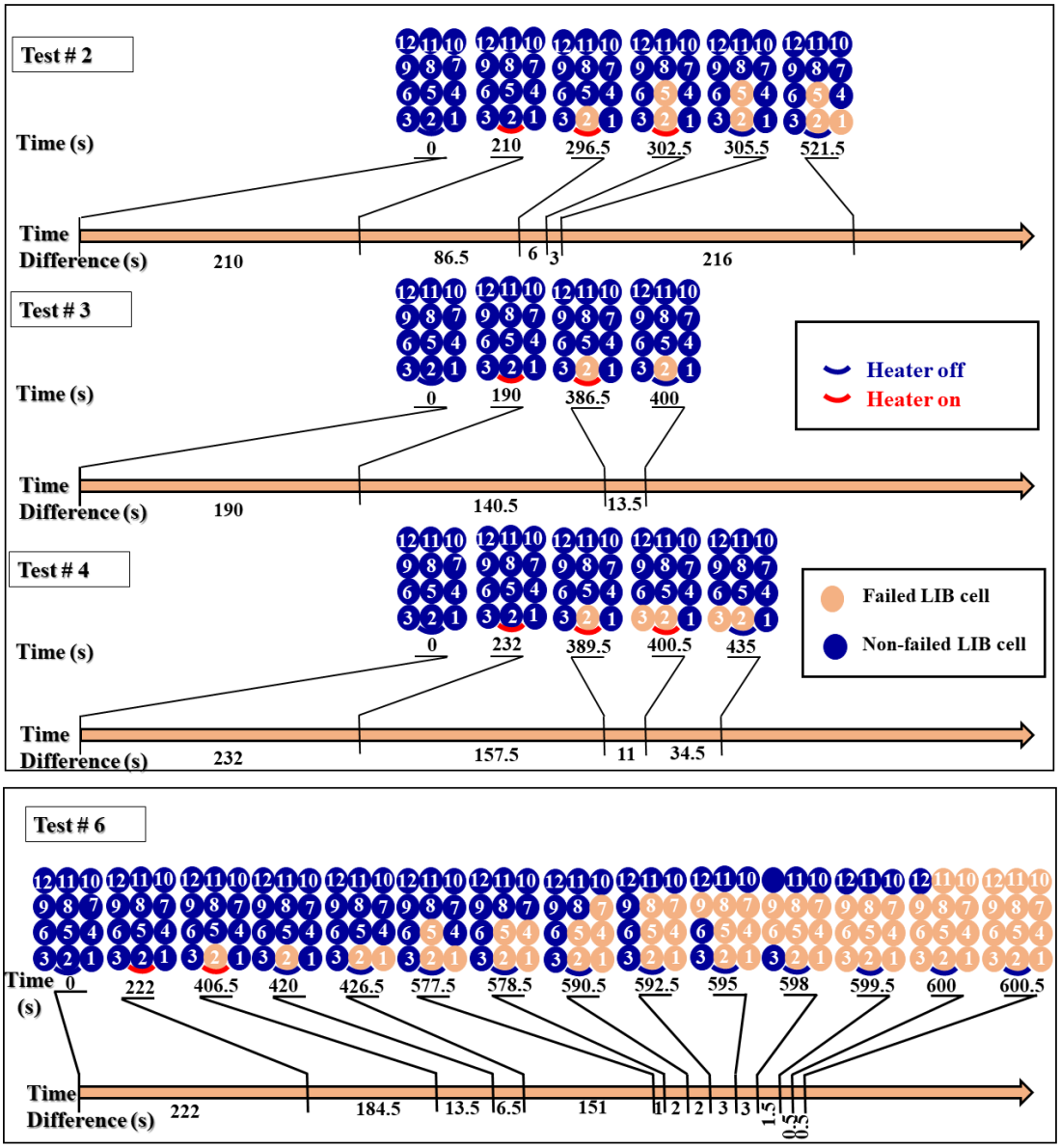

Figure C. 15. Thermal runaway propagation charts for 15.2 vol.% Novec1230 tests. Test repetitions 2, 3, 4 and 6.

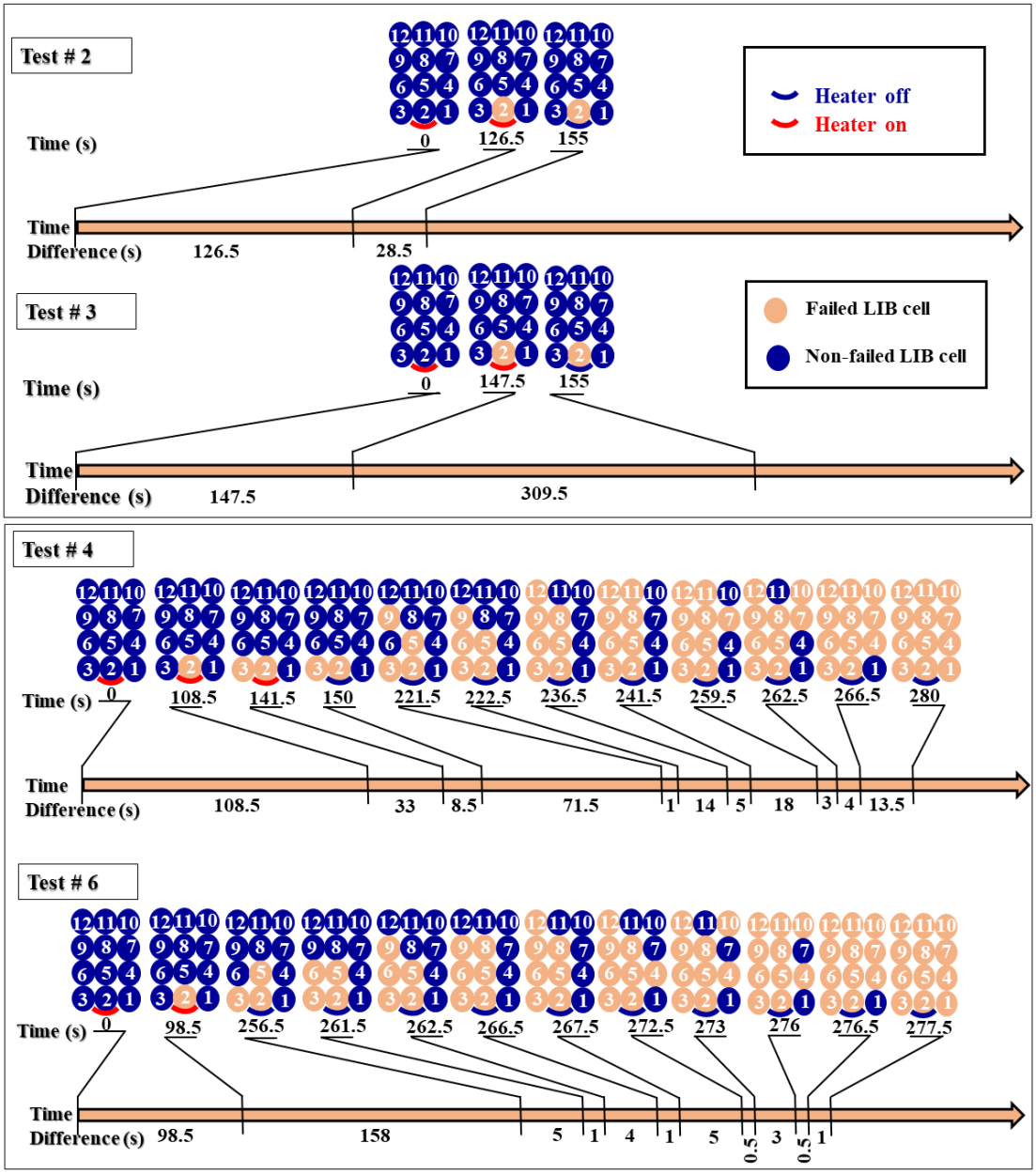

Figure C. 16. Thermal runaway propagation charts for 11.1 wt.% water mist tests. Test repetitions 2, 3, 4 and 6.

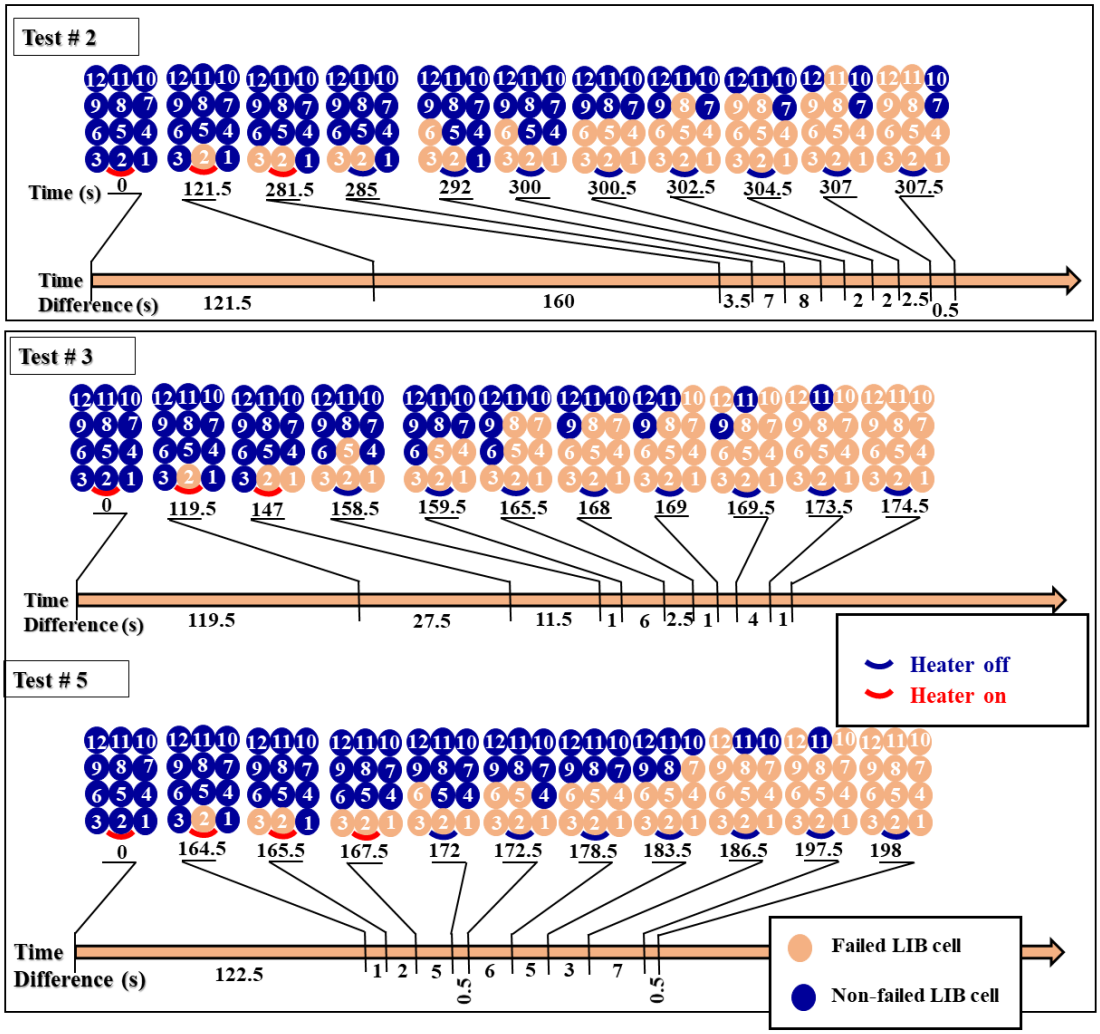

Figure C. 17. Thermal runaway propagation charts for 14.1 wt.% water mist tests. Test repetitions 2, 3 and 5.

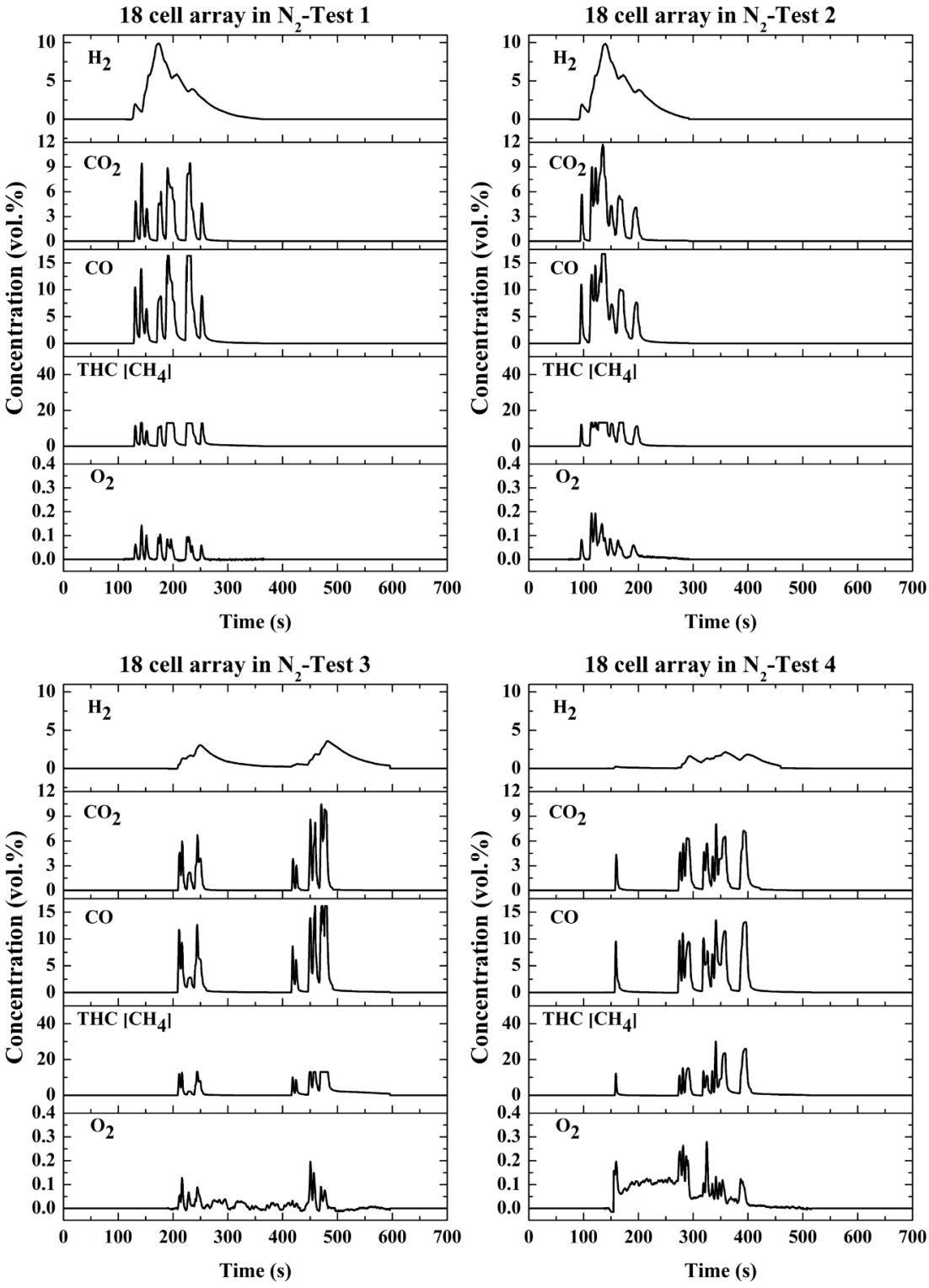

Figure C. 18. Gas concentration profiles obtained from test repetitions 1, 2, 3, and 4 on 18 LCO cell arrays tested in N_2 (186 l min^{-1}).

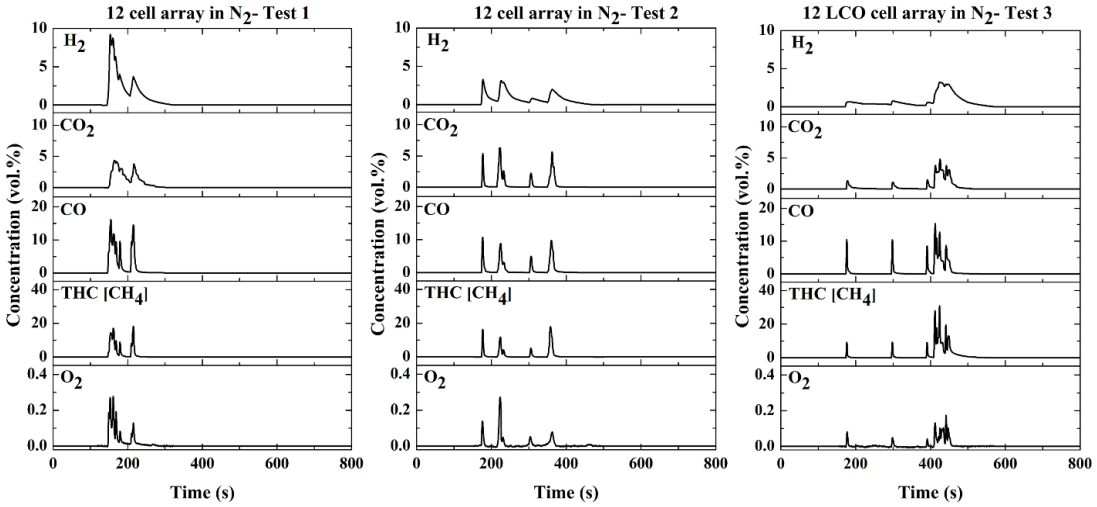

Figure C. 19. Gas concentration profiles obtained from tests on 12 LCO cell arrays tested in N_2 (186 l min^{-1}). Test repetitions 1, 2, and 3.

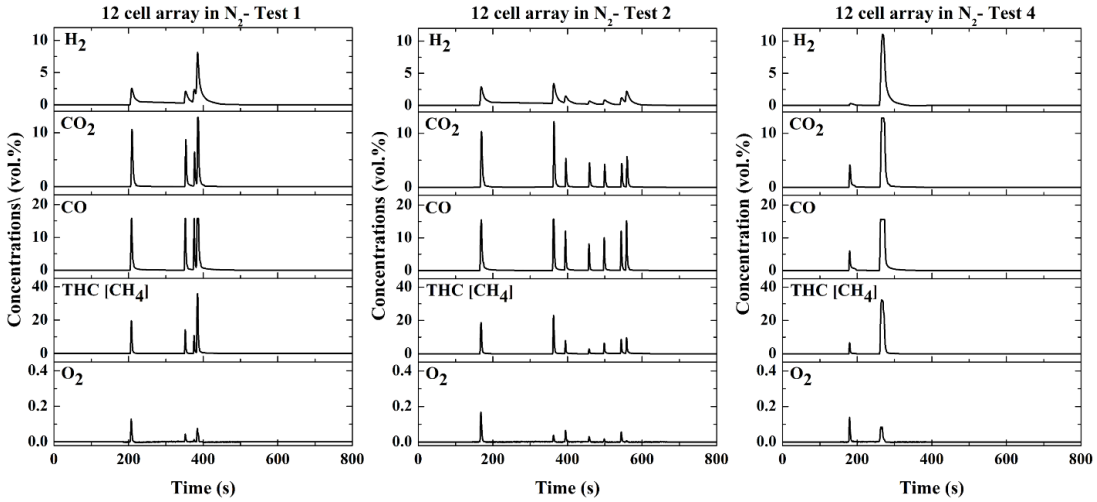

Figure C. 20. Gas concentration profiles obtained from test repetitions 1, 2, and 4 on 12 NMC cell arrays tested in N_2 (186 l min^{-1}).

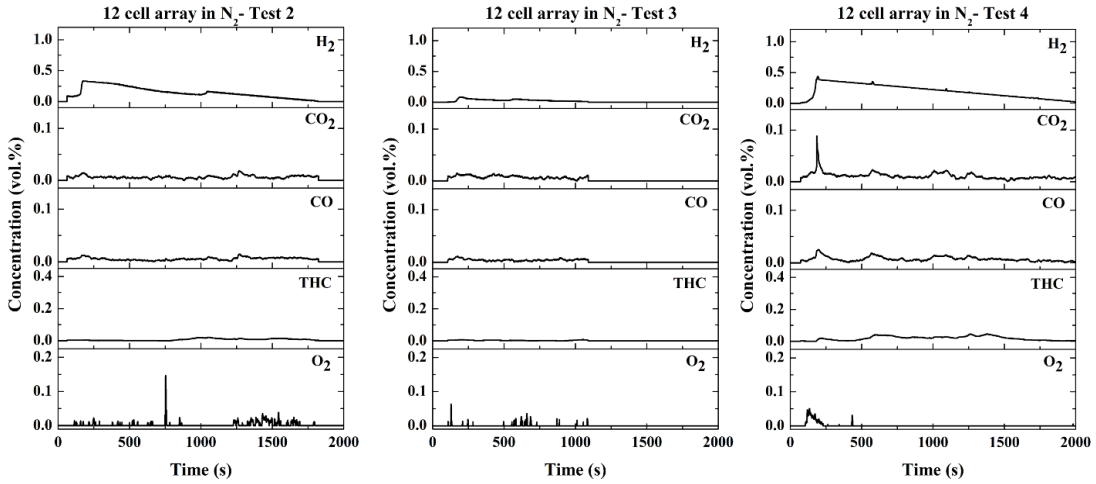

Figure C. 21. Gas concentration profiles obtained from test repetitions 2, 3, and 4 on 12 LFP cell arrays tested in N_2 (186 l min^{-1}).

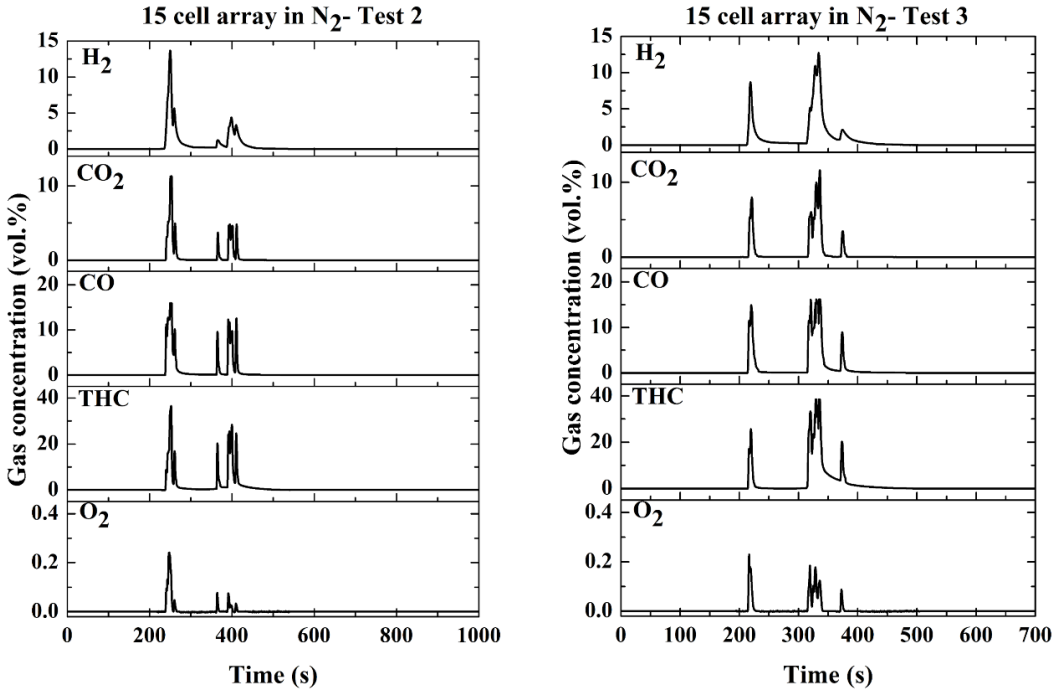

Figure C. 22. Gas concentration profiles obtained from test repetitions 2 and 3 on 15 LCO cell arrays tested in N_2 (186 l min^{-1}) with 5 mm empty gaps.

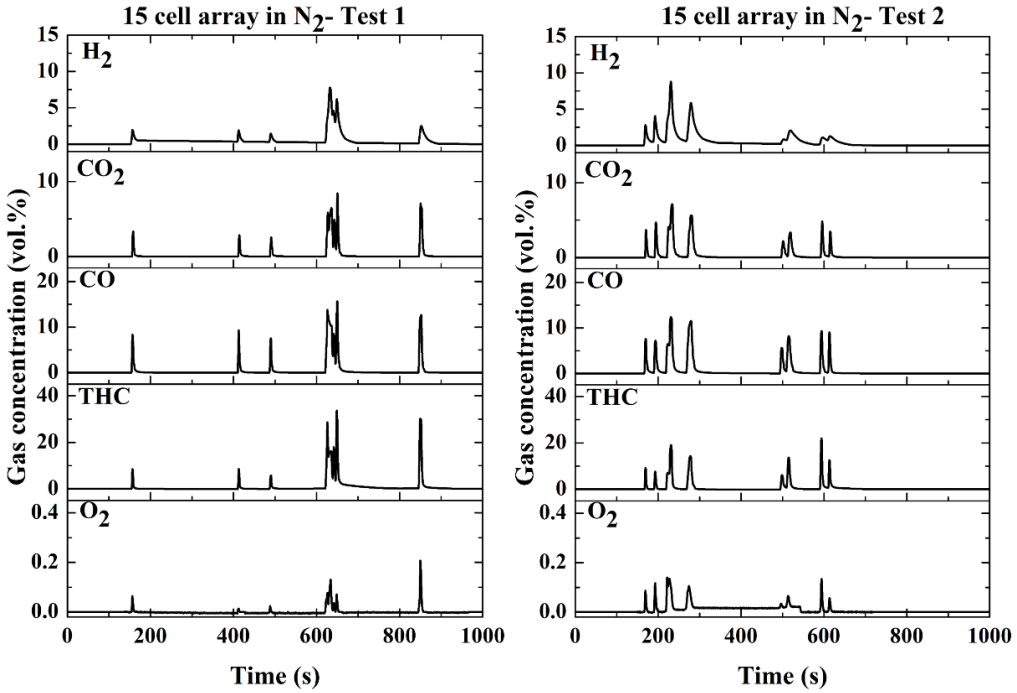

Figure C. 23. Gas concentration profiles obtained from test repetitions 1 and 2 on 15 LCO cell arrays tested in N_2 (186 l min^{-1}) with stainless steel barrier.

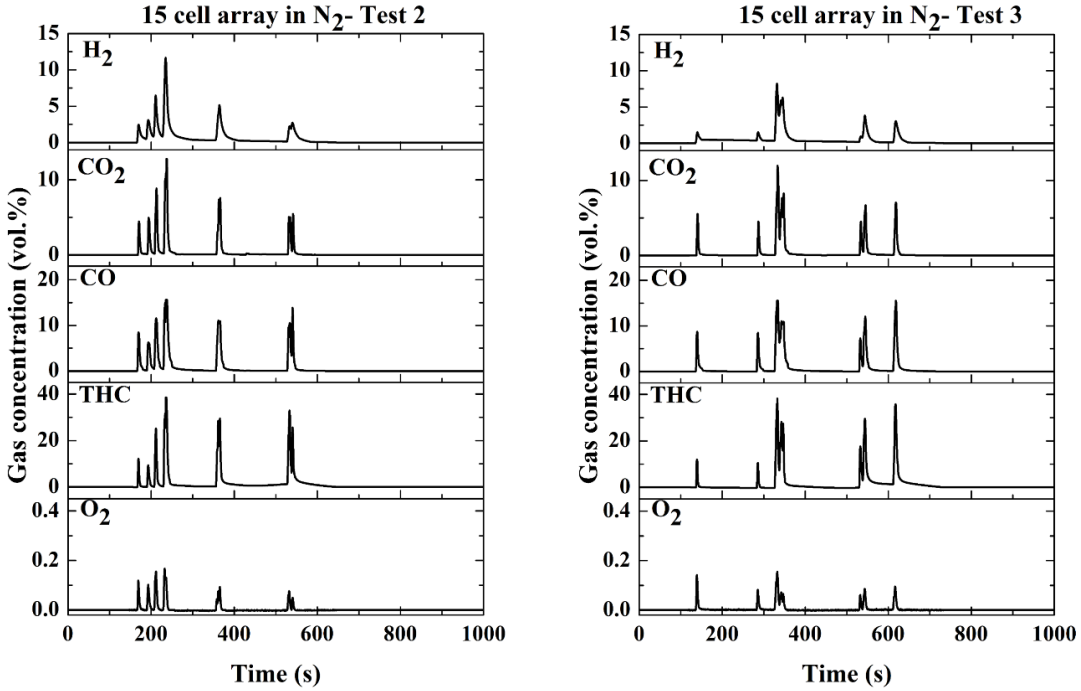

Figure C. 24. Gas concentration profiles obtained from test repetitions 2 and 3 on 15 LCO cell arrays tested in N_2 (186 l min^{-1}) with intumescent barrier.

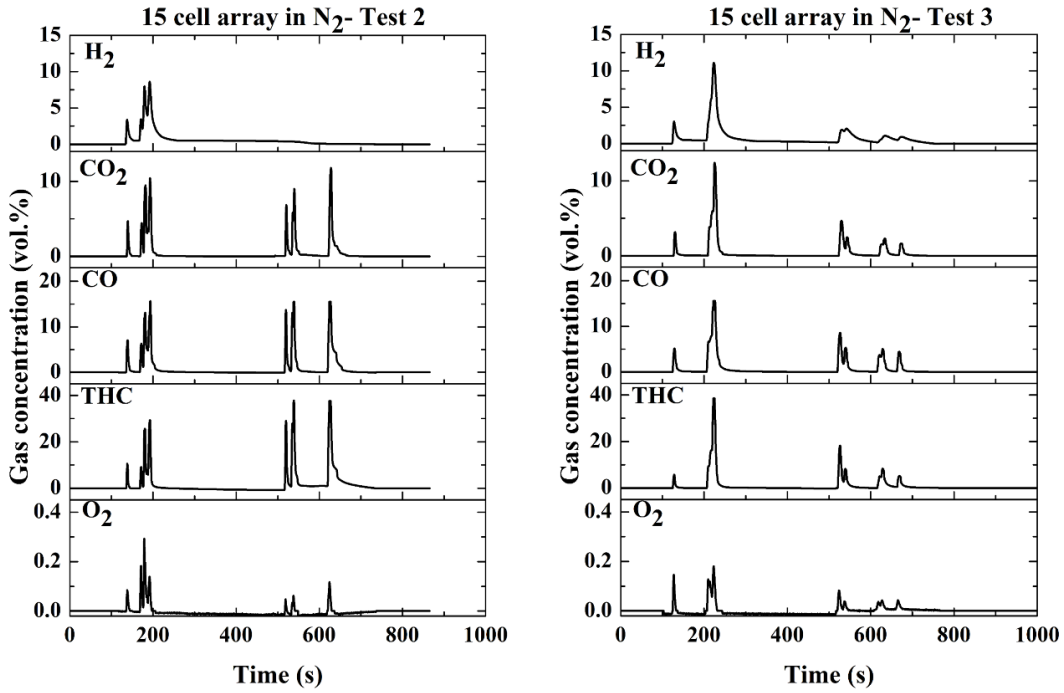

Figure C. 25. Gas concentration profiles obtained from test repetitions 2 and 3 on 15 LCO cell arrays tested in N_2 (186 l min^{-1}) with ceramic fiber barrier.

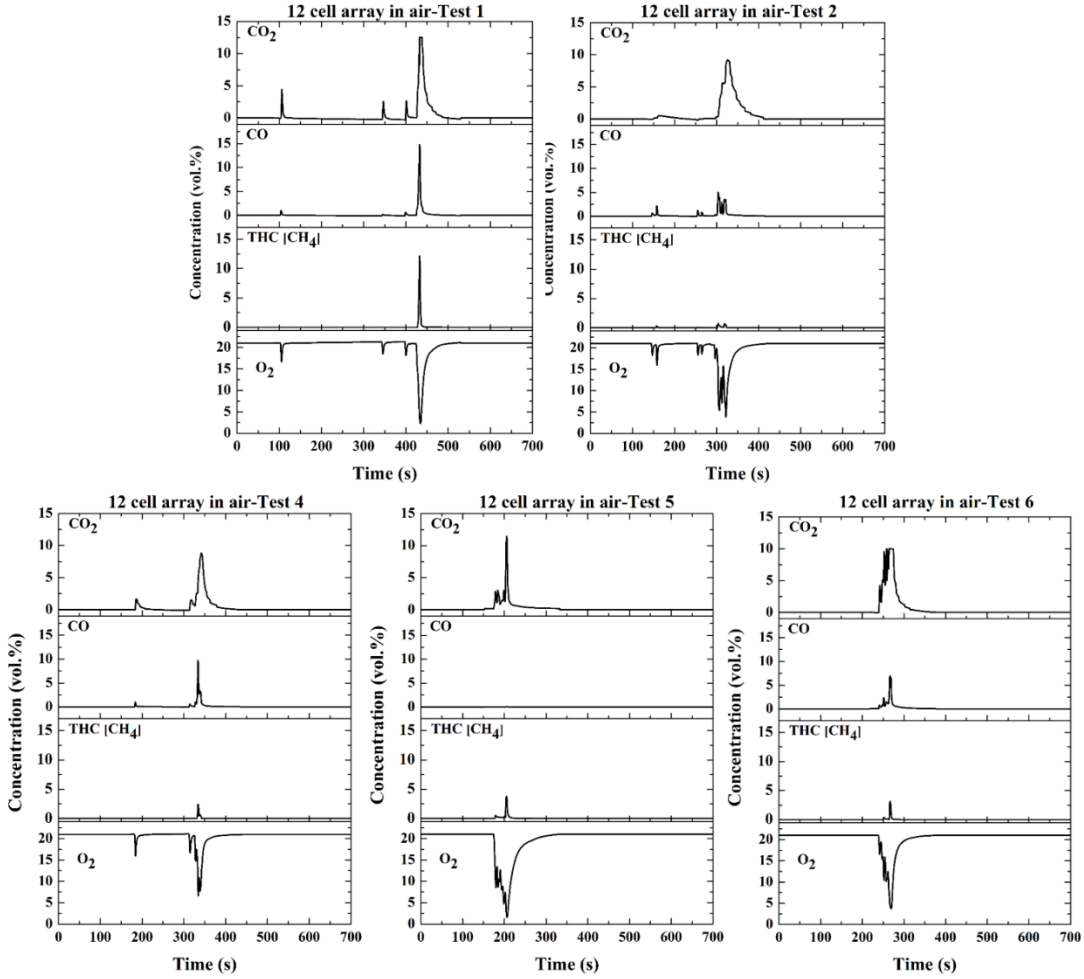

Figure C. 26. Gas concentration profiles obtained from test repetitions 1, 2, 4, 5 and 6 on 12 LCO cell arrays tested in air (640 l min^{-1}).

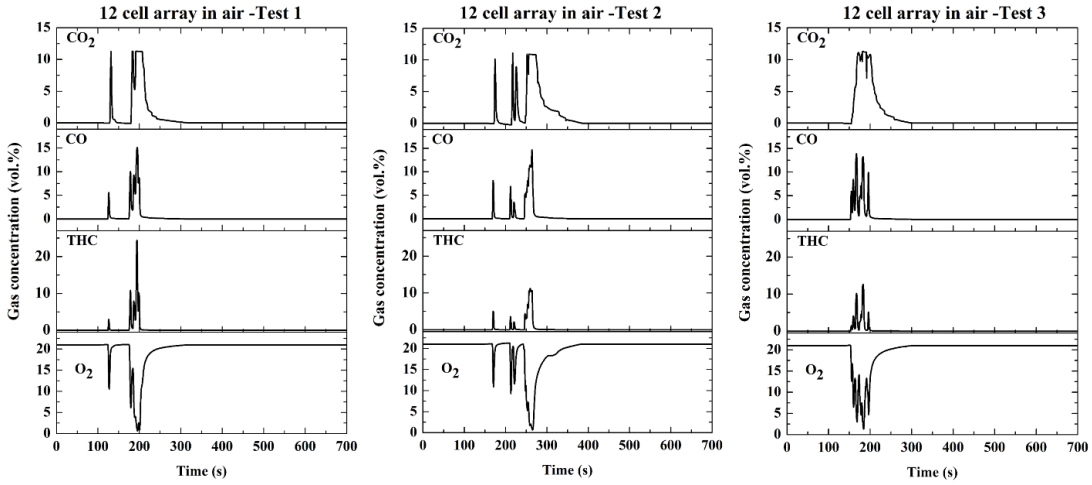

Figure C. 27. Gas concentration profiles obtained from test repetitions 1, 2, and 3 on 12 LCO cell arrays tested in air (320 l min^{-1}).

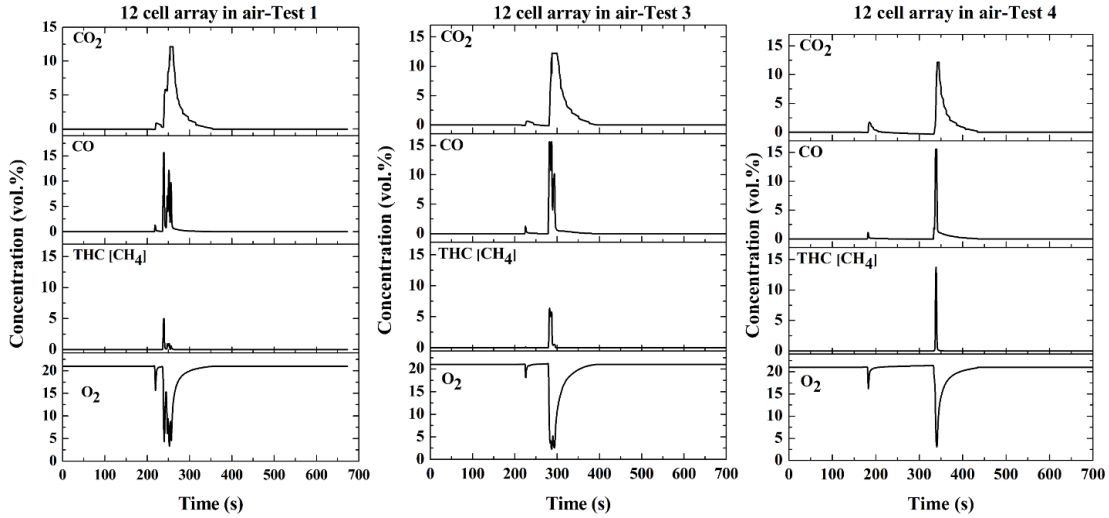

Figure C. 28. Gas concentration profiles obtained from test repetitions 1, 2, and 3 on 12 NMC cell arrays tested in air (640 l min^{-1}).

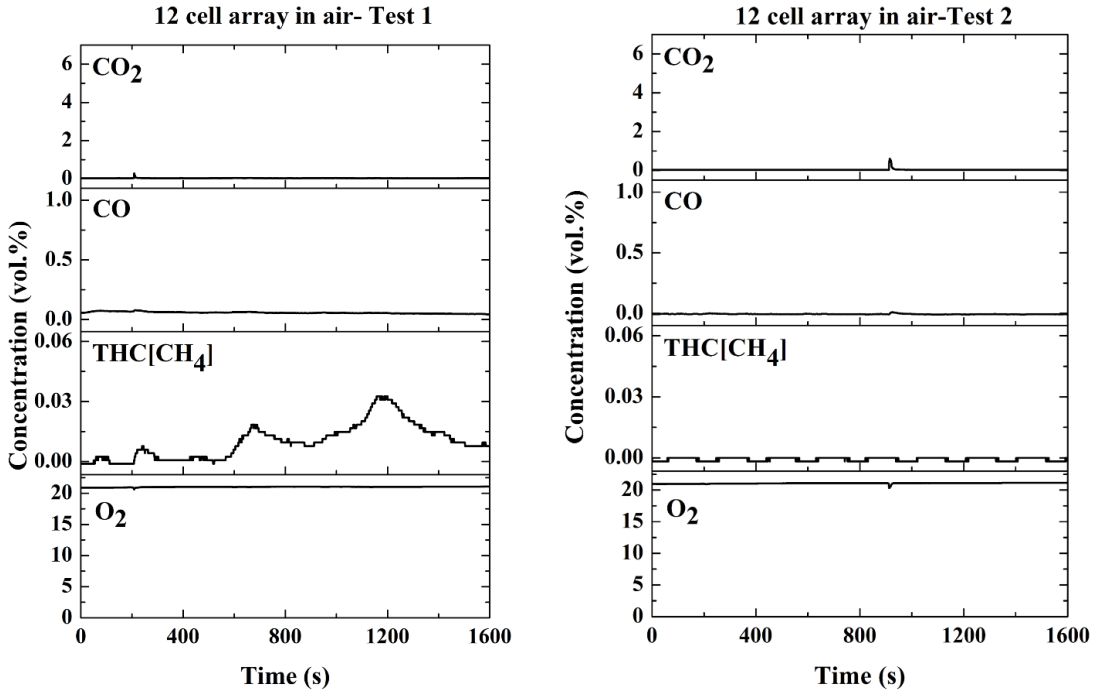

Figure C. 29. Gas concentration profiles obtained from test repetitions 1 and 2 on 12 LFP cell arrays tested in air (640 l min^{-1}).

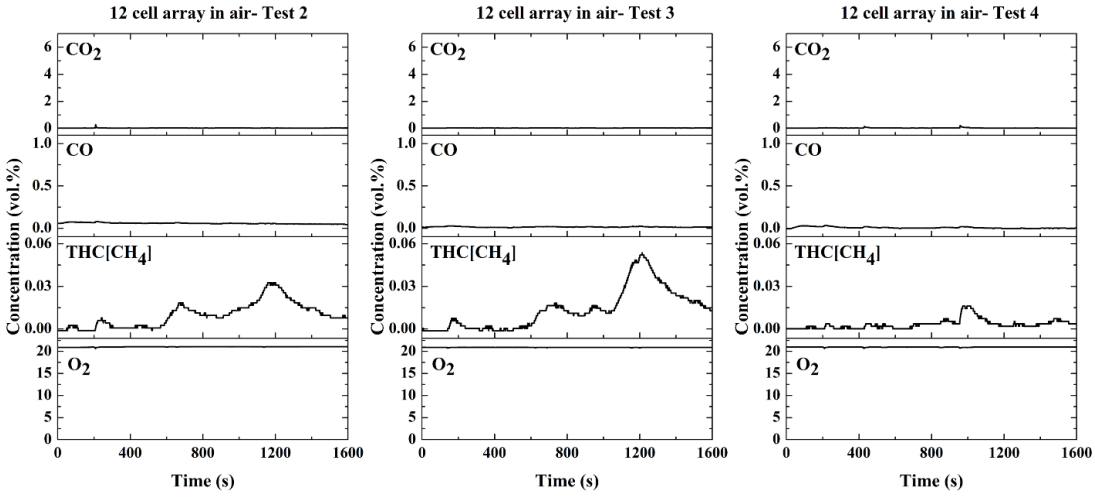

Figure C. 30. Gas concentration profiles obtained from test repetitions 2, 3, and 4 on 12 LFP cell arrays tested in air (186 l min^{-1}).

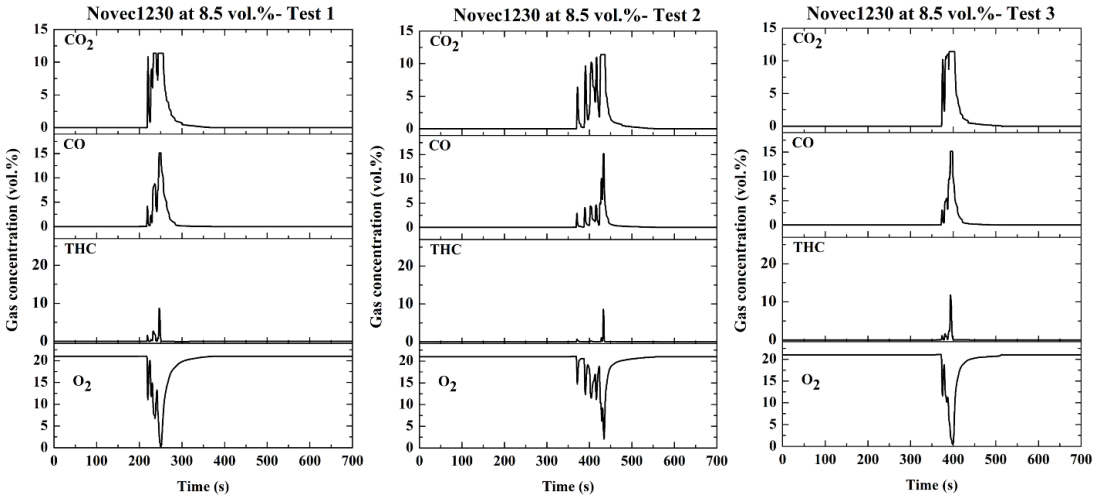

Figure C. 31. Gas concentration profiles obtained from 8.5 vol.% Novec1230 test repetitions 1, 2, and 3.

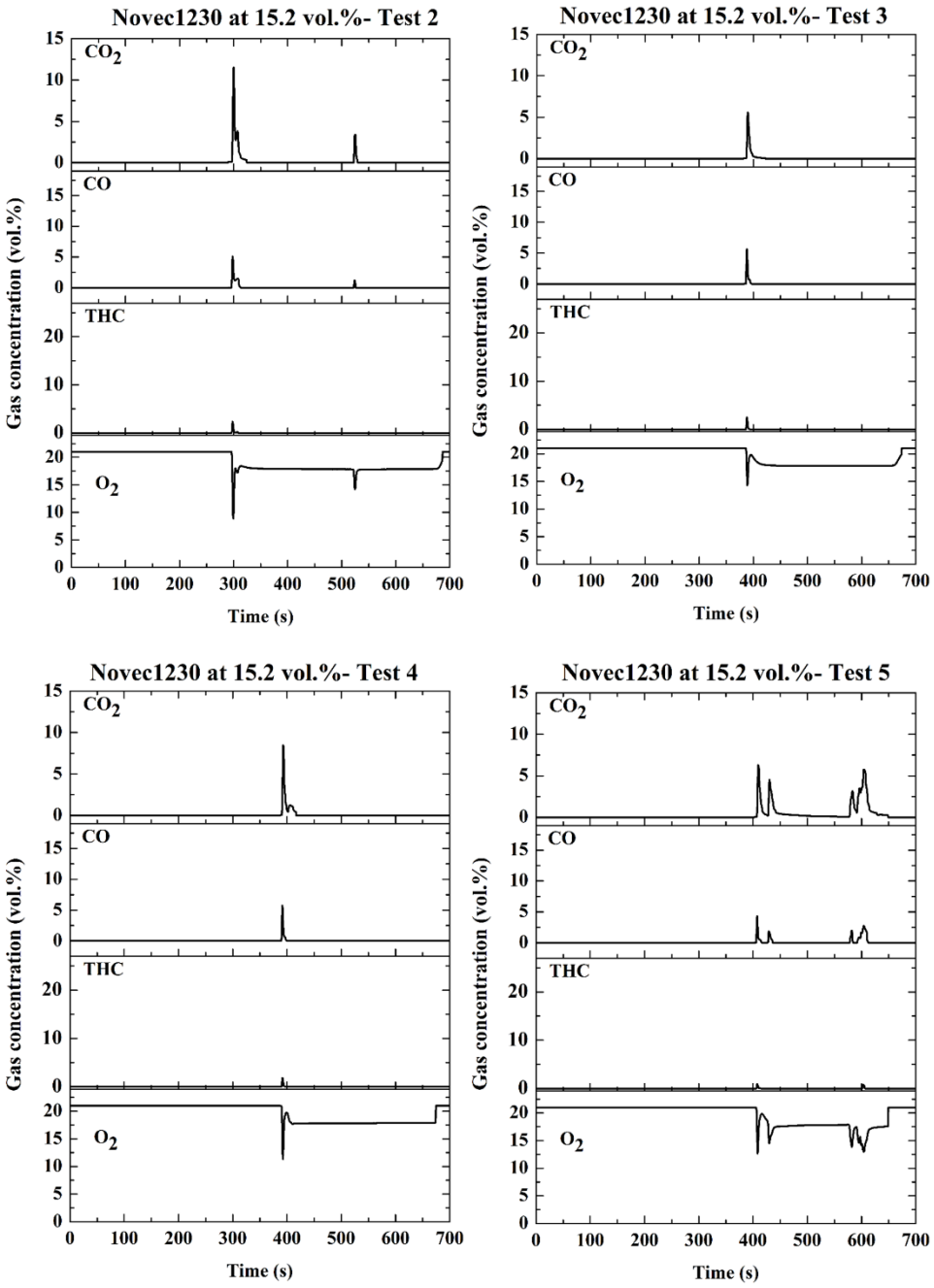

Figure C. 32. Gas concentration profiles obtained from 15.2 vol.% Novec1230 test repetitions 2, 3, 4, and 5.

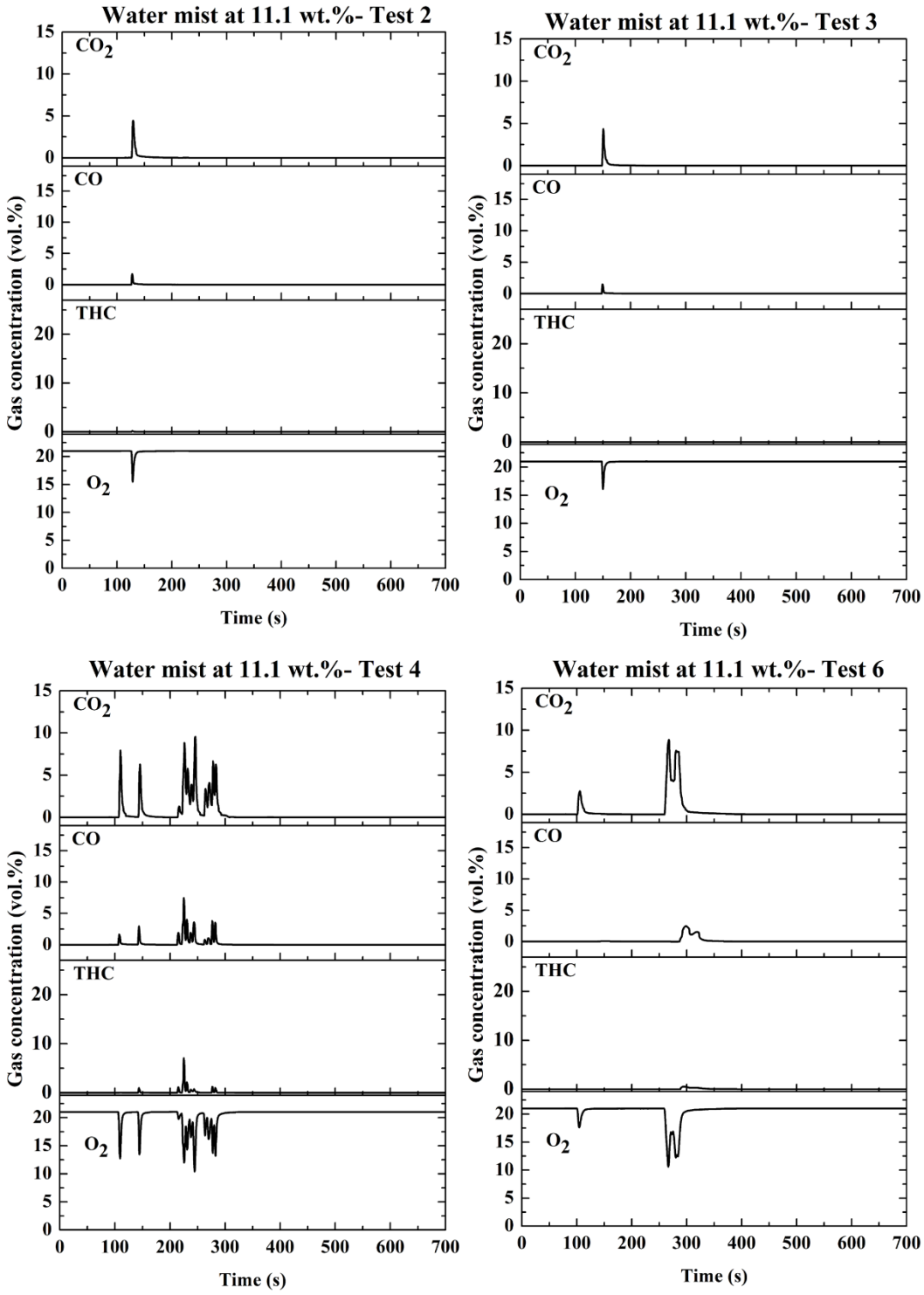

Figure C. 33. Gas concentration profiles obtained from 11.1 wt.% water mist test repetitions 2, 3, 4, and 6.

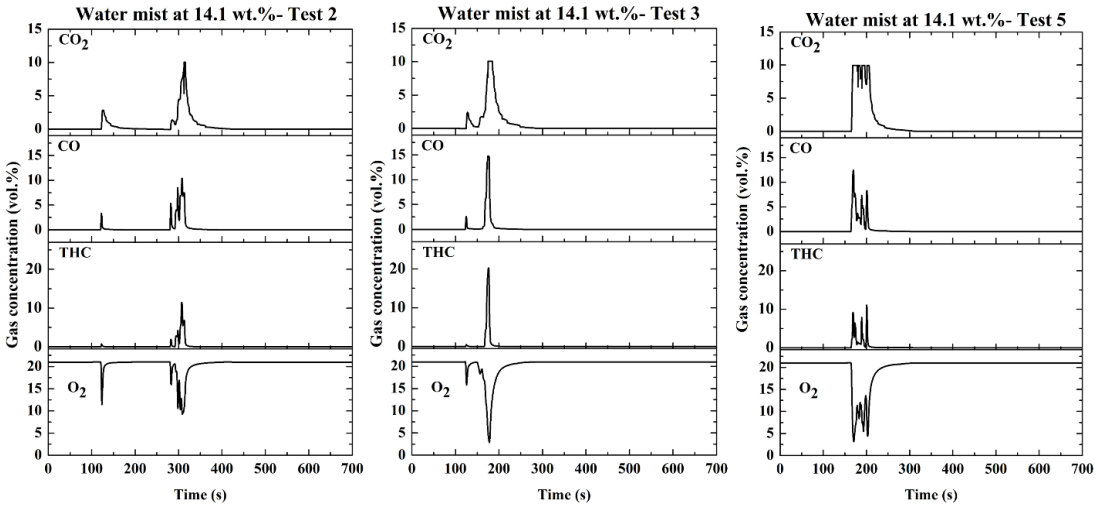

Figure C. 34. Gas concentration profiles obtained from 14.1 wt.% water mist test repetitions 2, 3, and 5.

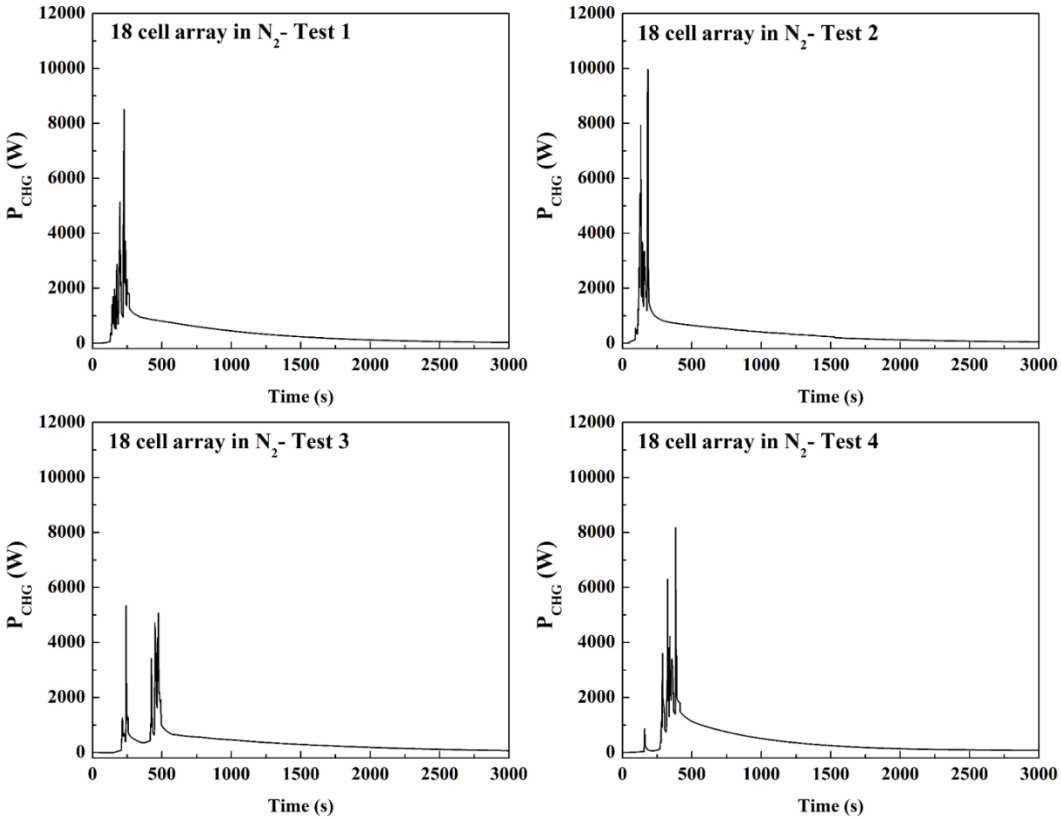

Figure C. 35. Rates of chemical heat generation computed for 18 cell arrays examined in an N_2 environment. Test repetitions 1, 2, 3, and 4.

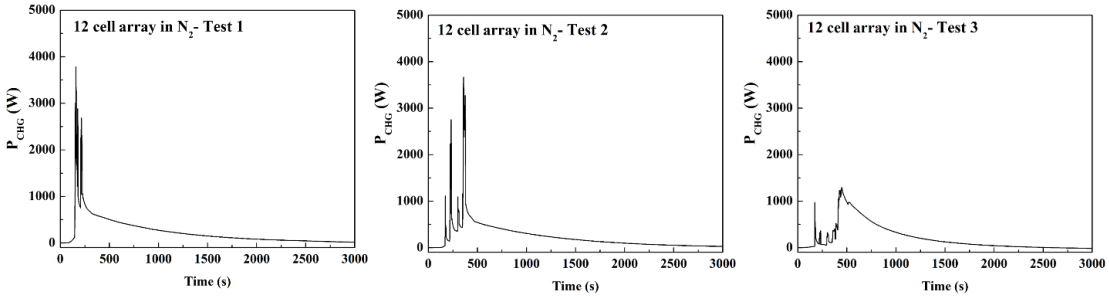

Figure C. 36. Rates of chemical heat generation computed for 12 cell arrays examined in an N_2 environment. Test repetitions 1, 2, and 3.

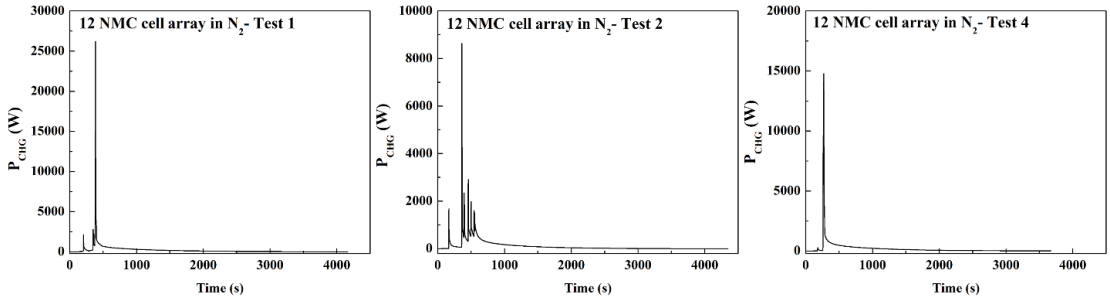

Figure C. 37. Rates of chemical heat generation computed for representative 12 NMC cell arrays tested in N_2 (186 l min^{-1}). Test repetitions 1, 2, and 4.

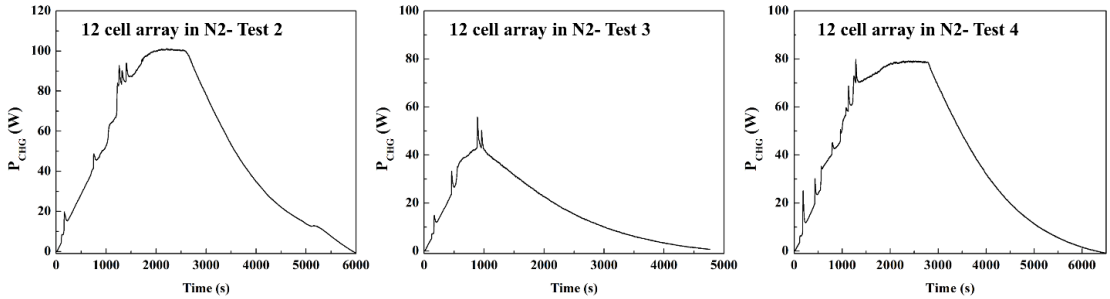

Figure C. 38. Rates of chemical heat generation computed for representative 12 LFP cell arrays tested in N_2 (186 l min^{-1}). Test repetitions 2, 3, and 4.

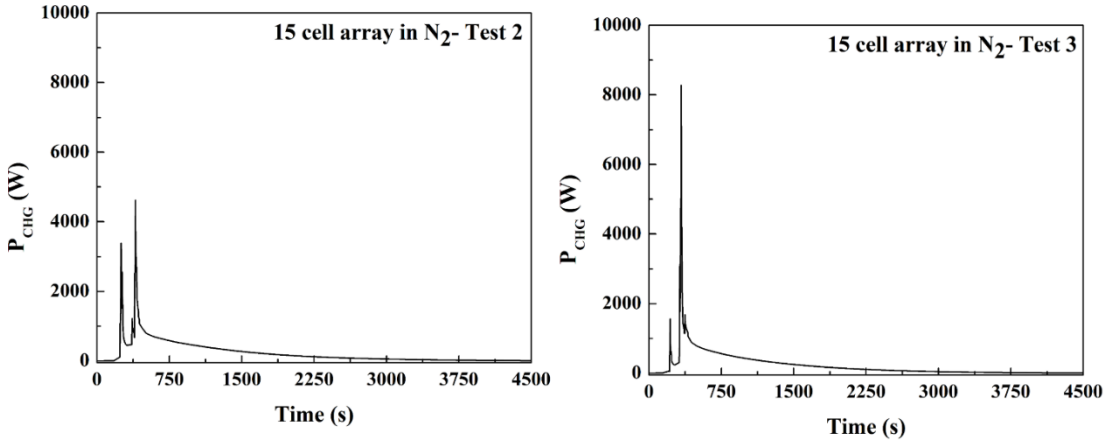

Figure C. 39. Rates of chemical heat profiles obtained from test repetitions 2 and 3 on 15 LCO cell arrays tested in N_2 (186 l min^{-1}) with 5 mm empty gaps.

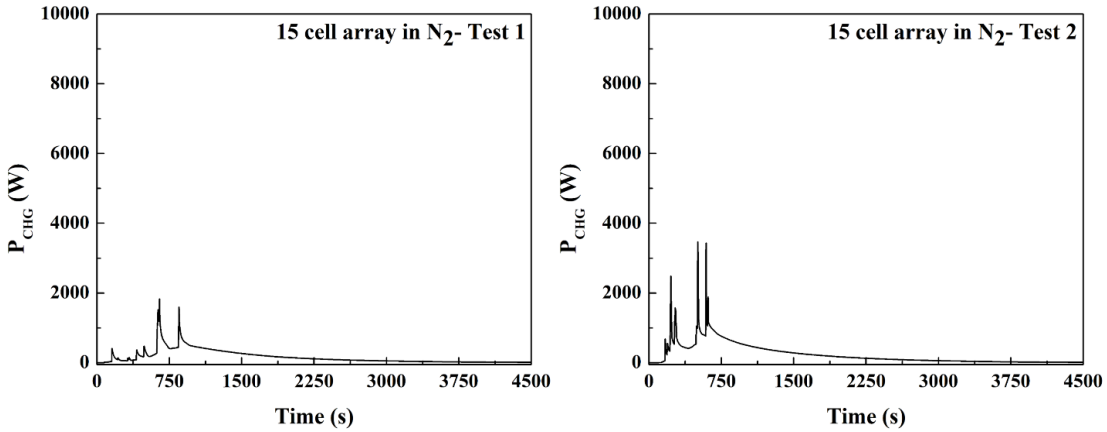

Figure C. 40. Rates of chemical heat generation obtained from test repetitions 1 and 2 on 15 LCO cell arrays tested in N_2 (186 l min^{-1}) with stainless steel barrier.

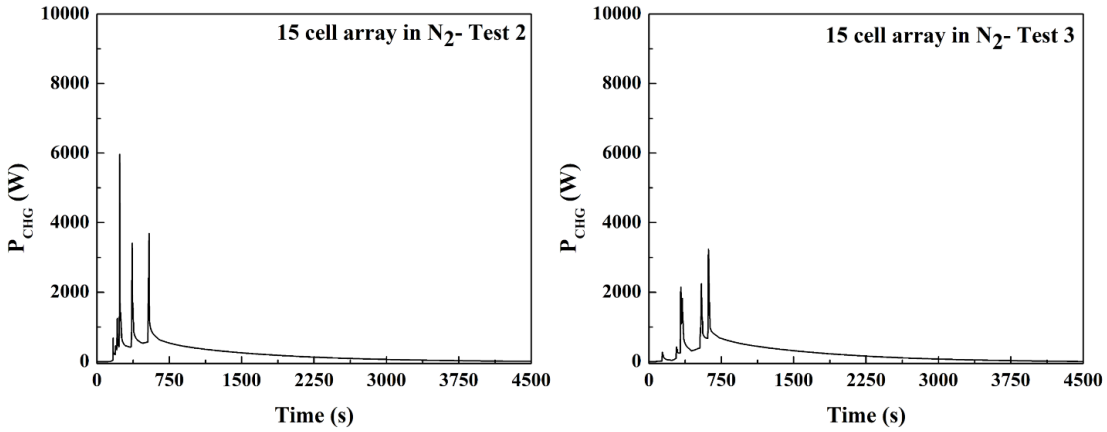

Figure C. 41. Rates of chemical heat generation obtained from test repetitions 2 and 3 on 15 LCO cell arrays tested in N_2 (186 l min^{-1}) with intumescent barrier.

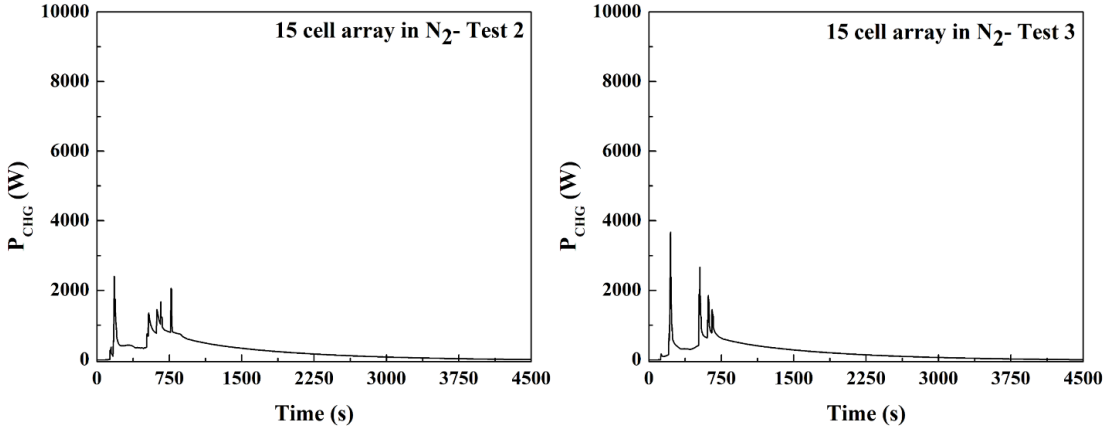

Figure C. 42. Rates of chemical heat profiles obtained from test repetitions 2 and 3 on 15 LCO cell arrays tested in N_2 (186 l min^{-1}) with ceramic fiber barrier.

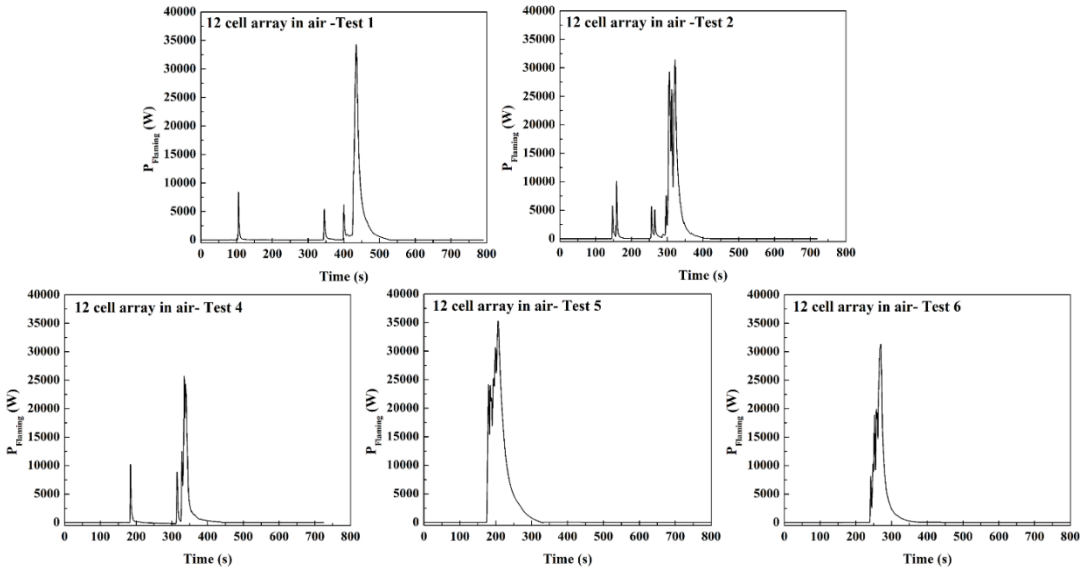

Figure C. 43. Heat release rate due to flaming combustion of ejected materials from 12 LCO cell arrays tested in air (640 l min^{-1}). Test repetitions 1, 2, 4, 5 and 6.

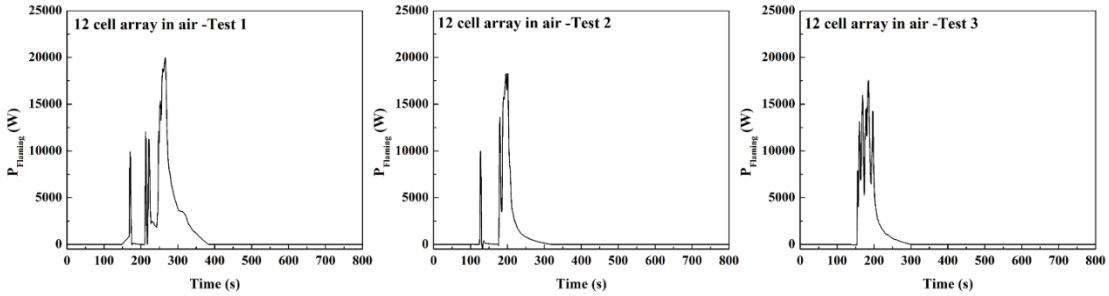

Figure C. 44. Heat release rate due to flaming combustion of ejected materials from 12 LCO cell arrays tested in air (320 l min^{-1}). Test repetitions 1, 2, and 3.

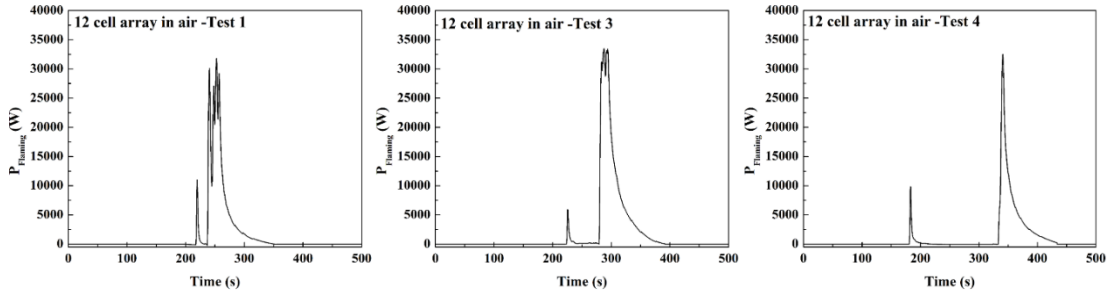

Figure C. 45. Heat release rate due to flaming combustion of ejected materials from 12 NMC cell arrays tested in air (640 l min^{-1}). Test repetitions 1, 3, and 4.

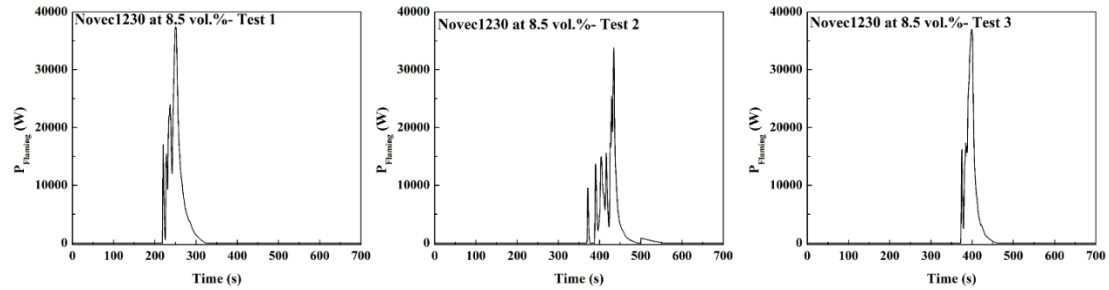

Figure C. 46. Heat release rate due to flaming combustion of ejected materials from 12 LCO cell array tested in air and suppressed with Novec1230 at 8.5 vol.%. Test repetitions 1, 2, and 3.

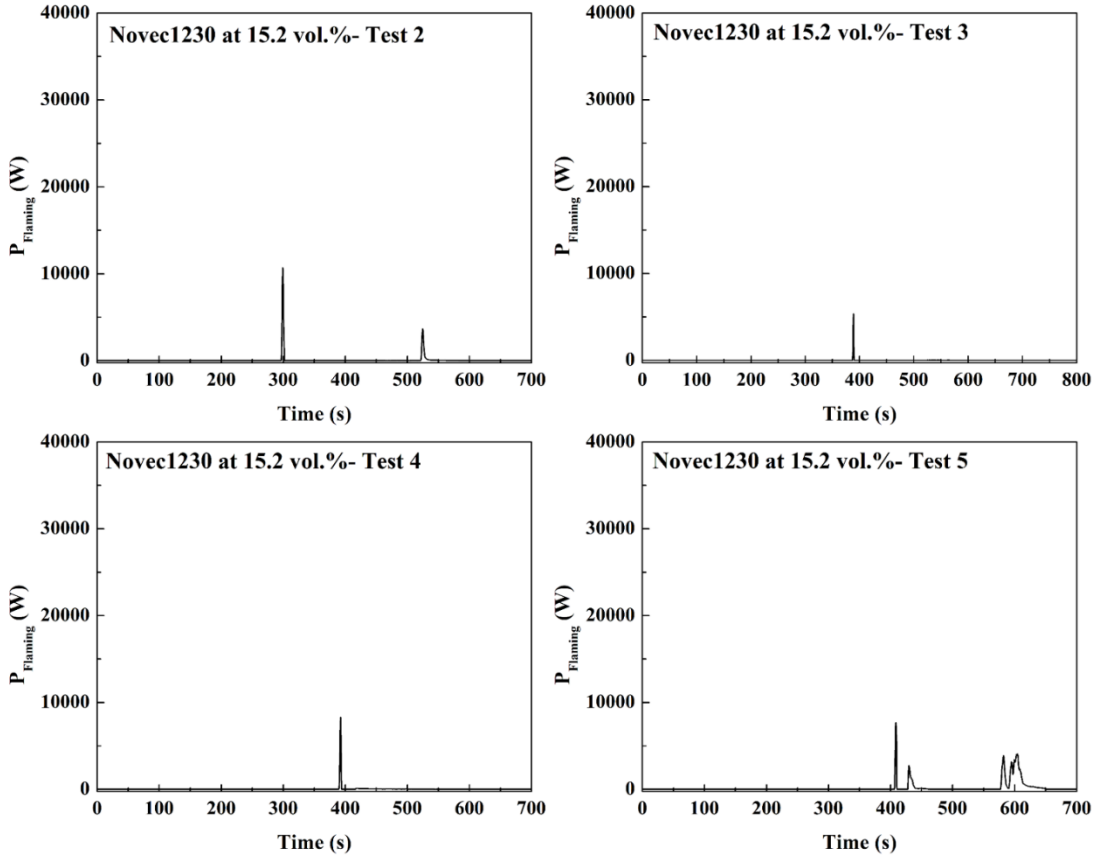

Figure C. 47. Heat release rate due to flaming combustion of ejected materials from 12 LCO cell array tested in air and suppressed with Novec1230 at 15.2 vol.%. Test repetitions 2, 3, 4, and 5.

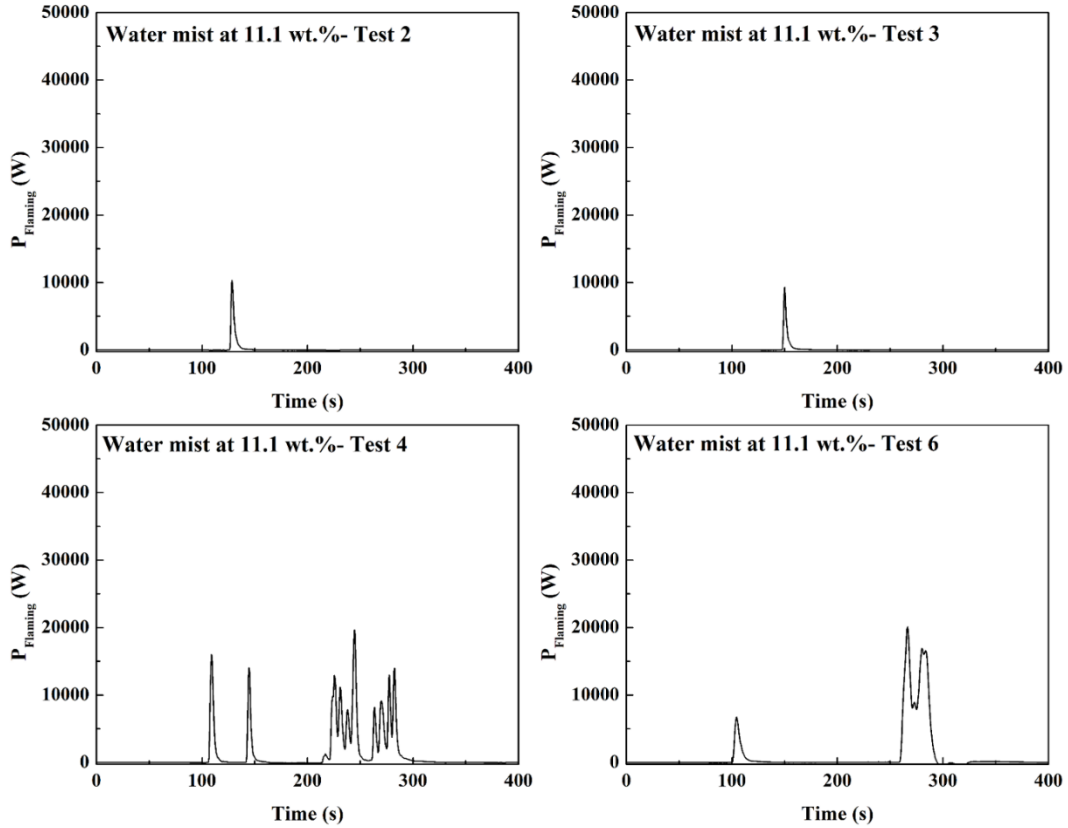

Figure C. 48. Heat release rate due to flaming combustion of ejected materials from 12 LCO cell array tested in air and suppressed with water mist at 11.1 wt.%. Test repetitions 2, 3, 4, and 5.

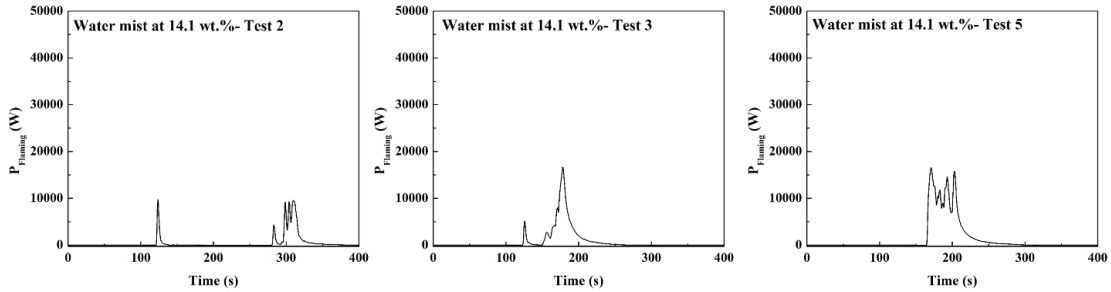

Figure C. 49. Heat release rate due to flaming combustion of ejected materials from 12 LCO cell array tested in air and suppressed with water mist at 14.1 wt.%. Test repetitions 2, 3, and 5.

References

[1] Poizot P, Dolhem F, Clean energy new deal for a sustainable world: from non-CO_2 generating energy sources to greener electrochemical storage devices, Energy & Environmental Science, 2011;4: 2003-19.

[2] Wang Q, Ping P, Zhao X, Chu G, Sun J, Chen C, Thermal runaway caused fire and explosion of lithium ion battery, Journal of Power Sources, 2012;208: 210-24.

[3] Wang Q, Mao B, Stoliarov SI, Sun J, A review of lithium ion battery failure mechanisms and fire prevention strategies, Progress in Energy and Combustion Science, 2019;73: 95-131.

[4] Linden D, Reddy TB, Handbook of batteries, 3rd ed., McGraw-Hill, New York, USA, 2001. ISBN 0-07-135978-8.

[5] https://www.bloomberg.com/news/articles/2016-09-18/quicktake-q-a-samsung-and-its-lithium-ion-battery-headache.

[6] https://www.bloomberg.com/news/articles/2018-05-15/electric-car-era-threatens-firefighters-with-new-roadside-risks.

[7] Maloney T, Dadia DD, Passive protection of lithium battery shipments, Report no. DOT/FAA/TC-15/38, U.S. Department of Transportation, 2016.

[8] Maloney T, Lithium battery thermal runaway vent gas analysis, Report no. DOT/FAA/TC-15/59, U.S. Department of Transportation, 2016.

[9] Maloney T, Impact of lithium battery vent gas ignition on cargo compartment fire protection, Report no. DOT/FAA/TC-16/34, U.S. Department of Transportation, 2016.

[10] Walters R N, Lyon RE, Measuring energy release of lithium-ion battery failure using a bomb calorimeter, Report no. DOT/FAA/TC-15/40, U.S. Department of Transportation, 2016.

[11] Quintiere JQ, Crowley SB, Walters RN, R.E. Lyon, D. Blake, Fire hazards of lithium batteries, Report no. DOT/FAA/TC-TN15/17, U.S. Department of Transportation, 2016.

[12] https://www.richtek.com/battery-management/en/designing-liion.html.

[13] https://batteryuniversity.com/learn/article/a_look_at_cell_formats_and_how_to_build_a_good_battery.

[14] Balakrishnan PG, Ramesh R, Kumar TP, Safety mechanisms in lithium-ion batteries, Journal of Power Sources, 2006;155: 401-14.

[15] van Schalkwijk WA, Scrosati B, Advances in lithium-ion batteries, 1st ed., Springer US, New York, 2002, ISBN 978-0-306-47508-5.

[16] Yuan X, Liu H, Zhang J, Lithium-ion batteries: advanced materials and technologies, CRC press, 2011. ISBN 978-1-4398-4128-0.

[17] BASF, Material safety data sheet of propylene carbonate, Document no. 30073261/SDS_GEN_US/EN. https://worldaccount.basf.com/wa/NAFTA/Catalog/ChemicalsNAFTA/doc4/BASF/PRD/30073261/.pdf?asset_type=msds/pdf&language=EN&validArea=US&urn=urn:documentum:ProductBase_EU:09007af8800980d9.pdf

[18] Mikolajczak C, Kahn M, Whitle K, Long RT, Lithium-ion batteries hazard and use assessment, Document no. 1100034.000 A0F0 0711 CM01, 2011. http://www.prba.org/wp-content/uploads/Exponent_Report_for_NFPA_-_20111.pdf

[19] Harris SJ, Timmons A, Pitz WJ, A combustion chemistry analysis of carbonate solvents used in Li-ion batteries, Journal of Power Sources, 2009;193: 855-58.

[20] An SJ, Li J, Du Z, Daniel C, Wood DL, Fast formation cycling for lithium ion batteries, Journal of Power Sources, 2017;342: 846-52.

[21] Mikolajczak C, Kahn M, White K, Long RT, Lithium-ion batteries hazard and use assessment, Springer, Boston, 2011. ISBN 978-1-4614-3485-6.

[22] http://power-topics.blogspot.com/2016/05/constant-voltage-constant-current.html

[23] Finegan DP, Darcy E, Keyser M, Tjaden B, Heenan TMM, Jervis R, Bailey JJ, Vo NT, Magdysyuk OV, Drakopoulos M, Michiel MD, Rack A, Hinds G, Brett DJL, Shearing PR, Identifying the cause of rupture of li-ion batteries during thermal runaway, Advanced Science, 2018;5: 170036.

[24] Said AO, Liu X, Wu Z, Lee C, Stoliarov SI. Time resolved analysis of thermal failure of prismatic lithium ion batteries. 10th U.S. National Combustion Meeting, 23-26 April (2017); College Park; Maryland; USA.

[25] Said AO, Lee C, Liu X, Wu Z, Stoliarov SI, Simultaneous measurement of multiple thermal hazards associated with a failure of prismatic lithium ion battery, Proceedings of the Combustion Institute, 2019;37: 4173-80.

[26] Liu X, Wu Z, Stoliarov SI, Denlinger M, Masias A, Snyder K, A thermo-kinetic model of thermally-induced failure of a lithium ion battery: development, validation and application, Journal of The Electrochemical Society, 2018;165: 10.

[27] Richard MN, Dahn JR, Accelerating rate calorimetry study on the thermal stability of lithium intercalated graphite in electrolyte I. Experimental, Journal of The Electrochemical Society, 1999;146: 2068-77.

[28] Wang QS, Sun JH, Yao XL, Chen CH, Thermal behavior of lithiated graphite with electrolyte in lithium-ion batteries, Journal of The Electrochemical Society, 2006;153: A329-A33.

[29] Spotnitz R, Franklin J, Abuse behavior of high-power, lithium-ion cells, Journal of Power Sources, 2003;113: 81-100.

[30] Wang Q, Sun J, Chen C, Effects of solvents and salt on the thermal stability of lithiated graphite used in lithium ion battery, Journal of Hazardous Materials, 2009;167: 1209-14.

[31] Jiang J, Dahn JR, Effects of particle size and electrolyte salt on the thermal stability of $Li_{0.5}$ CoO_2, Electrochimica Acta, 2004;49: 2661-66.

[32] Yang H, Shen X-D, Dynamic TGA–FTIR studies on the thermal stability of lithium/graphite with electrolyte in lithium-ion cell, Journal of Power Sources, 2007;167: 515-19.

[33] Kawamura T, Kimura A, Egashira M, Okada S, Yamaki J-I, Thermal stability of alkyl carbonate mixed-solvent electrolytes for lithium ion cells, Journal of Power Sources, 2002;104: 260-64.

[34] Wang Q, Sun J, Yao X, Chen C, Thermal stability of LiPF6/EC+DEC electrolyte with charged electrodes for lithium ion batteries, Thermochimica Acta, 2005;437: 12-16.

[35] Du Pasquier A, Disma F, Bowmer T, Gozdz AS, Amatucci G, Tarascon JM, Differential Scanning Calorimetry Study of the Reactivity of Carbon Anodes in Plastic Li-Ion Batteries, Journal of The Electrochemical Society, 1998;145: 472-77.

[36] Biensan P, Simon B, Peres JP, de Guibert A, Broussely M, Bodet JM, Perton F, On safety of lithium-ion cells, Journal of Power Sources, 1999;81: 906-12.

[37] Maleki H, Deng GP, Anani A, Howard J, Thermal stability studies of Li-ion cells and components, Journal of The Electrochemical Society, 1999;146: 3224-29.

[38] MacNeil DD, Lu Z, Chen Z, Dahn JR, A comparison of the electrode/electrolyte reaction at elevated temperatures for various Li-ion battery cathodes, Journal of Power Sources, 2002;108: 8-14.

[39] Roth EP, Doughty DH, Franklin J, DSC investigation of exothermic reactions occurring at elevated temperatures in lithium-ion anodes containing PVDF-based binders, Journal of Power Sources, 2004;134: 222-34.

[40] Yang H, Bang H, Amine K, Prakash J, Investigations of the exothermic reactions of natural graphite anode for Li-ion batteries during thermal runaway, Journal of The Electrochemical Society, 2005;152: A73-A79.

[41] Townsend DI, Tou JC, Thermal Hazard Evaluation by an Accelerating Rate Calorimeter, Thermochimica Acta, 1980;37: 1-30.

[42] von Sacken U, Nodwell E, Sundher A, Dahn JR, Comparative thermal stability of carbon intercalation anodes and lithium metal anodes for rechargeable lithium batteries, Journal of Power Sources, 1995;54: 240-45.

[43] Maleki H, Howard JN, Role of the cathode and anode in heat generation of Li-ion cells as a function of state of charge, Journal of Power Sources, 2004;137: 117-27.

[44] Al Hallaj S, Maleki H, Hong JS, Selman JR, Thermal modeling and design considerations of lithium-ion batteries, Journal of Power Sources, 1999;83: 1-8.

[45] Feng X, Fang M, He X, Ouyang M, Lu L, Wang H, Zhang M, Thermal runaway features of large format prismatic lithium ion battery using extended volume accelerating rate calorimetry, Journal of Power Sources, 2014;255: 294-301.

[46] Jhu CY, Wang YW, Wen CY, Chiang CC, Shu CM, Self-reactive rating of thermal runaway hazards on 18650 lithium-ion batteries, Journal of Thermal Analysis and Calorimetry, 2011;106: 159-63.

[47] Jhu CY, Wang YW, Shu CM, Chang JC, Wu HC, Thermal explosion hazards on 18650 lithium ion batteries with a VSP2 adiabatic calorimeter, Journal of Hazardous Materials, 2011;192: 99-107.

[48] Wen C-Y, Jhu C-Y, Wang Y-W, Chiang C-C, Shu C-M, Thermal runaway features of 18650 lithium-ion batteries for LiFePO4 cathode material by DSC and VSP2, Journal of Thermal Analysis and Calorimetry, 2012;109: 1297-302.

[49] Wang Q, Sun J, Yao X, Chen C, C80 calorimeter studies of the thermal behavior of LiPF6 solutions, Journal of Solution Chemistry, 2006;35: 179-89.

[50] Wang QS, Sun JH, Yao XL, Chen CH, Micro calorimeter study on the thermal stability of lithium-ion battery electrolytes, Journal of Loss Prevention in the Process Industries, 2006;19: 561-69.

[51] Wang QS, Sun JH, Chen CH, Zhou XM, Thermal properties and kinetics study of charged LiCoO2 by TG and C80 methods, Journal of Thermal Analysis and Calorimetry, 2008;92: 563-66.

[52] Lyon RE, Walters RN, Energetics of lithium ion battery failure, Journal of Hazardous Materials, 2016;318: 164-72.

[53] Liu X, Stoliarov SI, Denlinger M, Masias A, Snyder K, Comprehensive calorimetry of the thermally-induced failure of a lithium ion battery, Journal of Power Sources, 2015;280: 516-25.

[54] Liu X, Wu ZB, Stoliarov SI, Denlinger M, Masias A, Snyder K, Heat release during thermally-induced failure of a lithium ion battery: Impact of cathode composition, Fire Safety Journal, 2016;85: 10-22.

[55] Quintiere JG, On methods to measure the energetics of a lithium ion battery in thermal runaway, Fire Safety Journal, 2020;111: 102911.

[56] Ribiere P, Grugeon S, Morcrette M, Boyanov S, Laruelle S, Marlair G, Investigation on the fire-induced hazards of Li-ion battery cells by fire calorimetry, Energy & Environmental Science, 2012;5: 5271-80.

[57] Brohez S, Marlair G, Delvosalle C, Fire calorimetry relying on the use of the fire propagation apparatus. Part I: early learning from use in Europe, Fire and Materials, 2006;30: 131-49.

[58] ASTM, Standard test method for heat and visible smoke release rates for materials and products using an oxygen consumption calorimeter, E1354 − 16a, 2016.

[59] Ping P, Wang Q, Huang P, Li K, Sun J, Kong D, Chen C, Study of the fire behavior of high-energy lithium-ion batteries with full-scale burning test, Journal of Power Sources, 2015;285: 80-89.

[60] Wang Q, Huang P, Ping P, Du Y, Li K, Sun J, Combustion behavior of lithium iron phosphate battery induced by external heat radiation, Journal of Loss Prevention in the Process Industries, 2017;49: 961-69.

[61] Larsson F, Andersson P, Blomqvist P, Lorén A, Mellander B-E, Characteristics of lithium-ion batteries during fire tests, Journal of Power Sources, 2014;271: 414-20.

[62] Sun J, Li J, Zhou T, Yang K, Wei S, Tang N, Dang N, Li H, Qiu X, Chen L, Toxicity, a serious concern of thermal runaway from commercial Li-ion battery, Nano Energy, 2016;27: 313-19.

[63] Andersson P, Blomqvist P, Lorén A, Larsson F, Using Fourier transform infrared spectroscopy to determine toxic gases in fires with lithium-ion batteries, Fire and Materials, 2016;40: 999-1015.

[64] Bertilsson S, Larsson F, Furlani M, Albinsson I, Mellander B-E, Lithium-ion battery electrolyte emissions analyzed by coupled thermogravimetric/Fourier-transform infrared spectroscopy, Journal of Power Sources, 2017;365: 446-55.

[65] Larsson F, Bertilsson S, Furlani M, Albinsson I, Mellander B-E, Gas explosions and thermal runaways during external heating abuse of commercial lithium-ion graphite-LiCoO 2 cells at different levels of ageing, Journal of Power Sources, 2018;373: 220-31.

[66] Fernandes Y, Bry A, de Persis S, Identification and quantification of gases emitted during abuse tests by overcharge of a commercial Li-ion battery, Journal of Power Sources, 2018;389: 106-19.

[67] Larsson F, Andersson P, Blomqvist P, Mellander BE, Toxic fluoride gas emissions from lithium-ion battery fires, Sci Rep, 2017;7: 10018.

[68] Park S, Jung D, Battery cell arrangement and heat transfer fluid effects on the parasitic power consumption and the cell temperature distribution in a hybrid electric vehicle, Journal of Power Sources, 2013;227: 191-98.

[69] Li X, He F, Ma L, Thermal management of cylindrical batteries investigated using wind tunnel testing and computational fluid dynamics simulation, Journal of Power Sources, 2013;238: 395-402.

[70] Yang N, Zhang X, Li G, Hua D, Assessment of the forced air-cooling performance for cylindrical lithium-ion battery packs: A comparative analysis between aligned and staggered cell arrangements, Applied Thermal Engineering, 2015;80: 55-65.

[71] Sabbah R, Kizilel R, Selman JR, Al-Hallaj S, Active (air-cooled) vs. passive (phase change material) thermal management of high power lithium-ion packs: Limitation of temperature rise and uniformity of temperature distribution, Journal of Power Sources, 2008;182: 630-38.

[72] Kizilel R, Lateef A, Sabbah R, Farid MM, Selman JR, Al-Hallaj S, Passive control of temperature excursion and uniformity in high-energy Li-ion battery packs at high current and ambient temperature, Journal of Power Sources, 2008;183: 370-75.

[73] Lamb J, Orendorff CJ, Steele LAM, Spangler SW, Failure propagation in multi-cell lithium ion batteries, Journal of Power Sources, 2015;283: 517-23.

[74] Feng XN, Sun J, Ouyang MG, Wang F, He XM, Lu LG, Peng HE, Characterization of penetration induced thermal runaway propagation process within a large format lithium ion battery module, Journal of Power Sources, 2015;275: 261-73.

[75] Ouyang D, Liu J, Chen M, Weng J, Wang J, Thermal failure propagation in lithium-ion battery modules with various shapes, Applied Sciences, 2018;8: 1263.

[76] Lopez CF, Jeevarajan JA, Mukherjee PP, Experimental analysis of thermal runaway and propagation in lithium-ion battery modules, Journal of The Electrochemical Society, 2015;162: A1905-A15.

[77] Zhong GB, Li H, Wang C, Xu KQ, Wang QS, Experimental analysis of thermal runaway propagation risk within 18650 lithium-ion battery modules, Journal of The Electrochemical Society, 2018;165: A1925-A34.

[78] Summer SM. Flammability assessment of lithium-ion and lithium-ion polymer battery cells designed for aircraft power usage, Report no. DOT/FAA/AR-09/55, U.S. Department of Transportation, 2010.

[79] Wang Q, Li K, Wang Y, Chen H, Duan Q, Sun J, The efficiency of dodecafluoro-2-methylpentan-3-one on suppressing the lithium ion battery fire, Journal of Electrochemical Energy Conversion and Storage, 2018;15.

[80] Liu Y, Duan Q, Xu J, Chen H, Lu W, Wang Q, Experimental study on the efficiency of dodecafluoro-2-methylpentan-3-one on suppressing lithium-ion battery fires, RSC Advances, 2018;8: 42223-32.

[81] Ditch B, The impact of thermal runaway on sprinkler protection recommendations for warehouse storage of cartoned lithium-ion batteries, Fire Technology, 2017;54: 359-77.

[82] Liu T, Liu Y, Wang X, Kong X, Li G, Cooling control of thermally-induced thermal runaway in 18,650 lithium ion battery with water mist, Energy Conversion and Management, 2019;199: 111969.

[83] Doughty DH, Butler PC, Jungst RG, Roth EP, Lithium battery thermal models, Journal of Power Sources, 2002;110: 357-63.

[84] Pals CR, Thermal modeling of the lithium/polymer battery, Journal of The Electrochemical Society, 1995;142: 3274.

[85] Pals CR, Thermal modeling of the lithium/polymer battery, Journal of The Electrochemical Society, 1995;142: 3282.

[86] Forgez C, Vinh Do D, Friedrich G, Morcrette M, Delacourt C, Thermal modeling of a cylindrical LiFePO4/graphite lithium-ion battery, Journal of Power Sources, 2010;195: 2961-68.

[87] Chen S-C, Wang Y-Y, Wan C-C, Thermal analysis of spirally wound lithium batteries, Journal of The Electrochemical Society, 2006;153: A637.

[88] Chen SC, Wan CC, Wang YY, Thermal analysis of lithium-ion batteries, Journal of Power Sources, 2005;140: 111-24.

[89] Hatchard TD, MacNeil DD, Basu A, Dahn JR, Thermal model of cylindrical and prismatic lithium-ion cells, Journal of The Electrochemical Society, 2001;148: A755.

[90] Kim G-H, Pesaran A, Spotnitz R, A three-dimensional thermal abuse model for lithium-ion cells, Journal of Power Sources, 2007;170: 476-89.

[91] Guo G, Long B, Cheng B, Zhou S, Xu P, Cao B, Three-dimensional thermal finite element modeling of lithium-ion battery in thermal abuse application, Journal of Power Sources, 2010;195: 2393-98.

[92] Feng XN, He XM, Ouyang MG, Lu LG, Wu P, Kulp C, Prasser S, Thermal runaway propagation model for designing a safer battery pack with 25 Ah LiNixCoyMnzO2 large format lithium ion battery, Applied Energy, 2015;154: 74-91.

[93] Feng XN, Lu LG, Ouyang MG, Li JQ, He XM, A 3D thermal runaway propagation model for a large format lithium ion battery module, Energy, 2016;115: 194-208.

[94] Wang T, Tseng KJ, Zhao J, Wei Z, Thermal investigation of lithium-ion battery module with different cell arrangement structures and forced air-cooling strategies, Applied Energy, 2014;134: 229-38.

[95] Tenergy Co., Specification approval sheet: T-energy ICR18650 lithium ion battery, Model: 30005–0. 2010; Available from: http://www.all-battery.com/datasheet/30005-0_datasheet.pdf.

[96] LG Co., Specification approval sheet: LG HG218650 lithium ion battery. Available from: https://www.18650batterystore.com/v/files/lg_hg2_data_sheet.pdf.

[97] K2energy, Specification approval sheet: K2energy lithium ion battery, model: K218650E02; Available from: https://k2battery.com/product/k2-lithium-ion-energy-cells-3/.

[98] Tenergy Co., Material safety data sheet 2015; Available from: https://www.robotshop.com/media/files/pdf2/tenergy_li-ion_sds_2016.pdf.

[99] Tenergy Co., Material safety data sheet, 2017; Available from: https://www.mouser.com/catalog/additional/Parallax_Li_ion_SDS_2017.pdf.

[100] K2energy, Material safety data sheet, 2017; Available from: https://k2battery.com/request-a-data-sheet/.

[101] LG, Material safety data sheet, 2015; Available from: http://www.idealind.mx/pdf/msds/lg-li-ion-msds.pdf.

[102] LG, Material safety data sheet, 2016; Available from: http://www.batteryspace.com/prod-specs/6626_1.pdf.

[103] Said AO, Lee C, Stoliarov SI, Marshall AW, Comprehensive analysis of dynamics and hazards associated with cascading failure in 18650 lithium ion cell arrays, Applied Energy, 2019;248: 415-28.

[104] Said AO, Lee C, Stoliarov SI, Experimental investigation of cascading failure in 18650 lithium ion cell arrays: Impact of cathode chemistry, Journal of Power Sources, 2020;446: 227347.

[105] Said AO, Lee C, Stoliarov SI. Comprehensive analysis of dynamics and hazards associated with cascading failure in lithium-ion cell arrays. 11th U.S. National Combustion Meeting; 24-27 March (2019); Pasadena; California; USA.

[106] Lee C, Said AO, Stoliarov SI, Impact of state of charge and cell arrangement on thermal runaway propagation in lithium ion battery cell arrays, Transportation Research Record, 2019;2673: 408-17.

[107] Lee C, Said AO, Stoliarov SI, Passive mitigation of thermal runaway propagation in dense 18650 lithium ion cell assemblies, The Journal of The Electrochemical Society, (Submitted January 2020), (Manuscript ID JES-100432).

[108] https://www.tfpglobal.com/products/fire-protection.

[109] http://www.lynnmfg.com/wp-content/uploads/2015/10/DATA-TC-514-700.pdf.

[110] Leventon IT, Li J, Stoliarov SI, A flame spread simulation based on a comprehensive solid pyrolysis model coupled with a detailed empirical flame structure representation, Combustion and Flame, 2015;162: 3884-95.

[111] Mousavi M, Hoque S, Rahnamayan S, Dincer I, Naterer GF, Optimal design of an air-cooling system for a li-ion battery pack in electric vehicles with a genetic algorithm, 2011 Ieee Congress on Evolutionary Computation (Cec), 2011: 1848-55.

[112] Bergman TL, Lavine AS, Incropera FP, Dewitt DP, Fundamentals of heat and mass transfer, 7th ed., John Wiley & Sons, Inc., New York, 2011. ISBN 978-0470917855.

[113] https://www.3m.com/3M/en_US/novec-us/applications/fire-suppression/.

[114] Downie B, Polymeropoulos C, Gogos G, Interaction of a water mist with a buoyant methane diffusion flame, Fire Safety Journal, 1995;24: 359-81.

[115] Ndubizu CC, Ananth R, Tatem PA, Motevalli V, On water mist fire suppression mechanisms in a gaseous diffusion flame, Fire Safety Journal, 1998;31: 253-76.

[116] Ananth R, Mowrey RC, Ultra-fine water mist extinction dynamics of a co-flow diffusion flame, Combustion Science and Technology, 2008;180: 1659-92.

[117] White JP, Verma S, Keller E, Hao A, Trouvé A, Marshall AW, Water mist suppression of a turbulent line fire, Fire Safety Journal, 2017;91: 705-13.

[118] Yoshida A, Kashiwa K, Hashizume S, Naito H, Inhibition of counterflow methane/air diffusion flame by water mist with varying mist diameter, Fire Safety Journal, 2015;71: 217-25.

[119] Santangelo PE, Characterization of high-pressure water-mist sprays: Experimental analysis of droplet size and dispersion, Experimental Thermal and Fluid Science, 2010;34: 1353-66.

[120] M.J. Hurley, SFPE handbook of fire protection engineering, Springer, New York, 2016. ISBN 978-1-4939-2565-0.

[121] McAllister S, Chen JY, Fernandez-Pello AC, Fundamentals of combustion processes, Springer-Verlag New York Inc. , New York, 2011. ISBN 978-1-4419-7943-8.

[122] Borgnakke C, Sonntag RE, Fundamentals of thermodynamics, 7th ed., John Wiley & Sons, Inc., New York, 2009. ISBN 978-0470041925.

[123] Butland ATD, Maddison RJ, The specific heat of graphite: An evaluation of measurements, Journal of Nuclear Materials, 1973;49: 45-56.

[124] Orfanidis SJ, Introduction to signal processing, Prentice-Hall, Inc., 1996. ISBN: 0-13-209172-0.

[125] Bandhauer TM, Garimella S, Fuller TF, A critical review of thermal issues in lithium-ion batteries, Journal of The Electrochemical Society, 2011;158: R1.

[126] Feng X, Ouyang M, Liu X, Lu L, Xia Y, He X, Thermal runaway mechanism of lithium ion battery for electric vehicles: A review, Energy Storage Materials, 2018;10: 246-67.

[127] Pagliaro JL, Linteris GT, Sunderland PB, Baker PT, Combustion inhibition and enhancement of premixed methane–air flames by halon replacements, Combustion and Flame, 2015;162: 41-49.

[128] Xu W, Jiang Y, Ren X, Combustion promotion and extinction of premixed counterflow methane/air flames by C6F12O fire suppressant, Journal of Fire Sciences, 2016;34: 289-304.